5-2019

Simulations of Unsteady Shocks via a Finite-Element Solver with High-Order Spatial and Temporal Accuracy

Kevin Raymond Holst
University of Tennessee, kholst@vols.utk.edu

To the Graduate Council:

I am submitting herewith a dissertation written by Kevin Raymond Holst entitled "Simulations of Unsteady Shocks via a Finite-Element Solver with High-Order Spatial and Temporal Accuracy." I have examined the final electronic copy of this dissertation for form and content and recommend that it be accepted in partial fulfillment of the requirements for the degree of Doctor of Philosophy, with a major in Aerospace Engineering.

John Schmisseur, Major Professor

We have read this dissertation and recommend its acceptance:

Ryan Glasby, James Coder, Ryan Bond, Gregory Peterson

Accepted for the Council:

Dixie L. Thompson

Vice Provost and Dean of the Graduate School

(Original signatures are on file with official student records.)

Simulations of Unsteady Shocks via a Finite-Element Solver with High-Order Spatial and Temporal Accuracy

A Dissertation Presented for the

Doctor of Philosophy

Degree

The University of Tennessee, Knoxville

Kevin Raymond Holst

May 2019

Acknowledgments

I would like to thank my advisor and committee chair, Dr. John Schmisseur, for his support, for his patience, and for his advice over the past several years. I would also like to thank Dr. Ryan Glasby for the invaluable guidance and encouragement that he has provided me throughout this project, and I am grateful that I will be continuing this work with you. I give my sincere gratitude to my committee members: Dr. Ryan Bond, Dr. James Coder, and Dr. Gregory Peterson. You have been very generous with your knowledge and your time, and I hope to have the opportunity to pay it forward to future students. Finally I would like thank my family and friends for their companionship through this journey. I truly believe that your love and support are the reasons that I have completed this task with my sanity and hair largely intact.

I think that when we know that we actually do live in uncertainty, then we ought to admit it; it is of great value to realize that we do not know the answers to different questions. This attitude of mind – this attitude of uncertainty – is vital to the scientist, and it is this attitude of mind which the student must first acquire.

RICHARD P. FEYNMAN

Abstract

This research aims to improve the modeling of stationary and moving shock waves by adding an unsteady capability to an existing high-spatial-order, finite-element, streamline upwind/Petrov-Galerkin (SU/PG), steady-state solver and using it to examine a novel shock capturing technique. Six L-stable, first- through fourth-order time-integration methods were introduced into the solver, and the resulting unsteady code was employed on three canonical test cases for verification and validation purposes: the two-dimensional convecting inviscid isentropic vortex, the two-dimensional circular cylinder in cross flow, and the Taylor-Green vortex. Shock capturing is accomplished in the baseline solver through the application of artificial diffusion in supersonic cases. When applied to inviscid problems, especially those with blunt bodies, numerical errors from the baseline shock sensor accumulated in stagnation regions, resulting in non-physical wall heating. Modifications were made to the solver's shock capturing approach that changed the calculation of the artificial diffusion flux term ($\boldsymbol{F}_{ad}$) and the shock sensor. The changes to $\boldsymbol{F}_{ad}$ were designed to vary the application of artificial diffusion directionally within the momentum equations. A novel discontinuity sensor, derived from the entropy gradient, was developed for use on inviscid cases. The new sensor activates for shocks, rapid expansions, and other flow features where the grid is insufficient to resolve the high-gradient phenomena. This modified shock capturing technique was applied to three inviscid test cases: the blunt-body bow shock of Murman, the planar Noh problem, and the Mach 3 forward-facing step of Colella and Woodward.

Table of Contents

List of Tables

List of Figures

Nomenclature

Latin

A_{ij}	Deviator of strain rate tensor
a_{ij}	RK matrix values
b_i	RK weights
c_i	RK nodes
D	Diameter
$\mathcal{E}$	Enstrophy
e	Internal energy
$\boldsymbol{F}$	Flux vector
f	Function or frequency
h	Length scale or enthalpy
k	General order of accuracy
Kn	Knudsen number
M	Mach number
$\mathcal{M}$	Riemannian metric tensor
p	Pressure or spatial order of accuracy

$\boldsymbol{Q}$	Conservation variables
q	Solution variable
$\boldsymbol{R}$	Residual vector
R	Gas constant
$R(z)$	Numerical stability function
r, s, t	Computational domain coordinates
Re	Reynolds number
$\tilde{s}$	Exponential entropy
S	Numerical stability region
s	Number of RK stages or entropy
S_{ij}	Strain rate tensor
St	Strouhal number
Δt	Time step size
T	Temperature
t	Time
$\boldsymbol{u}$	Velocity vector
u, v, w	Velocity components
x, y, z	Cartesian coordinates

Greek

α	Angle
δ_{ij}	Kronecker delta

ϵ	Numerical error
$\epsilon_{\tilde{s}}$	Exponential-entropy gradient sensor
ϵ_{shock}	Shock indicator
η_h	Homotopy diffusion coefficient
γ	Ratio of specific heats
κ	Shock sensor parameter
λ	Second viscosity coefficient or wave speed
μ	Viscosity
ϕ_i	Finite-element basis functions
ρ	Density or correlation coefficient
σ	Standard deviation
τ	Time step size or viscous stress tensor

Superscripts

$\prime$	Derivative with respect to independent variable

Subscripts

∞	Freestream
ad	Artificial diffusion
b	Bulk viscosity component
c	Convection component
D	Discretized
disp	Dispersive component

diss	Dissipative component
s	Spatial
T	True
t	Temporal
t	Total
tot	Total
v	Viscous component

Acronyms

ABV	Artificial bulk viscosity
BDF	Backward differential formulae
BVP	Boundary value problem
CFD	Computational fluid dynamics
CFL	Courant-Fredrichs-Lewy
COFFE	Conservative Field Finite Element
CREATE-AV	Computational Research and Engineering for Acquisition Tools and Environments - Air Vehicles
DG	Discontinuous Galerkin
DIRK	Diagonally implicit Runge-Kutta
DoD	Department of Defense
DOF	Degree of freedom
ENO	Essentially non-oscillatory

FDM	Finite-difference method
FEM	Finite-element method
FIRK	Fully implicit Runge-Kutta
FVM	Finite-volume method
GFEM	Generalized finite-element method
HPCMP	High Performance Computer Modernization Program
KHI	Kelvin-Helmholtz instability
LES	Large eddy simulation
PG	Petrov-Galerkin
PUM	Partition of unity method
RK	Runge-Kutta
RK4	4^{th}-order explicit Runge-Kutta method
SBLI	Shock/boundary layer interaction
SDIRK	Singly diagonally implicit Runge-Kutta
SPD	Symmetric positive definite
SU/PG	Streamline upwind/Petrov-Galerkin
V&V	Verification and validation
XFEM	Extended finite-element method

Chapter 1

Introduction

1.1 Motivation and Research Goals

Modeling shock waves in an Eulerian reference frame with computational fluid dynamics (CFD) is a very challenging endeavor, due in large part to non-linear changes in field properties that occur over a distance on the order of the mean free path. [1, 2] Modeling *moving* shock waves further increases the complexity of the problem because the phenomenon must be resolved as it convects across grid cells. As the demand for high-speed flight vehicles in both the military and commercial sectors increases, [3–5] so too does the need for adequate simulation techniques to model phenomena that arise from interactions between high-speed flow and structures with complex geometries. The extreme dynamic surface loads generated by unsteady shock/boundary layer interactions (SBLI) are a perfect illustration of the challenges facing designers of high-speed flight vehicles. [6, 7] Advancing the state of the art in this area of modeling and simulation will aid in the creation of new high-speed aircraft and reduce the overall time needed to develop and operate complex systems.

The vast majority of CFD work is conducted using codes that are spatially and temporally first- or second-order accurate, where order of accuracy describes how the overall error behaves with respect to the spatial or temporal scale, h, and a kth order scheme means that error is proportional to h^k. *Higher-order*[1] schemes, have mostly been relegated to

[1] Wang et al. [8] define "higher-order" as 3rd-order or greater.

the research community, in part because for years 2^{nd}-order codes have produced solutions accurate enough for most engineering applications.

In the published review article "High-order CFD methods: current status and perspective," Wang et al. [8] discuss the motivations for and results from the 1^{st} International Workshop on High-Order CFD Methods, held prior to the American Institute of Aeronautics and Astronautics 50^{th} Aerospace Sciences Meeting. In this article Wang et al. contend that there are no special properties of 2^{nd}-order schemes that ideally suit them for efficient simulations. The higher accuracy and lower numerical dissipation of higher-order schemes make them especially well suited to tackle vortex-dominated flows and aeroacoustics, and although lower-order schemes may produce acceptable levels of error for key parameters, those errors may compound and reach unacceptable levels for others.

Unsteady calculations contain both spatial and temporal discretization errors. High-order schemes are typically focused on decreasing errors related to spatial discretization, but recent research [9, 10] has shown that higher-order temporal schemes play a critical role in lowering the overall error by reducing the component resulting from temporal discretization. Explicit time-stepping schemes like the common 4^{th}-order Runge-Kutta (RK4) offer minimal temporal error, but they can place burdensome requirements on the size of the time step, Δt, when resolving small spatial scales, like those within boundary layers. Implicit methods eliminate the time step size requirement; however, they are often more difficult to implement because they require the formation of a matrix and the solution of a linear algebra problem, $\boldsymbol{A}x = b$. The most commonly used implicit methods, the backward differential formulae 1 and 2 (BDF1 and BDF2), are first or second-order accurate, respectively. Given the definition of higher-order schemes, it stands to reason that an unsteady higher-order code should be 3^{rd}-order, or higher, accurate with respect to both spatial *and* temporal discretizations.

NASA's CFD Vision 2030 document [11] is a forecast of the CFD technologies that will be required in 2030, according to a broad group of experts in aerodynamics, aerospace engineering, applied mathematics, and computer science, and recommendations for reaching these goals. Recommendation 1 in the document describes the development of a Revolutionary Computational Aerosciences (RCA) Program, and within this program, higher-order discretizations are identified as emphasis areas. The document states that the

use of higher-order methods could lead to more accurate and scalable solvers, and that "the demonstration of complete configuration-grid convergence technology in the 2020 time frame relies on the use of robust higher-order discretizations combined with improved scalable solvers and adaptive h-p refinement." [11]

Wang et al. [8] state that "robust, accuracy-preserving, and parameter-free shock capturing" for steady flow problems with higher-order discretizations is one area that is in need of development. Some research has been conducted in this area, [12–15] but more work is needed, especially in the area of *un*steady shock problems. If progress is made with respect to unsteady shock capturing, higher-order solvers may play a critical role in increasing the aerospace community's understanding of SBLIs, which often feature prominent, unsteady vortical structures in separated regions.

The goal of this research was to assess the ability of a finite-element CFD solver with high spatial and temporal order of accuracy to model stationary and moving shocks on non-shock-aligned grids. To this end, a high-temporal-order time integration capability was introduced into the high-spatial-order, finite-element, steady-state CFD solver, Conservative Field Finite Element (COFFE) CFD solver, developed by the Department of Defense (DoD) High Performance Computer Modernization Program Computational Research and Engineering for Acquisition Tools and Environments - Air Vehicles (HPCMP CREATE^{TM}-AV) Program. Verification and validation tests were conducted on these components to ensure that methods were implemented properly and that the results conform to experimental results and other accepted numerical solutions. Finally a new artificial diffusion shock capturing technique was implemented in COFFE, and several cases were run to assess the ability of the newly-extended, unsteady, high-order solver to simulate flow fields containing stationary and moving shock waves on a variety of grid types.

1.2 Outline of Document

In Chapter 2 of this document, the current state of the art is reported with respect to three specific areas of interest: the underlying method for discretizing the boundary value problem, the time-integration methods used for unsteady simulations, and the technique for

handling shock waves on a discretized grid. The rationale for using higher-order methods is also addressed. Chapter 3 contains a description of COFFE and the modifications that were made to the code for this effort. Chapters 4 and 5 describe each of the test cases relating to time-integration methods and stationary/moving shocks, respectively. Finally, the overall conclusions from the research are summarized in Chapter 6.

Chapter 2

Literature Review

The purpose of this literature review is to assess the state of the art in modeling stationary and moving shocks. This assessment will be made with respect to three different areas:

- The underlying method for discretizing the boundary value problem.
- The time-integration methods used for unsteady simulations.
- The technique for handling shock waves on a discretized grid.

The direction of the dissertation was guided by this assessment with the goal of advancing the state of the art in modeling and simulation techniques and identifying difficulties that result from new approaches.

2.1 Boundary Value Problem Discretization

The choice of spatial discretization method is core to any CFD problem. Decisions made at this foundational level dictate a solver's strengths and weaknesses with respect to complex geometry, spatial order of accuracy, numerical stability, ability to handle flow discontinuities like shock waves, and a myriad of other qualities. For a CFD code to be useful for real-world problems with moving shock waves, it must be easy to apply to complex geometries, which means it should handle unstructured grids, and it must manage shock waves, preferably on non-shock-aligned grids, without introducing an excessive amount of error to the flow field in the shock region.

The three most commonly used methods for boundary value problems (BVP) are the finite-difference method (FDM), the finite-volume method (FVM), and the finite-element method (FEM). All three methods accomplish the same task, which is to approximate the value of a given function at finite points on a discretized mesh, but each accomplishes this task in a different manner. A high-level comparison between the three methods applied to the function $u = \sin(4\pi x)$ with grid points at $x = 0$ to 1 in steps of 0.1 is shown in Fig. 2.1. The FDM finds approximate solutions to the equation at the nodal points. Only these points are used in calculations, and functional information between nodes is ignored. The FVM sets the value of a cell to the average of the function within the cell. This incorporates information between the nodes, but it does not retain the value of the function at any specific point.

The FEM approximates the value within each element using a Method of Weighted Residuals (MWR) [16] with a chosen set of basis functions that satisfy the boundary conditions. A trial solution, $u^*(\boldsymbol{x})$, is created, which is a linear combination of the basis functions, $u_i(\boldsymbol{x})$, such that the boundary condition, $u_s(\boldsymbol{x}) = f_s$, is satisfied.

$$u^*(\boldsymbol{x}) = u_s(\boldsymbol{x}) + \sum_{i=1}^{N} c_i u_i(\boldsymbol{x}) \tag{2.1}$$

The trial solution is substituted into the differential equation to create a residual equation, $\boldsymbol{R}$, which is ultimately driven to zero through the proper selection of constants, c_i. In the example case, only linear and constant basis functions were used, so the FEM creates a linear approximation of the function within the element. Like the FVM method, the FEM does not retrain the exact value of the function at any specific point, but it does a better job of approximating the value between the nodes. The FVM is actually limiting case of FEM, where the only basis function is a top-hat filter.

2.1.1 Finite-Difference Method

The finite-difference method is considered to be the simplest discretization scheme to implement. OVERFLOW [17] is an example code that employs FDM. The solutions to BVPs are found at discrete nodes on a numerical grid, and the partial derivatives in the governing equations are replaced by truncated Taylor series expansions, which are algebraic

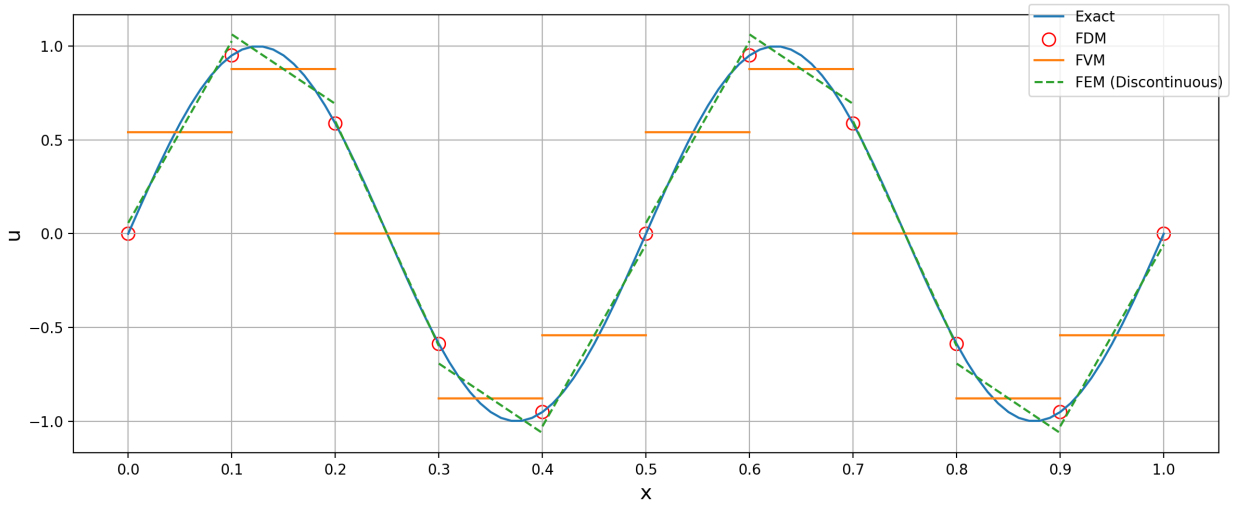

Figure 2.1: Comparison between finite-difference, finite-volume, and discontinuous finite-element methods applied to a 1-dimensional function.

combinations of values at different nodes. Solutions are then found either by explicit or implicit numerical algorithms. [18]

FDM requires structured grids, and the grid spacing in the computational domain must be uniform. [19] Mappings are used to transform from non-equidistant point in the physical domain to the computational domain. Without employing overlapping grids, structured grids are more difficult to implement than unstructured grids for complex geometries.

First and second orders of spatial accuracy are often achieved using standard forward (or backward) difference and central difference schemes, respectively. [18] Spatial order of accuracy refers to the rate at which the numerical error reduces with mesh refinement, also called h-refinement. The numerical error is proportional to the mesh spacing raised to the order of accuracy of the scheme, or $\epsilon \propto h^p$, where p is the spatial order of accuracy. h-refinement is more effective for higher orders of accuracy. In the FDM, higher-order spatial accuracy (greater than 2^{nd}-order) can be achieved by using data from more points in the Taylor series expansion; however, this can be an issue at boundaries, where central differences from interior points transition to one-sided differences at boundaries. This change can result in a loss of accuracy at boundaries. [19]

Another shortcoming applicable to this dissertation topic, is that it is difficult to calculate 1^{st}-order derivatives in the presence of shock waves. Lim, Le Lann, and Joulia [20] showed

that only 1st-order and essentially non-oscillatory (ENO) type schemes produced stable results near shock waves. Higher-order schemes resulted in spurious oscillations in properties downstream of the shock, which is often referred to as being a manifestation of the Gibbs phenomenon. [21] These oscillations could result in a number of errors including, but not limited to, those related to force accounting on a surface, shock position/stand-off distance, and surface heat transfer.

2.1.2 Finite-Volume Method

The finite-volume method is by far the most commonly used discretization method, with implementations in numerous research[1] and commercial[2] solvers. Varga [27] first discussed this method in 1965, which was then referred to as the integration method. [28] The FVM arrives at the approximate solution to the governing equations (that are also conservation laws) through the balancing of fluxes integrated around cell boundaries, which naturally conserves properties. The use of the integral form, rather than the differential form, is a critical philosophical difference between FVM and FDM, particularly in the presence of discontinuities such as shock waves. The integral form allows for discontinuities between control volumes, while the differential form implicitly assumes that flow properties are continuous. For this reason, Anderson [29] states that "this is a strong argument for the integral form of the equations to be considered *more fundamental* than the differential form."

The numerical grid on which FVM operates could be better described as a collection of cells with finite volumes rather than a grid created between specific nodal points. The cells may be structured or unstructured, and nodal spacing need not be uniform or require mapping to a uniform computational domain. This relaxation of gridding requirements affords FVM a major advantage over FDM for flow simulations over complex geometries.

First and second orders of spatial accuracy are typically found in FVM applications. Higher-order methods do exist [30, 31]; however, in practice these are difficult to apply on unstructured meshes due to stencil requirements.

[1] Loci/CHEM [22], FUN3D [23], USM3D [24], US3D [25], and OpenFOAM [26] to name a few.
[2] Such as CFD++® from Metacomp Technologies and Fluent® from ANSYS.

At a high level, cell-centered, first-order methods use the cell-averaged solution information to calculate fluxes at the cell faces. Second-order methods use a larger stencil to calculate fluxes, as opposed to just the local cell-averaged solution. These algorithms are conceptually similar to the forward (or backward) difference and central difference schemes of FDM. Local errors for FVM can be reduced through mesh refinement (recall, also called h-refinement).

2.1.3 Finite-Element Method

The finite-element method is a numerical approach for approximating the solution to BVPs that relies on the weak, or variational, formulation of continuous systems. This document is not intended to be a comprehensive description of FEM, several other excellent resources exist for that purpose,[3] rather it highlights key differences between FEM, FVM, and FDM in order to show why FEM is an attractive choice for CFD solvers. A practitioner utilizing FEM approximates the solution to the governing equations by first subdividing the overall domain into smaller elements and then calculating weights for a given set of basis functions that approximate the solution to the governing equations on each of the elements. The overall solution to the BVP is then the collection of all of the smaller elements.

The numerical grids used for FEM can be structured or unstructured, like FVM grids, which is advantageous for problems involving complex geometries. FEM grids can contain elements that are of any polynomial order, where the polynomial order describes the order of the basis functions used within the element, and the elements within a domain do not all have to be the same order. FVM is a limiting case of FEM whose grids contain only zeroth-order elements. Truly curved boundaries are possible with higher-order elements, due to their curvilinear basis functions. [34] Lower-order grids, to include FVM grids, approximate curved surfaces using a series of straight lines, which appears rough when inspected closely, and can be a source of error in the solution. [35–37]

Since the order of accuracy is controlled at the element level, local p-refinement is more readily available than in FDM or FVM. p-refinement produces diminishing returns at higher orders, and the extra computational cost due to basis function computations, quadrature,

[3] See Hughes [32] and Zienkiewicz, Taylor, and P. Nithiarasu [33]

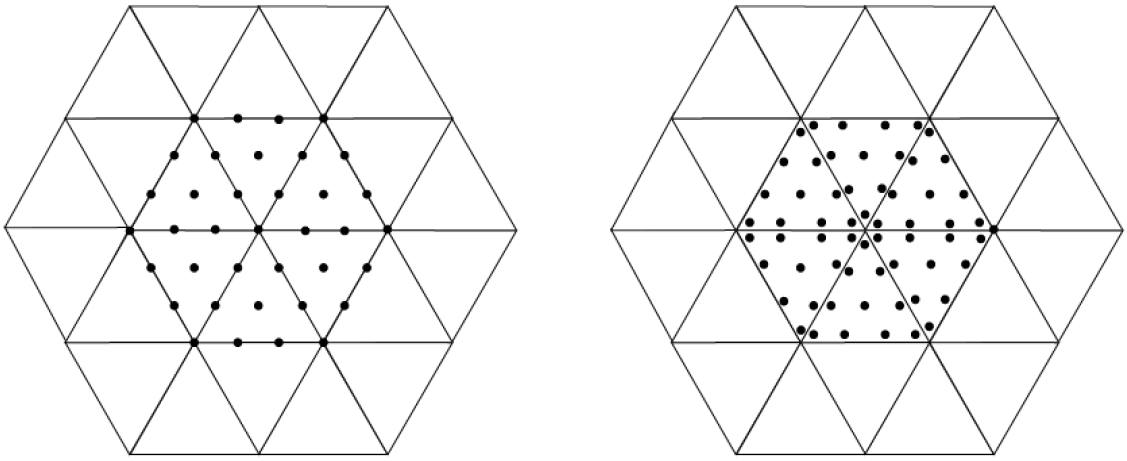

(a) 4^{th}-order Continuous Galerkin **(b)** 4^{th}-order Discontinuous Galerkin

Figure 2.2: Comparison of element degrees of freedom for Continuous Galerkin and Discontinuous Galerkin schemes. Figures from Erwin [42].

and a denser matrix must be balanced with the required error. Mitchell [38] concluded that $p = 3$ or 4 was adequate for non-singular problems, and for problems requiring high accuracy, there was little to gain by going beyond $p = 10$. Fidkowski et al. [39] showed that p-refinement outperformed h-refinement for the smooth problems (i.e., no shocks) that they considered.

Continuous versus Discontinuous Galerkin

Continuous Galerkin (CG) and Discontinuous Galerkin (DG) methods are distinct in how unknowns are handled within the element and between adjacent elements. In CG methods values are common between adjoining elements at nodes, and in DG schemes, nodal values are owned by an element and not shared between elements. As a result, the storage requirements for DG methods are higher than CG schemes. [40, 41] Erwin [42] detailed the work disparity between CG and DG methods. A comparison between CG and DG node arrangements for a regular two-dimensional triangular grid is shown in Fig. 2.2. Each node is a degree of freedom (DOF) that must be solved for numerically, and more DOFs equate to a higher computational cost. It is clear from the figures that the CG method requires fewer DOFs than the equivalent DG method due to the fact that values are continuous between elements, and thus nodes are shared.

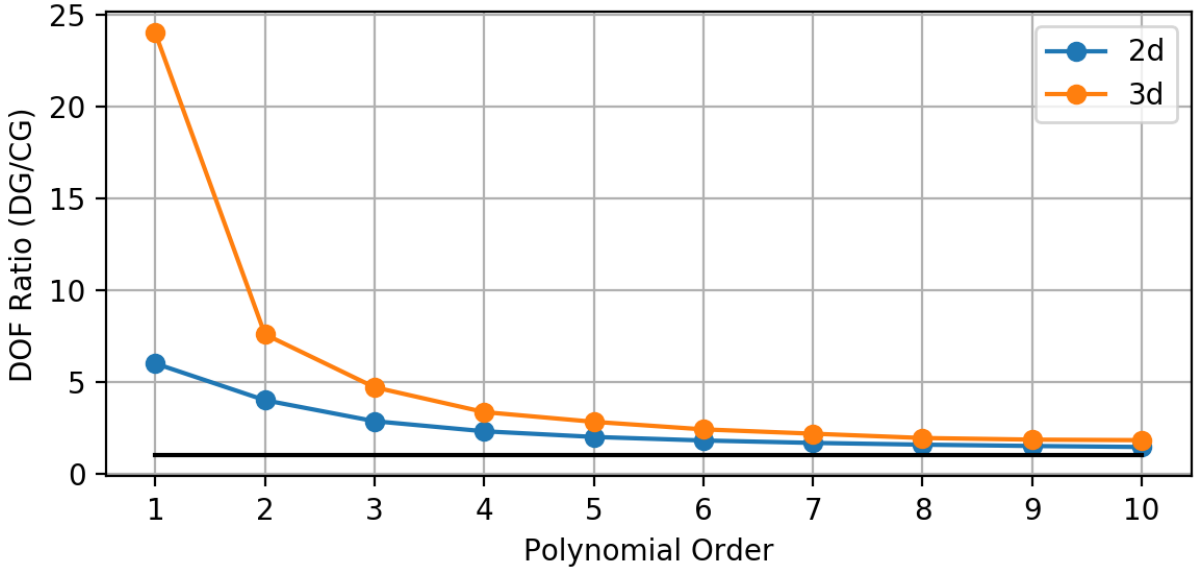

Figure 2.3: Ratio of DOFs DG-to-CG versus Element Polynomial Order

The ratio of DOFs (DG-to-CG) versus element polynomial order is shown in Fig. 2.3. The two-dimensional values are derived from a triangle grid, like the one shown in Fig. 2.2. There is not a three-dimensional analogue to this simple two-dimensional grid, but Erwin [42] used an icosahedron, with 12 connecting edges and 20 connecting tetrahedra, as a representative grid for comparison. The ratio asymptotically approaches unity as more unshared interior nodes are added at higher polynomial orders. For $p \leq 4$, the two-dimensional DOF ratio ranges from 6 at $p = 1$ to 2.3 at $p = 4$, and the three-dimensional DOF ratio ranges from 24 at $p = 1$ to 3.4 at $p = 4$. This demonstrates that DG schemes require significantly more resources than PG schemes, especially for three-dimensional grids.

Anderson et al. [43] compared a CG scheme, more specifically a Petrov-Galerkin (PG) scheme, with a DG method for Maxwell's equations and found that, when applied to the same grid, the L_1 errors were nearly identical (less than 1% difference) between the two schemes, but the L_2 error for the DG scheme was as much as 40% lower than the PG scheme. The L_1 error is the average error in the system, which is a measure of global accuracy. The L_2 error is the average of the squares of the errors, which is effectively a weighted average in which larger errors contribute more to the resulting value. The difference between L_1 and $\sqrt{L_2}$ is a

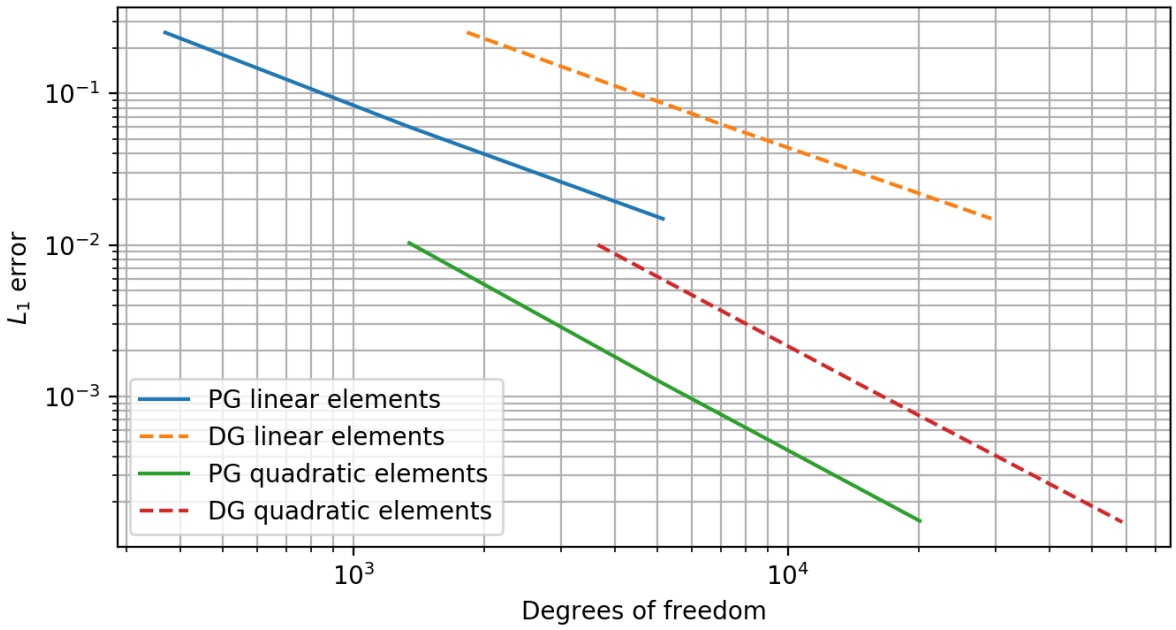

Figure 2.4: Comparison between L_1 error for PG and DG schemes for different numbers of DOFs using linear and quadratic elements. Data are from Anderson et al. [43].

measure of the variance of the frequency distribution of the errors within the system, where $L_1 = \sqrt{L_2}$ indicates that there is no variance because all errors are the same size.

Anderson's results show that the global accuracy, quantified by the L_1 error, of PG and DG schemes applied to the same grid is nearly identical, but the variation in the frequency distribution of the errors within the system is higher in the PG results. When computational cost is factored in, PG schemes have been shown to produce the same global accuracy as DG methods, but at a fraction of the DOFs, and thus computational cost. [43, 44] If, rather than employing the two schemes on the same grid, they were applied to grids with the *same number of DOFs*, the PG method would result in a significantly lower global error, as illustrated in Fig. 2.4.

Stabilized Galerkin

When the standard continuous Galerkin FEM is applied to convection-dominated flow problems, spurious, non-physical oscillations upstream of rapidly changing flow features can appear due to numerical instabilities in the underlying method. An example of these numerical "wiggles" from Brooks and Hughes [45] is shown in Fig. 2.5. These aberrations

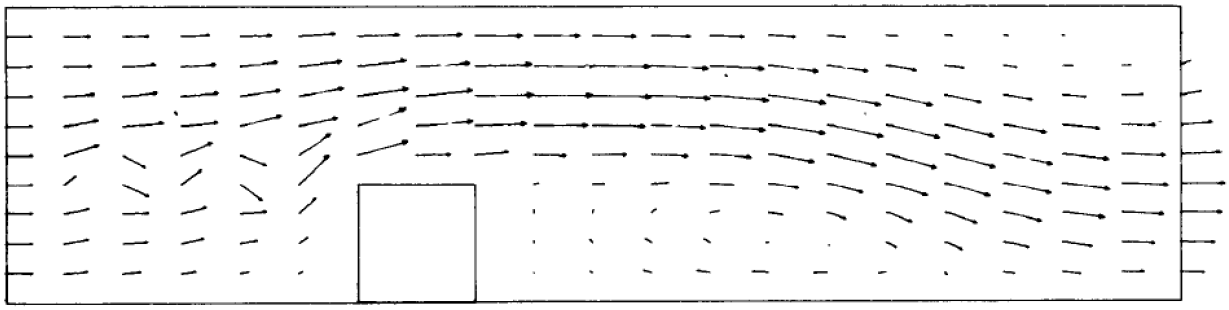

Figure 2.5: Non-physical oscillations generated upstream of a block (Re = 200). Figure from Brooks and Hughes [45].

satisfy the system of equations, in a least-squares sense, but they are not physical, and they can only be eliminated through excessive h-refinement, when using the Galerkin method.

In order to eliminate these oscillations without the use of h-refinement, practitioners have implemented stabilization with upwind-based schemes through various modifications to the standard central-difference-type Galerkin. The two most prominent modified schemes are the Streamline Upwind/Petrov-Galerkin (SU/PG) method [45–52] and the aforementioned Discontinuous Galerkin method [40, 41, 53–59]. The SU/PG scheme implements upwinding by modifying the Galerkin weighting function. [45] DG methods apply upwinding by treating elements as separate entities and imposing a flux jump condition at interfaces. [44]

2.2 Temporal Integration Methods for Unsteady Simulations

An abundance of numerical methods exists to solve initial value problems, such as the unsteady moving shock problem that is the focus of this work. The decision of which temporal discretization method to use should be driven by the method's numerical stability, temporal order of accuracy, and computational expense. Ideally, the time step size should be chosen based on the flow physics of interest, rather than the grid size, and it should introduce minimal temporal error to the simulation. Numerical stability and temporal order of accuracy directly affect these properties.

Methods can be categorized as either *explicit* or *implicit*. A method is explicit if the values at the next time step can be solved for using only the current time step (and possibly previous time steps). If, however, the method requires solving a system of equations that include the current and the next time steps, then the method is implicit. Implicit methods require the implementation of a matrix solver to solve the system of nonlinear equations, which is much more computationally expensive than explicit methods.

The methods discussed in this section are also categorized as either *multi-step* or *multi-stage*. Multi-step methods require values from the current time step and possibly one or more previous time steps, and the next time step is computed directly. Multi-stage methods only require values from the current time step, but one or more intermediate stages between the current and the next time step are calculated. Each intermediate stage requires the solution of the system of nonlinear equations.

2.2.1 Temporal Stability

The concept of stability, as it pertains to a numerical method for solving an initial value problem, refers to the behavior of the numerical solution in response to small perturbations, often caused by numerical errors. Stable methods will dampen small perturbations, while unstable methods can amplify them, resulting in erroneous values that grow with each time step. There are two major categories of stability: *zero-stability* and *absolute stability*. The former describes a solution's response as the step size approaches zero, $\Delta t \to 0$, at a fixed time, t, and the latter relates its behavior as $t \to \infty$ for a fixed Δt. A numerical method must possess both zero and absolute stability in order to be useful in CFD modeling.

Zero-Stability

Suli and Mayers [60] define zero-stability for linear multi-step methods as:

> A linear k-step method (for the ordinary differential equation $y' = f(x, y)$) is said to be zero-stable if there exists a constant K such that, for any two sequences (y_n) and (z_n) that have been generated by the same formulae but different starting

values $y_0, y_1, ..., y_{k-1}$ and $z_0, z_1, ..., z_{k-1}$, respectively, we have

$$|y_n - z_n| \leq K \max\{|y_0 - z_0|, |y_1 - z_1|, ..., |y_{k-1} - z_{k-1}|\},$$

for $x_n \leq X_M$, and as Δt tends to 0, where $x \in [x_0, X_M]$.

Expressed a different way, a numerical method is zero-stable if a small perturbation in the initial condition, $y_0 + \epsilon$, does not change the solution by more than $K\epsilon$, where K is a constant that does not depend on Δt.

Test equations are used to assess the stability of a numerical method. The test equation used to evaluate zero-stability is simply $y' = 0$, which tests the characteristics of the solution as $\Delta t \to 0$. [61] In order to be zero stable, the first characteristic polynomial of the numerical method must satisfy the root condition, which states that all of the roots of the polynomial lie on the unit disc in the complex plane, and any that lie on the unit circle must be simple. [60] *The numerical methods used in CFD modeling must be zero-stable.*

Absolute-Stability

Suli and Mayers [60] define absolute stability for linear multi-step methods as:

> A linear multi-step method is said to be absolutely stable for a given value of $\lambda\Delta t$ if each root $z_r = z_r(\lambda\Delta t)$ of the associated stability polynomial $\pi(\,\cdot\,; \lambda\Delta t)$ satisfies $|z_r(\lambda\Delta t)| < 1$.

Dahlquist [62] originally introduced absolute stability in reference to linear multi-step methods, but it is also an applicable concept for single-step, multi-stage methods, like Runge-Kutta methods. [63] To describe absolute stability more clearly, it is useful to start by looking at Dahlquist's test equation applied to two simple methods, the forward and backward

Euler methods, given in Eqs. (2.2a) and (2.2b), which are explicit and implicit methods, respectively.

$$y_{n+1} - y_n = \Delta t f_n \tag{2.2a}$$

$$y_{n+1} - y_n = \Delta t f_{n+1} \tag{2.2b}$$

Dahlquist's test equation to assess absolute stability of a numerical method is

$$y' = \lambda y, \qquad y(0) = 1.$$

The exact solution to this equation is $y = e^{\lambda t}$, where $\lambda \in \mathbb{C}$. The solution, y, is bounded and approaches zero as $t \to \infty$ for all Re $\lambda < 0$ and $\Delta t > 0$. The attribute of absolute stability is related to conditions in which the solution to the test equation approaches zero for finite time steps because those conditions will dampen rather than amplify small perturbations.

One time step of the forward Euler method applied to the test equation results in

$$y_1 = y_0 + \Delta t f_0 = y_0 + z y_0 = R(z) y_0,$$

where $z = \Delta t \lambda$, $f_0 = y'$, and $R(z) = 1 + z$. $R(z)$ is the *stability function* of the numerical method, and it can be used to find the method's *stability region*, which is defined by Hairer and Wanner [63] as the region in which the magnitude of the stability function is less than or equal to 1, or

$$S = \{ z \in \mathbb{C} \; ; \; |R(z)| \leq 1 \} . \tag{2.3}$$

Small perturbations are amplified when $|R(z)|$ is greater than 1, damped for $|R(z)|$ less than 1, and neither amplified nor damped for $|R(z)|$ equal to 1.

One time step of the backward Euler method applied to the test equation results in

$$y_1 = y_0 + \Delta t f_1 = y_0 + z y_1 = R(z) y_0,$$

where the stability function $R(z) = \frac{1}{1-z}$.

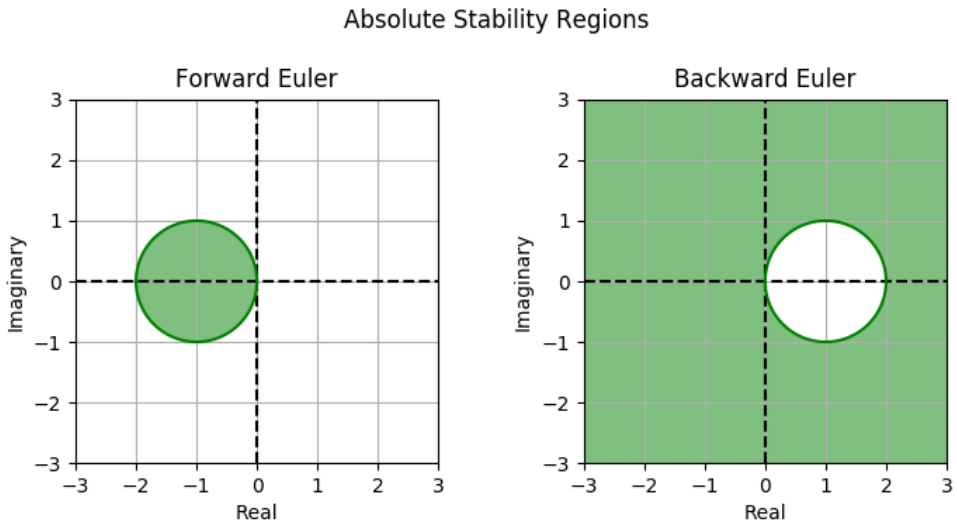

Figure 2.6: Stability regions for the forward and backward Euler methods

The stability region for the forward Euler method is on a unit disc centered at $z = -1$ on the complex plane. The stability region for the backward Euler is the entire complex plane outside of the unit disk centered at $z = 1$. Plots of the stability regions are shown in Fig. 2.6, where the stability region is shaded. It is clear from the figure that the backward Euler method results in a more extensive stability region than the forward Euler. This is because the forward Euler method is *explicit*, while the backward Euler method is *implicit*. It follows that time steps for explicit methods like the forward Euler are *always* subject to restrictions to ensure numerical stability.

Explicit methods force CFD practitioners to select a time step that satisfies the Courant-Fredrichs-Lewy (CFL) condition, [64] which defines the maximum allowable Courant number (C) that a particular numerical method can handle stably. The Courant number is a non-dimensional time step that indicates the speed at which information passes through elements. Blazek [65] defines the Courant number for unstructured grids as

$$C = \frac{\Delta t}{\Omega} \sum_i \left(\hat{\Lambda}_c^{x_i} + K \hat{\Lambda}_v^{x_i} \right) \tag{2.4}$$

where Ω is the element volume, $\hat{\Lambda}_c^{x_i}$ and $\hat{\Lambda}_v^{x_i}$ are the convective and viscous spectral radii, and K is a scalar for the viscous spectral radii that is set based on the choice of spatial discretization. The convective radii are calculated by

$$\hat{\Lambda}_c^{x_i} = (|u_i| + a)\Delta\hat{S}^{x_i} \tag{2.5}$$

where a is the speed of sound and $\Delta\hat{S}^{x_i}$ is a planar projection of the control volume, given by

$$\Delta\hat{S}^{x_i} = \frac{1}{2}\sum_{J=1}^{N_F} |S_{x_i}|_J \tag{2.6}$$

and S_{x_i} is the x_i component of the face vector $\boldsymbol{S} = \hat{\boldsymbol{n}} \cdot \Delta S$.

A-Stability, A(α)-Stability, and L-Stability

A-stability is descriptor applied to numerical methods that possess absolute stability regardless of the chosen step size. Dahlquist [62] stated that a k-step method was A-stable if all of the solutions to any ODE of the form $y' = \lambda y$ tend to zero as $n \to \infty$ when Δt is a fixed positive number and λ is a complex constant with a negative real part. In short, A-stability requires that a method's stability region include the entire left side of the complex plane.

Dahlquist's "Second Barrier," as stated by Suli and Mayers [60], contains three rules pertaining to A-stability.[4]

1. No explicit linear multi-step method is A-stable.

2. No A-stable linear multi-step method can have an order greater than 2.

3. The second-order A-stable linear multi-step method with the smallest error constant is the trapezoidal rule.

Dahlquist [62] stated that A-stability is a desirable property to have for certain classes of differential equations. A-stability is desirable for stiff equations, like those found in CFD applications, because it does not impose burdensome restrictions on the selected time step

[4]The "First Barrier" was proven by Dahlquist [66], but it is less relevant to this discussion. For more information, see Suli and Mayers [60] or Hairer and Wanner [61].

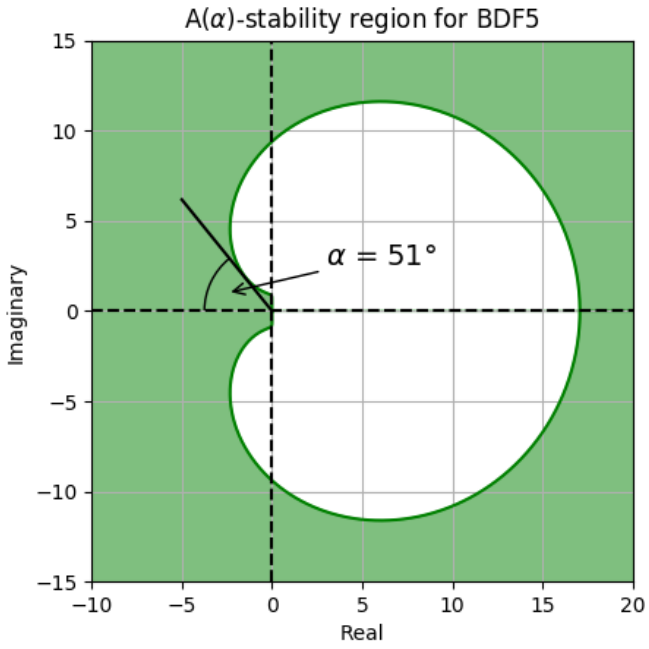

Figure 2.7: A(α)-stability sector definition for BDF5

in order to maintain numerical stability. This allows CFD practitioners to select a time step capable of capturing the flow features of interest with little concern about how it relates to the CFL condition.

A-stability can prove to be too strong of a requirement in some cases, because it excludes some methods that may be acceptable in certain instances. A(α)-stability is used to describe methods that are implicit and zero-stable but not necessarily A-stable. In A(α)-stability, α refers to the half-angle of the sector created by rays from the origin that are tangent to a method's stability curve (the border of the stability region). Low values of α imply small regions of stability, and high α's indicate large stability regions. Methods that are A-stable have α=90°.

The absolute stability region and A(α)-stability sector for the 5^{th}-order backward difference formulae method (BDF5), described by

$$y_{n+5} - \frac{300}{137}y_{n+4} + \frac{300}{137}y_{n+3} - \frac{200}{137}y_{n+2} + \frac{75}{137}y_{n+1} - \frac{12}{137}y_n = \frac{60}{137}\Delta t f_{n+5},$$

is shown in Fig. 2.7. This method is zero-stable, but not A-stable. Its A(α)-stability is 51°.

L-stability is a special case of A-stability where the stability function, $R(z)$, approaches zero as $z \to \infty$. Expressed in mathematical terms,

$$\lim_{z\to\infty} R(z) = 0.$$

Methods that are L-stable are also A-stable, but the opposite is not true. L-stability places an additional, more stringent requirement on a method beyond A-stability. This property makes these methods particularly useful for stiff equations because they dampen out rapid transients much more quickly than methods without L-stability.

The backward Euler method (Eq. (2.2b)) is an A-stable method. Its stability function is $R(z) = \frac{1}{1-z}$, which approaches zero as $z \to \infty$, and as a result, it also L-stable. The trapezoidal method, shown in Eq. (2.7), is a second-order A-stable method with the smallest error constant, according to Dahlquist's Second Barrier. Its stability function is $R(z) = \frac{1+z/2}{1-z/2}$, which does *not* approach zero as $z \to \infty$.

$$y_{n+2} = y_{n+1} + \frac{1}{2}\Delta t\,(f_{n+2} + f_{n+1}) \tag{2.7}$$

Hairer and Wanner [63] demonstrated the benefits of L-stability for stiff equations by comparing backward Euler and trapezoidal solutions to

$$y' = -2000(y - \cos x), \qquad y(0) = 0, \qquad 0 \le x \le 1.5. \tag{2.8}$$

Fig. 2.8 shows a comparison between the trapezoidal and backward Euler methods applied to Eq. (2.8). It is clear that the response of the backward Euler method is much more desirable than that of the trapezoidal method for stiff equations. For CFD applications, this property could be especially useful when modeling a moving shockwave.

Only methods that are at least A-stable are being considered for use in this work, with preference placed on those methods that are also L-stable. This excludes all explicit methods, but it should create a more robust solver whose stability is not tied to the user's choice of time step, allowing users to use time steps dictated by flow phenomena rather than numerical stability. Methods with L-stability are preferred for cases with moving shock waves due to

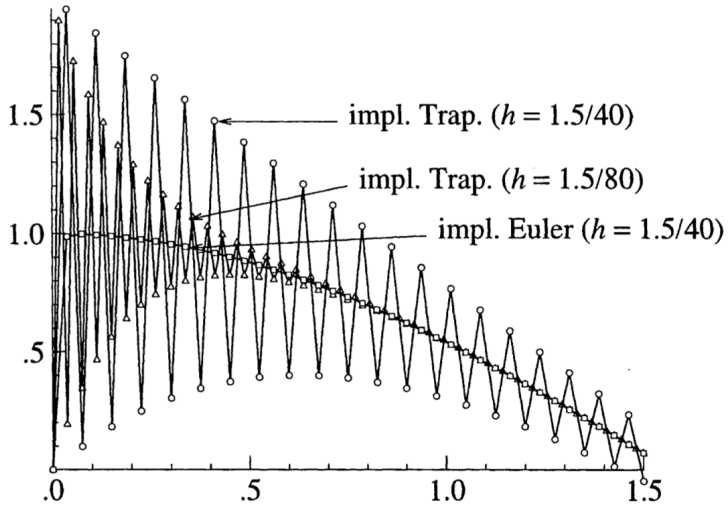

Figure 2.8: Comparison between trapezoidal and backward Euler methods for Eq. (2.8). Figure from Hairer and Wanner [63]

the rapid property transients that occur with a shock waves travels through a domain. An L-stable method is apt to accurately model a rapid transient without introducing the non-physical, numerical ringing shown in Fig. 2.8.

2.2.2 Linear Multi-step Methods

Linear multi-step methods are a class of numerical methods for ordinary differential equations that use a linear combination of the values, y_i, and first derivatives with respect to time, $f(t_i, y_i)$ or just f_i, from s previous solutions to approximate solutions to initial value problems of the form

$$y' = f(t, y), \quad y(t_0) = y_0.$$

These methods are of the form

$$y_{n+s} + a_{s-1}y_{n+s-1} + \cdots + a_0 y_n = \Delta t(b_s f_{n+s} + b_{s-1}f_{n+s-1} + \cdots + b_0 f_n),$$

where s is the number of steps and the order of the particular method, Δt is the time step size, and the a and b coefficients are determined by each particular method. Linear multi-step

methods can be either explicit or implicit, and the coefficient b_s can be used to distinguish between the two, where $b_s = 0$ for explicit methods, and $b_s \neq 0$ for implicit ones.

Linear multi-step methods are computationally efficient because they utilize data retained from previous solutions and do not require intermediate time steps to be calculated and subsequently discarded. Retaining previous time steps does require additional storage in memory, but this is typically not an issue for modern computers. Higher orders of accuracy require more previous time steps, but order of accuracy is ultimately limited by numerical stability. Methods of order greater than one are not self-starting, meaning that initial time steps must be solved at a lower order of accuracy until enough time steps are obtained.

2.2.3 Runge-Kutta Methods

Runge-Kutta (RK) methods [61] are a family of multi-stage, single-step numerical methods that are utilized to solve the Cauchy, or initial value, problem for systems of ordinary differential equations. These methods are self-starting because they only require information from one previous time step or the initial value.

The general equation for a RK method with s stages is given in Eq. (2.9). A particular method is identified by the RK matrix (a_{ij}), the weights (b_i), and the nodes (c_i). The RK matrix specifies how intermediate stages are calculated, the weights are used to compute the solution at the next time step, which is the weighted average of the intermediate solutions, and the nodes define where the intermediate solutions are assessed relative to the overall time step. Each row in the RK matrix describes an intermediate stage, where the a_{ij} values are weights used to calculate an intermediate solution, similar to b_i. The sum of each row is equal to the associated node, c_i ($c_i = \sum_{j=1}^{s} a_{ij}$). RK methods are typically presented in a *Butcher tableau*. The form for a Butcher tableau is shown in Eq. (2.10), where A is the RK matrix, $\mathbf{b}$ is the weights vector, and $\mathbf{c}$ is the nodes vector.

$$y_{n+1} = y_n + \Delta t \sum_{i=1}^{s} b_i k_i \tag{2.9}$$

where,

$$k_i = f\left(t_n + c_i\Delta t, y_n + \Delta t \sum_{j=1}^{s} a_{ij}k_j\right), \quad i = 1, ..., s$$

$$\begin{array}{c|cccc} c_1 & a_{11} & a_{12} & \dots & a_{1s} \\ c_2 & a_{21} & a_{22} & \dots & a_{2s} \\ \vdots & \vdots & \vdots & \ddots & \vdots \\ c_s & a_{s1} & a_{s2} & \dots & a_{ss} \\ \hline & b_1 & b_2 & \dots & b_s \end{array} = \begin{array}{c|c} \mathbf{c} & A \\ \hline & \mathbf{b^T} \end{array} \tag{2.10}$$

RK methods may be either explicit (ERK) or implicit (IRK), and a particular method can be categorized using the RK matrix. If the matrix is only lower triangular, with the main diagonal zero, the method is explicit. If any values along the main diagonal or above it are non-zero, the method is implicit. Explicit schemes were originally proposed by Runge [67] in 1895 and developed by Kutta [68] in 1901, but they will not be included here because they are not A-stable.

There are a number of categories within the family of IRK methods.

- Diagonally implicit RK (DIRK) – All coefficients above the main diagonal in the RK matrix are zero, but one or more of the main diagonal coefficients are non-zero.
- Singly diagonally implicit RK (SDIRK) – All coefficients along the main diagonal are the same value.
- Fully implicit RK (FIRK) – All coefficients within the RK matrix are non-zero.

FIRK methods are attractive due to their high stage order and high overall order per stage. Gauss-Legendre methods, for example, have order $2s$, and Radau methods have order $2s-1$, where s is the number of stages. In practice these methods are difficult to implement efficiently because all stages must be solved simultaneously. [69] FIRK methods were not implemented for this reason.

DIRK methods are easier to implement, as only one new variable is present at each ensuing stage, which is to say each stage can be solved sequentially rather than all at once. SDIRK methods, with their constant value along the main diagonal, have the added benefit

of having a constant Jacobian over all stages. [70] This greatly reduces the computational cost of these methods.

2.2.4 Dissipation and Dispersion Errors

Numerical errors resulting from spatial and temporal discretization can manifest as additional, non-physical dissipation or dispersion in a solution. Dissipation reduces the amplitude of a traveling wave, which acts to smooth out gradients. Dispersion affects the propagation speed of a traveling wave based on its wave number, which induces spurious oscillations to appear in a non-oscillatory solution. Dispersion errors are particularly evident in regions of large or discontinuous gradients in field properties, such as shock waves, because advection in these regions is characterized by flow at many different wave numbers. [71, 72] Numerical schemes that are odd-order are dominated by dissipation errors, while those that are even-order are dispersive. [73, 74]

Takacs [75] described a method for separating the total numerical error into dissipative and dispersive parts. The method is used in upcoming data analysis, so it warrants further description here. For this method, the total error is defined as the mean square error,

$$E_{tot} = \frac{1}{M} \sum_{j} (q_T - q_D)_j^2, \tag{2.11}$$

where q_T is the true solution, q_D is the discretized solution, and M is the number of discretization points. Takacs [75] then applies the definition of variance and rearranges the terms to show that,

$$E_{tot} = [\sigma_T - \sigma_D]^2 + (\bar{q}_T - \bar{q}_D)^2 + 2(1 - \rho)\sigma_T \sigma_D, \tag{2.12}$$

where ρ is the correlation coefficient between q_T and q_D, σ_T and σ_D are the standard deviations of the true and discretized solutions, and overbars indicate mean. The correlation coefficient, ρ, is the ratio of the covariance between two variables to the product of their standard deviations, $\rho = \text{cov}(T, D)/\sigma_T \sigma_D$, where $\rho = 1$ indicates that q_T and q_D are exactly

correlated and all of the error is dissipative. With this understanding, the dissipative and dispersive errors are defined, respectively, by

$$E_{diss} = [\sigma_T - \sigma_D]^2 + (\bar{q}_T - \bar{q}_D)^2 \tag{2.13}$$

and

$$E_{disp} = 2(1 - \rho)\sigma_T\sigma_D \tag{2.14}$$

2.3 Shock Wave Handling in Continuum Modeling

Holian et al. [76] describes a shock wave profile as the interaction between two phenomena. The higher sound speed in the post-shock region steepens the shock wave, increasing the velocity gradient, while the larger velocity gradient results in a large viscous stresses, which tend to spread the shock region out. Hirschfelder, Curtiss, and Bird [77] showed that the shock width resulting from this interaction was on the order of the mean free path, which implies that a shock wave is not a continuum field structure. [76, 78] The Knudsen number is the ratio of the mean free path to a physical length scale, and it can be shown to be proportional to the Mach number divided by the Reynolds number ($Kn \propto M/Re$). A small Knudsen number means that the mean free path is small in relation to a physical length scale, and since the shock width is on the order of the mean free path, it is also small in relation to the same physical length scale. In fact, in the inviscid limit, where $Re \to \infty$, the shock wave is a discontinuity as there is no viscosity to spread the shock region out. Moretti and Salas [79] investigated the thickness of viscous shocks numerically, in part to determine at what Reynolds numbers shock waves behave in an inviscid (discontinuous) manner. They stated that "for Reynolds numbers of the order of 1,000 or higher, the shock thickness can be neglected and a sharp discontinuity, satisfying the Rankine-Hugoniot conditions, can be assumed in a flow." As a result of this discontinuity, the governing equations are no longer differentiable, and only the weak solution can be obtained. [80]

Most Eulerian CFD techniques (FEM, FVM, and FDM) rely on a continuum flow field assumption.[5] The governing equations (typically the Navier-Stokes or Euler equations) are solved at points on a mesh, which enforces a numerical width on the shock region that is typically much larger than its physical width. Two classes of methods were developed to manage this scale disparity: *shock capturing* and *shock fitting*. Shock capturing and fitting allow a solver to model this discontinuous phenomena while still solving the governing equations and applying the continuum flow field assumption. Both methods have been used effectively in countless cases, but each has distinct shortcomings.

2.3.1 Shock Capturing

Shock capturing techniques work by either applying local artificial viscosity to smear out the shock and turn the discontinuity into a rapidly changing, but continuous, surface, as in the method introduced by Von Neumann and Richtmyer [81], or approximating the solution to the one-dimensional Riemann problem using a Godunov-type scheme [82], such as those of Roe [83] and Osher and Solomon [84]. These methods tend to overestimate the physical shock width, [85] which results in the creation of non-physical "filler" states that introduce a variety of numerical errors that diminish but do not disappear with increased grid resolution or accuracy. [86] Despite the introduction of non-physical features to the solution, shock capturing techniques remain popular due to their ease of implementation and use, relative to shock fitting methods, especially on simulations with moving shock waves.

Artificial bulk viscosity

Bulk viscosity, $\mu_b = \lambda + 2\mu/3$, where λ is the second (dilatational) viscosity coefficient, describes the dissipation of energy when a fluid is compressed or expanded. It is only present in compressible flows, because in the momentum equation, μ_b is multiplied by the divergence of velocity (or dilation), $\boldsymbol{\nabla} \cdot \boldsymbol{u}$, which is zero in incompressible flows. Stokes' hypothesis [87] states $\mu_b = 0$, and thus $\lambda = -2\mu/3$, and this simplification is broadly leveraged among compressible flow simulations. [88] White [89] states that there are two cases in which $\lambda \neq$

[5] Methods for rarified gas flows, such as Direct Simulation Monte Carlo (DSMC), will not be discussed in this document.

$-2\mu/3$, and μ_b cannot be neglected: sound wave absorption/attenuation and the normal shock wave. Landau and Lifshitz [90] related bulk viscosity to the relaxation time required to restore a fluid to thermodynamic equilibrium after any rapid compression or expansion, such as a shock wave, stating that increasing μ_b results in a larger dissipation of energy and a longer relaxation time. Emanuel and Argrow [91] related this to shock wave thickness and showed that thickness also increases with increasing μ_b.

Shock capturing through the application of artificial bulk viscosity[6] (ABV) and artificial thermal conductivity is an active research area. [14, 15, 92–96] These methods are relatively easy to apply, since they are modifications to physical transport properties based on calculated flow features as determined through detector functions, such as the strain rate tensor, and they are designed such that the artificial properties are applied directly to the discontinuity location through the use of shock switches or sensors, such as the Ducros et al. [97] sensor. The previously referenced methods [14, 15, 92–96] all utilize 4^{th}-derivatives of detector functions, which could prove difficult to implement in codes where those derivatives are not readily available. These high derivatives are used to isolate the application to areas where rapid changes in flow properties are present. The proper detector functions and shock switches to use for a given application is an area of development. Early work by Cook and Cabot [92] suggested using the strain rate tensor for the ABV detector function, but later investigations by Mani, Larsson, and Moin [98] suggested that dilation would be a better detector because it affects only shock waves and not vortical structures present in turbulent flows. This finding was verified by Kawai, Shankar, and Lele [93].

Olson and Lele [15, 99] advanced the concept of ABV by applying the viscous diffusion independently along each grid direction rather than uniformly in all directions. They showed that scalar application of ABV to high aspect ratio cells, like those found in boundary layers, resulted in too much dissipation which led to an increase in numerical stiffness. The results from Olson and Lele show that their directional application made captured shocks more crisp and reduced numerical artifacts resulting from non-shock-aligned grids. It should be noted that Olson and Lele used the strain rate tenor rather than the dilation as a detector function

[6] Artificial shear viscosity is included in Cook and Cabot [92], but it is more useful as a subgrid scale turbulence model for large eddy simulations. Kawai, Shankar, and Lele [93] showed that it produced results similar to the dynamic Smagorinsky model.

for the ABV application. The results would likely improve if dilation were used, especially for LES test cases.

Artificial diffusion

Other researchers [12, 97, 100, 101] have introduced an additional artificial diffusion term that acts in a similar manner to the artificial viscosities previously discussed. Artificial diffusion differs from artificial viscosity in that it is strictly numerical diffusion added to smooth out discontinuities; it has no connection to any physical properties. Artificial diffusion is also typically added to all of the governing equations, rather than just those affected by the addition of viscosity and thermal conductivity. These differences are often neglected, and the terms are commonly used interchangeably in literature.

Artificial diffusion is applied by adding a new flux term to the governing equations. The structure of this term, as described by Holst et al. [102], is

$$F_{ad,i} = h\lambda_{max}\epsilon_{shock}\frac{\partial q_i}{\partial x_j} \tag{2.15}$$

where $\boldsymbol{q} = [\rho, \rho\boldsymbol{u}, \rho h_t]^T$, h is the characteristic length of the cell, λ_{max} is the maximum wave speed in the domain, and ϵ_{shock} is a shock indicator. All of the artificial diffusion schemes found in the literature [12, 97, 100, 101, 103–105] have a similar structure, specifically that the spatial gradient of $\boldsymbol{q}$ is scaled by a value derived from the size of the cell and a shock indicator.

The Jameson–Schmidt–Turkel (JST) shock capturing method [100] was one of the earliest schemes to utilize artificial diffusion. This method was originally applied to the Euler equations, and the following high-level description, adapted from Jameson [106], outlines how it is applied to a one-dimensional case on a grid with uniform spacing. The JST method utilizes a pressure switch, s_j where j in this case is the discrete node index, to activate F_{ad}.

$$s_j = \left|\frac{p_{j+1} - 2p_j + p_{j-1}}{p_{j+1} + 2p_j + p_{j-1}}\right| \tag{2.16}$$

This pressure switch was used to scale the dissipative flux, $\Delta w_{j+(1/2)}$, which was then subtracted from the inviscid flux.

$$\Delta w_{j+(1/2)} = \left\{ \begin{array}{c} \rho_{j+1} - \rho_j \\ (\rho u)_{j+1} - (\rho u)_j \\ (\rho h_t)_{j+1} - (\rho h_t)_j \end{array} \right\} \tag{2.17}$$

This artificial diffusion for the JST method serves to smooth out discontinuous features that manifest as large pressure gradients. Jameson [106] provides more details about the JST method, including the history of its development.

Barter and Darmofal [101] showed that there were benefits to applying artificial diffusion smoothly across cells rather that discretely at affected cells. The smooth application increased the robustness of the solution and significantly reduced oscillatory errors downstream of the shock. Ching, Lv, and Ihme [12], Barter and Darmofal [101], and Yano, Modisette, and Darmofal [104] utilized an elliptic partial differential equation to smooth the diffusion application across the solution, which is a robust approach, but it increases the computational cost of the solution.

Additionally, two modifications to h have been shown to be helpful. Persson and Peraire [103] scaled h by $1/p$, where p is the polynomial order of the finite element basis functions. By doing this they were able to take advantage of the sub-grid scale resolution from higher-order elements to produce shocks that were thinner than the element size. Ching, Lv, and Ihme [12], much like Olson and Lele [15, 99], used a directional h to ensure that diffusion was applied appropriately for anisotropic cells.

Errors introduced

For higher-order methods, possibly the most pernicious issue introduced by shock capturing is that of the reduction in spatial order accuracy to unity in the downstream region. Carpenter and Casper [107] studied supersonic flow around a blunt, two-dimensional cylinder using 1^{st}, 2^{nd}, and 4^{th}-order spatial discretization schemes, and they found that each method asymptotically approached 1^{st}-order as grid was refined. This finding showed that the 1^{st}-order error introduced by the shock capturing method was independent of the chosen spatial discretization scheme. Carpenter and Casper point out that their finding does not necessarily "prove that captured shocks are destined only to be 1^{st}-order accurate;" however, Roy [108]

also observed this phenomenon in his investigation of Mach 8 inviscid flow over a blunted cone. Banks, Aslam, and Rider [109] demonstrated less-than 1^{st}-order convergence on an advecting shock problem and provided a detailed explanation for the mechanism that results in a degradation in spatial order of accuracy. Pirozzoli [110] went so far as to say "these [order of accuracy] limitations, related to the misrepresentation of discontinuities on a mesh with finite spacing, can only be overcome by some form of shock-fitting." Casper and Carpenter [111] also found out that this applied to unsteady problems. The order of accuracy for a higher-order method was reduced to unity, but the overall error was lower when compared to a linear method applied to the same problem.

Other numerical anomalies that are created due to the over-estimation of the shock width include, but are not limited to, the carbuncle aberration, Gibbs phenomenon, and wall heating. The carbuncle phenomenon is a large discontinuous error in the shock wave at the stagnation streamline. An example of a carbuncle is shown in Fig. 2.9, where Powers, Bruns, and Jemcov [112] have simulated Mach 5.73 flow over a circular cylinder with physical diffusion neglected ($\mu = k = 0$). The carbuncle aberration was first reported by Peery and Imlay [113] when they used the flux difference method of Roe [83] to calculate Mach 6 flow solutions around a circular cylinder. It is actually a valid solution of the Euler equations [114], but it is undesirable in numerical simulations as it is not found in nature. This error was found in the flux-difference Riemann solvers of Roe [83] and Osher and Solomon [84], but it was not found in the flux-splitting methods presented by Peery and Imlay [113], Steger and Warming [115], and Leer [116], nor was it present when Lin [117] added dissipation to Roe's flux-difference method.

Excess wall heating is a numerical error common to methods that rely on artificial viscosity. Noh [118] identified a simple test case to demonstrate this issue. A perfect gas impinges on a rigid wall at the origin, and a rightward moving shockwave emanates from the wall. The downstream conditions and shock speed are known from inviscid calculations. An example of the wall heating error illustrated with the planar Noh problem is shown in Fig. 2.10a, where the phenomenon is seen as a sharp decrease in density at the left boundary.

Noh [118] states that "wall heating is inherent in all such shock-smearing procedures" because "too much work is done when a shock starts up, or as here, when a shock is formed

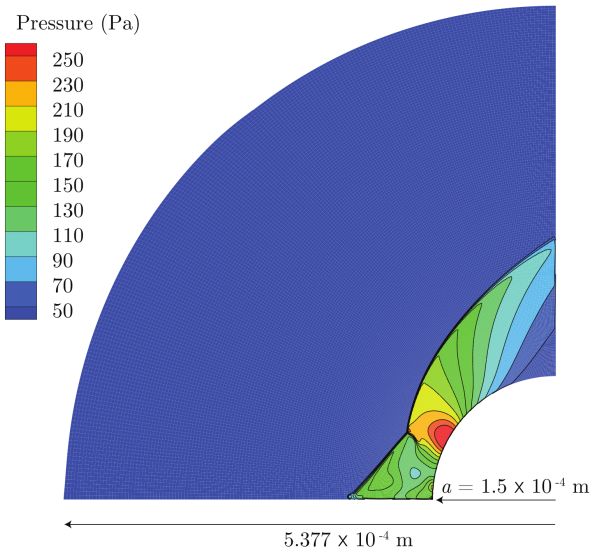

Figure 2.9: Carbuncle phenomenon demonstrated with Mach 5.73 flow over a circular cylinder by Powers, Bruns, and Jemcov [112]

by bringing the gas to rest." To expand on this, when the shock forms at the wall, the momentum equation ensures that the correct pressure level is reached downstream of the shock. The artificial viscosity added at the shock generates heat through the energy equation, which is not dissipated due to the lack of thermal conductivity. [119] Noh suggested that a way to alleviate this issue was to introduce artificial heat flux at the site of the shock in addition to the artificial viscosity. This refined method was applied to the same example problem, and the results are shown in Fig. 2.10b. The wall heating error is gone, and the oscillations in the region downstream of the shock are also nearly eliminated.

The Gibbs phenomenon [120] refers to spurious oscillations that form when a discontinuous function is approximated by the sum of a series of continuous functions. A common example of this error is present in the Fourier series approximation of a square wave, as seen in Fig. 2.11. As more terms are added in the approximation, the overshoot error is reduced in magnitude, but it is not eliminated. This phenomenon can manifest in the region downstream of a shock wave as well, see Fig. 2.10.

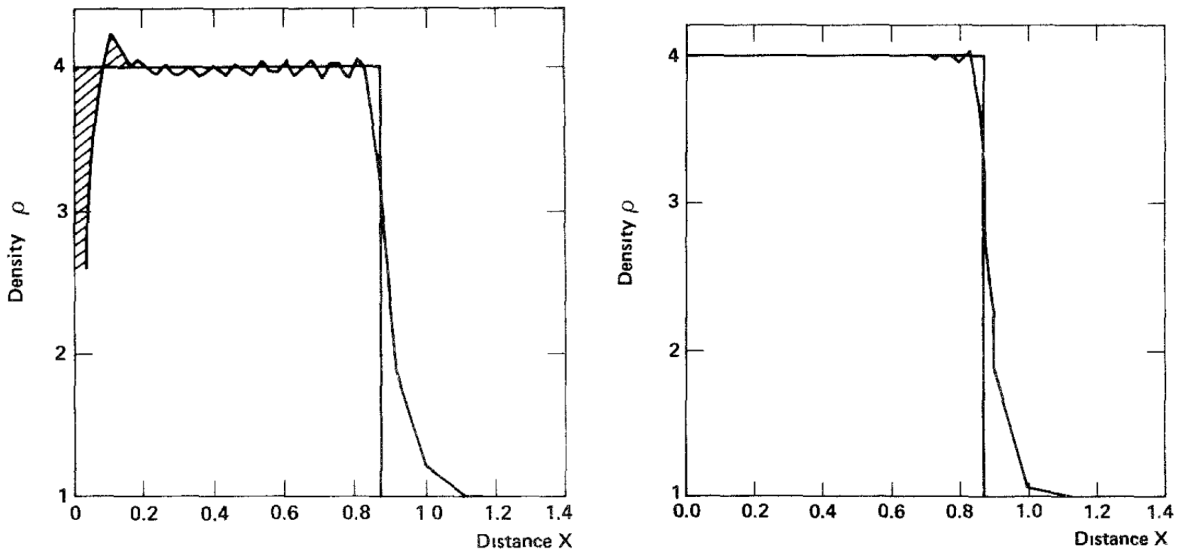

(a) Without artificial heat flux **(b)** With artificial heat flux

Figure 2.10: Wall heating errors using the shock capturing method of Von Neumann and Richtmyer [81] with and without artificial heat flux. Wall heating manifests as a sharp decrease in density at the left boundary. Figures from Noh [118].

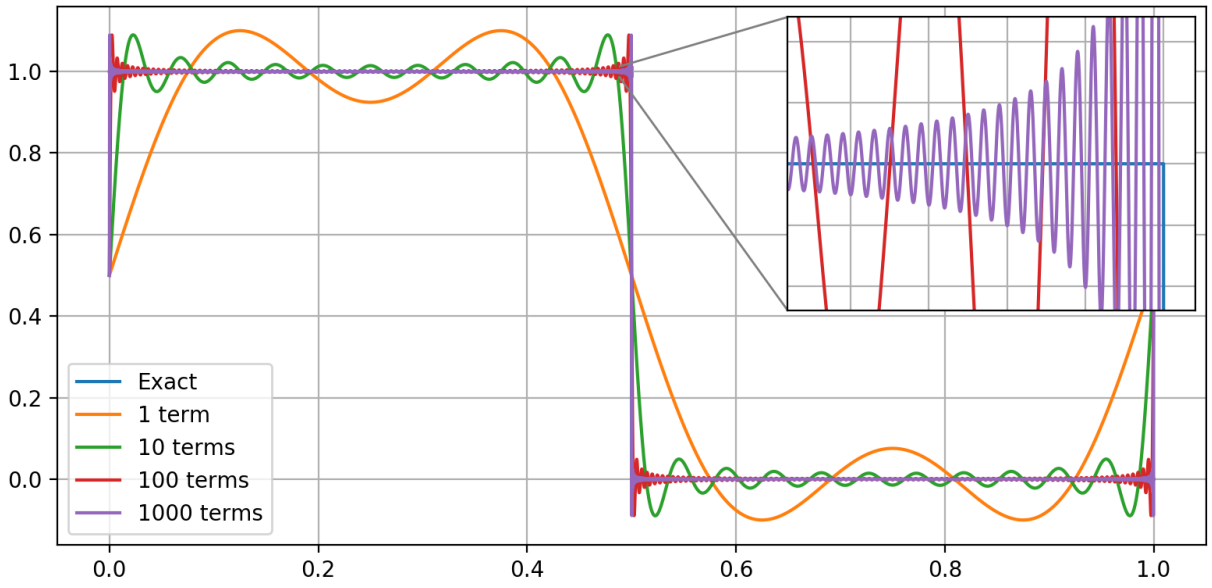

Figure 2.11: Fourier series approximation of square wave using 1, 10, 100, and 1,000 terms, highlighting the Gibbs phenomenon.

2.3.2 Shock Fitting

Shock fitting was first used by Emmons [121] in 1944. This class of methods treats the shock wave as an explicit discontinuity over which the Riemann problem is solved or approximated through the application of the Rankine-Hugoniot jump condition. Typically the jump condition is applied to the control volume face, which results in an underestimate of the physical shock width. [122] This technique for managing shock waves is not subject to any of the error sources discussed in the previous section (reduced order of accuracy, carbuncle, wall heating, and Gibbs phenomenon), which makes it a very attractive option for shock modeling.

Shock fitting methods impose a major requirement on the numerical grid, as the locations of shocks must either be known *a priori* or tracked dynamically through a simulation. Historically this has been the largest challenge for shock fitting techniques, but progress has been made in the development of algorithms to detect and track these discontinuities on an unstructured grid. [123] This method was applied to cases with complex flow topologies, including shock-shock interactions, by Ivanov et al. [124] and Paciorri and Bonfiglioli [85].

The dynamic shock-fitting technique described by Bonfiglioli et al. [123] involves seven steps:

1. Remove cells around the shock front
2. Re-meshing local area around the shock front
3. Compute tangent and normal unit vectors
4. Compute upstream shock state on the new mesh
5. Compute downstream shock state and shock speed by enforcing the Rankine–Hugoniot jump relations
6. Compute displacement of the shock at time $t + \Delta t$
7. Interpolate results on to phantom nodes surrounding local area around shock

Steps 1 and 2 are particularly challenging and computationally intensive because they require the creation of new elements after the mesh has been initialized and partitioned, and these steps would need to be performed at each time step.

The ability to add elements dynamically during a simulation is currently not available in COFFE, and adding it to the code would be an undertaking beyond the scope of this dissertation. The simulation results from shock fitting are widely considered to be superior to those from shock capturing; [125–128] however, the benefits come with increased code complexity and computational cost.

2.3.3 Enriched Finite Elements

Finite element methods have seen widespread use for many years on simulating structural problems, where discontinuities can arise in the form of cracks. Modeling cracks in a solid structure presents a similar problem, numerically, to modeling a shock wave in a fluid, in that the underlying finite element method is predicated on the assumption that field variables are continuous across an element[7], and a crack or shock wave breaks that assumption. So it stands to reason that finite element fluid solvers could leverage crack modeling innovations made by structural solvers for fluid dynamic discontinuities.

Fries and Belytschko [129] reviews the application of *enriched* shape functions within finite elements to model discontinuities. They refer to the method as the eXtended Finite Element Method (XFEM) [129–131]; however, their discussion also applies to the Partition of Unity Method (PUM) [132–134] and the Generalized Finite Element Method (GFEM) [135, 136], as all three of these methods are functionally the same.

The general form of XFEM is given in Eq. (2.18), which is Equation 11 in Fries and Belytschko [129]. In this equation, N_i and N_i^* are standard FEM shape functions, and they are often chosen to be identical, I is the set of all nodes within the domain, and I^* is a subset of those nodes ($I^* \subset I$) on which enrichment is applied. $\psi(\boldsymbol{x})$ is an *enrichment function* that provides the FE approximation with more flexibility to handle, in this case, discontinuous solutions such as shocks. For discontinuities this enrichment function is typically taken to

[7]Field variables for Discontinuous Galerkin methods are discontinuous between adjacent elements, but still continuous across individual elements.

be a Heaviside function (or a slightly smoothed-out Heaviside function for viscous flow, as described by Abbas, Alizada, and Fries [137]), but it could be different for other applications such as boundary layer flow. [137–139]

$$u(\boldsymbol{x}) = \underbrace{\sum_{i \in I} N_i(\boldsymbol{x}) u_i}_{\text{standard FE approx.}} + \underbrace{\sum_{i \in I^*} N_i^*(\boldsymbol{x}) \cdot [\psi(\boldsymbol{x}) - \psi(\boldsymbol{x_i})] a_i}_{\textit{enrichment}} \tag{2.18}$$

Abbas, Alizada, and Fries [137] applied XFEM, without any upwinding stabilization like SU/PG and DG, to fluid problems with high-gradients and found that errors were significantly reduced with XFEM on coarse meshes, but that the errors converged with mesh refinement. They also showed that the spurious oscillations commonly found downstream of steep gradients (Gibbs phenomenon) were not present in the XFEM results.

XFEM appears to produce results similar to shock fitting without the need for dynamically remeshing or clustering grid points at high-gradient regions. It is unknown if XFEM solutions downstream of shocks are able to maintain high-spatial order, or if they succumb to the same order of accuracy reduction issue identified by Carpenter and Casper [107].

Chapter 3

Numerical Methodology

3.1 COFFE Description

The Conservative Field Finite Element (COFFE) CFD solver was developed by the Department of Defense (DoD) High Performance Computer Modernization Program Computational Research and Engineering for Acquisition Tools and Environments - Air Vehicles (HPCMP CREATE^{TM}-AV) Program. CREATE is to address the need for a software package to be extensible with respect to spatial and temporal order of accuracy, available physics, and execution on modern compute architectures. [140–144] COFFE resides within the Kestrel component of CREATE-AV. It was chosen as the foundation for this effort because it is a high-order, finite-element solver that is currently under development, and it is representative of the next-generation of numerical solvers for engineering applications. The advancements made in COFFE resulting from this undertaking will impact engineering design and analyses over the lifetime of the code.

COFFE utilizes the Streamline Upwind/Petrov-Galerkin (SU/PG) finite-element method [45–52] to spatially discretize the governing equations, and higher-order spatial accuracy is achieved with Lagrangian basis functions. It was originally designed as a steady-state solver. [145–147] Many flow phenomena of interest to air vehicle designers, such as aeroacoustics, fluid/structure interactions, combustion, and shock wave/boundary layer interactions, are inherently unsteady. Part of this effort included the introduction of a time-accurate capability

to the solver. Several time-integration methods were investigated, and six were implemented within COFEE with 1^{st} to 4^{th} orders of accuracy.

3.1.1 Governing Equations

The conservative form of the Navier-Stokes equations is presented in Eq. (3.1). Note that all equations in this section assume three spatial dimensions and that no turbulence modeling is included.

$$\frac{\partial \boldsymbol{Q}}{\partial t} + \frac{\partial}{\partial x_j}(\boldsymbol{F}_c(\boldsymbol{Q}) - \boldsymbol{F}_v(\boldsymbol{Q}, \boldsymbol{\nabla Q})) = 0 \tag{3.1}$$

$\boldsymbol{Q}$ contains the conservation variables, which are given in Eq. (3.2), where $\{u_j,\ j = 1, 2, 3\}$ are the Cartesian velocity components, ρ is the density, and e_t is the total energy.

$$\boldsymbol{Q} = \begin{Bmatrix} \rho \\ \rho u_j \\ \rho e_t \end{Bmatrix} \tag{3.2}$$

$\boldsymbol{F}_c$ and $\boldsymbol{F}_v$ contain the convective and viscous fluxes, which are given in Eqs. (3.3) and (3.4), respectively.

$$\boldsymbol{F}_c = \begin{Bmatrix} \rho u_j \\ \rho u_j u_i + p\delta_{ij} \\ (\rho e_t + p)u_j \end{Bmatrix} \tag{3.3}$$

$$\boldsymbol{F}_v = \begin{Bmatrix} 0 \\ \tau_{ji} \\ u_i \tau_{ij} - q_j \end{Bmatrix} \tag{3.4}$$

τ_{ij} is the viscous stress tensor, δ_{ij} is the Kronecker delta, p is the pressure, and $q_j = -\lambda \partial T / \partial x_j$ is heat flux. τ_{ij} is described by Eq. (3.5) for a Newtonian fluid, where A_{ij}, given in Eq. (3.6), denotes the deviator of the strain tensor, which is the part of the strain tensor that represents shape change at constant volume. In Eq. (3.6) $S_{ij} = \frac{1}{2}(g_{ij} + g_{ji})$ is the strain tensor, and

$g_{ij} = \partial u_i / \partial x_j$ is the velocity gradient tensor. This formulation relies on Stokes' hypothesis, which assumes that the bulk viscosity can be neglected, and thus $\tau_{kk} = 0$.

$$\tau_{ij} = 2\mu A_{ij} \tag{3.5}$$

$$A_{ij} = S_{ij} - \frac{1}{3}\frac{\partial u_k}{\partial x_k}\delta_{ij} \tag{3.6}$$

Lastly the ideal equation of state ($p = \rho RT$) is used to describe the total energy in the flow, as shown in Eq. (3.7), where γ is the ratio of specific heats.

$$\rho e_t = \frac{p}{1-\gamma} + \frac{1}{2}\rho u_i u_i \tag{3.7}$$

3.2 Temporal Integration Methods

The COFFE solver operates by driving the overall residual, $\boldsymbol{R}$, to zero through an implicit Newton method that utilizes a Generalized Minimum Residual (GMRES) [148] linear solver. In the steady-state solver, convergence in $\boldsymbol{R}$ is achieved by reducing the temporal and spatial components, $\boldsymbol{R}_t = \frac{\partial \boldsymbol{Q}}{\partial t}$ and $\boldsymbol{R}_s = \frac{\partial}{\partial x_j}(\boldsymbol{F}_c - \boldsymbol{F}_v)$, to zero via a non-linear path to convergence. [145] The Newton iteration method is applied to the overall residual in Eq. (3.8).

$$\boldsymbol{R}^{n+1} = \boldsymbol{R}^n + \frac{\partial \boldsymbol{R}^n}{\partial \boldsymbol{Q}^n}\Delta \boldsymbol{Q}^{n+1} \tag{3.8}$$

The left hand side is set to zero, and the solution update vector, $\Delta \boldsymbol{Q}^{n+1}$, is solved for using Eq. (3.9).

$$\frac{\partial \boldsymbol{R}^n}{\partial \boldsymbol{Q}^n}\Delta \boldsymbol{Q}^{n+1} = -\boldsymbol{R}^n \tag{3.9}$$

The non-linear path for the steady-state solver employs a pseudo-time-stepping method that rapidly achieves convergence but is not directly relatable to physical time. The unsteady, time-accurate solver also reduces the overall residual to zero, but it does so by reducing the sum of the temporal and spatial components at each time step, since $\boldsymbol{R} = \boldsymbol{R}_t + \boldsymbol{R}_s$. The

spatial residual is handled with the same SU/PG discretization as the steady-state solver, and the temporal residual is calculated using one of the methods described in Section 2.2. Note that the temporal residual is also calculated in the steady-state solver using a 1st-order backward Euler method. The overall unsteady calculation algorithm is given in Algorithm 1.

```
for time = timeStep to endTime by timeStep do
    for stage = 1 to numberStages do
        newtonianIterations = 0;
        converged = False;
        while not converged do
            R = buildResidual(q, qOld);
            if initial or newtonianIterations > iterationLimit then
                dRdQ = linearizeResidual(R, q, qOld);
            end
            dQ = calculateDeltaQ(R, dRdQ);
            q += dQ;
            ++newtonianIterations;
            converged = checkConvergence();
        end
    end
end
```

Algorithm 1: Unsteady algorithm

3.2.1 Linear Multi-step Methods Implemented

The Backward Difference Formulae (BDF) family of implicit, linear, multi-step numerical methods were first described by Curtiss and Hirschfelder [149] and subsequently popularized by Gear [150]. These methods were the first introduced to solve stiff ordinary differential equations (ODE) [63] and are the most efficient at solving them. [60]

The equations for the 1st through 6th-order BDF methods (BDF1-BDF6) are given in Eqs. (3.10a) to (3.10f), where f is the derivative of y with respect to time. [60] BDF1-BDF6 are all zero-stable. BDF1 is also called the backward Euler method and is common among

other families of implicit methods. These methods are implicit because the unknown, y at t_{n+1}, is dependent on f at that same time step. They can be derived by fitting a Lagrange interpolating polynomial to the values at each time step, differentiating that polynomial with respect to time, and evaluating the derivative at t_{n+1}.

$$y_{n+1} - y_n = \Delta t f_{n+1} \tag{3.10a}$$

$$y_{n+2} - \frac{4}{3}y_{n+1} + \frac{1}{3}y_n = \frac{2}{3}\Delta t f_{n+2} \tag{3.10b}$$

$$y_{n+3} - \frac{18}{11}y_{n+2} + \frac{9}{11}y_{n+1} - \frac{2}{11}y_n = \frac{6}{11}\Delta t f_{n+3} \tag{3.10c}$$

$$y_{n+4} - \frac{48}{25}y_{n+3} + \frac{36}{25}y_{n+2} - \frac{16}{25}y_{n+1} + \frac{3}{25}y_n = \frac{12}{25}\Delta t f_{n+4} \tag{3.10d}$$

$$y_{n+5} - \frac{300}{137}y_{n+4} + \frac{300}{137}y_{n+3} - \frac{200}{137}y_{n+2} + \frac{75}{137}y_{n+1} - \frac{12}{137}y_n = \frac{60}{137}\Delta t f_{n+5} \tag{3.10e}$$

$$\begin{aligned} y_{n+6} - \frac{360}{147}y_{n+5} + \frac{450}{147}y_{n+4} - \frac{400}{147}y_{n+3} + \frac{225}{147}y_{n+2} \\ - \frac{72}{147}y_{n+1} + \frac{10}{147}y_n = \frac{60}{147}\Delta t f_{n+6} \end{aligned} \tag{3.10f}$$

Only the 1st and 2nd-order BDF methods are L-stable. Orders 3 - 6 are A(α)-stable. Orders above 6th are not zero-stable, so they are not included. The absolute stability regions for the BDFs 1-6 are given in Fig. 3.1. The stability region for each BDF is outside of the curve, and in order to be A-stable, which is a requirement for L-stability, the stability region must include the entire left half of the complex plane (negative real values). The zoomed in view shows that the stability curves for orders 3 - 6 extend into the left half of the complex plane, and thus the methods are not A-stable. L-stability requires that a method's stability function, $R(z)$, approaches zero as $z \to -\infty$. This is shown in Eqs. (3.11) and (3.12) for BDF1 and BDF2, respectively.

$$\lim_{z\to\infty} R(z) = \lim_{z\to\infty} \frac{1}{1-z} = 0 \tag{3.11}$$

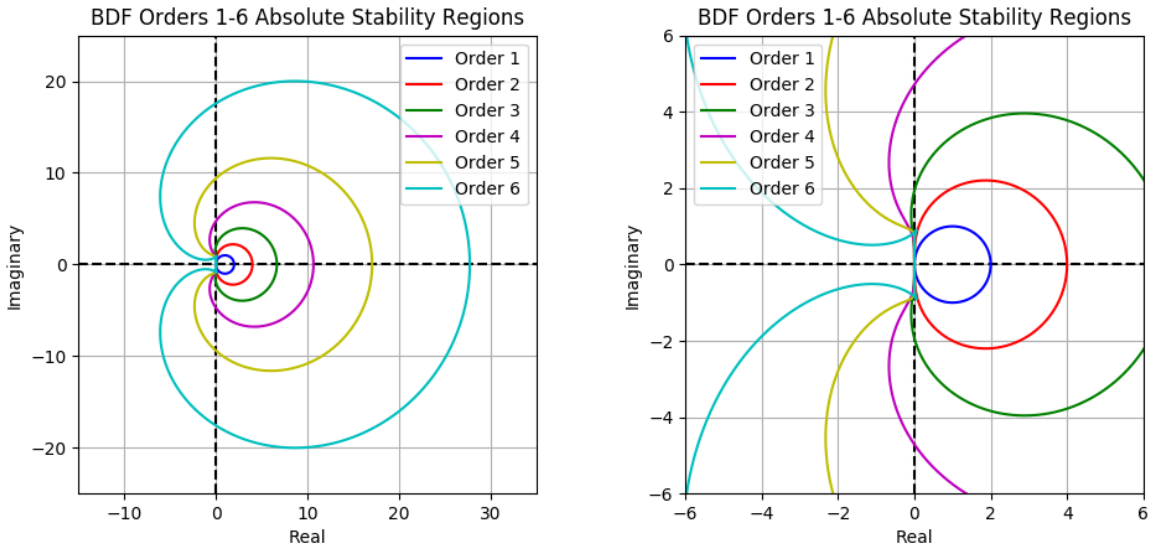

(a) Overall view **(b)** Zoomed view

Figure 3.1: Stability regions for Backward Difference Formulae orders 1-6, exterior of curves

$$\lim_{z\to\infty} R(z) = \lim_{z\to\infty} \frac{4 \pm \sqrt{16 - 4\,(3 - 2z)}}{2\,(3 - 2z)} = 0 \tag{3.12}$$

The time residual in COFFE is simply the derivative of the conservative variables, q, with respect to time. Eqs. (3.10a) to (3.10f) can be rearranged to solve for f and expressed as a single equation, Eq. (3.13), where k is the BDF order and the coefficients $\bar{\alpha}_i$ are given in Table 3.1. This simplification method was also employed by Newman and Anderson [9].

$$\mathbf{R}_{time}(q_{n+1}) = \left.\frac{\partial q}{\partial t}\right|_{n+1} \approx \frac{1}{\Delta t} \sum_{i=-1}^{k-1} \bar{\alpha}_i q_{n-i} \tag{3.13}$$

Vatsa, Carpenter, and Lockard [151] identified a method by which BDF2 can be combined with BDF3 and BDF4 to produce 2$^{\text{nd}}$-order L-stable schemes with lower error constants than the traditional BDF2 method. They called these methods BDF2OPT4 and BDF2OPT5, where the 4 and 5 denote the number of time steps required for the calculation. BDF2OPT4 (Eq. (3.14a)) is a linear combination of BDF2 and BDF3, whereas BDF2OPT5 (Eq. (3.14b)) is a linear combination of BDF2, BDF3, and BDF4. The stability regions for BDF2OPT4 and BDF2OPT5 compared to BDF3 and BDF4 are shown in Fig. 3.2. Note that the stability

Table 3.1: Recast Backward Difference Formulae Coefficients

k	$\bar{\alpha}_{-1}$	$\bar{\alpha}_0$	$\bar{\alpha}_1$	$\bar{\alpha}_2$	$\bar{\alpha}_3$	$\bar{\alpha}_4$	$\bar{\alpha}_5$
1	1	-1					
2	$\frac{3}{2}$	-2	$\frac{1}{2}$				
3	$\frac{11}{6}$	-3	$\frac{3}{2}$	$-\frac{1}{3}$			
4	$\frac{25}{12}$	-4	3	$-\frac{4}{3}$	$\frac{1}{4}$		
5	$\frac{137}{60}$	-5	5	$-\frac{10}{3}$	$\frac{5}{4}$	$-\frac{1}{5}$	
6	$\frac{49}{20}$	-6	$\frac{15}{2}$	$-\frac{20}{3}$	$\frac{15}{4}$	$-\frac{6}{5}$	$\frac{1}{6}$

Table 3.2: Recast Optimized 2nd-order Backward Difference Formulae Coefficients

OPT	$\bar{\alpha}_{-1}$	$\bar{\alpha}_0$	$\bar{\alpha}_1$	$\bar{\alpha}_2$	$\bar{\alpha}_3$
4	$\frac{5}{3}$	$-\frac{5}{2}$	1	$-\frac{1}{6}$	
5	$\frac{25}{12}\gamma + \frac{11}{6}\beta_5 + \frac{3}{2}\delta$	$-4\gamma - 3\beta_5 - 2\delta$	$3\gamma + \frac{3}{2}\beta_5 + \frac{1}{2}\delta$	$-\frac{4}{3}\gamma - \frac{1}{3}\beta_5$	$\frac{1}{4}\gamma$

curves for the OPT schemes do not extend into the left half of the complex plane, but that the stability curve for BDF2OPT5 touches the vertical axis at two points. The method is neutrally stable at those two points, which could have implications for stability in a CFD calculation.

$$\text{BDF2OPT4}(\beta_4) = (\beta_4)\text{BDF3} + (1-\beta_4)\text{BDF2} \tag{3.14a}$$

$$\text{BDF2OPT5}(\beta_5, \gamma) = (\gamma)\text{BDF4} + (\beta_5)\text{BDF3} + (1-\beta_5-\gamma)\text{BDF2} \tag{3.14b}$$

The coefficients that provide the lowest error constant are $\beta_4 = \frac{1}{2}$ for BDF2OPT4 and $\beta_5 = -\frac{5}{2} + 2\sqrt{2}$ and $\gamma = 1 - \frac{1}{\sqrt{2}}$ for BDF2OPT5. The accuracy for BDF2OPT4 and BDF2OPT5 is still 2nd-order; however, the optimization techniques reduce the leading-order truncation error of the BDF2 scheme by a factor of 2 and $\frac{2}{5-3\sqrt{2}} \approx 2.64$, respectively. [151] Coefficients for use in COFFE with Eq. (3.13) are given in Table 3.2, where $\delta = (1-\beta_5-\gamma)$.

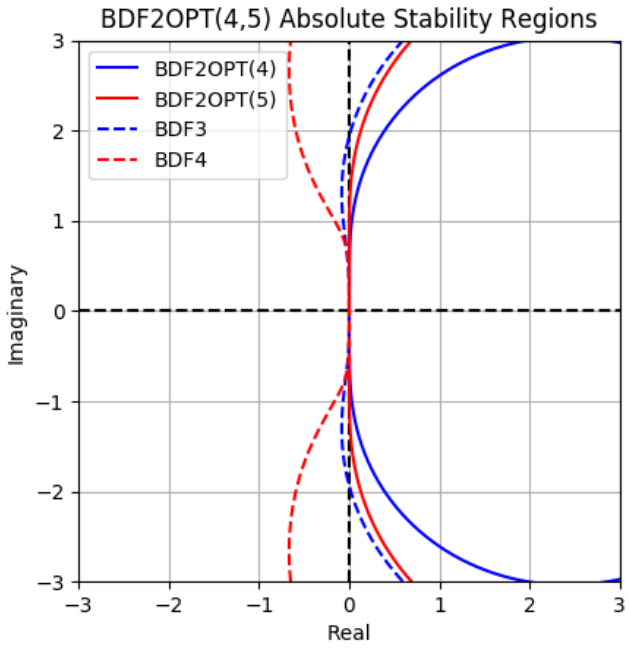

Figure 3.2: Stability regions for Four and Five-time-level Optimized 2nd-order Backward Difference Formulae compared to 3rd and 4th-order Backward Difference Formulae, zoomed, exterior of curves

3.2.2 Runge-Kutta Methods Implemented

Kennedy and Carpenter [152] conducted an extensive review of DIRK methods ranging from 2nd to 6th-order. Their review guided the selection of two L-stable SDIRK methods: a 3rd-order accurate, three-stage method (SDIRK33) and a 4th-order accurate, five-stage SDIRK method (SDIRK45). SDIRK33 was derived by Alexander [153] and was employed by Persson [154]. The tableau for SDIRK33 is shown in Eq. (3.15). SDIRK45 was outlined by Hairer and Wanner [63] and also used by Newman and Anderson [9]. The tableau for this method is shown in Eq. (3.16).

$$\begin{array}{c|cccc} 0.4358665215 & 0.4358665215 & & & \\ 0.7179332608 & 0.2820667392 & 0.4358665215 & & \\ 1 & 1.208496649 & -0.644363171 & 0.4358665215 & \\ \hline & 1.208496649 & -0.644363171 & 0.4358665215 & \end{array} \tag{3.15}$$

$$
\begin{array}{c|ccccc}
\frac{1}{4} & \frac{1}{4} & & & & \\
\frac{3}{4} & \frac{1}{2} & \frac{1}{4} & & & \\
\frac{11}{20} & \frac{17}{50} & -\frac{1}{25} & \frac{1}{4} & & \\
\frac{1}{2} & \frac{371}{1360} & -\frac{137}{2720} & \frac{15}{544} & \frac{1}{4} & \\
1 & \frac{25}{24} & -\frac{49}{48} & \frac{125}{16} & -\frac{85}{12} & \frac{1}{4} \\
\hline
 & \frac{25}{24} & -\frac{49}{48} & \frac{125}{16} & -\frac{85}{12} & \frac{1}{4}
\end{array}
\tag{3.16}
$$

The absolute stability function for RK methods is given in Eq. (3.17) from Hairer and Wanner [61]. The stability regions for SDIRK33 and SDIRK45 are shown in Fig. 3.3. For both methods, the entire left side of the complex plane is in the stability region, which indicates that the methods are A-stable. Both SDIRK33 and SDIRK45 are also L-stable, as shown in Eqs. (3.18) and (3.19).

$$
R(z) = \frac{\det(I - z\mathbf{A} + z\mathbb{1}\mathbf{b}^{\mathbf{T}})}{\det(I - z\mathbf{A})} \tag{3.17}
$$

$$
\lim_{z\to\infty} R(z) = \lim_{z\to\infty} \frac{-0.2376606908z^2 - 0.3075995645z + 1}{(-0.4358665215z + 1)^3} = 0 \tag{3.18}
$$

$$
\lim_{z\to\infty} R(z) = \lim_{z\to\infty} \frac{7z^4/768 + z^3/96 - z^2/8 - z/4 + 1}{-z^5/1024 + 5z^4/256 - 5z^3/32 + 5z^2/8 - 5z/4 + 1} = 0 \tag{3.19}
$$

3.2.3 Modified Frequency Analysis

Modified frequency analysis is akin to modified wave number analysis [155] and is a method of analyzing the effect of discretization on spectral content within the solution of a differential equation. Starting with the same test equation used in Dahlquist's absolute stability analysis, which was discussed in Section 2.2.1,

$$
y' = \lambda y, \qquad y(0) = y_0, \qquad \lambda \in \mathbb{C}
$$

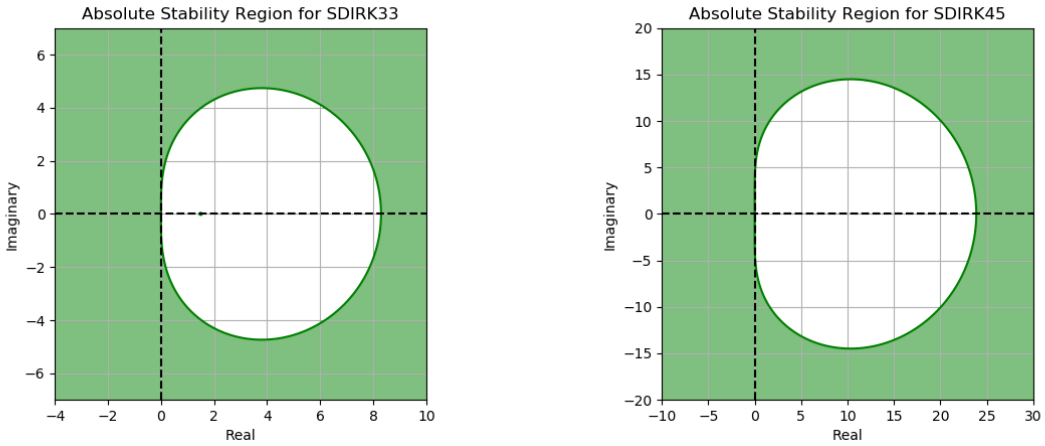

(a) SDIRK33 **(b)** SDIRK45

Figure 3.3: Stability regions for SDIRK methods

The analytical solution to this equation is $y = y_0 e^{\lambda t}$. If we discretize this solution and march from t to $t + \Delta t$,

$$y(t + \Delta t) = y_0 e^{\tilde{\lambda}(t+\Delta t)} = y_0 e^{\tilde{\lambda} t} e^{\tilde{\lambda}\Delta t} = y(t) e^{\tilde{\lambda}\Delta t} \tag{3.20}$$

This can be rearranged to solve for $\tilde{\lambda}\Delta t$, now called $\tilde{z}$, which is referred to as the *modified frequency*.

$$\tilde{\lambda}\Delta t = \tilde{z} = \ln\left(\frac{y(t + \Delta t)}{y(t)}\right) = \ln\left(R(z)\right) \tag{3.21}$$

The quantity $\frac{y(t+\Delta t)}{y(t)}$ was previously defined as the stability function, $R(z)$. By injecting a signal, $z = [0, i\pi]$, into the natural log of the stability function, one can assess each discretization method's dissipative and dispersive qualities as a function of frequency. The deviation of the imaginary component of the result from the injected signal represents dispersion error, and the real component represents amplification error. The modified frequency analyses for the BDF1, BDF2, SDIRK33, and SDIRK45 methods are shown in Fig. 3.4. The imaginary component of the modified frequency is shown in Fig. 3.4a, and deviations from the exact line represent dispersion errors. This plot shows that BDF1 and BDF2 have similar levels of dispersion, as do SDIRK33 and SDIRK45. The amplitude error, defined as $|e^{Re(\tilde{z})}|$, is shown in Fig. 3.4b, and this plot shows that BDF2 and SDIRK33

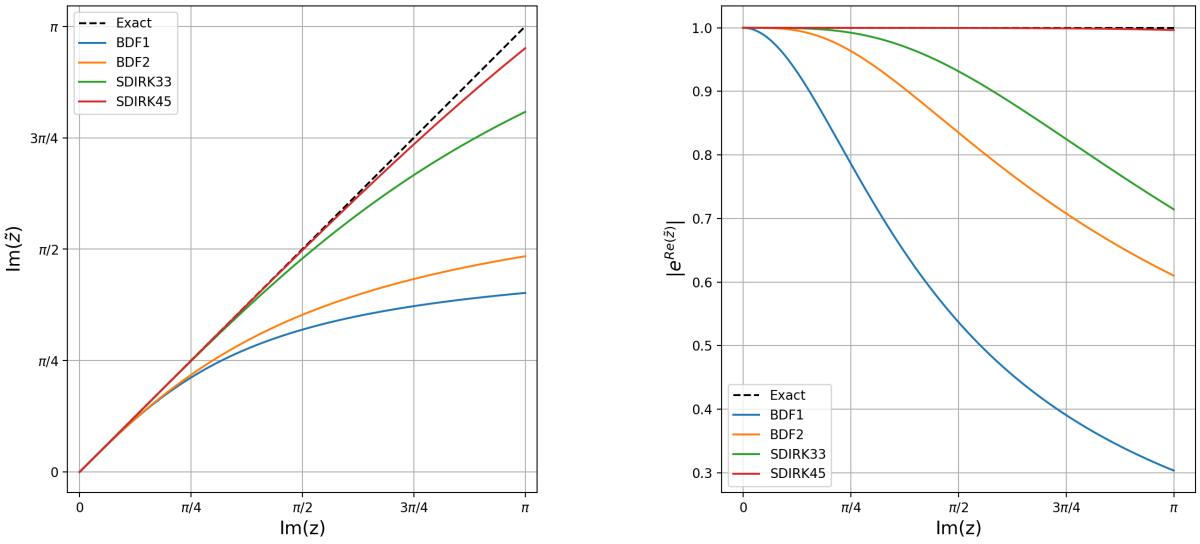

(a) Dispersion error

(b) Dissipation error

Figure 3.4: Modified frequency analyses for BDF1, BDF2, SDIRK33, and SDIRK45 methods.

have similar levels of dissipation. For both cases, the first-order BDF1 scheme is the worse performer, and the fourth-order SDIRK45 scheme is the best, as expected.

3.3 Diffusion Continuation as a Nonlinear Strategy

When running COFFE unsteady, a nonlinear system of equations is formed at each stage for SDIRK methods or each time step for BDF methods. This system, shown in Eq. (3.22) where $\mathbf{R}$ is the transient residual, is solved via Newton's method. The update to the solution vector $\Delta \boldsymbol{Q}$ is solved for using Eq. (3.23), and an under-relaxation parameter, ω^n in Eq. (3.24), is applied to the update for robust convergence. For large time steps, this system of equations can become very stiff and exceedingly difficult to solve. To alleviate this issue, constant, global artificial diffusion, shown in Eq. (3.25), is applied to the system of equations, where η_h is the homotopy diffusion coefficient. η_h is decreased to zero as the Newton system converges. Typical Newton system convergence with artificial diffusion is shown in Fig. 3.5.

$$0 = \mathbf{R}^{n+1} = \mathbf{R}^n + \frac{\partial \mathbf{R}^n}{\partial \boldsymbol{Q}^n} \Delta \boldsymbol{Q}^{n+1} \tag{3.22}$$

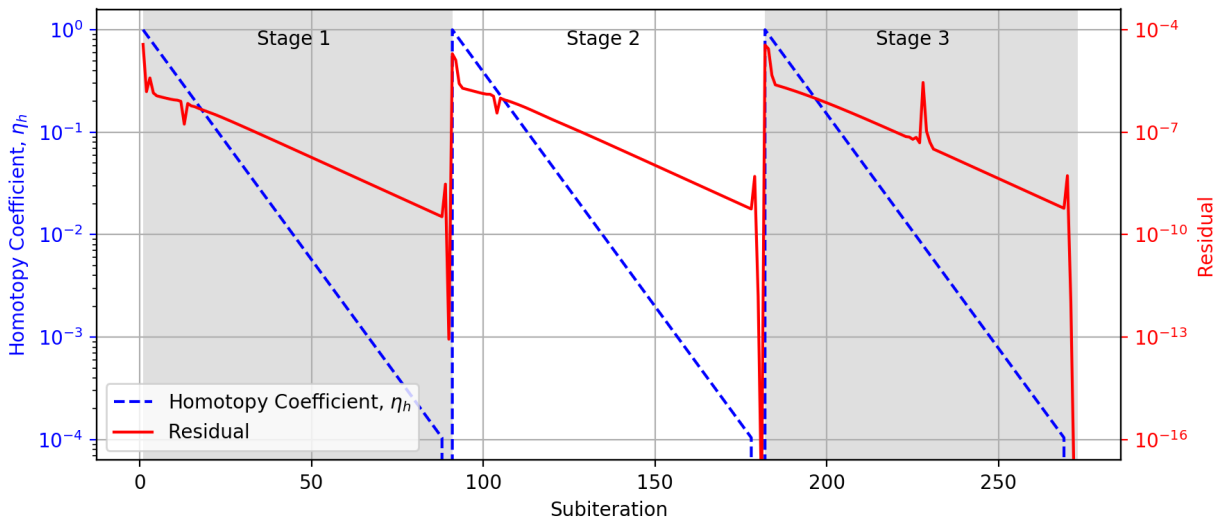

Figure 3.5: Example Newton convergence history for 3rd-order, 3-stage SDIRK method. Homotopy diffusion is bled off before convergence is declared.

$$\frac{\partial \mathbf{R}^n}{\partial \boldsymbol{Q}^n} \Delta \boldsymbol{Q}^{n+1} = -\mathbf{R}^n \tag{3.23}$$

$$\boldsymbol{Q}^{n+1} = \boldsymbol{Q}^n + \omega^n \Delta \boldsymbol{Q}^{n+1} \tag{3.24}$$

$$\boldsymbol{F}_{hd} = \left\{ \begin{array}{c} h_j \lambda_{max} \eta_h \frac{\partial \rho}{\partial x_j} \\ h_j \lambda_{max} \eta_h \frac{\partial \rho u_i}{\partial x_j} \\ h_j \lambda_{max} \eta_h \frac{\partial \rho h_t}{\partial x_j} \end{array} \right\} \tag{3.25}$$

3.4 Shock Capturing Technique

Shock capturing methods involve the inclusion of non-physical properties, such as artificial viscosity, as described by Von Neumann and Richtmyer [81], that smooth out the apparent discontinuity so that it may be modeled on a general numerical grid. This smoothing-out process over-estimates the physical width of the shock, which is on the order of the mean free path, so that it is proportional to the grid size, allowing the governing equations to be

solved. This introduces numerical anomalies, including, but not limited to, shock position [156] and inappropriate entropy generation [86].

COFFE utilizes artificial diffusion for shock capturing, and the present technique for its application is given below. The conservative form of the Navier-Stokes equations, with artificial diffusion flux added, are presented in Eq. (3.26). Note that all equations in this section assume three spatial dimensions, no turbulence modeling is included.

$$\frac{\partial \boldsymbol{Q}}{\partial t} + \frac{\partial}{\partial x_j}(\boldsymbol{F}_c - \boldsymbol{F}_v - \boldsymbol{F}_{ad}) = 0 \tag{3.26}$$

$\boldsymbol{Q}$, $\boldsymbol{F}_c$, and $\boldsymbol{F}_v$ were previously defined in Eqs. (3.2) to (3.4). $\boldsymbol{F}_{ad}$ contains the artificial diffusion flux used for shock capturing. The current definition of $\boldsymbol{F}_{ad}$ is given in Eq. (3.27). Within this term, h is an element length at each quadrature point, shown in Eq. (3.28), where ϕ_i are the basis functions. λ_{max}, defined in Eq. (3.29), is the maximum wave speed in the element, and ϵ_{shock} is the current shock sensor that is defined in Eq. (3.30). Within ϵ_{shock}, κ_{shock} is a user adjustable parameter that modifies the sensitivity of the sensor.

$$\boldsymbol{F}_{ad} = \begin{Bmatrix} h\lambda_{max}\epsilon_{shock}\frac{\partial \rho}{\partial x_j} \\ h\lambda_{max}\epsilon_{shock}\frac{\partial \rho u_i}{\partial x_j} \\ h\lambda_{max}\epsilon_{shock}\frac{\partial \rho h_t}{\partial x_j} \end{Bmatrix} \tag{3.27}$$

$$h = \frac{1}{\sqrt{\boldsymbol{\nabla}\phi_i \cdot \boldsymbol{\nabla}\phi_i}} \tag{3.28}$$

$$\lambda_{max} = |\boldsymbol{u}| + c \tag{3.29}$$

$$\epsilon_{shock} = \begin{cases} \frac{(\boldsymbol{u}\cdot\boldsymbol{\nabla}p)h}{(\boldsymbol{u}\cdot\boldsymbol{\nabla}p)h+\kappa_{shock}pc} & \boldsymbol{u}\cdot\boldsymbol{\nabla}p > 0 \\ 0 & \boldsymbol{u}\cdot\boldsymbol{\nabla}p \leq 0 \end{cases} \tag{3.30}$$

The current shock sensor, ϵ_{shock}, does not possess Galilean invariance, which is to say it operates differently depending on the inertial reference frame. This is due to the usage of the velocity field vector, $\boldsymbol{u}$, which is independent of any rigid-body motion. The hypersonic circular cylinder case, described in Appendix C.1, was used to demonstrate the consequences

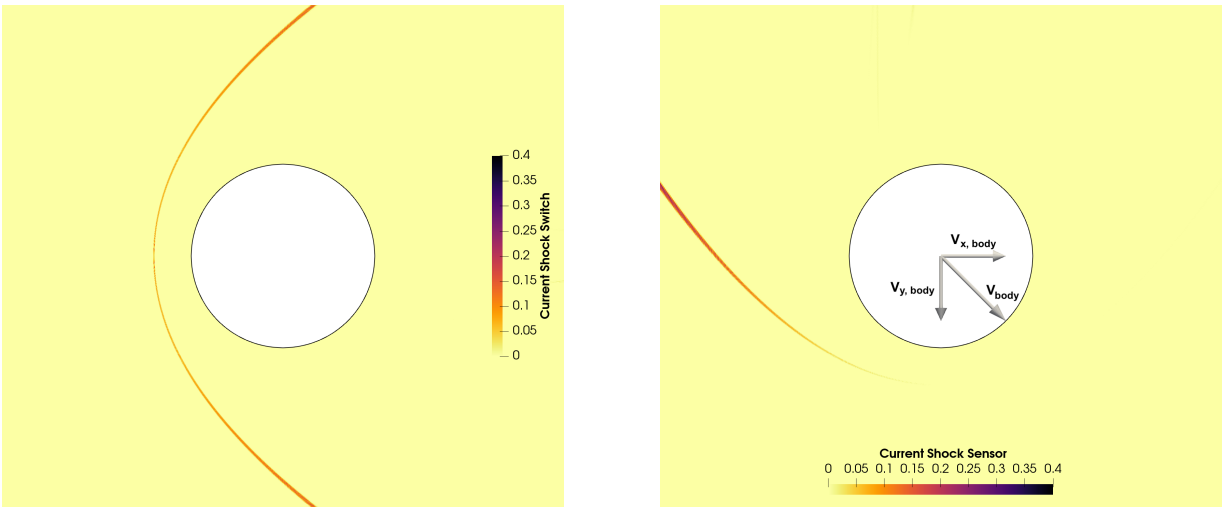

(a) Stationary cylinder **(b)** Moving cylinder

Figure 3.6: Comparison between calculated values of current shock sensor for stationary and moving bodies.

of lack of Galilean invariance. In this case, flow in the domain is from left to right at 5 km/s. In Fig. 3.6a the circular cylinder is stationary, and the shock sensor activates at the shock locations, as expected. In Fig. 3.6b the circular cylinder is moving through the domain with $V_{x,body} = V_{y,body} = 5\ km/s$. This body motion negates the bulk flow velocity in the domain, and it should result in the same shock pattern rotated counterclockwise 90 degrees. The current shock sensor only activates where the bulk flow velocity is aligned with a positive pressure gradient, and as a result, the current shock sensor is only active over a portion of shock.

3.4.1 Modified Shock Capturing Technique

For this effort, modifications have been made to the calculation of the artificial diffusion flux term, $\boldsymbol{F}_{ad}$, as well as the shock sensor. The changes to $\boldsymbol{F}_{ad}$ were designed to vary the application of artificial diffusion directionally within the momentum equations, in the same manner as Olson and Lele [99]. The shock sensor was modified to detect additional discontinuous features and apply artificial diffusion smoothly, analogous to the approach used by Barter and Darmofal [101].

The modified artificial diffusion flux term is shown in Eq. (3.31). Details on the changes to include directional h, h_j, and the new sensor, $\epsilon_{\tilde{s}}$, are described in this section.

$$\boldsymbol{F}_{ad} = \begin{Bmatrix} h_j \lambda_{max} \epsilon_{\tilde{s}} \frac{\partial \rho}{\partial x_j} \\ h_j \lambda_{max} \epsilon_{\tilde{s}} \frac{\partial \rho u_i}{\partial x_j} \\ h_j \lambda_{max} \epsilon_{\tilde{s}} \frac{\partial \rho h_t}{\partial x_j} \end{Bmatrix} \tag{3.31}$$

Riemannian Metric Tensor

The size and shape of an element is used to scale the amount of artificial diffusion applied to that element in a specific direction and its overall shock sensor value. The non-directional element length, h, used with the current shock sensor is calculated from Eq. (3.28). The inner product results in a single value for element length, calculable at each quadrature point. This provided information about the size of the cell, but not its shape. Numerous authors [12, 15, 99] have shown that a directional h, which accounts for element shape, can help apply diffusion properly for anisotropic cells.

In two dimensions, determining directional element lengths for a unit square aligned with the coordinate axes is a trivial task. In real-world problems, elements are rarely, if ever, uniformly shaped and aligned with coordinate axes. The Riemannian metric Tensor, $\mathcal{M}$, is a rotationally invariant symmetric positive definite (SPD) tensor that specifies the elements' size and shape by describing the mapping of the physical element in Cartesian coordinates, $\{x, y, z\}$, to the reference element in computational coordinates, $\{r, s, t\}$. It is commonly used for mesh generation and adaptation. [157–160]

The Riemannian metric tensor is defined as

$$\mathcal{M} = \boldsymbol{D}\boldsymbol{D}^T \tag{3.32}$$

where $\boldsymbol{D}$ is a tensor containing $D_{ij} = {}^{\partial x_i}/_{\partial r_j}$, which are obtained from the element nodal coordinates and derivatives of the basis functions. The directional h values, h_j, used in Eq. (3.31) are taken to be the square root of the main diagonal values of $\mathcal{M}$, or

$$h_j = \sqrt{\mathcal{M}_{jj}}$$

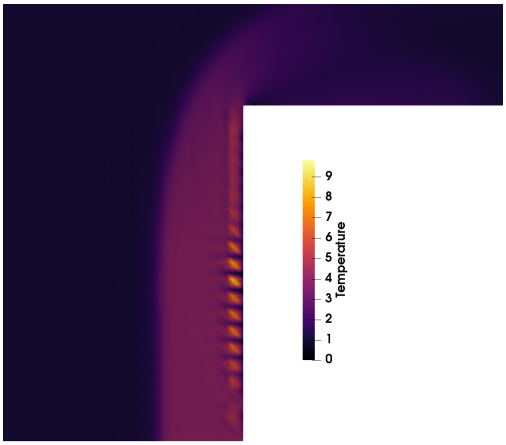

Figure 3.7: Temperature at the base of forward-facing step in the inviscid Mach 3 case from Woodward and Colella [161], with the current shock sensor used, and showing non-physical wall heating is present at the step's forward surface.

Exponential-Entropy Gradient Sensor

The current shock sensor has been shown to operate well on viscous problems, [102] but when it is applied to inviscid problems, especially those with blunt bodies, numerical errors resulting in non-physical wall heating have been observed in the stagnation region. In these regions numerical error accumulates rapidly and, with no viscosity to disperse it, causes the simulation to fail. The base of the forward facing step in the inviscid Mach 3 case popularized by Woodward and Colella [161] is shown in Fig. 3.7 shortly after startup using the current shock sensor. The wall heating issue is clearly identified by high/low temperature regions at the front surface of the step. If artificial diffusion were applied in this region, the erroneous temperature oscillations would dissipate, and the simulation would be allowed to proceed. The current shock sensor would need to be modified so that it would be triggered in these areas. The resulting sensor would not be purely a "shock" sensor, but would be more appropriately called a "smoothness" sensor.

The modified sensor is given in Eq. (3.33). It has a structure similar to the current shock sensor, shown in Eq. (3.30). The $\boldsymbol{u} \cdot \boldsymbol{\nabla} p$ term of the current shock sensor is the component that detects the presence of a shock. This term is replaced by the weighted magnitude of the gradient of a nondimensional exponential-entropy, $\tilde{s} = p/\rho^{\gamma}$. Nondimensional entropy is defined as $s = \ln\left(p/\rho^{\gamma}\right)$, and the natural log resulted in negative values that proved

problematic. A comparison between the exponential-entropy gradient sensor and an entropy gradient sensor is shown in Fig. 3.8. Due to the zero-crossing of entropy, the entropy gradient sensor has a line of erroneous activation emanating from the primary bow shock below the triple point. This line is not present in the exponential-entropy gradient sensor plot, and it is an artifact of the form of Eq. (3.33).

The magnitude of the exponential-entropy gradient is weighted by the Riemannian metric. The current sensor relies on a hyperbolic tangent function to smoothly apply artificial diffusion, per recommendations of Barter and Darmofal [101]. This smoothing is modified by multiplying the hyperbolic tangent function by the sensor value. This smoothly approaches zero and uniformly applies smoothing away from zero, as shown in Fig. 3.9.

$$\epsilon_{\tilde{s}} = \psi \tanh\left(10\psi\right), \quad \psi = \frac{\xi}{\xi + \kappa_{\tilde{s}}\tilde{s}} \tag{3.33}$$

where ξ is the weighted magnitude of the gradient of a nondimensional exponential-entropy

$$\xi = \sqrt{\boldsymbol{\nabla}\tilde{s}\mathcal{M}\boldsymbol{\nabla}\tilde{s}^T}.$$

A comparison between the current shock sensor and the exponential-entropy gradient sensor at the base of forward-facing step in the inviscid Mach 3 case is shown in Fig. 3.10. For this figure, $\kappa_{shock} = \kappa_{\tilde{s}} = 0.5$. Both sensors capture the upstream shock well, but the exponential-entropy gradient sensor also activates at the face of the step, where the wall heating error is present.

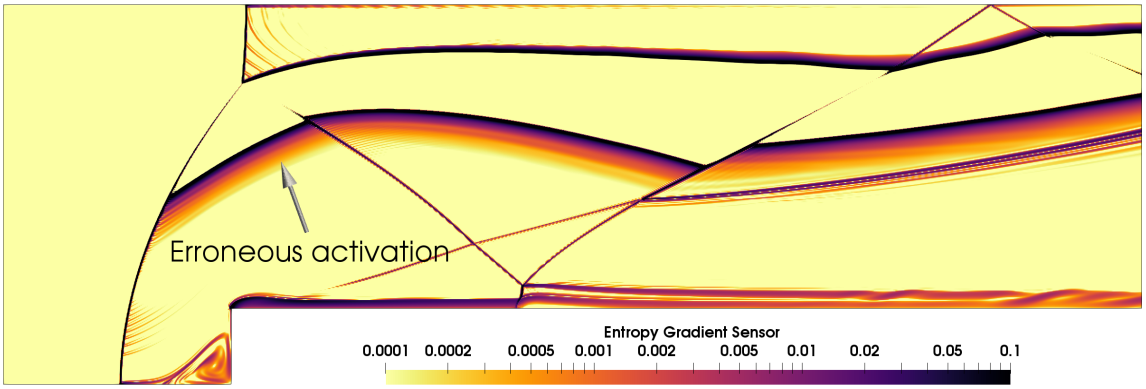

(a) Entropy Gradient Sensor

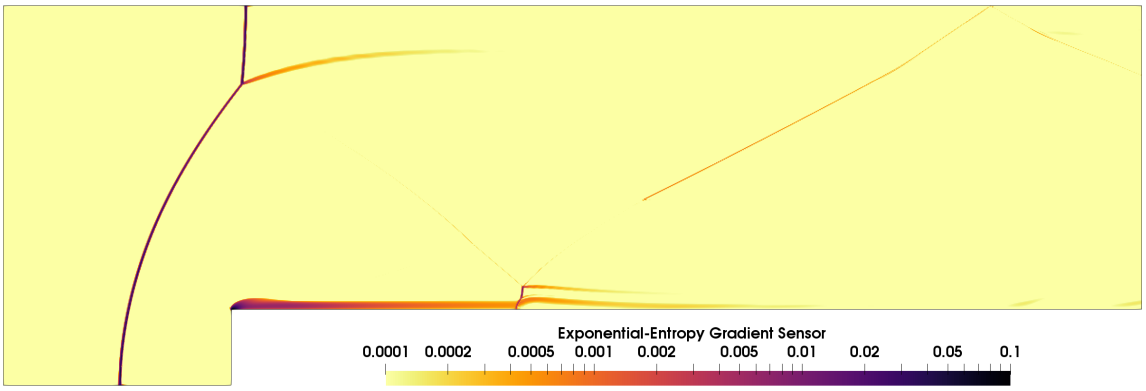

(b) Exponential-Entropy Gradient Sensor

Figure 3.8: Comparison between entropy gradient sensor and exponential-entropy gradient sensor on the inviscid Mach 3 case from Woodward and Colella [161].

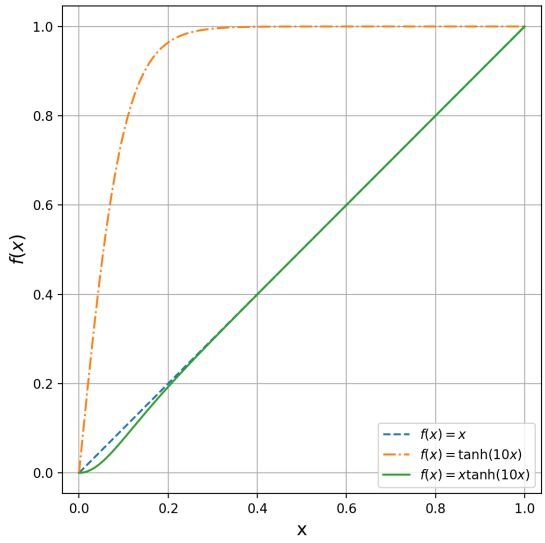

Figure 3.9: Modified sensor smoothing.

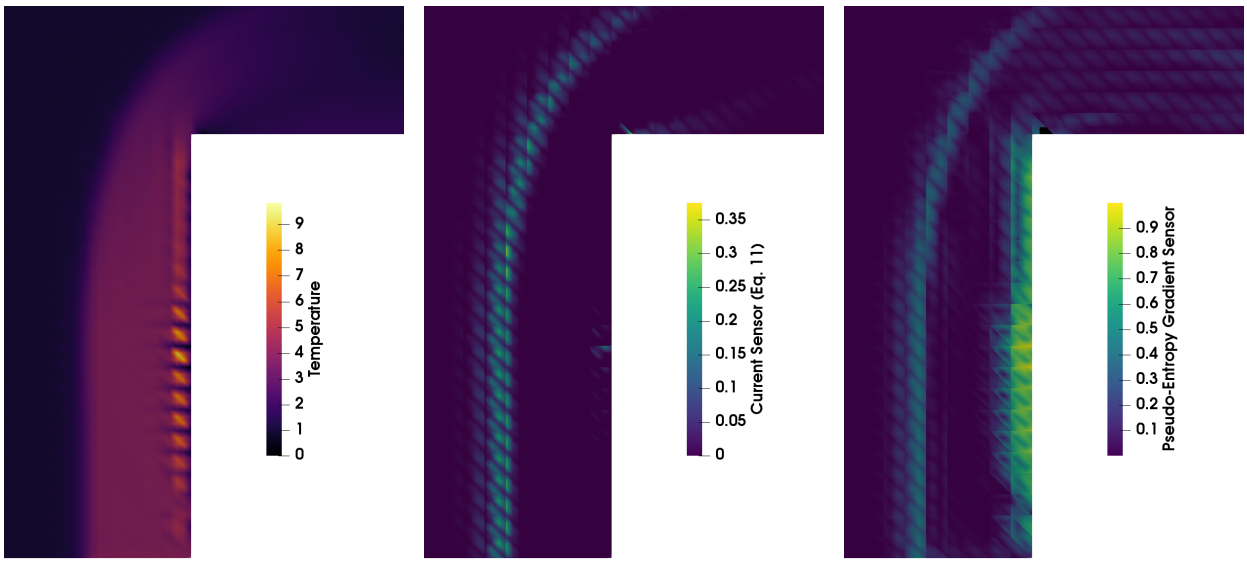

(a) Temperature

(b) Current Shock Sensor

(c) Exponential-Entropy Gradient Sensor

Figure 3.10: Comparison between current shock sensor and exponential-entropy gradient sensor at the base of forward-facing step in the inviscid Mach 3 case from Woodward and Colella [161].

Chapter 4

Temporal Integration Methods Verification and Validation

For this research, a new capability was added to COFFE to allow unsteady, time-accurate simulations with a variety of temporal integration methods. These methods range from 1st to 4th order of accuracy. The three verification and validation (V&V) test cases detailed in this chapter were used to ensure that the code functioned properly and that outputs compare well with accepted experimental or numerical results. A sound time-accurate solver is the foundation for moving shock simulations, and these cases aim to build confidence that the added capability is able to accurately model unsteady flow phenomena.

4.1 2-D Inviscid Isentropic Vortex

The 2-D inviscid isentropic vortex is a simple test case with an exact solution that has been used by several authors to verify a numerical method's ability to preserve a vortex without unwanted dissipation. [162–164] For this case, a vortex is initialized and convected horizontally over a distance $u_\infty t$ in order to assess the temporal accuracy. This case was run using the BDF1, BDF2, BDF2OPT4, BDF2OPT5, SDIRK33, and SDIRK45 methods. For the multi-step BDF2, BDF2OPT4, and BDF2OPT5 cases, exact solutions were used to initialize each of the previous time steps required by the method, since these methods are not self-starting.

Non-dimensionalized freestream values for the mean flow density, horizontal and vertical velocities, pressure, and temperature were set as $(\rho_\infty, u_\infty, v_\infty, T_\infty) = (1, 1, 0, 1)$. The freestream values were perturbed by δu, δv, and δT, given in Eq. (4.1), in order to produce the initial vortex at point (x_0, y_0). These initial values are similar to those of Yee, Sandham, and Djomehri [162] but corrected for COFFE's non-dimensionalization. All other conserved quantities were calculated assuming isentropic flow, $p/\rho^\gamma = 1$, and a perfect gas equation of state, $T = p\gamma/\rho$, where $\gamma = 1.4$ is the ratio of specific heats.

$$\delta u = -\frac{\beta}{2\pi}(y - y_0)e^{(1-r^2)/2} \tag{4.1a}$$

$$\delta v = \frac{\beta}{2\pi}(x - x_0)e^{(1-r^2)/2} \tag{4.1b}$$

$$\delta T = -\frac{\beta^2(\gamma - 1)}{8\pi^2}e^{(1-r^2)} \tag{4.1c}$$

where,

$$r = \sqrt{(x - x_0)^2 + (y - y_0)^2}.$$

In the perturbation equations, $\beta = 5$ is the specified vortex strength and r is the radial distance from the vortex center. The equations for the initial conditions are given in Eq. (4.2).

$$u = u_\infty + \delta u = 1 - \frac{\beta}{2\pi}(y - y_0)e^{(1-r^2)/2} \tag{4.2a}$$

$$v = v_\infty + \delta v = \frac{\beta}{2\pi}(x - x_0)e^{(1-r^2)/2} \tag{4.2b}$$

$$\rho = T^{1/(\gamma-1)} = (T_\infty + \delta T)^{1/(\gamma-1)} = \left[1 - \frac{\beta^2(\gamma - 1)}{8\pi^2}e^{(1-r^2)}\right]^{5/2} \tag{4.2c}$$

A rectangular grid over $x \in [-5, 9]$ and $y \in [-5, 5]$ was used for this case. The grid contained 112,000 uniform triangle elements with P2 (formally 3$^{\text{rd}}$-order accurate) spatial discretization, and all of the boundaries were set to freestream characteristic. The grid is shown in Fig. 4.1. The vortex was initially centered at $(x_0, y_0) = (0, 0)$ and allowed to convect

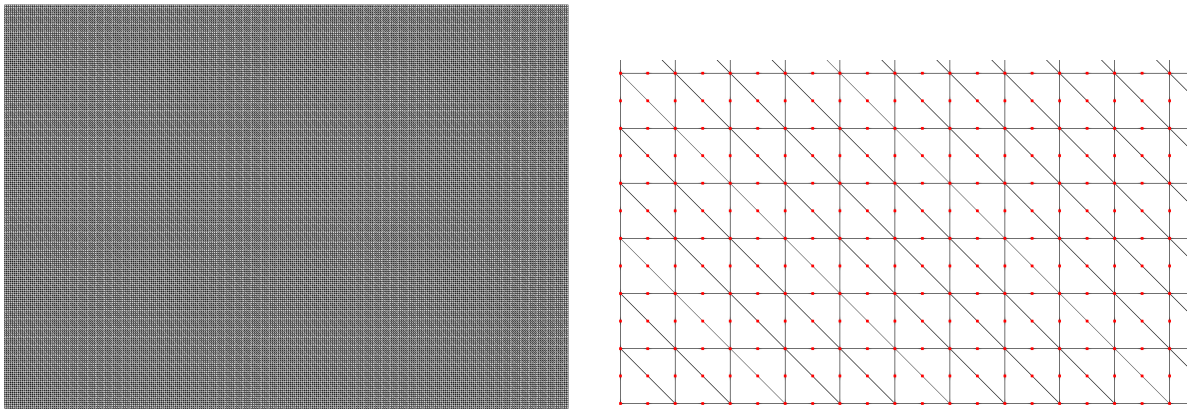

(a) Overall grid

(b) Zoomed view of lower left corner of grid, red dots indicate nodes

Figure 4.1: Grid for Euler vortex case

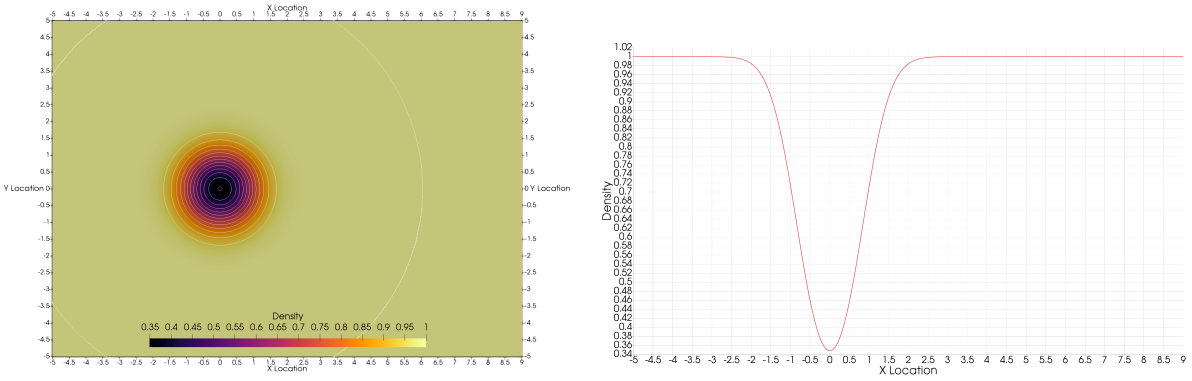

(a) Overall contour

(b) Line plot at $y = 0$

Figure 4.2: Initial density field for Euler vortex case

horizontally for non-dimensional time $t = 4$ (time non-dimensionalized by L/V_∞), after which the vortex would be centered at $(x, y) = (4, 0)$. The initial density field is shown in Fig. 4.2.

Each time-integration method was run at non-dimensional time steps of $\Delta t = 0.5$, 0.25, 0.125, 0.0625, 0.03125, and 0.01. Density profiles at $y = 0$ are shown in Figs. 4.3 and 4.4. The plots are grouped by time-integration method in Fig. 4.3 and by time step in Fig. 4.4. The exact solution is also presented on each plot.

The SDIRK45 time-integration method provided the best resolution of the vortex for each time step, which was expected since it is has the highest order of accuracy (4^{th}-order). The numerical errors present for the BDF1 case were dominated by diffusion, which served to dissipate the strength of the vortex as the time step increased. For large time steps

($\Delta t \geq 0.25$) the BDF2, BDF2OPT4, and BDF2OPT5 cases exhibited a lateral shift in the vortex. This shift is the result of numerical dispersion errors that are dominant in even-order schemes.

The overall error of any CFD simulation is the sum of spatial and temporal discretization errors. This verification effort is focused on the temporal error (ϵ_t), and isolating it from the spatial discretization error was accomplished by comparing the results at a given time step to results at $\Delta t = 0.01$, which Wang and Mavriplis [163] call the "numerical exact" solution. This assumes that there is negligible interaction between the spatial and temporal errors, and therefore the "numerical exact" solution contains the same spatial error as results for larger time step sizes.

The errors presented in Fig. 4.5 are the RMS values of the differences in all conserved quantities ($\rho, \rho u, \rho v, \rho e_t$) between a given time step and the "numerical exact" values at each of the grid points. Temporal order of accuracy, P_t, is related to ϵ_t and Δt through the expression $\epsilon_t = f\left(\Delta t^{P_t}\right)$, order of accuracy is simply the slope of the ϵ_t versus Δt when plotted on a log-log plot. Verification of temporal order of accuracy for each time-integration method is shown in Fig. 4.5. *Each method matches its theoretical order of accuracy*, and the BDF2OPT methods showed the same 2^{nd}-order accuracy as the BDF2 method, but with a lower error coefficient, as expected. Thus, it appears the time integration methods were implemented correctly in COFFE.

The temporal error was further decomposed using the method of Takacs [75], described in Section 2.2.4. The error in density (ρ) was used for this assessment. The dissipation and dispersion components of the temporal errors for each method and time step are shown in Table 4.1. Dissipation error is only present in appreciable quantities in the odd-order schemes (BDF1 and SDIRK33), and it is the dominant error source for BDF1. The even-order schemes (BDF2, BDF2OPT4/5, and SDIRK45) were dominated by dispersion errors; however, it should be noted that the overall error for SDIRK45 was orders of magnitude smaller than the BDF2 methods at each time step.

The errors in the SDIRK45 method were too low to be detectable in the line plots shown in Fig. 4.3. That is not the case for the BDF2 and BDF2OPT4/5 methods, and as a result the interaction between dissipation and dispersion error can be observed in the these results.

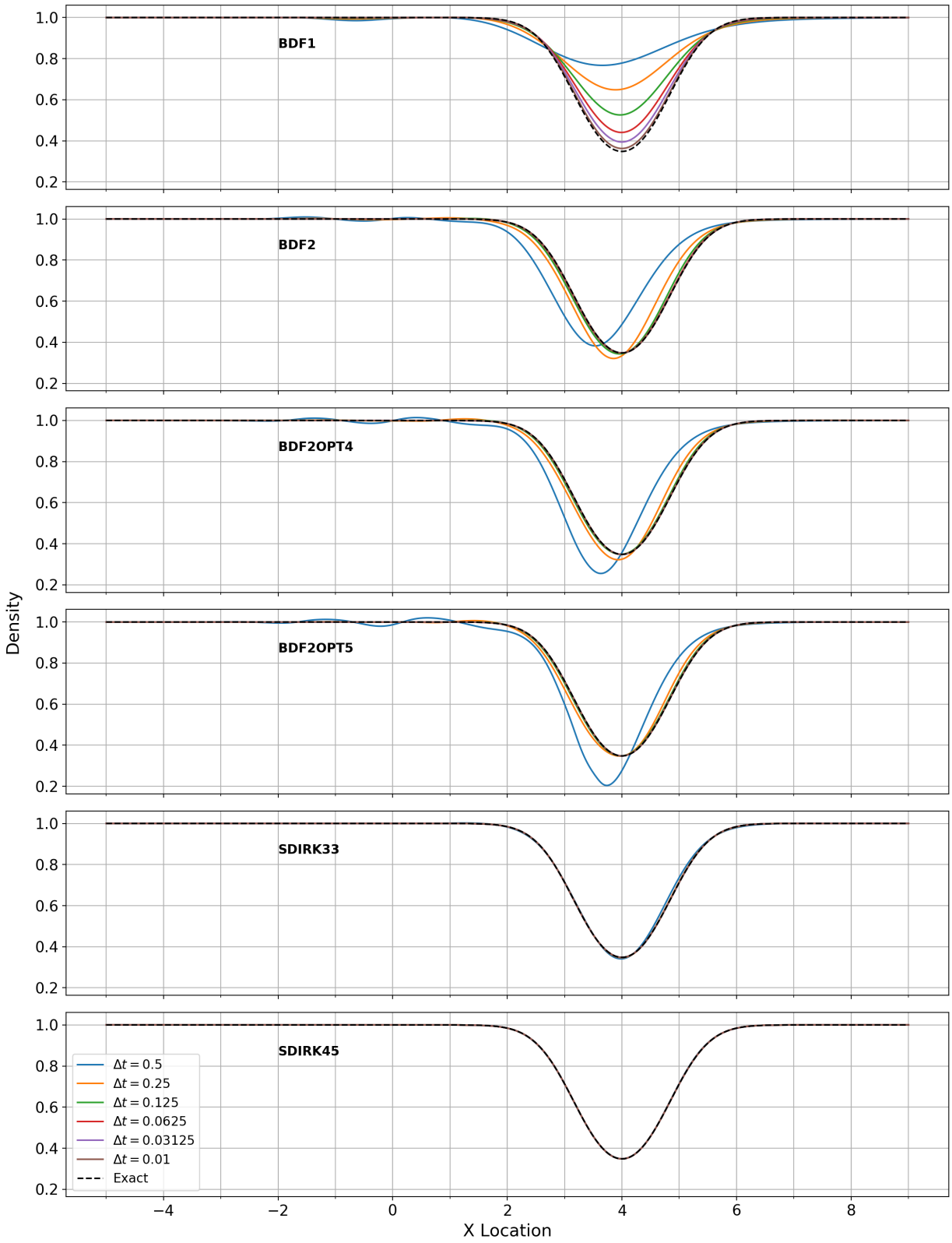

Figure 4.3: Density profiles for Euler vortex case at $t = 4$, grouped by time-integration method

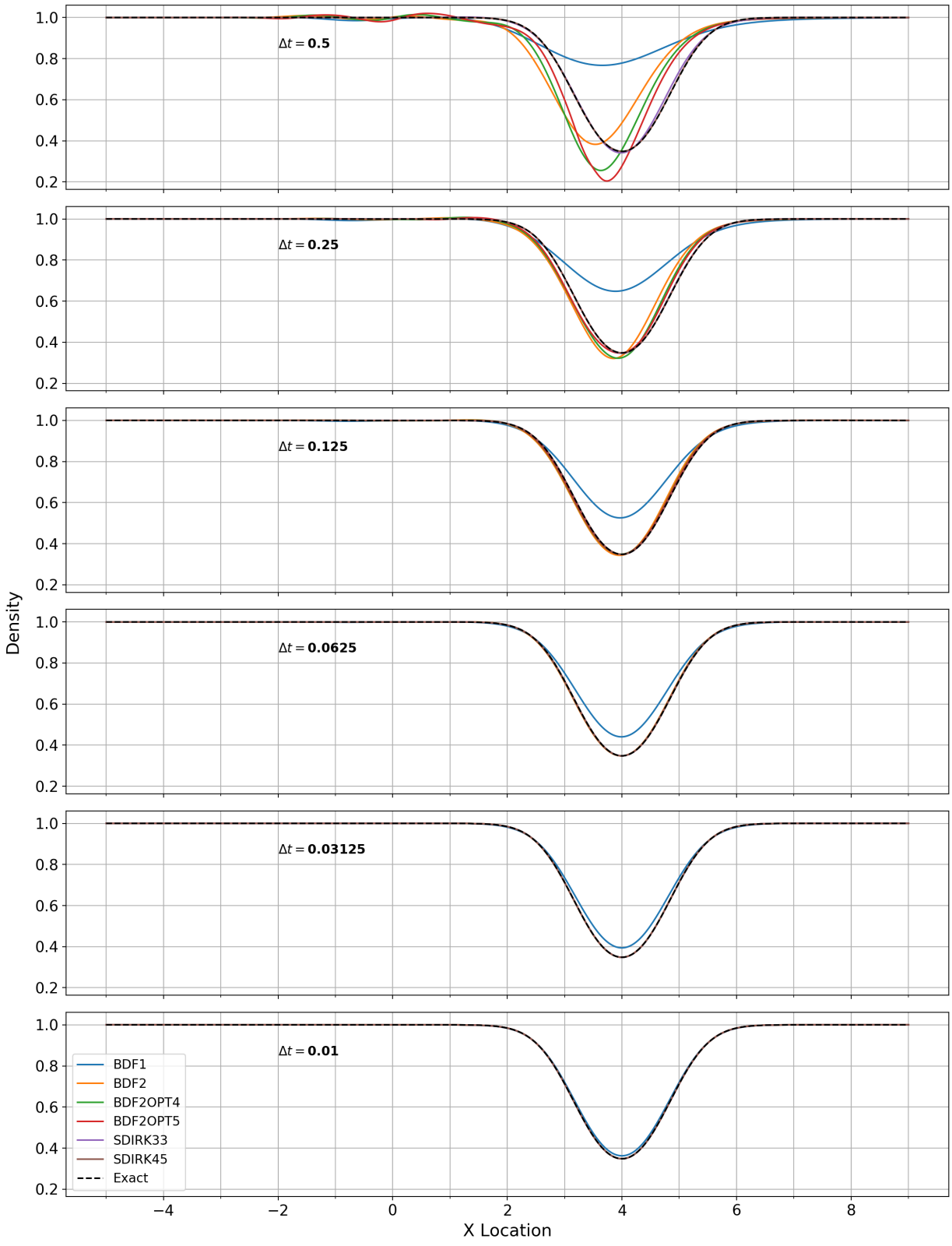

Figure 4.4: Density profiles for Euler vortex case at $t = 4$, grouped by time step

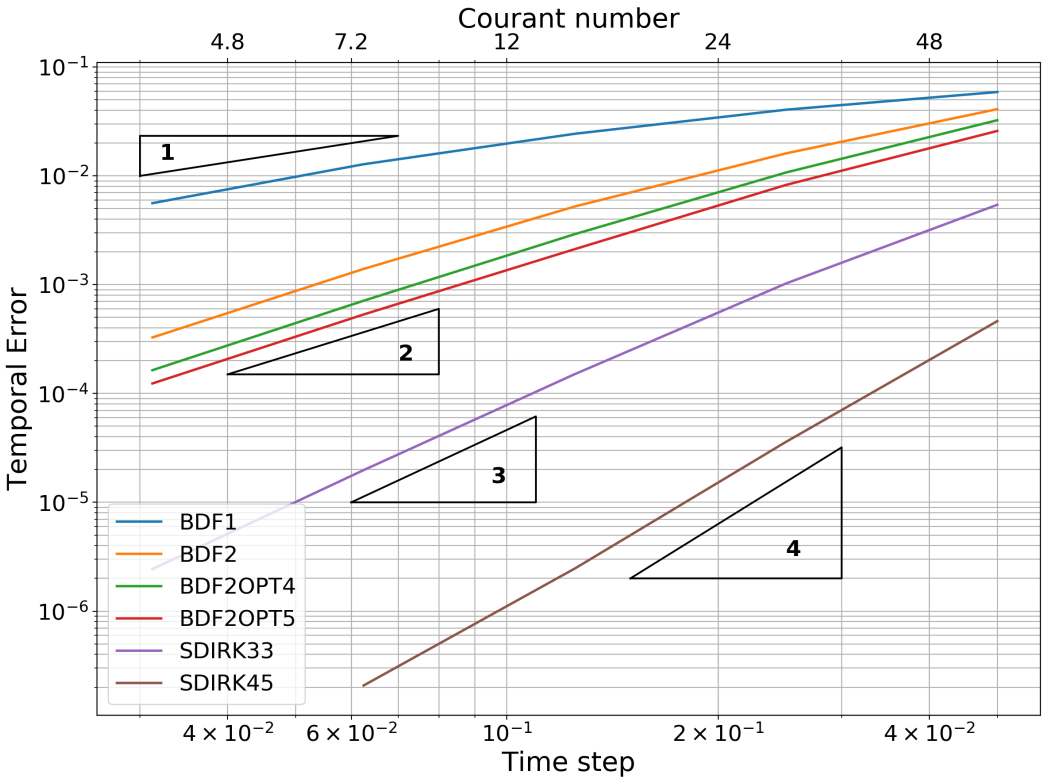

Figure 4.5: Temporal order of accuracy for BDF1, BDF2, BDF2OPT4, BDF2OPT5, SDIRK33 and SDIRK45 methods using data from Euler vortex runs

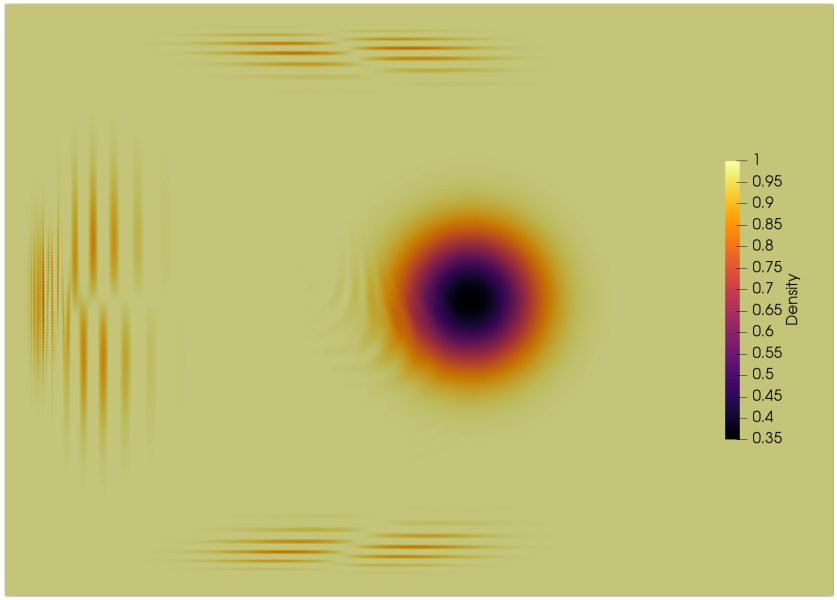

Figure 4.6: Density field for Euler vortex case using BDF5 after 46 time steps at $\Delta t = 0.0625$ (C=7.5)

At the largest time step ($\Delta t = 0.5$), approximately 7% of the error for the BDF2 case is attributable to dissipation. The BDF2OPT4/5 cases exhibit a marked decrease in the dissipation error, relative to the dispersion error, and this is evident in the line plots. The wiggles to the left of the density deficit, which are a characteristic feature of dispersion errors, are more prominent in the BDF2OPT4/5 cases than in the BDF2 case. A small amount of dissipation in the BDF2 case was effective at damping the wiggles.

The importance of numerical stability was detailed in Section 2.2.1, and A-stability was identified as a desirable property for a numerical method to possess because it allows the CFD practitioner to choose a time step size based on the physics of interest rather than numerical stability. To demonstrate how an unstable method can affect a simulation, the BDF5 method, which is not A-stable, was also run on the isentropic vortex at a relatively large time step. The density field for this case using the BDF5 after 46 time steps at $\Delta t = 0.0625$ (C = 7.5 calculated using Eq. (2.4)) is shown in Fig. 4.6. The striations at the top, bottom, and left of the flow field result from the temporal instability of the underlying method.

Table 4.1: Dissipation and dispersion components of density temporal errors in isentropic vortex case

Method	Δt	C	E_{total}	E_{diss}	$\%_{diss}$	E_{disp}	$\%_{disp}$
SDIRK45	0.5	60	3.258e-04	6.868e-06	0.04	3.257e-04	99.96
	0.25	30	2.580e-05	4.597e-07	0.03	2.580e-05	99.97
	0.125	15	1.759e-06	1.499e-08	0.01	1.759e-06	99.99
	0.0625	7.5	1.228e-07	2.045e-10	0.00	1.228e-07	100.00
	0.03125	3.75	2.980e-08	2.908e-11	0.00	2.989e-08	100.00
SDIRK33	0.5	60	3.239e-03	1.765e-03	29.70	2.715e-03	70.30
	0.25	30	5.752e-04	2.700e-04	22.03	5.079e-04	77.97
	0.125	15	8.192e-05	3.504e-05	18.29	7.405e-05	81.71
	0.0625	7.5	1.050e-05	4.365e-06	17.27	9.553e-06	82.73
	0.03125	3.75	1.276e-06	5.293e-07	17.22	1.161e-06	82.78
BDF2OPT5	0.5	60	1.978e-02	2.509e-03	1.61	1.962e-02	98.39
	0.25	30	5.399e-03	3.151e-05	0.00	5.398e-03	100.00
	0.125	15	1.456e-03	7.490e-06	0.00	1.456e-03	100.00
	0.0625	7.5	3.672e-04	1.604e-06	0.00	3.672e-04	100.00
	0.03125	3.75	8.543e-05	2.582e-07	0.00	8.543e-05	100.00
BDF2OPT4	0.5	60	2.349e-02	8.440e-04	0.13	2.348e-02	99.87
	0.25	30	7.172e-03	1.410e-04	0.04	7.171e-03	99.96
	0.125	15	1.987e-03	1.426e-05	0.01	1.987e-03	99.99
	0.0625	7.5	4.917e-04	1.198e-06	0.00	4.917e-04	100.00
	0.03125	3.75	1.133e-04	2.470e-07	0.00	1.133e-04	100.00
BDF2	0.5	60	2.797e-02	7.297e-03	6.81	2.700e-02	93.19
	0.25	30	1.078e-02	1.673e-03	2.41	1.065e-02	97.59
	0.125	15	3.461e-03	2.622e-04	0.57	3.451e-03	99.43
	0.0625	7.5	9.456e-04	3.708e-05	0.15	9.449e-04	99.85
	0.03125	3.75	2.243e-04	4.771e-06	0.05	2.243e-04	99.95
BDF1	0.5	60	4.562e-02	4.043e-02	78.53	2.114e-02	21.47
	0.25	30	3.208e-02	2.905e-02	81.99	1.361e-02	18.01
	0.125	15	1.927e-02	1.766e-02	83.92	7.728e-03	16.08
	0.0625	7.5	1.000e-02	9.181e-03	84.28	3.965e-03	15.72
	0.03125	3.75	4.340e-03	3.976e-03	83.90	1.742e-03	16.10

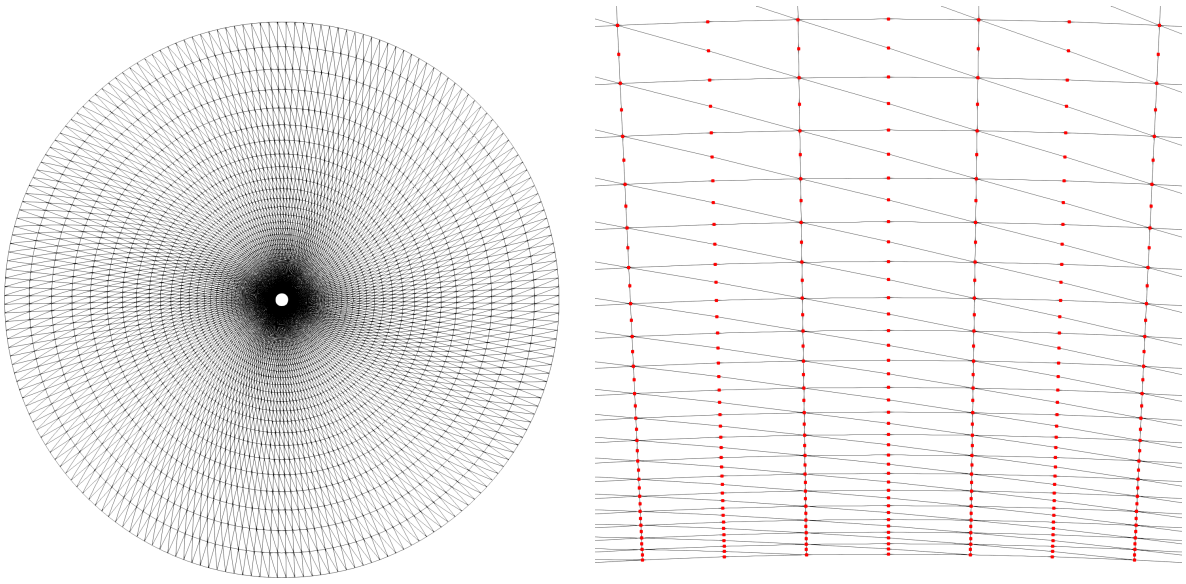

(a) Overall grid **(b)** Zoomed view of cylinder

Figure 4.7: Grid for 2-d circular cylinder case

4.2 2-D Circular Cylinder

The second test case was vortex shedding around a two-dimensional circular cylinder at a Mach number of 0.2 and various Reynolds numbers, based on cylinder diameter, D. The computational grid for this case is shown in Fig. 4.7. It consisted of 32,000 P2 triangle elements, which were created by diagonalizing a 200-by-80 (θ-by-r) element O-grid. The initial wall spacing was $0.001D$ with growth rate of 1.1. The outer boundary was approximately $42D$ and set to freestream, and the cylinder boundary was set to no-slip, adiabatic wall.

Zdravkovich [165] assembled virtually all of the available experimental, analytical, and numerical data on circular cylinders in cross flow between 1938 and his publication in 1997, and he identified several flow regimes characterized by Reynolds number based on cylinder diameter. The regimes of interest for this investigation are listed below.

- Laminar vortex shedding (L3) – $48 < Re < 180$
- Turbulent transition in wake (TrW) – $180 < Re < 400$
- Turbulent transition in shear layer (TrSL) – $400 < Re < 200,000$

Flow in the L3[1] regime is laminar and two-dimensional, whereas the TrW and TrSL regimes are three-dimensional in nature due to turbulent transition in the wake and shear layers, respectively. Mittal and Balachandar [166] found that three-dimensionality in the flow, which manifests as streamwise vortices, cannot be modeled in a two-dimensional simulation. These streamwise vortices extract energy from the vortex shedding motion, reducing the Reynolds stresses, and ultimately reducing the magnitude of the mean base pressure and thus the drag. For this reason, two-dimensional simulations in the L3 regime were compared to numerical and experimental data, while simulations in the TrW and TrSL regimes were only compared to published two-dimensional numerical results. Comparing the results in the TrW and TrSL regimes to experimental data would not be appropriate because the two-dimensional simulations are not capable of modeling key flow features.

Henderson [167] published results for numerical simulations at Reynolds numbers from 10 to 1,000. A curve fit of Strouhal number ($St = fD/U_\infty$) as a function of Reynolds number of these two-dimensional cases is given in Eq. (4.3). [168] This curve fit has an average error-of-fit of 0.0004, and it diverges from experimental and three-dimensional numerical simulations at approximately $Re = 180$, which is consistent with the TrW regime, where turbulent transition occurs in the wake.

$$St = 0.2731 - \frac{1.1129}{\sqrt{Re}} + \frac{0.4821}{Re} \tag{4.3}$$

4.2.1 Re = 1,200

The first set of cases investigated the impact of time step and time-integration method on lift coefficient at $Re = 1,200$, which is in the TrSL regime. Flow at this Reynolds number is three-dimensional, with period vortex shedding and turbulent transition occurring in the shear layer. No comparisons will be made to experimental results, as the present simulation is two-dimensional, but comparisons will be made to Eq. (4.3), which was created using results from other two-dimensional simulations.

Each time-integration method was run at non-dimensional time steps of $\Delta t = 2^{-n}$ for $n = 1$ to 6 and a total time of 100. Only data for time between 50 and 100 were used

[1]The L1 and L2 regime refer to creeping flow and laminar flow with a steady separation, respectively.

Table 4.2: Strouhal numbers for $Re = 1,200$ at various Δt and time methods, Eq. (4.3) value is 0.2414

Δt	BDF1	BDF2	BDF2OPT4	BDF2OPT5	SDIRK33	SDIRK45
0.5	0.1621	0.1915	0.2101	0.2202	0.2331	0.2448
0.25	0.1851	0.2233	0.2297	0.2260	0.2444	0.2427
0.125	0.2037	0.2397	0.2447	0.2430	0.2434	0.2416
0.0625	0.2187	0.2426	0.2424	0.2422	0.2421	0.2414
0.03125	0.2302	0.2421	0.2417	0.2416	0.2415	0.2414
0.015625	0.2365	0.2416	0.2414	0.2414	0.2414	0.2414

Table 4.3: RMS lift coefficient for $Re = 1,200$ at various Δt and time methods

Δt	BDF1	BDF2	BDF2OPT4	BDF2OPT5	SDIRK33	SDIRK45
0.5	0.0944	0.7185	0.8245	0.8856	0.9819	1.1273
0.25	0.4862	0.9640	1.0548	1.0734	1.0768	1.1475
0.125	0.7317	1.0491	1.0609	1.0839	1.1314	1.1501
0.0625	0.8865	1.1074	1.1338	1.1390	1.1457	1.1511
0.03125	0.9893	1.1423	1.1486	1.1500	1.1505	1.1514
0.015625	1.0544	1.1502	1.1515	1.1516	1.1515	1.1516

for subsequent analyses. Lift coefficient grouped by time-integration method is plotted in Fig. 4.8. The Strouhal number and the RMS value for lift coefficient, $C_{l,RMS}$, were calculated for each of the solutions, and the values are presented in Tables 4.2 and 4.3, respectively.

The SDIRK45 time-integration method provided the best representation of the lift coefficient for each time step, which was expected since it is has the highest order of accuracy (4^{th}-order). BDF1 introduced the most numerical error, lowering the Strouhal number and decreasing the RMS amplitude of the periodic lift coefficient. Each method, except BDF1, approached the same Strouhal number (0.2414) as Δt decreased, and that value matched the number calculated from Eq. (4.3) to 4 significant digits. SDIRK45 converged to 0.2414 for $\Delta t < 0.0625$, which is a 4 times larger time step than BDF2OPT4/5. Each method, except BDF1, also approached the same $C_{l,RMS}$ value of 1.15.

A comparison between the density fields for the SDIRK45, SDIRK33, BDF2, and BDF1 methods at $t = 100$ for $\Delta t = 0.125$ is shown in 4.11. The contour lines reveal that the shed vortices maintain their strength longer in the higher-order SDIRK methods. The vertical

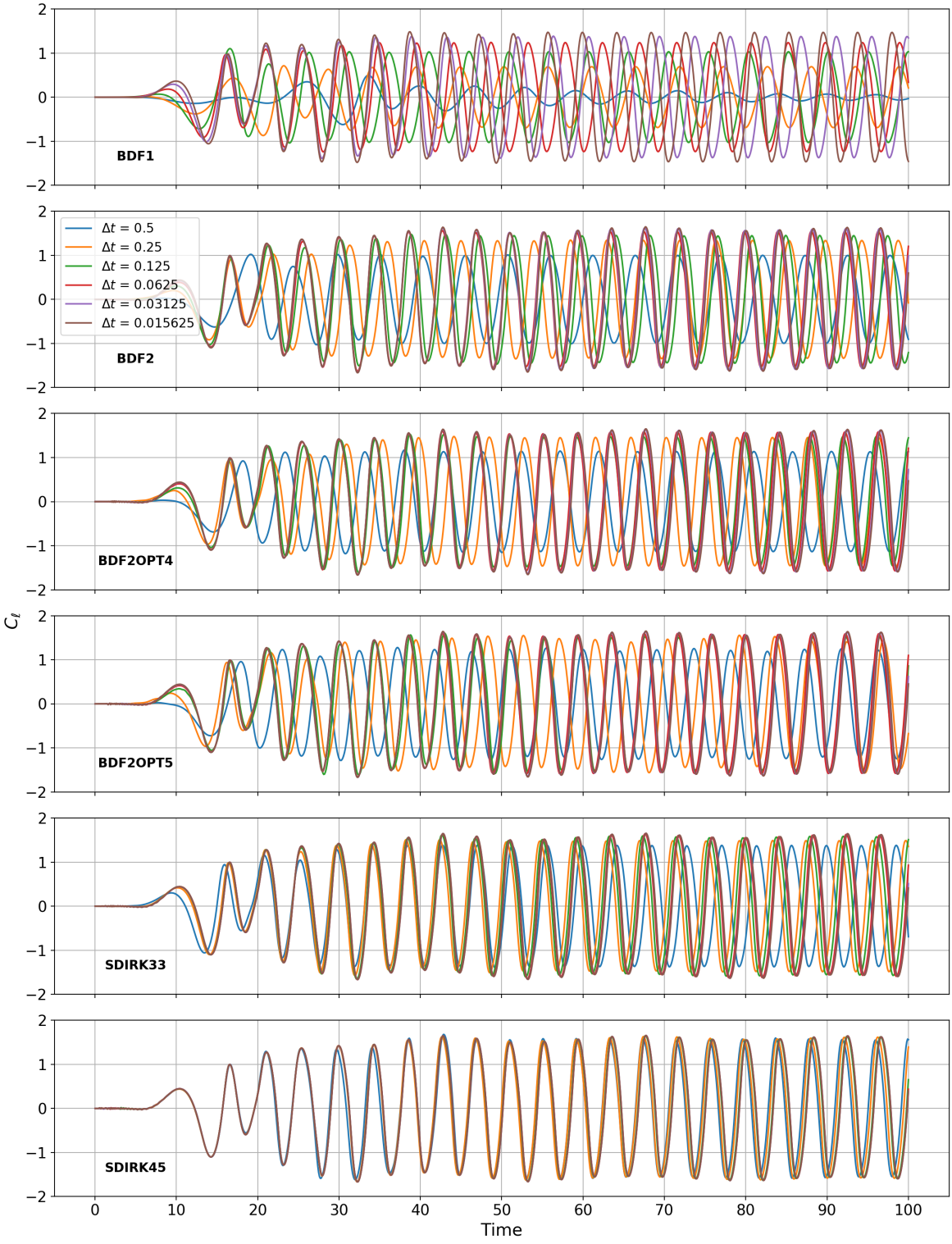

Figure 4.8: Lift coefficient for circular cylinder at $Re = 1,200$, grouped by time-integration method

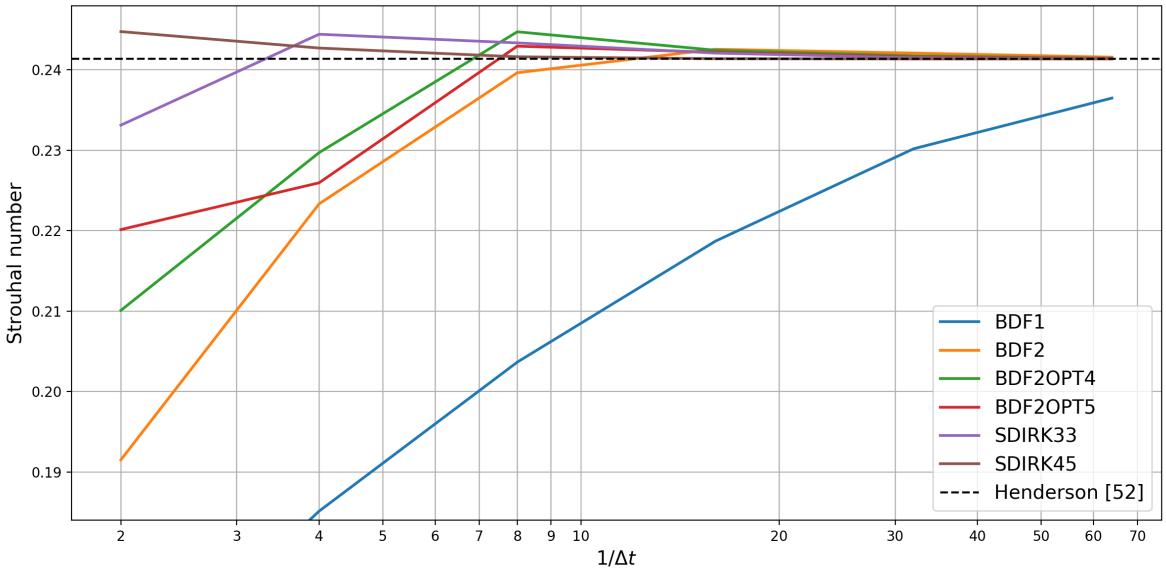

Figure 4.9: Strouhal numbers for $Re = 1,200$ plotted versus $1/\Delta t$ for various time methods

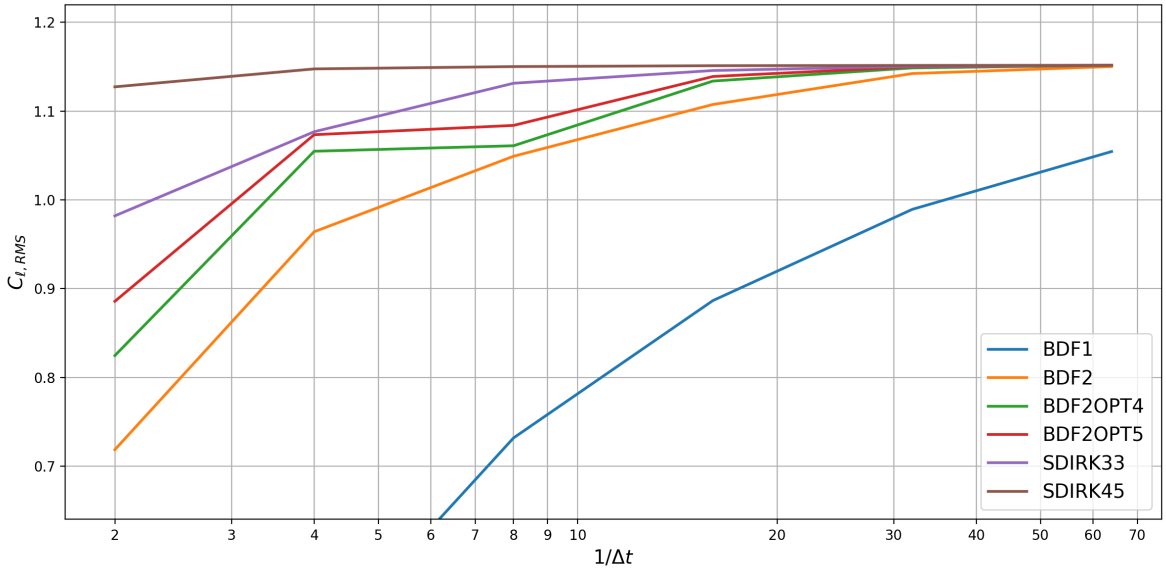

Figure 4.10: RMS lift coefficient for $Re = 1,200$ plotted versus $1/\Delta t$ for various time methods

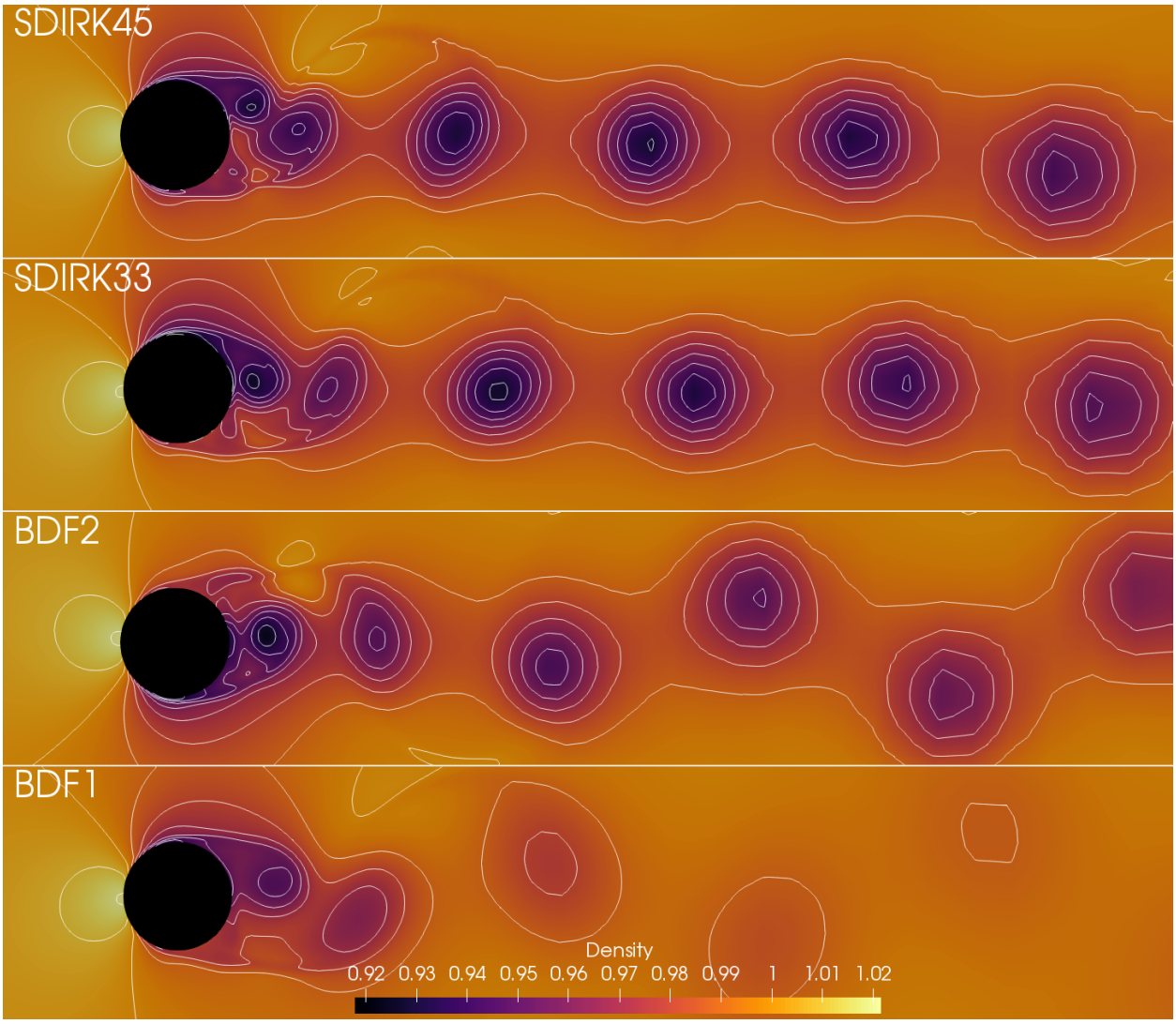

Figure 4.11: Density field for circular cylinder at $Re = 1,200$ at $t = 100$ for SDIRK45, SDIRK33, BDF2, and BDF1 methods using $\Delta t = 0.125$

position of the vortices downstream of the circle for the SDIRK methods is more uniform than those in the BDF2 method, which may be attributable to the higher dispersion error in the latter method. SDIRK45 is an even-ordered scheme, but the overall temporal error is much lower, which could be why the vortical disorder is not evident in its wake.

4.2.2 Re = 100-400

Periodic vortex shedding was investigated for five Reynolds numbers: 100, 200, 250, 300, and 400. These match the Reynolds number cases that were investigated by Rajani, Kandasamy, and Majumdar [169] in the L3 and TrW flow regimes. For each of the cases, the flow was initialized with the flow fields generated by the $Re = 1,200$ cases. This forced the periodic motion to set up more rapidly than it would have naturally, particularly in the $Re = 100$ case, and it is not believed to have adversely affected the current results because they match well with available data. All cases were run to $t = 200$ with $\Delta t = 0.0625$, and only data from $100 < t \leq 200$ were used for calculations to ensure that any effects from the initial flow field were no longer present in the domain. Lift and drag coefficients for $Re = 100 - 400$ are given in Fig. 4.12.

The Strouhal number and mean drag coefficient variation with Reynolds number is shown in Fig. 4.13. The calculated Strouhal number matched the curve fit provided by Henderson [167] (Eq. (4.3)) to within 1%, and the $Re = 100$ result matched experimental data from Williamson [170] to within 0.7%. As Reynolds number increased, the current results deviated from Williamson's data, due to the flow three-dimensionality described by Mittal and Balachandar [166]. The discontinuity between 175 and 250 is the result of two instability modes that are present in the TrW regime, which are further described in Williamson [170, 171]. The calculated mean drag coefficients were 2-4% higher than the values calculated by Rajani, Kandasamy, and Majumdar [169].

Comparisons of Strouhal number, RMS lift coefficient, mean drag coefficient, and base pressure coefficient at $Re = 300$ between the present numerical results and previous numerical and experimental results is shown in Table 4.4. The current results more closely aligned with the two-dimensional simulations by Mittalt and Balachandar [172], with values of Strouhal number and base pressure coefficient matching to within approximately 0.5% and lift and

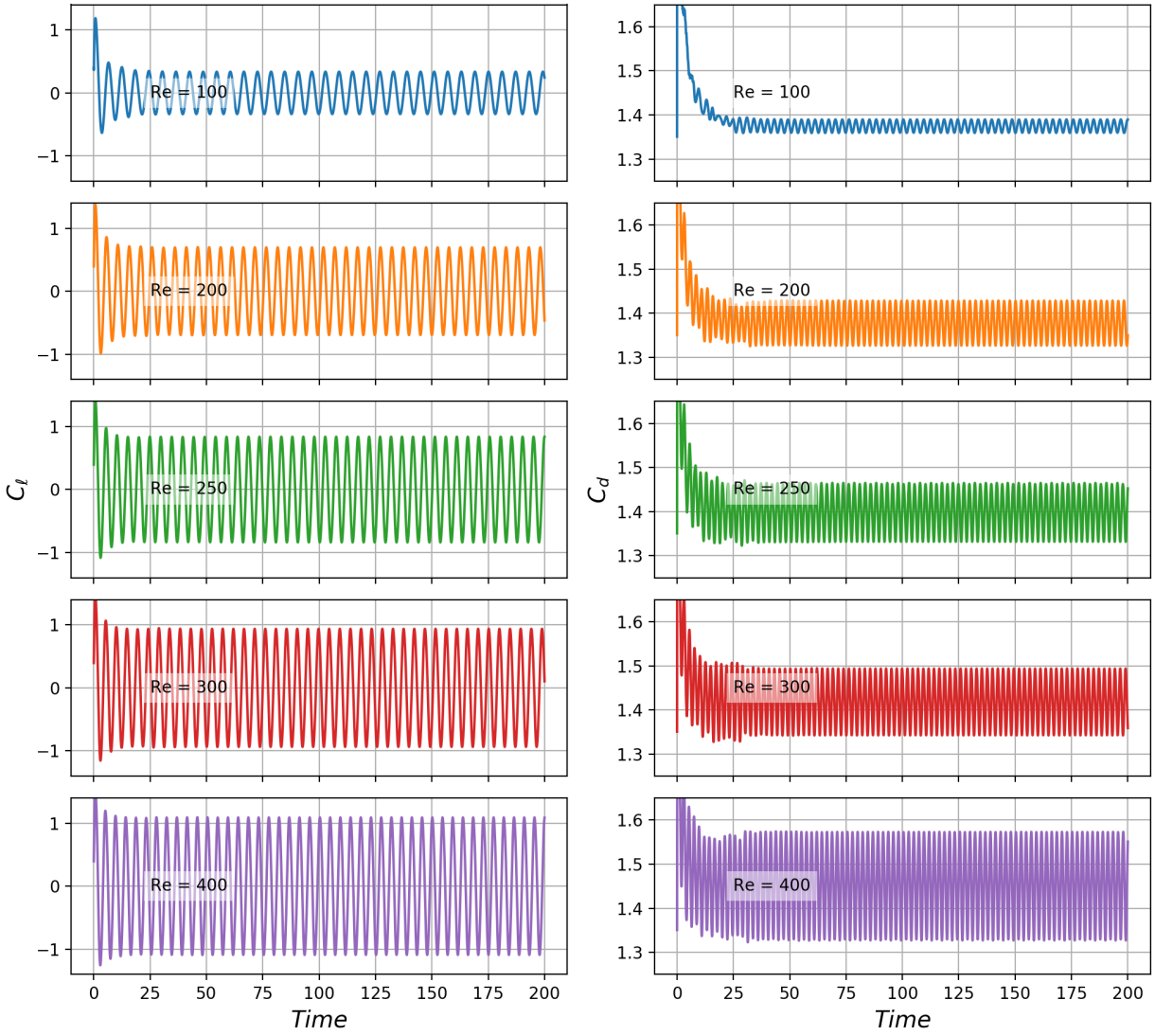

Figure 4.12: Lift and drag coefficients for circular cylinder at $Re = 100$, 200, 250, 300, and 400

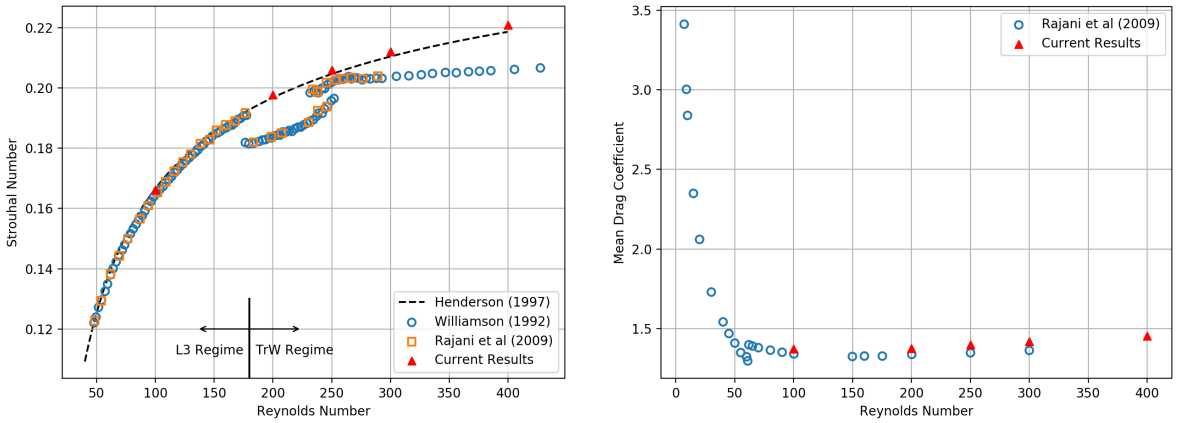

(a) Strouhal number **(b)** Mean drag coefficient

Figure 4.13: Variation in Strouhal number and mean drag coefficient with Reynolds number for 2-d circular cylinder

Table 4.4: Comparison between computations and measurements for circular cylinder at $Re = 300$

	St	$C_{l_{RMS}}$	C_d	$C_{p_{base}}$
Current results	0.212	0.662	1.42	-1.22
Rajani et al. [169] 2-d	0.215	0.602	1.37	-1.17
Mittal and Balachandar [166] 2-d	0.213	0.650	1.38	-1.22
Exp. Norberg [173]	0.203	0.435		
Exp. Williamson [171]	0.203			-0.96
Exp. Wieselsberger [174]			1.22	
Rajani et al. [169] 3-d	0.195	0.499	1.28	-1.01
Mittal and Balachandar [166] 3-d	0.203	0.380	1.26	-0.99

drag coefficients matching to within 3%. The current results significantly deviated from experimental measurements and three-dimensional simulations, which was expected as $Re = 300$ lies in the TrW flow regime where flow three-dimensionality must be taken into account.

4.3 Taylor-Green Vortex

The Taylor-Green vortex is an established test case that is used to assess a code's ability to model the decay of turbulent kinetic energy. Taylor and Green [175] proposed a simple and complete solution to the equations of motion as the starting point to study the "production

of small eddies from large ones." The initial conditions consist of a single vortex set up in a cubic volume. Atkins [176] provided general equations for the starting velocity and pressure fields.

The specific initial conditions and recommended post-processing analyses were supplied by the AIAA First International Workshop on High-Order Methods in Computational Fluid Dynamics, with one alteration made to the geometry. The test case specifies that the problem shall be solved on a triply-periodic cube of sides $-\pi L \leq x, y, z \leq \pi L$. Atkins [176] showed that results on this domain were identical (to machine zero) to results on a reduced domain with symmetric boundary conditions, $0 \leq x, y, z \leq \pi L$, so the current results were run on this reduced domain.

The initial flow field is given by Eq. (4.4). The flow conditions are $Re = 1,600$ and $M_0 = 0.1$ with a uniform temperature, $T = T_0$. The fluid is a perfect gas with $\gamma = 1.4$ and $Pr = 0.71$. The results were non-dimensionalized in the following way: divide t by $\frac{L}{V_0}$, E_k by V_0^2, ϵ by $\frac{V_0^3}{L}$, $\mathcal{E}$ by $\frac{V_0^2}{L^2}$.

$$u = V_0 \sin\left(\frac{x}{L}\right) \cos\left(\frac{y}{L}\right) \cos\left(\frac{z}{L}\right) \tag{4.4a}$$

$$v = -V_0 \cos\left(\frac{x}{L}\right) \sin\left(\frac{y}{L}\right) \cos\left(\frac{z}{L}\right) \tag{4.4b}$$

$$w = 0 \tag{4.4c}$$

$$p = p_0 + \frac{\rho_0 V_0^2}{16}\left(\cos\left(\frac{2x}{L}\right) + \cos\left(\frac{2y}{L}\right)\right)\left(\cos\left(\frac{2z}{L}\right) + 2\right) \tag{4.4d}$$

The grids consisted entirely of P2 hexahedral elements. Three levels of refinement were run: 32^3, 64^3, and 128^3. Since the domain was reduced by half in each direction from the original problem statement, it is appropriate to compare these results to grids of 64^3, 128^3, and 256^3, respectively, for the full domain. The 4^{th}-order SDIRK45 time-integration method was used with a time step of 0.01. Time steps of 0.04 and 0.0025 were also run for the 128^3 to verify temporal convergence. Isosurfaces of Q-criterion[2] equal to 0.0001 shaded by the

[2] *Q-criterion* was specified by Hunt, Wray, and Moin [177] and is used for vortex identification. A vortex is defined where $Q = 1/2[|\boldsymbol{\Omega}|^2 - |\boldsymbol{S}|^2] > 0$.

z-component of vorticity for select time steps are shown in Fig. 4.14. These results are for the 128^3 grid at $\Delta t = 0.0025$, and the results are mirrored and replicated so that they are comparable to simulations of the triply-periodic full grid.

The present results are compared to results from Rees et al. [178], who used a spectral code on a 512^3-element, full-domain grid. Spectral methods are highly accurate, and thus ideal for use as a reference, but they can only be easily applied to simple domains, like the triply-periodic cube of this case. [179] The temporal evolution of kinetic energy, E_k, integrated over the domain is displayed in Fig. 4.15. The 32^3 grid in Fig. 4.15a shows a lower kinetic energy value for $t \geq 12$, which indicates that dissipation rate is spatially dependent due to the spectral cutoff at high wave numbers. The time step values in Fig. 4.15b show a possible, albeit less pronounced, time-step dependence on dissipation rate.

Kinetic energy dissipation rate, ϵ, can be calculated two ways:

- Directly from the integrated kinetic energy, $\epsilon = -dE_k/dt$
- Using the relationship between enstrophy and dissipation rate for incompressible flow, $\epsilon = 2\frac{\mu}{\rho_0}\mathcal{E}$

Dissipation calculated using $-dE_k/dt$ is shown in Fig. 4.16, and calculated using enstrophy, $\mathcal{E}$, which is the square of vorticity integrated over the domain, is shown in Fig. 4.17. The two methods for calculating dissipation rate were in agreement, with one exception: Fig. 4.16a shows an increased dissipation rate after the peak for the 32^3 grid, as was indicated by the temporal evolution of kinetic energy shown in Fig. 4.15a. This feature was not picked up in the enstrophy calculated dissipation rate, as shown in Fig. 4.16a. The time step values in Figs. 4.16b, 4.16c, 4.17b and 4.17c indicate that time-step refinement brings the dissipation rate closer to the spectral values. The 128^3 grid at $\Delta t = 0.0025$ matched the time of peak dissipation to 0.0075 and the magnitude of the peak to within 1%. These results show that COFFE is able to match the accepted dissipation results from a highly-resolved simulation using a spectral solver. Modeling the correct dissipation rate is critical to properly simulating time-resolved, vorticity-dominated flows.

Isocontours of the dimensionless vorticity norm at levels of 1, 5, 10, 20, 30, on a subset of the $x/L = -\pi$ face at $t = 8$ are shown in Fig. 4.18 for the 128^3 grid at $\Delta t = 0.04, 0.01, 0.0025$

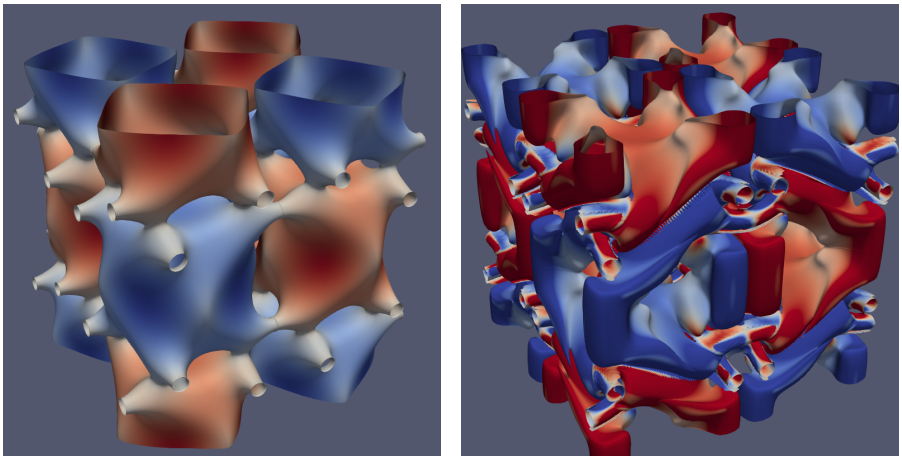

(a) $t = 1$ **(b)** $t = 5$

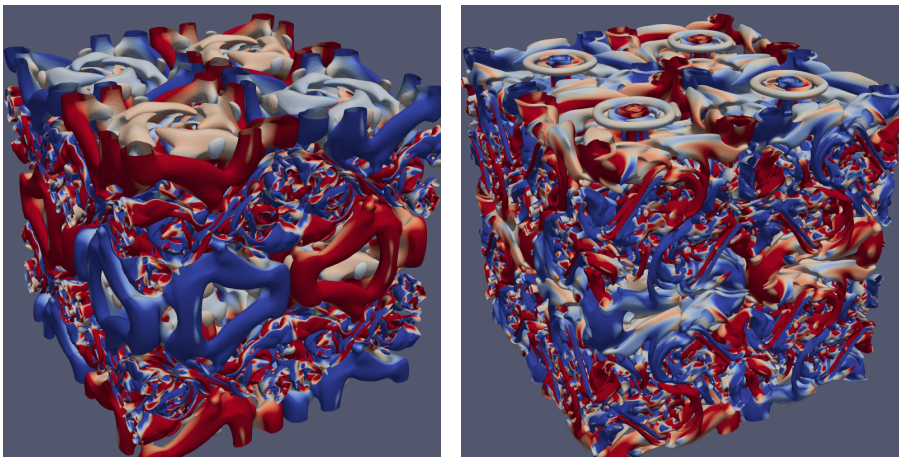

(c) $t = 9$, max dissipation rate **(d)** $t = 13$

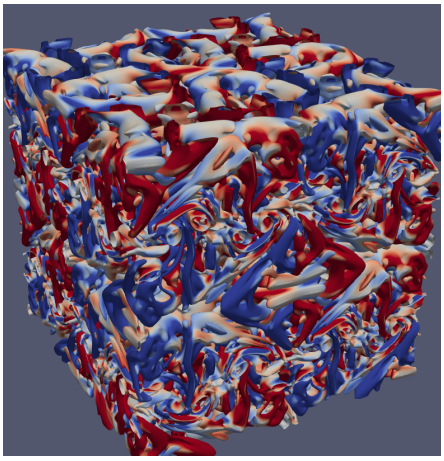

(e) $t = 17$

Figure 4.14: Taylor-Green vortex isosurfaces of Q-criterion = 0.0001 colored by the z-component of vorticity for the single-octant reduced 128^3 grid at $\Delta t = 0.0025$

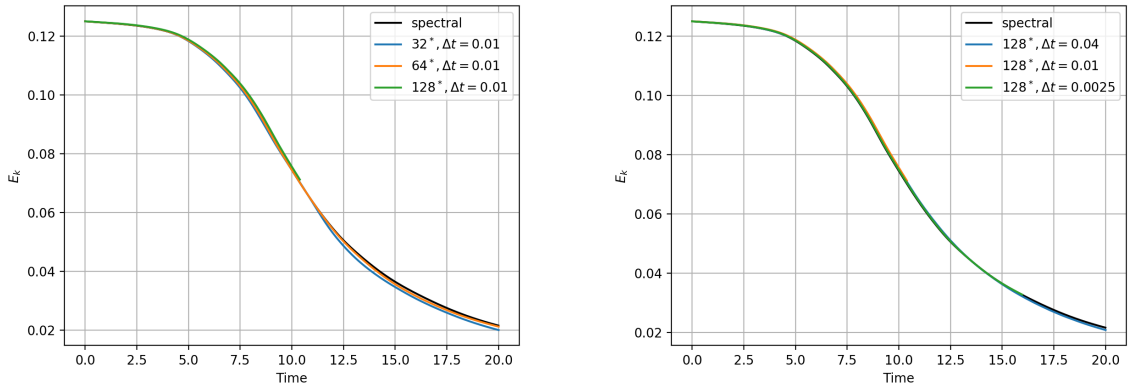

(a) All grids at $\Delta t = 0.01$ **(b)** 128^3 grid at $\Delta t = 0.04, 0.01, 0.0025$

Figure 4.15: Temporal evolution of kinetic energy integrated over the domain compared to results from Rees et al. [178] Note: results shown are from single-octant reduced grids.

compared to the spectral results of Rees et al. [178] The contours appear to vary with time step, which may indicate that the results have a time-step dependency.

The kinetic energy spectra can be calculated as a function of wave number, $E(K)$, for these cases using the technique detailed by Pope [180] and outlined here. The spatial cross correlation of the velocity vector is given as

$$R_{ij}(\boldsymbol{x}) = \langle u_i(\boldsymbol{x}_0), u_j(\boldsymbol{x}_0 + \boldsymbol{x}) \rangle. \tag{4.5}$$

Taking the three-dimensional Fourier transform of this results in the energy spectrum tensor, $E_{ij}(\boldsymbol{K})$, which is a function of the wave number vector, $\boldsymbol{K}$.

$$E_{ij}(\boldsymbol{K}) = \frac{1}{(2\pi)^3} \iiint_{-\infty}^{\infty} e^{-i\boldsymbol{K}\cdot\boldsymbol{x}} R_{ij}(\boldsymbol{x}) d\boldsymbol{x} \tag{4.6}$$

If we let $i = j$, $\boldsymbol{x} = 0$, and invert the Fourier transform to solve for R_{ii},

$$R_i i = \langle u_i^2 \rangle = \iiint_{-\infty}^{\infty} E_i i(\boldsymbol{K}) d\boldsymbol{K} \tag{4.7}$$

The turbulent kinetic energy is defined as $k = \frac{1}{2}\langle u_i^2 \rangle$. If we only consider the magnitude of the Fourier modes, neglecting directionality, and let $K = |\boldsymbol{K}|$, we can calculate the turbulent

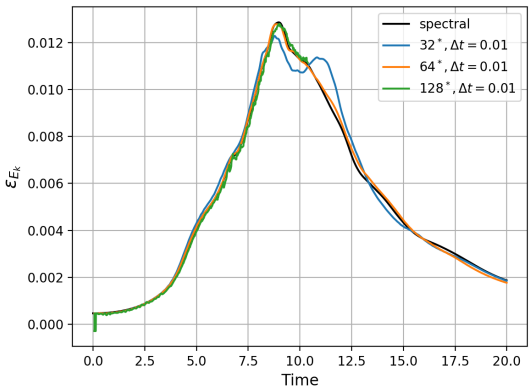

(a) All grids at $\Delta t = 0.01$

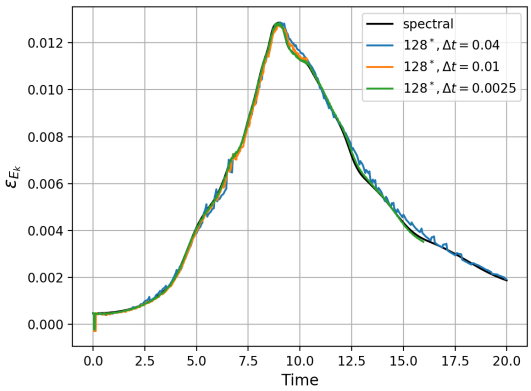

(b) 128^3 grid at $\Delta t = 0.04, 0.01, 0.0025$

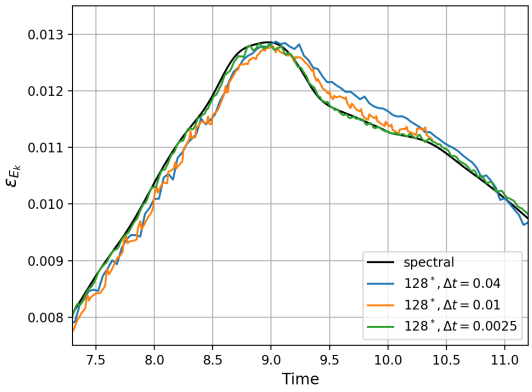

(c) 128^3 grid at $\Delta t = 0.04, 0.01, 0.0025$, zoomed to peak

Figure 4.16: Temporal evolution of kinetic energy dissipation, calculated using $-dE_k/dt$, compared to results from Rees et al. [178] Note: results shown are from single-octant reduced grids.

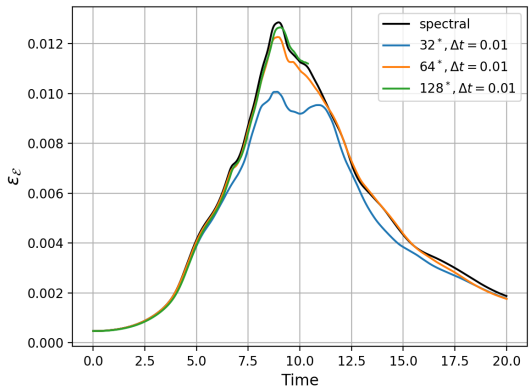

(a) All grids at $\Delta t = 0.01$

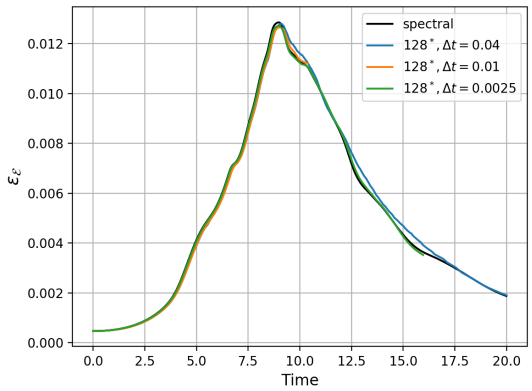

(b) 128^3 grid at $\Delta t = 0.04, 0.01, 0.0025$

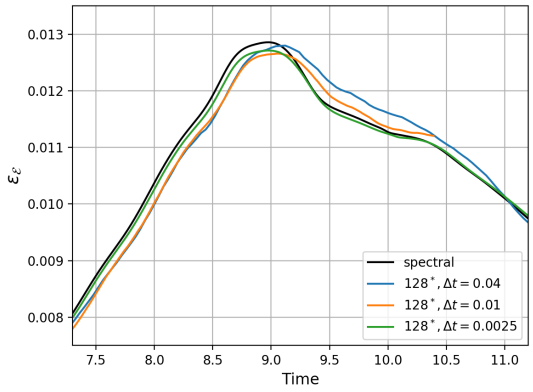

(c) 128^3 grid at $\Delta t = 0.04, 0.01, 0.0025$, zoomed to peak

Figure 4.17: Temporal evolution of kinetic energy dissipation, calculated using enstrophy, compared to results from Rees et al. [178] Note: results shown are from single-octant reduced grids.

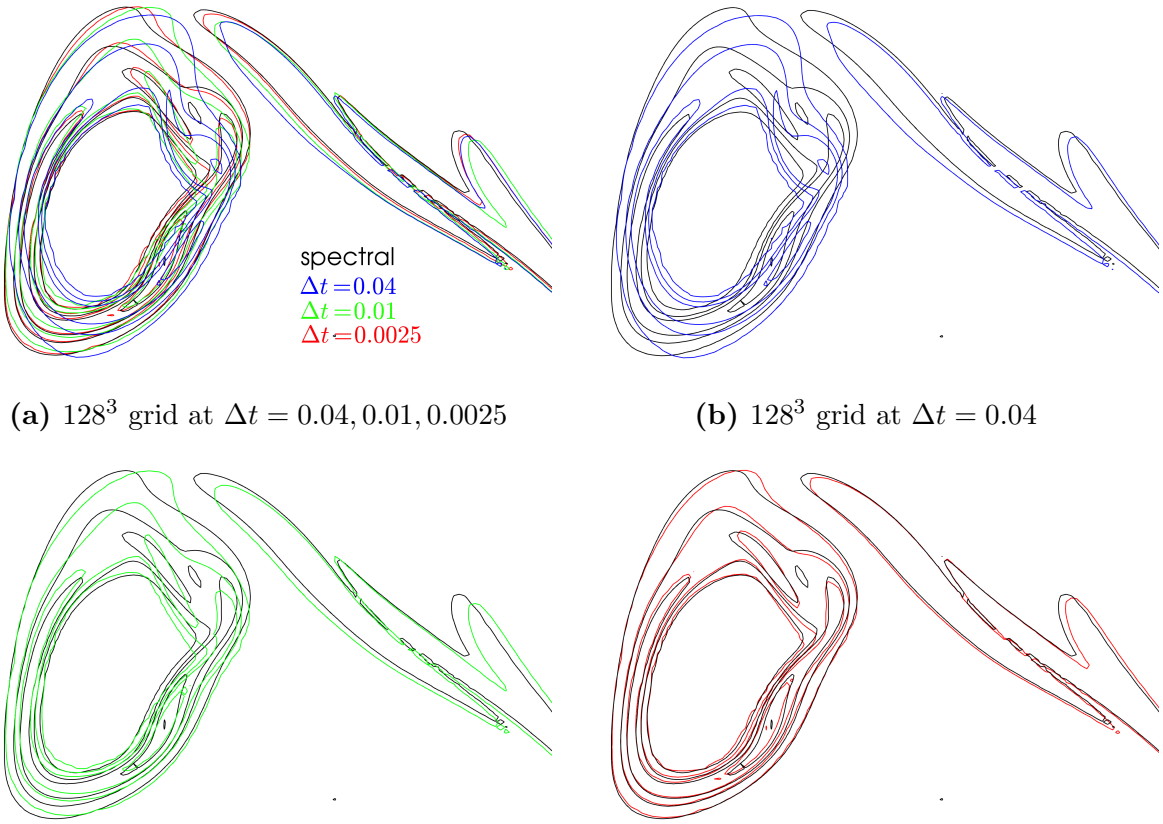

(a) 128^3 grid at $\Delta t = 0.04, 0.01, 0.0025$

(b) 128^3 grid at $\Delta t = 0.04$

(c) 128^3 grid at $\Delta t = 0.01$

(d) 128^3 grid at $\Delta t = 0.0025$

Figure 4.18: Isocontours of the dimensionless vorticity norm at levels of 1, 5, 10, 20, 30, on a subset of the $x/L = -\pi$ face at $t = 8$, compared to results from Rees et al. [178] Note: results shown are from single-octant reduced grids.

kinetic energy distribution as a function of wave number by integrating $E_i i$ over spheres of radius K.

$$k = \int_0^\infty \oint \frac{1}{2} E_i i(\boldsymbol{K}) d\mathcal{S}(K) dK. \tag{4.8}$$

We go on to define $E(K)$ as the turbulent kinetic energy spectral distribution as a function of wave number.

$$E(K) = \oint \frac{1}{2} E_i i(\boldsymbol{K}) d\mathcal{S}(K) \tag{4.9}$$

The turbulent kinetic energy spectra as a function of wave number, $E(K)$, for all three levels of grids at $\Delta t = 0.01$ are shown in Fig. 4.19. Higher wave numbers denote smaller eddy sizes, and the cutoff wave numbers decrease with number of elements due to implicit filtering. The $k^{-5/3}$ slope denotes the theoretical inertial-range scaling of the turbulent energy spectrum given by Kolmogorov. The calculated slopes for these spectra are approximately -1.8, which is 7.8% lower than the theoretical $-5/3$ value. This difference could be due to the fact that there is no energy influx into the domain to offset the energy dissipated by viscosity, which is a key assumption in Kolmogorov's inertial-range $k^{-5/3}$ slope. [181] Only the $\Delta t = 0.01$ spectrum for the 128^3 grid is shown because the effect of time step on the spectra was negligible.

4.4 Summary

The convecting isentropic vortex case was used to verify the order of accuracy of the time integration methods that were implemented. Order of accuracy relates to the rate of change of the temporal error with respect to changes in time step, but the isentropic vortex results also showed that the temporal error also decreased as order of accuracy increased at a given time step. This demonstrates that concept that increasing the order of accuracy itself results in lower temporal error.

Results from the isentropic vortex case were also used to establish the dissipative and dispersive components of the temporal error for each method. Dissipation was present in

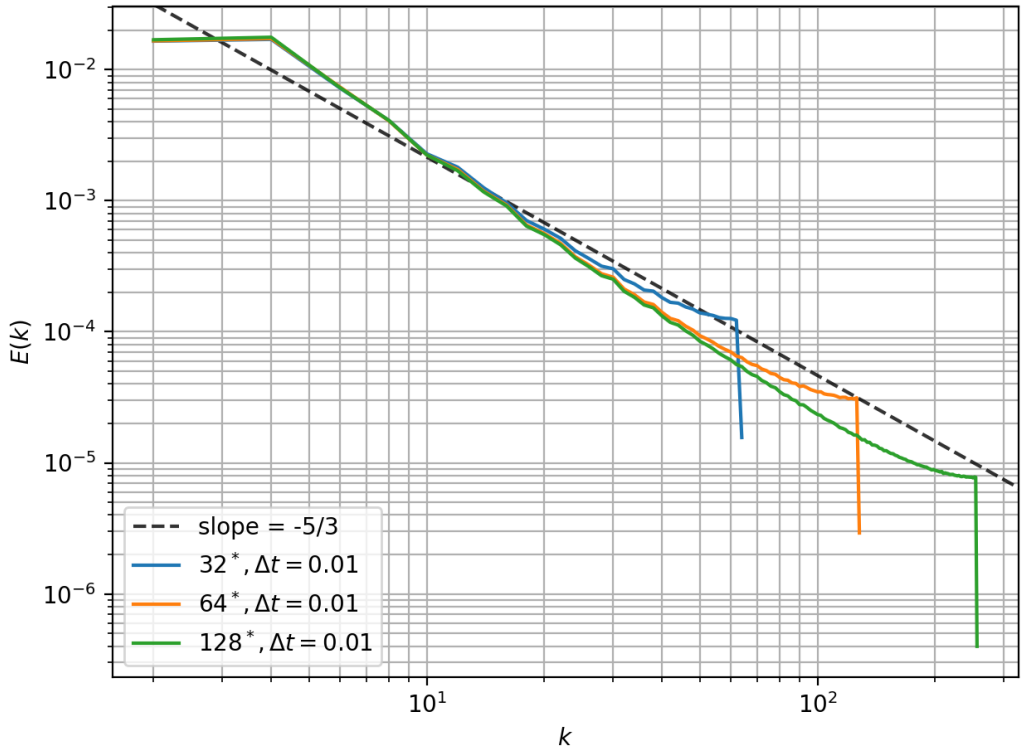

Figure 4.19: Energy spectra for all grids at $\Delta t = 0.01$. $k^{-5/3}$ slope line is included for reference.

appreciable quantities for the odd-order methods, and dispersion dominated in even-order methods. At larger time steps, the amount of dissipation relative to dispersion began rising in the 2$^{\text{nd}}$-order methods, but not to the level seen in the 1$^{\text{st}}$ and 3$^{\text{rd}}$-order methods. One new finding in this work was that the BDF2OPT4/5 methods tended to reduce the dissipation rise for larger time steps. The result of this decrease in dissipation was an accentuation of the wiggles upstream of the vortex that were created by the dispersion error.

The second test case, periodic vortex shedding around a two-dimensional circular cylinder, was used to assess the effects of temporal error on a less-trivial case, for which a wealth of experimental and numerical data exist. The $Re = 1,200$ runs showed that the higher-order SDIRK schemes reached temporal convergence with respect to Strouhal number and RMS lift coefficient more rapidly than the lower-order BDF methods, as expected. The SDIRK methods were able to propagate vortex structures more uniformly and maintain the vortex strength better than the BDF methods, for a given time step. One key feature to take away from this portion of the investigation is the importance of time-convergence studies for unsteady problems, especially those using lower-order time-integration methods. Just as grid-convergence studies should accompany steady problems, so too should time-convergence studies be included with unsteady ones.

Circular cylinder cases were also run at Reynolds numbers from 100 to 400 for validation. Experimental comparisons were only appropriate for the $Re = 100$ case, and the Strouhal number matched experimental data from Williamson [170] to within 0.7%. The remaining cases for Reynolds numbers from 200 to 400 were compared to accepted 2d numerical results. The Strouhal number matched the numerical data curve fit of Henderson [167] to within 1%, and the mean drag coefficient matched results from Rajani, Kandasamy, and Majumdar [169] to 2-4%.

The Taylor-Green vortex case tested COFFE's ability to handle vortex dynamics and turbulent dissipation. The current results compared favorably with the highly-resolved spectral results provided by Rees et al. [178]. Specifically the 128^3 grid at $\Delta t = 0.0025$ matched the kinetic energy dissipation peak time to within 0.0075 and magnitude to within 1%.

Chapter 5

Shock Simulations

Modeling moving shock waves is the crux of this dissertation; however, stationary shock waves were also be considered in order to assess the viability of shock capturing techniques applied to a high-spatial-order solver. The goal was to assess how the modified shock capturing technique, described in Section 3.4, performs on non-shock-aligned grids made up of tetrahedra and triangles. The stationary shock case was used to evaluate the shock capturing techniques independent of time, and the moving shock cases were used to evaluate the combined effect of high spatial and high temporal order.

The modified shock capturing technique was applied to three inviscid cases: the blunt-body bow shock, the planar Noh [118] problem, and the Mach 3 forward-facing step of Woodward and Colella [161]. COFFE's current shock capturing approach failed when running on inviscid cases because of its inability to dissipate numerical errors, so the modified technique was employed on inviscid cases to demonstrate that it could manage this issue.

5.1 Blunt-Body Bow Shock

The inviscid bow shock case was introduced by Scott Murman of NASA Ames Research Center at the AIAA Fifth International Workshop on High-Order Methods in Computational Fluid Dynamics (HOW5). It was designed to test the effectiveness of shock-capturing schemes for a steady, two-dimensional blunt body in inviscid, supersonic flow. This case is of particular interest because the large stagnation region on the blunt body allows numerical errors

produced at the shock to accumulate at the surface rather than convecting downstream. This case also is useful for testing the shock sensor's ability to operate on grids with a variety of element sizes and aspect ratios.

The geometry, pictured in Fig. 5.1, consisted of a flat center section one unit long, flanked by two quarter circles of radius one-half unit. The domain does not include the aft section because the focus of the test case was on the shock capturing region, not the wake. Although top-bottom symmetry exists, Murman elected to include the full domain to support any spurious flow behavior that may arise. The left and right boundaries were inflow and outflow, respectively, and the body surface boundary was an inviscid (slip) wall. The inflow conditions were uniform Mach 4.

Families of P1 quadrilateral grids with 5 refinement levels, designated grids 0 (coarse) through 4 (fine), were provided by the workshop. Triangle grids were created by diagonalizing the quadrilateral grids. The top half of the coarsest grid is shown in Fig. 5.1. The grids were shock-aligned using the standard OVERFLOW [182] 2^{nd}-order central-differencing scheme with 2^{nd}- and 4^{th}-order dissipation blended using a pressure sensor. Refinement was done by increasing the cell clustering in the shock and surface regions. The shock region was in the same location for each grid refinement level, and as a result, the calculated shock location on coarse meshes may not be within the refined region. These grids provide a good test for the utility of Riemannian metric within the exponential-entropy gradient sensor because they contain cells with high aspect ratios that are oriented in a variety of ways with respect to the incoming flow.

To reach steady state, the steady residual, as defined by the RMS of the residuals in all equations and cells, was driven to machine zero. A sample convergence history plot is shown in Fig. 5.2. For grid 0, the bow shock extended upstream of the refinement region and into cells that were too large to accommodate shock capturing. Machine-zero steady state was only reached for grids 1 through 4. Grids 3 and 4 required the addition of global artificial diffusion (see Section 3.3) in order to reach steady state. A discussion of the issues encountered will follow the presentation of the converged results. Steady state was also reached on two triangle grids created by diagonalizing the quadrilateral grids 2 and 3. Plots

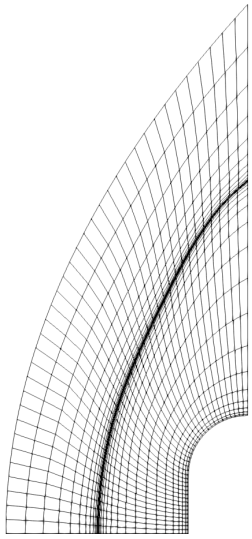

Figure 5.1: Top half of grid 0 for inviscid bow shock case.

of density, temperature, local Mach number, and pressure for grid 4 with quadrilaterals are shown in Fig. 5.3. The sonic line is shown in the local Mach number plot.

Contours of the local Mach number downstream of the shock on grid 2 with triangles are shown in Fig. 5.4. The computational mesh is overlaid to demonstrate that the solution is smooth and does not conform to the underlying mesh structure. The contours of constant Mach number form concentric rings about the stagnation point. This is an indication that the solution is independent of mesh topology, and that COFFE, with the modified shock capturing technique, is able to operate on non-shock-aligned grids.

A line plot of pressure along the stagnation streamline for quadrilaterals on grids 1 through 4 is shown in Fig. 5.5. This plot clearly shows the impact of grid refinement on the thickness of the captured shock. The shock was not fully captured within the refinement region of grid 1 because the location where refinement as implemented remained constant for each grid level. As a result artificial diffusion was applied in the larger cells upstream of the refinement region, and the shock was smeared across a wider area, causing this shock to be much thicker than the shocks of grids 2 through 4. The solver was able to handle the thicker shock for grid 1, but the issue is exacerbated with the larger cells of grid 0, and a solution was not reached.

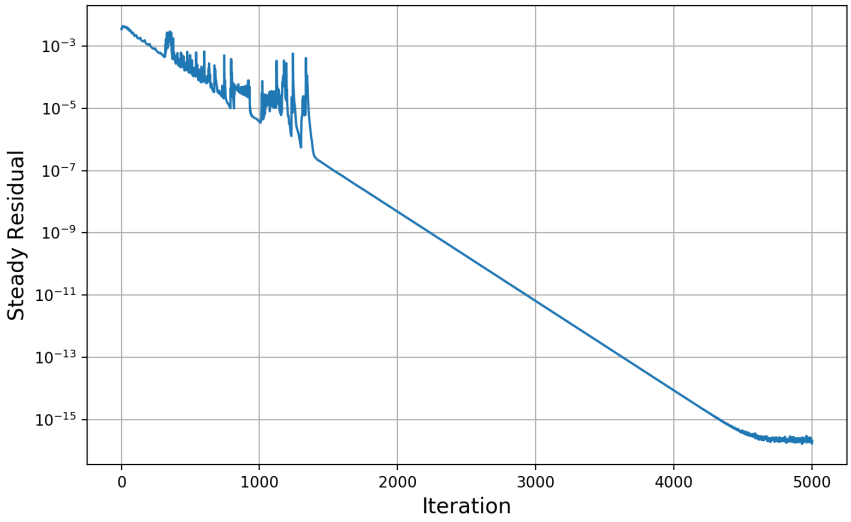

Figure 5.2: Non-linear convergence for inviscid bow shock case with P1 quadrilaterals on grid 1.

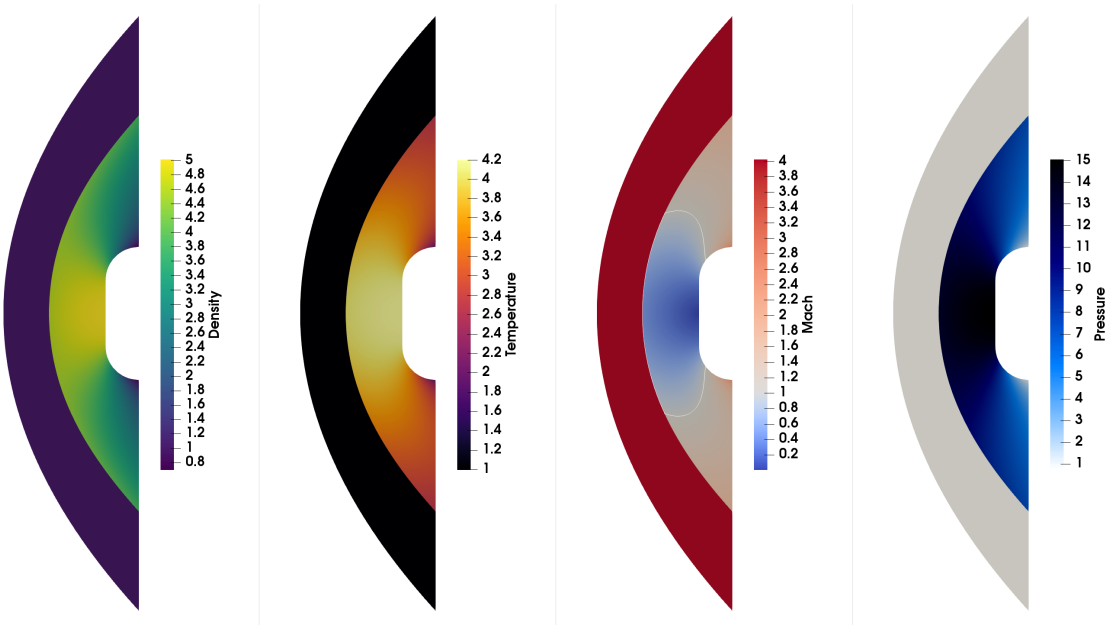

Figure 5.3: Density, temperature, local Mach number, and pressure for inviscid bow shock case with quadrilaterals on grid 4. The sonic line is indicated in the local Mach number plot.

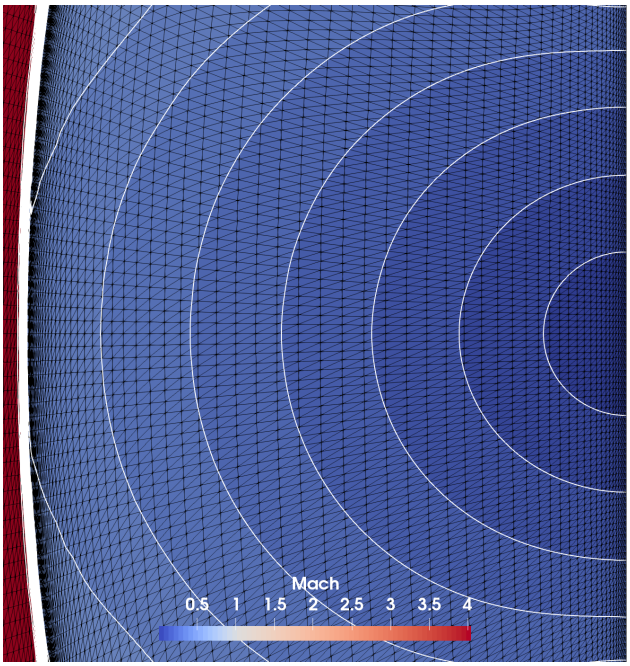

Figure 5.4: Local Mach number contours for inviscid bow shock case with triangles on grid 2, zoomed to stagnation region with computational meshed overlaid.

Two parameters were used for error quantification: the RMS error in the total enthalpy, Eq. (5.1), and a comparison of the stagnation pressure to the pressure resulting from the Rayleigh-Pitot formula. The total enthalpy should remain constant for steady inviscid flow, which makes it an ideal candidate for error quantification, and stagnation pressure was chosen because it is often required in engineering applications.

$$Err_H = \sqrt{\frac{\int_\Omega (H - H_{ref})^2 dV}{\int_\Omega dV}} \tag{5.1}$$

Total enthalpy error and stagnation pressure error for quadrilateral grids 1-4 and triangle grids 2-3 are shown in Fig. 5.6 plotted as a function of the inverse of the square root of the number of degrees of freedom (N_{dofs}). They are plotted along side example results from OVERFLOW provided by Murman in the HOW5 case description. The total enthalpy error is less sensitive to modeling parameters ($\kappa_{\tilde{s}}$ and global diffusion level) than the stagnation pressure error. This is reasonable because the total enthalpy error is an integrated quantity and the stagnation pressure error is a point quantity.

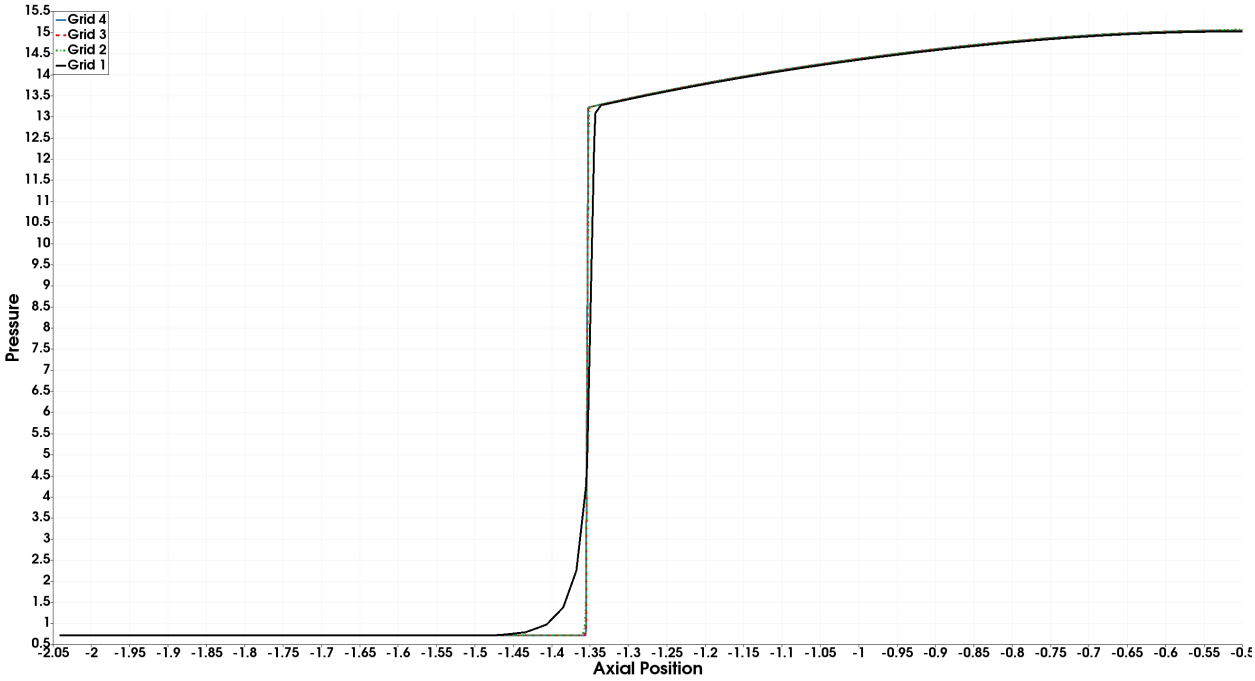

(a) Full view

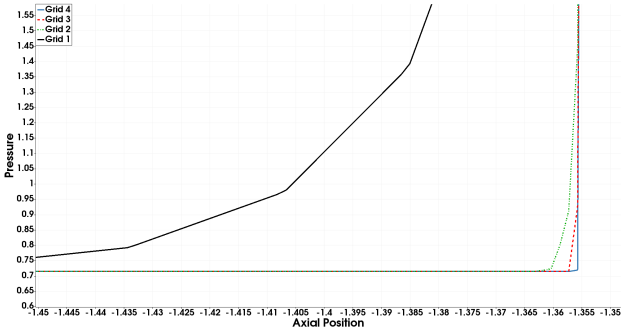

(b) Base of bow shock

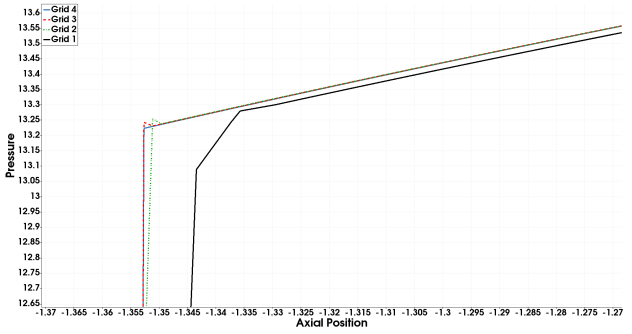

(c) Top of bow shock

Figure 5.5: Pressure along stagnation streamline for inviscid bow shock cases with quadrilaterals on grids 1-4.

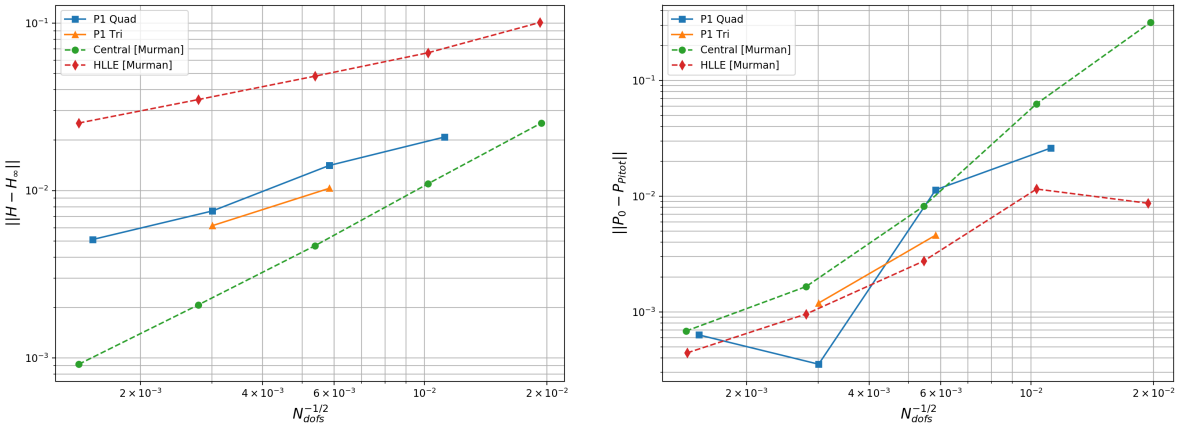

(a) Total Enthalpy Error **(b)** Stagnation Pressure Error

Figure 5.6: Error assessment for inviscid bow shock case.

The density gradient magnitude for grids 2 and 3 with quadrilaterals and triangles is shown in Fig. 5.7. At steady state, there is little discernible difference between results on quadrilateral and triangle grids. Reaching steady state with the triangle grids required the addition of more global diffusion than the quadrilateral grids, 0.005 for triangles compared to 0.001 for quadrilaterals.

Path to Steady State

Grids 2-4 required the addition of global diffusion in order to reach steady state. Without global diffusion, numerical error from the shock accumulates at the stagnation region. An example of the early stages of this error accumulation is shown in Fig. 5.8, which shows the stagnation region of grid 4 run with quadrilaterals and no global diffusion. Waves emanating from the shockwave on the left side of the figure are focused on the stagnation point, where a small aberration develops along the stagnation streamline. This resembles a carbuncle, only at the stagnation surface rather than the shock surface. If allowed to progress, a triangular region of stagnant fluid forms, creating a fluidic obstruction that the flow above and below is redirected around. Artificial global diffusion dissipated these waves before they reached the surface and began amassing.

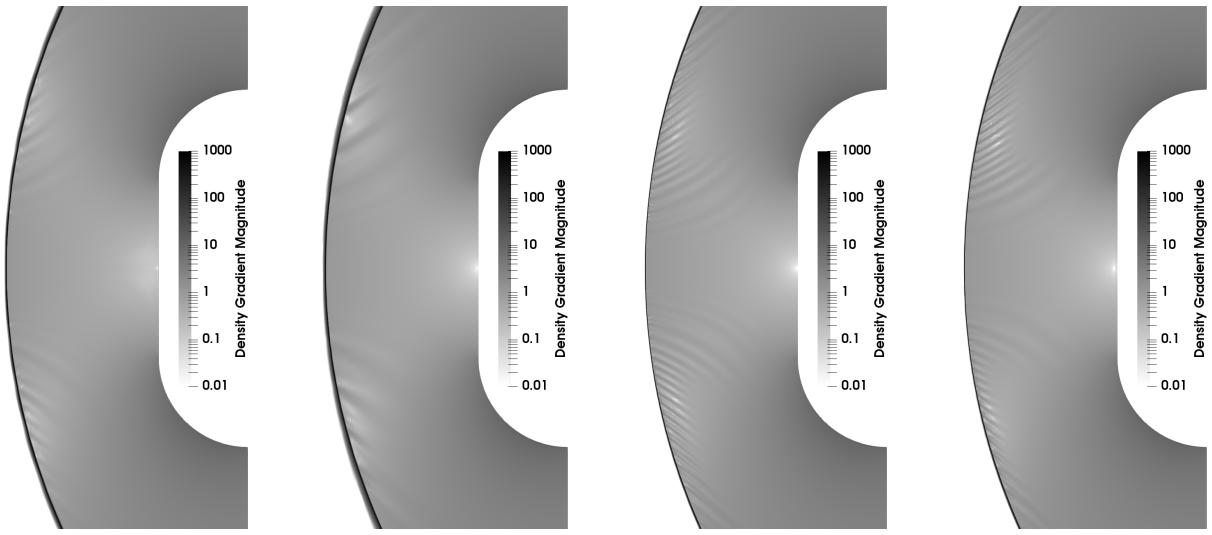

(a) Grid 2 quads **(b)** Grid 2 tris **(c)** Grid 3 quads **(d)** Grid 3 tris

Figure 5.7: Density gradient magnitude comparison for grids 2 and 3 with quadrilaterals and triangles.

Figure 5.8: Density gradient magnitude in stagnation region of grid 4 with quadrilaterals with no global diffusion.

5.2 Planar Noh Problem

Noh [118] introduced a validation case for studying moving shocks in which a gas with velocity $u_\infty = -1$ impinges on a rigid wall at the origin. A right-ward moving shockwave emanates from the wall, and the downstream conditions and shock speed are known from inviscid calculations. The planar shock case from Noh is simulated using the Euler equations, which presents a challenge for numerical techniques operating in an Eulerian reference frame because a shock is treated as a discontinuity that travels across a finite numerical grid. Noh's intent for this test problem was to investigate errors that arise from using artificial viscosity based shock capturing techniques and compare those to errors from his own technique that used artificial viscosity and heat flux.

Zaide and Roe [183] showed that the initial conditions for the planar Noh problem can be reduced to a family of conditions, given in Eq. (5.2), with Mach number, M_0, as a free parameter. The conditions downstream of the shock are provided in Eq. (5.3), with the shock speed, S, calculated from Eq. (5.4). The downstream conditions are calculated directly from the jump condition.

$$\rho_0 = 1, \qquad u_0 = -1, \qquad p_0 = \frac{1}{\gamma M_0^2} \tag{5.2}$$

$$\rho = 1 + \frac{1}{S}, \qquad u_0 = 0, \qquad p = p_0 + 1 + S \tag{5.3}$$

$$S = \frac{1}{4}\left((\gamma - 3) + \sqrt{(\gamma + 1)^2 + \frac{16}{M_0^2}}\right) \tag{5.4}$$

The Noh problem was run at Mach numbers 4 and 10 on a family of P1 rectangular grids with quadrilateral elements. This problem is nominally one-dimensional, but COFFE does not currently support the use of only one-dimensional elements, so two-dimensional grids were used, each with a length-to-height aspect ratio of 2-to-1. Four refinement levels were created, and each refinement level doubled the element count in each direction. The grid levels are identified by the number of degrees of freedom (DOFs) in the x-direction: 101, 201, 401, and 801. Grid 101, which consists of 100-by-50 quadrilateral elements, is shown

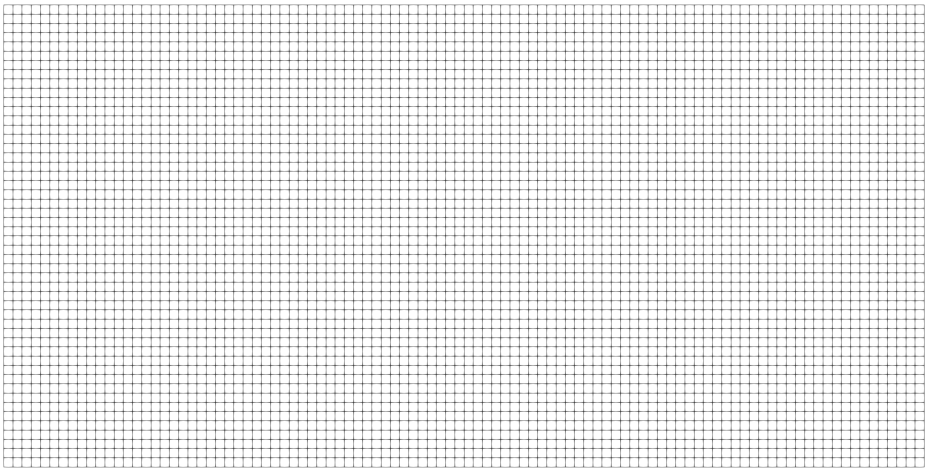

Figure 5.9: Noh problem grid 101 (100-by-50 elements)

Table 5.1: Calculated Conditions for Planar Noh Cases

	Case 1	Case 2
Mach	4	10
S	0.25	0.2083
ρ_0	1	1
p_0	4.464×10^{-2}	7.143×10^{-3}
T_0	0.0625	0.01
ρ	5	5.801
p	1.295	1.215
T	0.3625	0.2933
ρ/ρ_0	5	5.801
p/p_0	29	170.2
T/T_0	5.8	29.33

in Fig. 5.9. The conditions upstream and downstream of the shock wave, as calculated by Eqs. (5.2) to (5.4), are provided in Table 5.1. $\kappa_{\tilde{s}}$ was set to 0.5 for each of the runs. Each case was run with a time step of 0.001 for a total time of 2 using the 3$^{\text{rd}}$-order SDIRK33 scheme. Time was non-dimensionalized by L/u_∞.

Surface plots of density for the Mach 4 case on each grid level are shown in Fig. 5.10. These plots indicate that the flow is one-dimensional and also show how the shock becomes sharper with increasing refinement. Plots from the Mach 10 case show similar results. The coefficient of variation (c_v) of density in the vertical direction at each axial location was also used to further quantify how one-dimensional the flow fields were. Coefficient of variation

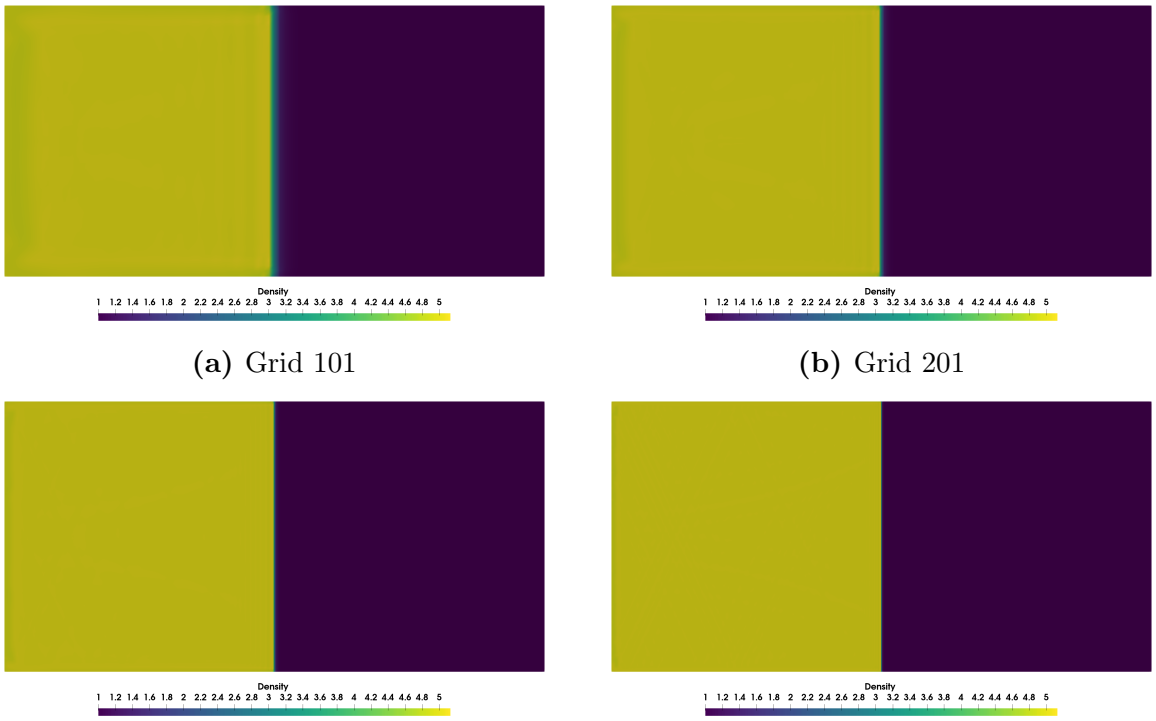

(a) Grid 101 **(b)** Grid 201

(c) Grid 401 **(d)** Grid 801

Figure 5.10: Surface plots of density for Mach 4 planar Noh case at each grid refinement level.

is the ratio of the standard deviation to the mean, and it is a measure of the variability within a data set. Line plots of c_v for Mach 4 and 10 cases on each grid level are shown in Fig. 5.11. Grid level 801 had a peak c_v of 0.011 and 0.014 in the shock region for Mach 4 and 10, respectively. In the region downstream of the shock, at $x = 0.2$, c_v values for Mach 4 and 10 were 0.0007 and 0.001, respectively. All subsequent analyses will use data from the centerline only.

Values of the exponential-entropy gradient sensor for the Mach 4 at each refinement level are shown in Fig. 5.12. In each plot the values range from 0 to 0.25. There is no vertical gradient in the sensor, and the horizontal gradient scales with grid refinement level.

Line plots of pressure, temperature, and density at $t = 2$ for the Mach 4 and 10 cases are shown in Figs. 5.13 and 5.14, respectively. Each plot contains data from the centerline of the domain for each grid refinement level along with the exact solution. The shock thicknesses, as defined by Gilbarg and Paolucci [1] in Eq. (5.5), for the Mach 4 and 10 cases for each grid

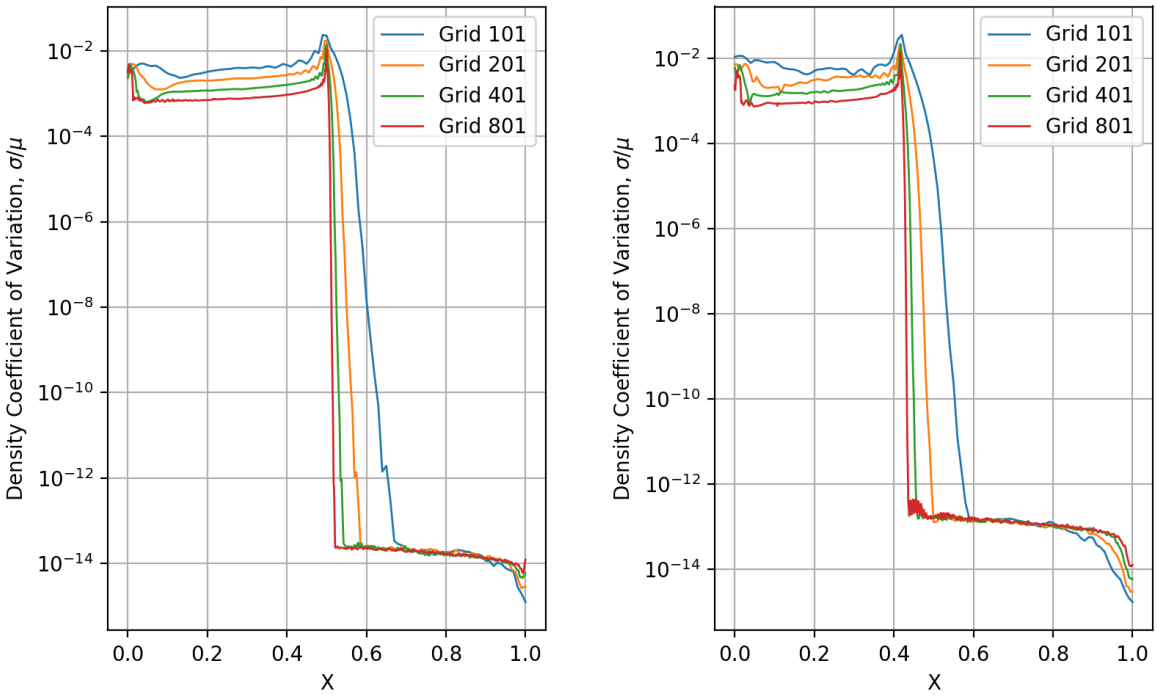

(a) Mach 4 **(b)** Mach 10

Figure 5.11: Coefficient of variation of density for Mach 4 and 10 planar Noh case at each grid refinement level.

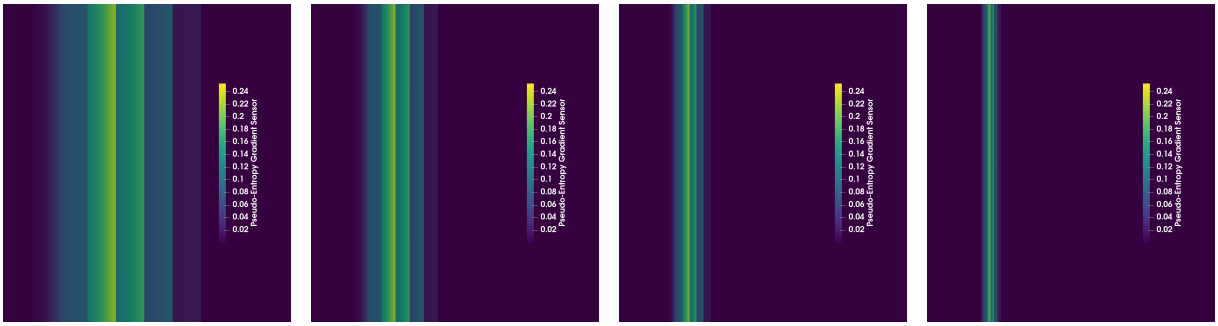

(a) Grid 101 **(b)** Grid 201 **(c)** Grid 401 **(d)** Grid 801

Figure 5.12: Exponential-entropy gradient sensor values for Mach 4 planar Noh case at each grid refinement level.

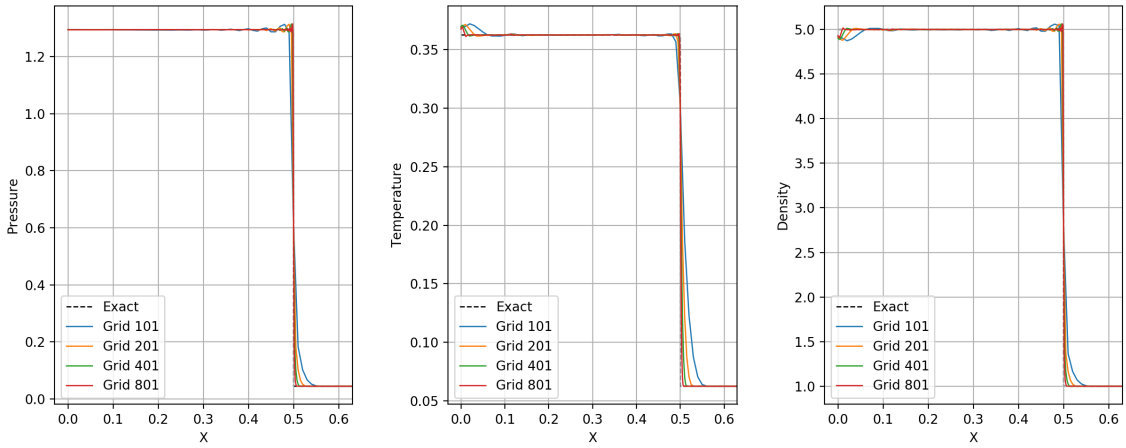

Figure 5.13: Pressure, temperature, and density along centerline for Mach 4 planar Noh case at each grid refinement level.

refinement level are shown in Fig. 5.15. The following observations were made from these figures:

- The shock speed appears to be correct for each of the cases shown, as indicated by the location of the jump compared to the exact location.
- The shock thickness decreases linearly with increasing N_{dofs} in the x-direction.
- Wall heating, described by Noh [118], is present when the exponential-entropy gradient sensor was used. Previous runs of this case with the current sensor (not shown in this document) also displayed wall heating.

$$\text{Thickness} = \frac{u_2 - u_1}{\left|\frac{\partial u}{\partial x}\right|_{max}} \tag{5.5}$$

5.3 Mach 3 Forward-Facing Step

The two-dimensional inviscid Mach 3 forward-facing step case was introduced by Emery [184], popularized by Colella and Woodward [185], and run most recently by Hendrickson, Kartha, and Candler [186]. This case is useful for assessing the shock sensor's ability to track a complex, unsteady shock structure. Additionally, and similar to the bow shock problem,

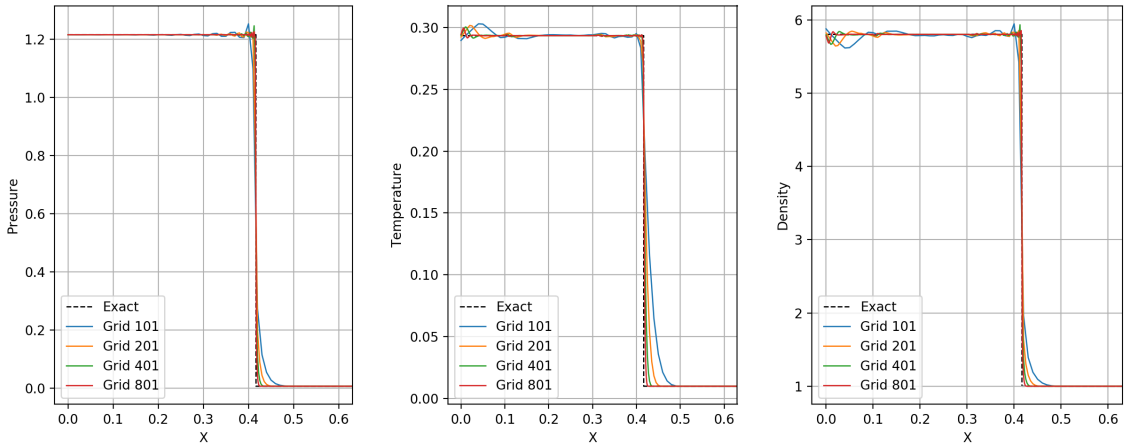

Figure 5.14: Pressure, temperature, and density along centerline for Mach 10 planar Noh case at each grid refinement level.

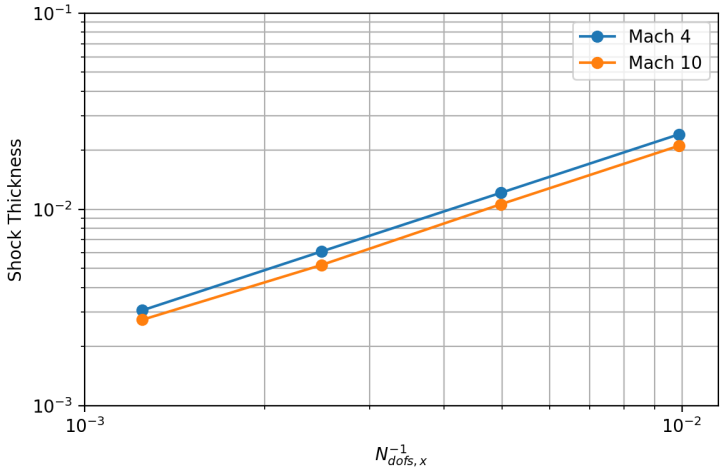

Figure 5.15: Shock thickness for Mach 4 and 10 planar Noh cases at each grid refinement level. Slope is unity.

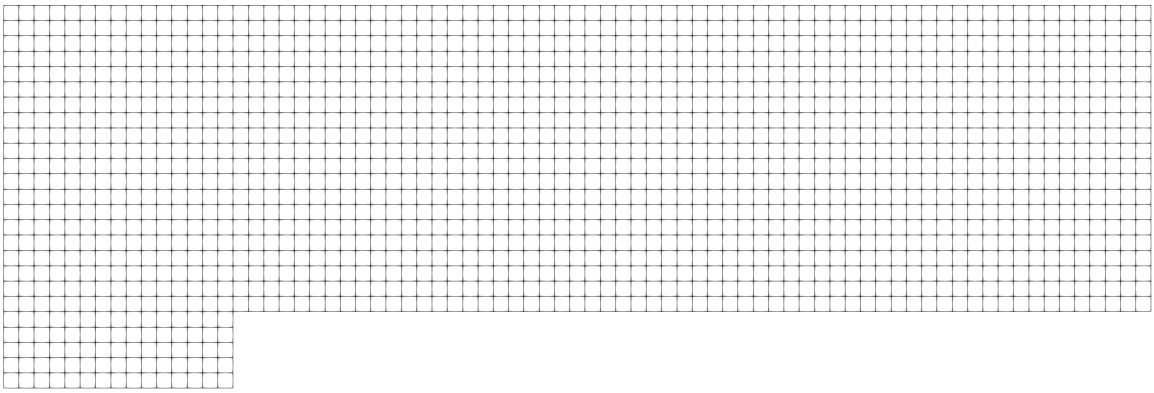

Figure 5.16: 75-by-25 quadrilateral grid for inviscid step case.

the stagnation region at the base of the step allows flow irregularities produced by numerical error at the shock to accumulate at the surface rather than convecting downstream. Previous attempts to run this case with the current shock sensor have failed due to an accumulation of numerical error in the stagnation region of the step that caused the simulation to crash because the accumulated error does not convect out of volume and there is no dissipation to remove it.

The geometry for this case was a 3-by-1 rectangular domain with a 20% vertical step located 20% from the inlet. The left and right boundaries were inflow and outflow, respectively, and the top and bottom boundaries were inviscid (slip) walls. The Euler equations were solved with a uniform Mach 3 inflow. The modified shock sensor parameter, $\kappa_{\tilde{s}}$, was set to 0.1 for all cases. Each run was started impulsively with the entire domain initialized to the freestream value of Mach 3.

Families of P1 and P2 grids were created by starting with a 75-by-25 grid (minus the step region) and refining by doubling the cell count in each direction up to 2400-by-800. Grids consisting of uniform quadrilaterals were created at each refinement level. Grids of triangular elements were created by diagonalizing the quadrilateral elements, and they will be referred to by the quadrilateral grid that was used create them. The 75-by-25 quadrilateral grid is shown in Fig. 5.16.

Cases were run with the BDF2, SDIRK33, and SDIRK45 temporal integration schemes. In order to assess spatial sensitivity, all of the grid combinations were run with the SDIRK33

Table 5.2: Temporal Sensitivity Runs for Mach 3 Forward-Facing Step

Δt	BDF2	SDIRK33	SDIRK45
0.0025	✓		
0.005	✓	✓	
0.01	✓	✓	✓
0.02	✓	✓	✓
0.04		✓	✓

method and $\Delta t = 0.01$. Temporal sensitivity was assessed by running the three temporal integration methods with various time step sizes, defined in Table 5.2, on the 2400-by-800 P1 quadrilateral grid.

The temporal evolution of the domain is shown in Fig. 5.17. Density contour plots are shown for $t = 1$ to 10 in increments of 1 on a 2400x800 grid of P1 quadrilaterals using the SDIRK33 integration scheme and $\Delta t = 0.01$. At $t = 1$ the bow shock created by the forward facing step grows out from the step. The bow shock has reaches the top wall and reflects down from it by $t = 2$ and a weak shock is visible just downstream of the sharp corner expansion. The shock reflecting from the top wall has crosses through the weak corner shock by $t = 3$ and reflects off of the bottom wall by $t = 4$. At $t = 5$ a normal shock is seen forming between the initial bow shock and the top wall, and at $t = 6$ a normal shock is present between the first reflected shock and the bottom wall. Also at $t = 6$ a Kelvin-Helmholtz instability (KHI) arises along the slip line emanating from the upper shock triple point. For $t = 7 - 10$, the normal shocks grow in height, the shock system continues to move upstream, and the KHI along the slip lines emanating from the upper and lower shock triple points become more prominent. A vortex is present at the base of the step for times $t = 4$ and above. Analysis of the temporal evolution of the density gradient magnitude indicates that this vortex is the result of trapped numerical error from the intersection of the bow shock and the lower wall.

Contour plots of density, temperature, and pressure are shown in Fig. 5.18 at $t = 10$ for P1 quadrilaterals on the 2400x800 grid using SDIRK33 and $\Delta t = 0.01$. The slip line emanating from the shock triple point where the initial bow and normal shocks meet is

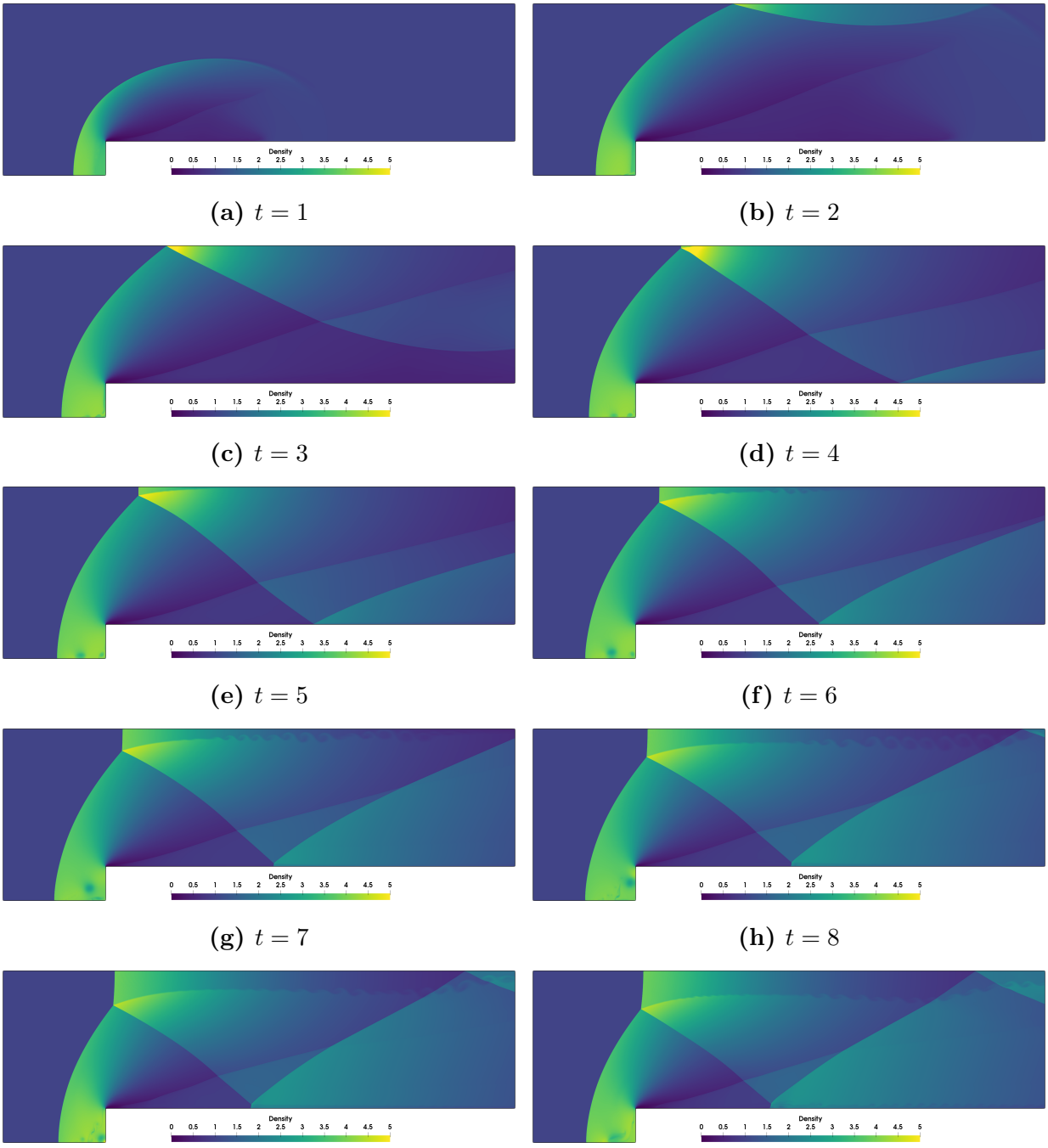

(a) $t = 1$ **(b)** $t = 2$

(c) $t = 3$ **(d)** $t = 4$

(e) $t = 5$ **(f)** $t = 6$

(g) $t = 7$ **(h)** $t = 8$

(i) $t = 9$ **(j)** $t = 10$

Figure 5.17: Time evolution of shock system development as indicated by density contours for the inviscid step case with the P1 quadrilateral 2400x800 grid using the SDIRK33 and $\Delta t = 0.01$.

clearly visible in the density and temperature plots, and it is not shown in the pressure plot, as expected since pressure is constant across a slip line.

The density gradient magnitude plotted on a log scale was found to highlight flow features well, and as a result it is used in subsequent spatial and temporal comparisons. Density gradient magnitude contour plots are shown in Fig. 5.19 for P1 quadrilateral grids 600x200, 1200x400, and 2400x800 using SDIRK33 and $\Delta t = 0.01$ at $t = 10$. As the grid is refined, the shock surfaces become sharper, and the slip lines emanating from the shock triple points evolves from a diffused region to a distinct KHIs. Many authors [161, 186–190] that have reported a KHI, which Isaev and Lysenko [187] believe to be driven by small oscillations in the entropy field at the triple point. The exponential-entropy gradient sensor values for the same grids at $t = 10$ are shown in Fig. 5.20. As the grid is refined, the sensor is active over a smaller region at the shocks and in the region downstream of the expansion corner.

A comparison of the density gradient magnitude on P1 and P2 grids, with the same number of degrees of freedom, composed of quadrilaterals and triangles, is shown in Fig. 5.21, again at $t = 10$ using SDIRK33 with $\Delta t = 0.01$. There is more small-scale noise in the P2 results, but the implications of this are not known. The onset of the KHI is sooner in the P2 results, which could be due to the additional small-scale noise exciting unstable wave numbers. There were minor differences in the flow features between the P1 and P2 grids, as indicated by the figures. The key difference appears to be the height of the unsteady region on the bottom surface downstream of the step. The region is taller in the P2 results. The major difference between the quadrilateral and triangle grids is the presence of a bump on the downstream side of the initial bow shock on the triangle grids. This is not believed to be physical, and the origin of it is unknown. The KHI for the triangle-grid cases is also marginally thinner than the quadrilateral cases.

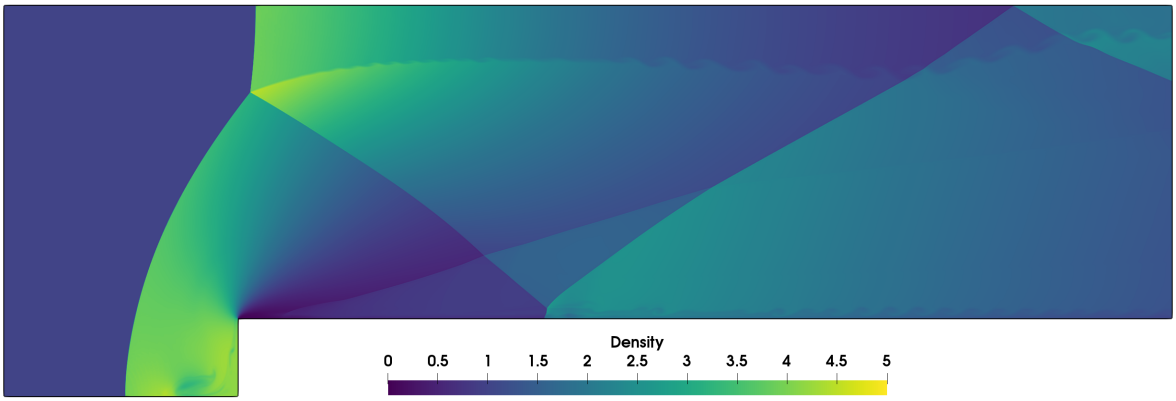

(a) Density

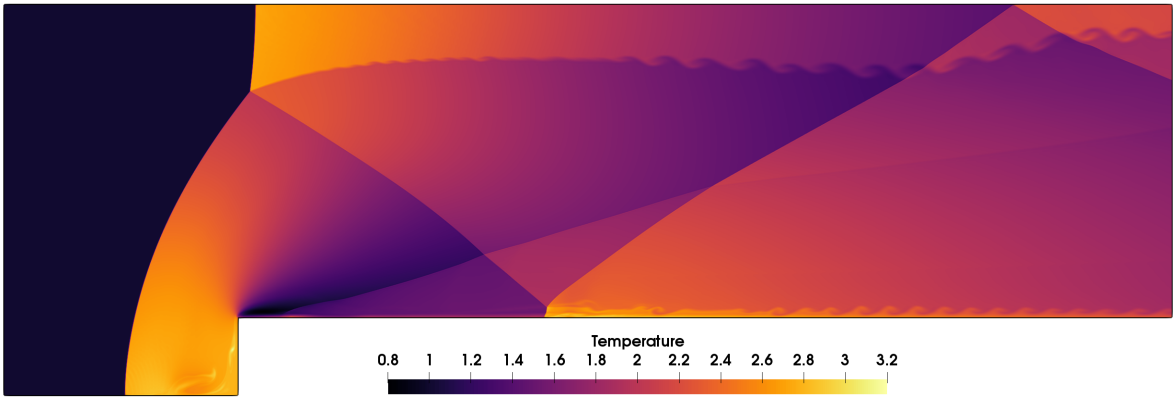

(b) Temperature

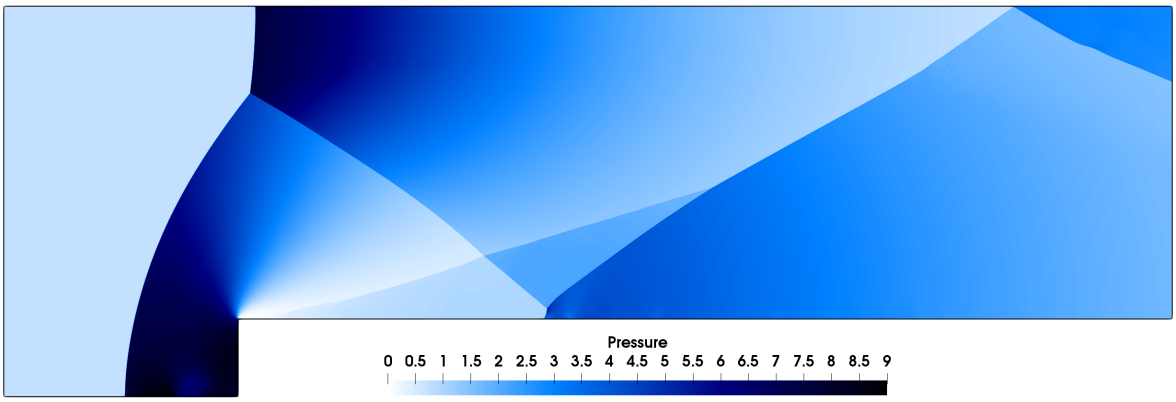

(c) Pressure

Figure 5.18: Density, temperature, and pressure contours at $t = 10$ for the inviscid step case with P1 quadrilaterals on grid 2400x800 using SDIRK33 and $\Delta t = 0.01$.

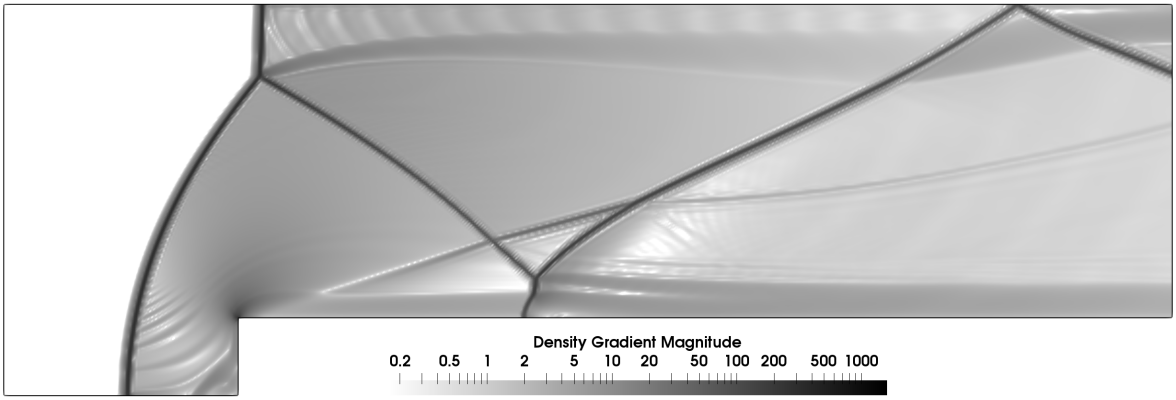

(a) Grid 600x200

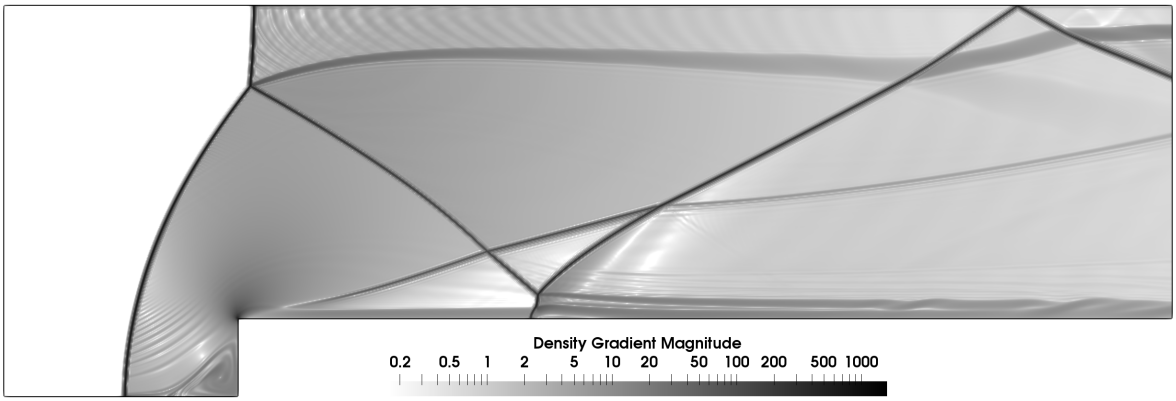

(b) Grid 1200x400

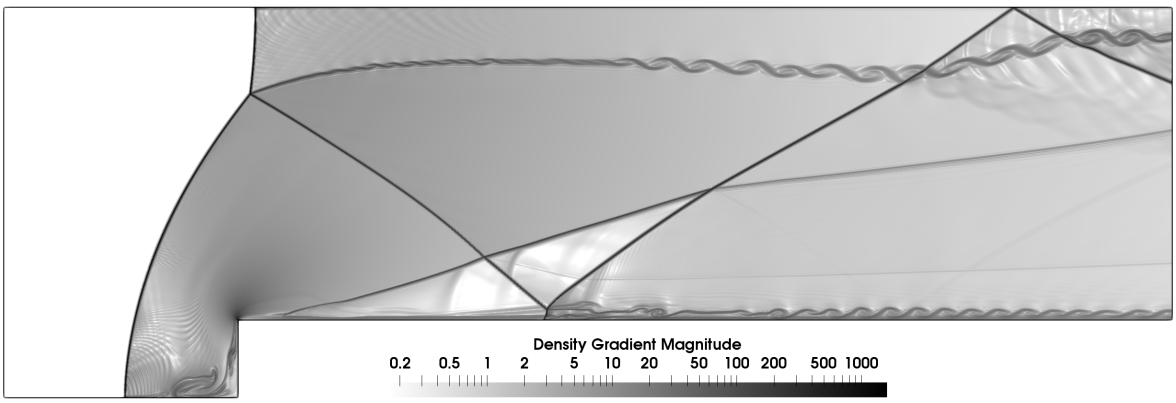

(c) Grid 2400x800

Figure 5.19: Density gradient magnitude contours at $t = 10$ for the inviscid step case with P1 quadrilateral grids 600x200, 1200x400, and 2400x800 using SDIRK33 and $\Delta t = 0.01$.

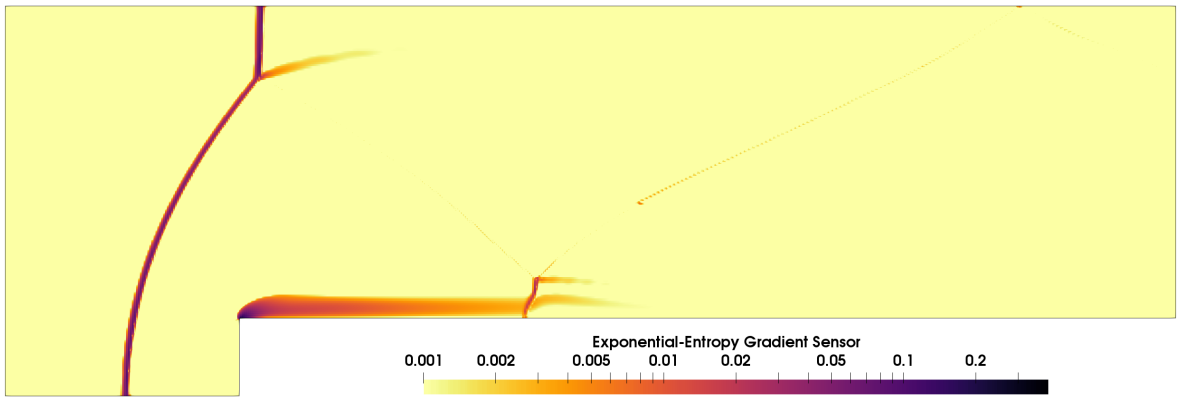

(a) Grid 600x200

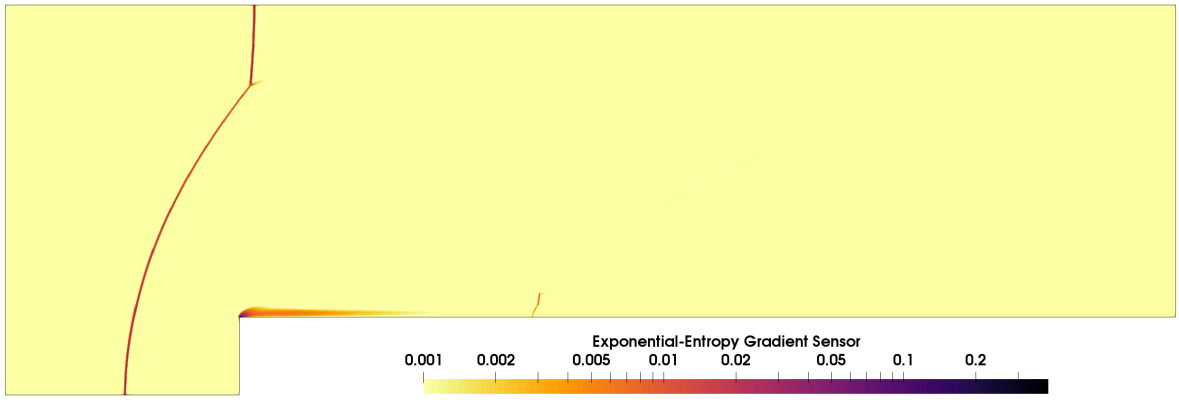

(b) Grid 1200x400

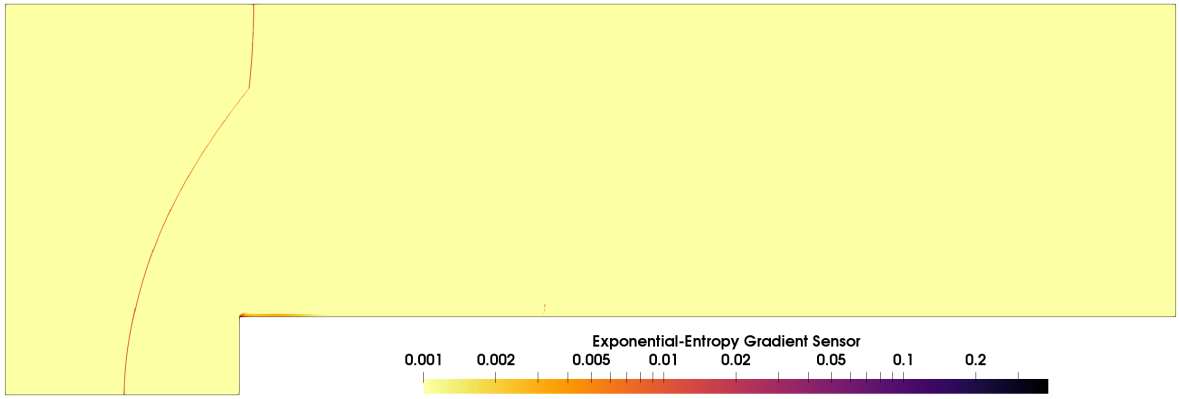

(c) Grid 2400x800

Figure 5.20: Exponential-entropy gradient sensor values at $t = 10$ for the inviscid step case with P1 quadrilateral grids 600x200, 1200x400, and 2400x800 using SDIRK33 and $\Delta t = 0.01$.

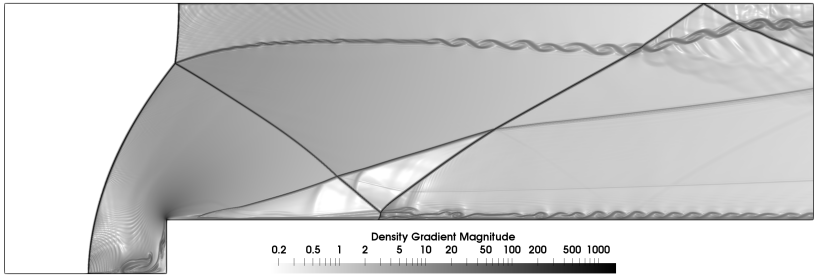

(a) P1 quadrilateral grid 2400x800 at $t = 10$

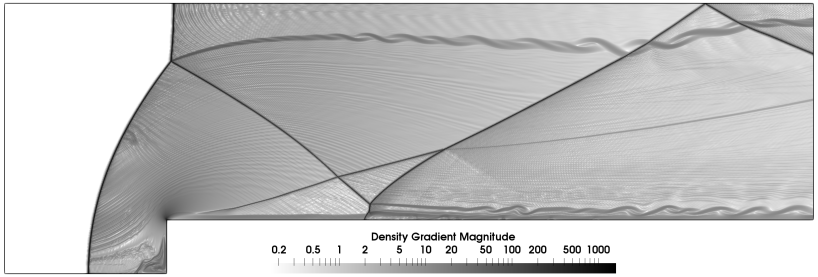

(b) P2 quadrilateral grid 1200x400 at $t = 10$

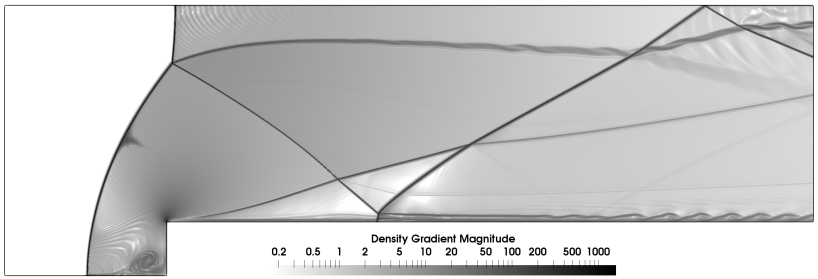

(c) P1 triangle grid 2400x800 at $t = 10$

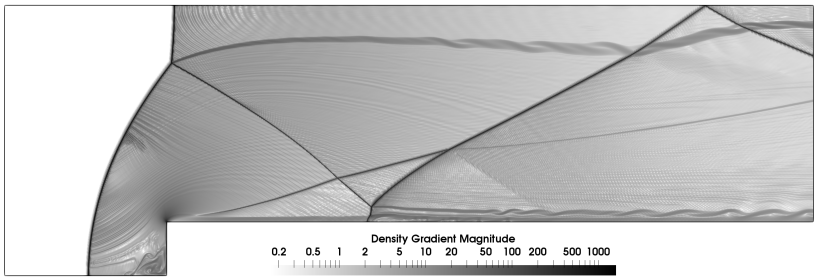

(d) P2 triangle grid 1200x400 at $t = 10$

Figure 5.21: Density gradient magnitude for the inviscid step case on P1 and P2 grids with the same N_{dofs} using SDIRK33 and $\Delta t = 0.01$.

Comparisons of density gradient magnitude on the 2400x800 P1 quadrilateral grid for various temporal integration methods and time step sizes are given in Figs. 5.22 and 5.23. The BDF2 and SDIRK33 methods are compared at time steps of 0.005, 0.01, and 0.02 in Fig. 5.22, and the SDIRK33 and SDIRK45 methods are compared at time steps of 0.01, 0.02, and 0.04 in Fig. 5.23. The main feature of interest used for comparison is the KHI along the slip line emanating from the upper shock triple point. Starting with the BDF2/SDIRK33 comparison, the KHI is present in the BDF2 results at $\Delta t = 0.005$, diminished at $\Delta t = 0.01$, and absent at $\Delta t = 0.02$. At large time steps, the temporal error dissipates this instability, completely removing the flow feature from the solution. The KHI is prominent in the SDIRK33 results at $\Delta t = 0.005$ and diminishes with increasing time step size, but is still present at $\Delta t = 0.02$. The small scale background waves present downstream of the normal shock and along the upper wall in the $\Delta t = 0.005$ cases are smoothed out in the $\Delta t = 0.02$ cases.

The findings for the SDIRK33/SDIRK45 comparison are similar. In this case the SDIRK33 method was run at $\Delta t = 0.04$, and the KHI was not present. The KHI is present in the SDIRK45 results at each time step, but as the time step size increases, the dispersion error increases, and the coherent vortices present for the $\Delta t = 0.01$ results are disorganized in the $\Delta t = 0.04$ results.

A closer inspection of the KHI of the BDF2 and SDIRK45 cases at the lowest time step sizes reveals oscillations upstream of the vortices that are not prominent in the SDIRK33 results. A detailed view of the KHI for BDF2 at $\Delta t = 0.0025$, SDIRK33 at $\Delta t = 0.005$, and SDIRK45 at $\Delta t = 0.01$ is shown in Fig. 5.24. The oscillations are believed to result from dispersion error that was shown in Section 4.1 to be prominent in even-ordered results (BDF2 and SDIRK45) and negligible in odd-order results (SDIRK33) results.

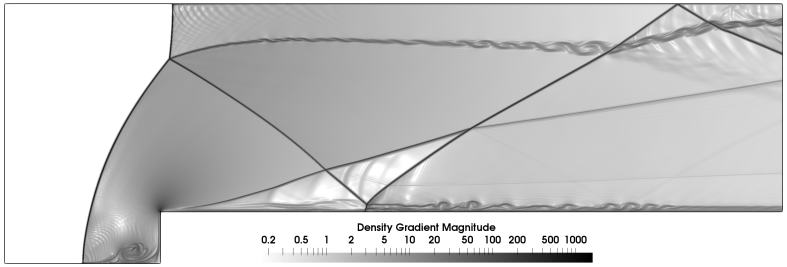

(a) BDF2 at $\Delta t = 0.005$

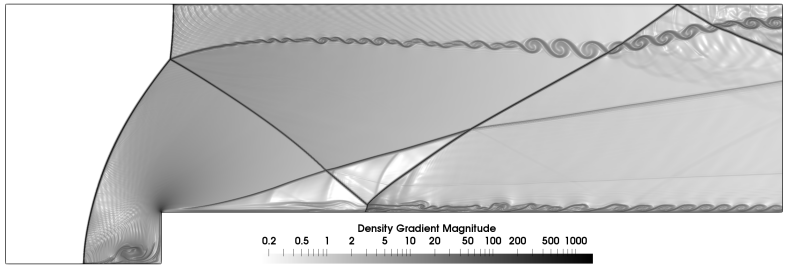

(b) SDIRK33 at $\Delta t = 0.005$

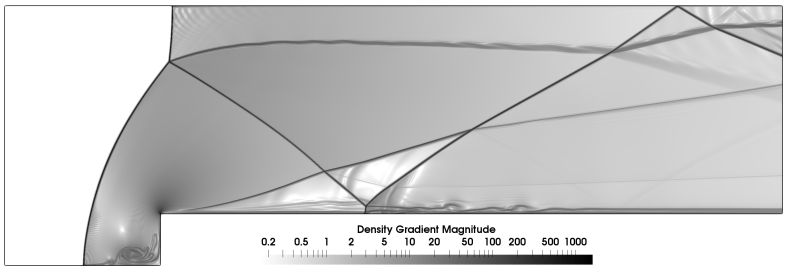

(c) BDF2 at $\Delta t = 0.01$

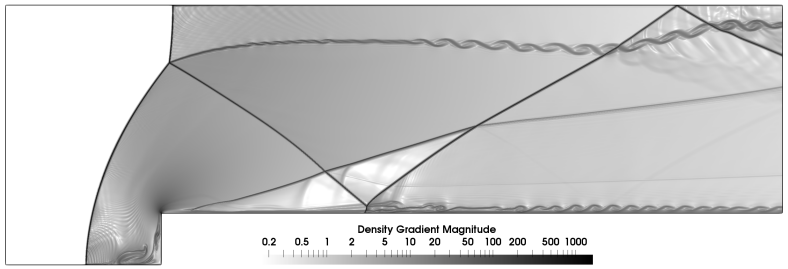

(d) SDIRK33 at $\Delta t = 0.01$

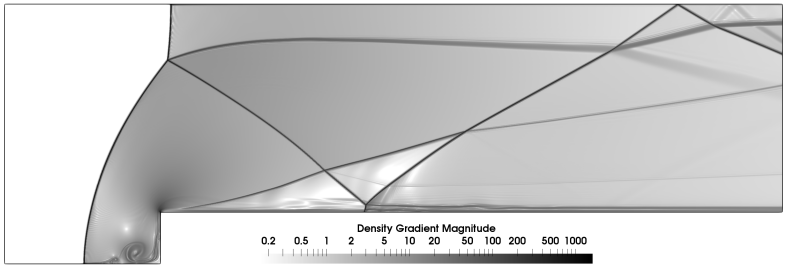

(e) BDF2 at $\Delta t = 0.02$

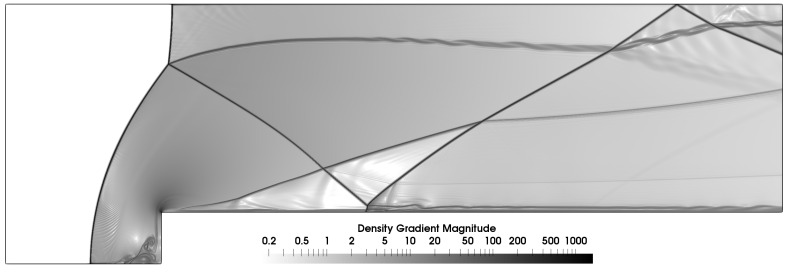

(f) SDIRK33 at $\Delta t = 0.02$

Figure 5.22: Density gradient magnitude for the inviscid step case with P1 quadrilaterals on grid 2400x800 using BDF2 and SDIRK33 and $\Delta t = 0.005, 0.01, 0.02$.

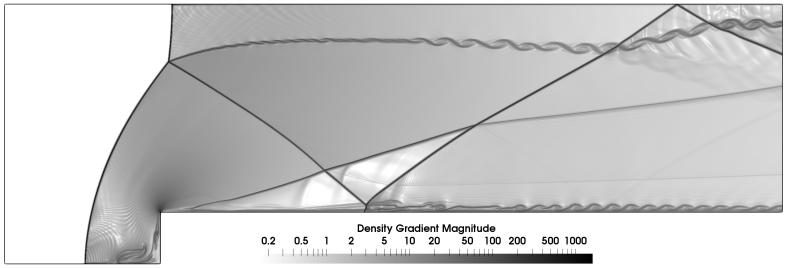

(a) SDIRK33 at $\Delta t = 0.01$

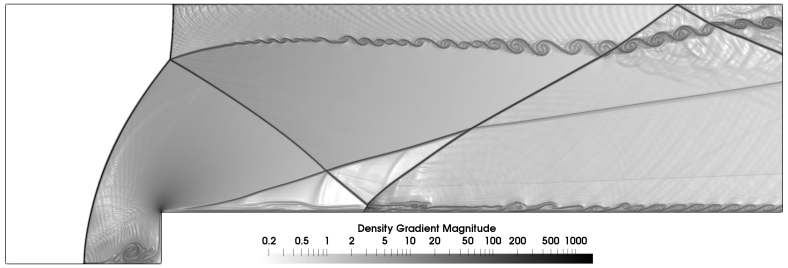

(b) SDIRK45 at $\Delta t = 0.01$

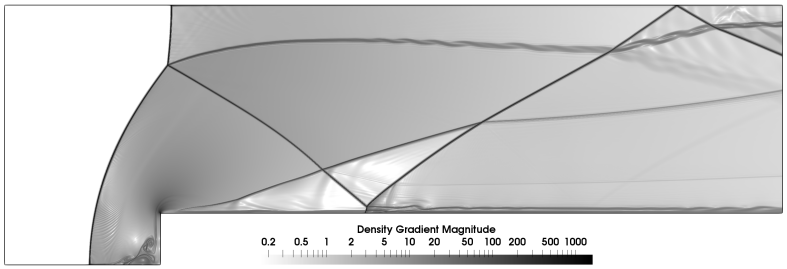

(c) SDIRK33 at $\Delta t = 0.02$

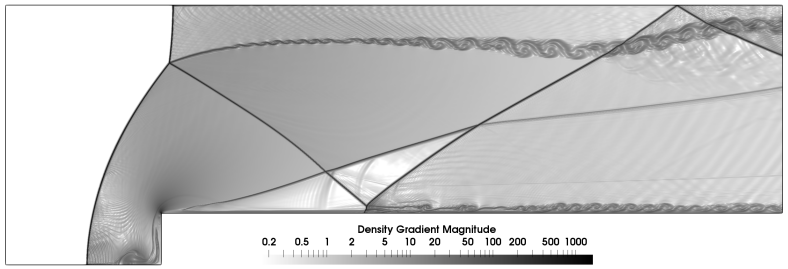

(d) SDIRK45 at $\Delta t = 0.02$

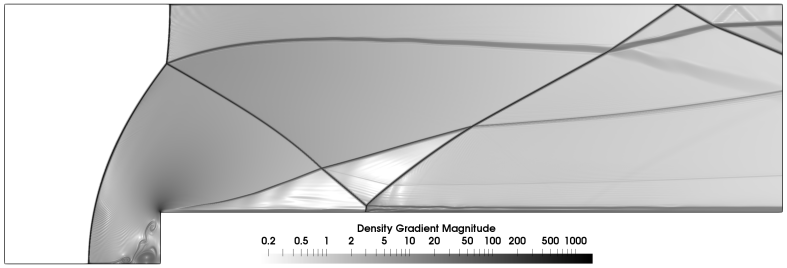

(e) SDIRK33 at $\Delta t = 0.04$

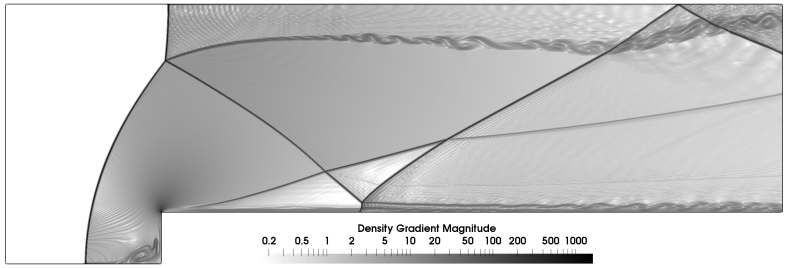

(f) SDIRK45 at $\Delta t = 0.04$

Figure 5.23: Density gradient magnitude for the inviscid step case with P1 quadrilaterals on grid 2400x800 using SDIRK33 and SDIRK45 and $\Delta t = 0.01, 0.02, 0.04$.

5.4 Summary

The bow shock case proved difficult for the new shock capturing method. The Riemannian metric tensor helped provide a smooth valued shock sensor along the surface of the shock, but spurious waves still emanated downstream and collected in the stagnation region. The sensor did not turn on for this accumulation of error, and so low-level global artificial diffusion was required in order to reach steady state. Only the P1 grids reached steady state. The results do not appear to be adversely affected by the addition of artificial global diffusion, as the total enthalpy and stagnation pressure errors were comparable to the example results provided by Murman.

The planar Noh problem was run at Mach numbers 4 and 10 on several P1 rectangular grids with quadrilateral elements at different levels of refinement. This case was devised by Noh [118] to assess the erroneous wall heating produced by many shock capturing methods, and wall heating was present in the results when the exponential-entropy gradient sensor was used in conjunction with COFFE's artificial diffusion method. The shock speed appears to be correct for each of the cases, as indicated by the location of the jump compared to the exact location, and as the level of grid refinement increases, the shock thickness decreases linearly.

The two-dimensional inviscid Mach 3 forward-facing step case is useful for assessing the shock sensor's ability to track a complex, unsteady shock structure. The results presented here showed that the new sensor activated in the shock regions, at the rapid expansion, and at the base of the step. Increasing grid resolution sharpened the shocks and brought out additional weak features, and the major difference between the results on P1 and P2 grids was that the P2 grids contained more small-scale noise that the P1 grids presumably filtered out.

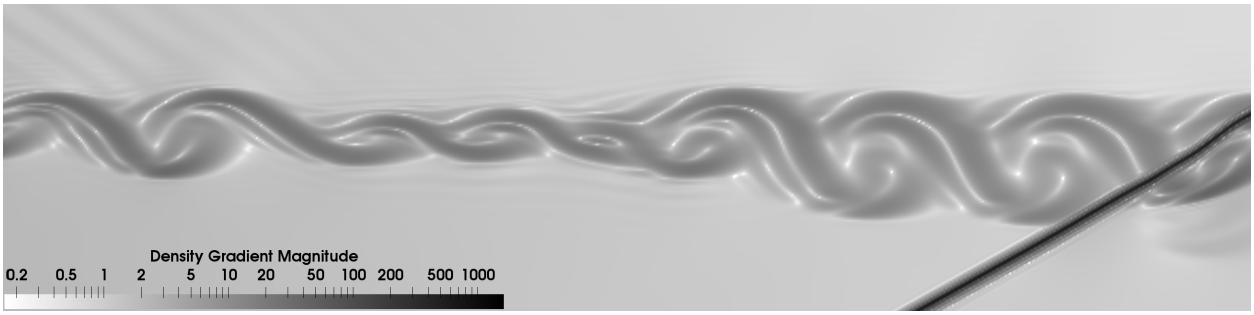

(a) BDF2 $\Delta t = 0.0025$

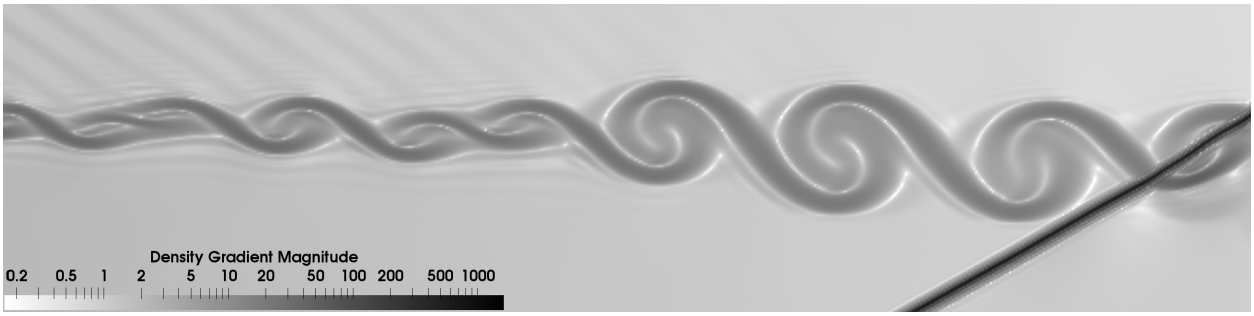

(b) SDIRK33 $\Delta t = 0.005$

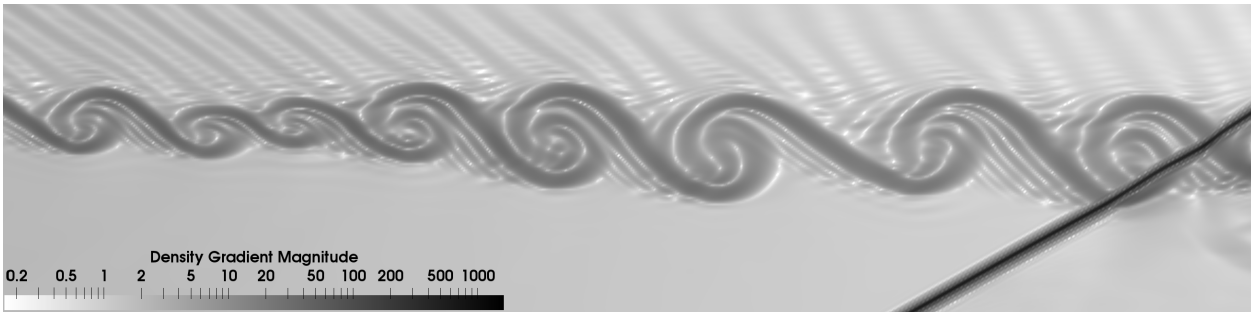

(c) SDIRK45 $\Delta t = 0.01$

Figure 5.24: Density gradient magnitude for the inviscid step case with P1 quadrilaterals on grid 2400x800 using BDF2, SDIRK33, and SDIRK45 at $\Delta t = 0.0025, 0.005, 0.01$, respectively, zoomed to KHI.

Chapter 6

Conclusions

6.1 Summary

The primary focus of this research was high-order, finite-element modeling of moving shock waves on non-shock-aligned grids. Two major components to this were the choice of time-integration method and the shock capturing technique. COFFE, an existing high-spatial-order, finite-element, streamline upwind/Petrov-Galerkin (SU/PG), steady-state solver, was modified to introduce an unsteady capability and a novel approach to shock capturing.

6.1.1 Time-Integration Methods

Six L-stable, first- through fourth-order time-integration methods (BDF1, BDF2, BDF2OPT4, BDF2OPT5, SDIRK33, and SDIRK45) were introduced into COFFE, and three canonical test cases were used to assess the methods and the temporal errors they introduced. The isentropic vortex case was used to verify the order of accuracy of each of the methods. The results from this case were also used to isolate the dissipative and dispersive components of the temporal error. A new finding in this work was that the BDF2OPT4/5 methods tended to reduce the dissipation rise for larger time steps. The result of this decrease in dissipation was an accentuation of the oscillations upstream of the vortex that resulted from dispersion error. This case also demonstrated that, for a given time step size, the overall temporal error decreases as order of accuracy increases. As a result, higher-order methods can achieve the

same temporal error level as lower-order methods with large time steps. This finding appears obvious, but order of accuracy refers to the behavior of error as the discretization is refined, not the absolute level of error.

The unsteady methods were evaluated further using the two-dimensional circular cylinder case, which is less-trivial than the isentropic vortex case and for which a wealth of experimental and numerical data exist. The higher-order SDIRK methods performed better than the lower-order BDF methods with respect to temporal convergence and vortex coherence. One key observation from this portion of the investigation is the importance of time-convergence studies for unsteady problems, especially those using lower-order time-integration methods. Just as grid-convergence studies should accompany steady problems, so too should time-convergence studies be included with unsteady ones.

Results from the Taylor-Green vortex case compared well with the highly-resolved spectral results provided by Rees et al. [178]. This case tested COFFE's modeling of turbulent dissipation and vortex dynamics. The kinetic energy dissipation rate as calculated by enstrophy was a key comparison between COFFE and the results from Rees et al. [178], and the kinetic energy dissipation rate peak on the 128^3 grid at $\Delta t = 0.0025$ matched time to within 0.0075 and peak magnitude to within 1%.

6.1.2 Shock Capturing Technique

A new shock capturing technique involving the gradient of a exponential-entropy parameter was outlined and evaluated on three inviscid test cases: the bow shock described by Murman in HOW5, the planar Noh [118] problem, and the Mach 3 forward facing step of Woodward and Colella [161]. The new sensor was designed to activate in areas where the grid resolution was not sufficient to resolve flow features, such as shock waves and the rapid expansion around the forward-facing step corner. It also activated in the stagnation regions of the bow shock and the forward-facing step when numerical error from the shock rapidly accumulated and did not convect downstream, though that activation was not enough to fully converge the bow shock case without additional global artificial diffusion. The new sensor was also designed to apply artificial diffusion smoothly, as indicated by Barter and Darmofal [101].

The new exponential-entropy gradient shock sensor was used in conjunction with modifications to the calculation of the artificial diffusion flux term, $\boldsymbol{F}_{ad}$. The changes to $\boldsymbol{F}_{ad}$ were designed to vary the application of artificial diffusion directionally within the momentum equations, in the same manner as Olson and Lele [99].

The bow shock case proved difficult for the new shock capturing method. Low-level global artificial diffusion was required, and only the P1 grids reached steady state. The results do not appear to be adversely affected by the addition of artificial global diffusion, as the total enthalpy and stagnation pressure errors were comparable to the example results provided by Murman.

The planar Noh problem was run at Mach numbers 4 and 10, and wall heating was present in the results with the new exponential-entropy gradient sensor and COFFE's artificial diffusion method. The shock speed appears to be correct for each of the cases, and as the level of grid refinement increases, the shock thickness decreases linearly.

The two-dimensional inviscid Mach 3 forward-facing step case demonstrated the new shock sensor's ability to track a complex, unsteady shock structure. The results presented here showed that the new sensor activated in the shock regions, at the rapid expansion, and at the base of the step. Increasing grid resolution sharpened the shocks and brought out additional weak features, and the major difference between the results on P1 and P2 grids was that the P2 grids contained more small-scale noise that the P1 grids presumably filtered out.

Bibliography

[1] D Gilbarg and D Paolucci. "The Structure of Shock Waves in the Continuum Theory of Fluids". In: *Journal of Rational Mechanics and Analysis* 2.1953 (1953), pp. 617–642. ISSN: 19435282, 19435290 (cit. on pp. 1, 93).

[2] M. Linzer and D. F. Hornig. "Structure of shock fronts in argon and nitrogen". In: *Physics of Fluids* 6.12 (1963), pp. 1661–1668. ISSN: 10706631. DOI: 10.1063/1.1711007 (cit. on p. 1).

[3] John Tirpak. "DARPA Chief Says National Hypersonics Effort Needed". In: *Air Force Magazine* (2018) (cit. on p. 1).

[4] Leslie Josephs. "Lockheed Martin wants to develop a supersonic business jet". In: *CNBC* (2017) (cit. on p. 1).

[5] Alex Gray. "Supersonic jets are making a comeback". In: *World Economic Forum* (2018) (cit. on p. 1).

[6] Sanjay Garg and Gary S. Settles. "Unsteady pressure loads generated by swept-shock-wave/boundary-layer interactions". In: *AIAA Journal* 34.6 (June 1996), pp. 1174–1181. ISSN: 0001-1452. DOI: 10.2514/3.13209 (cit. on p. 1).

[7] J. Delery and J. G. Marvin. *Shock-Wave Boundary Layer Interactions*. Tech. rep. AGARD, 1986 (cit. on p. 1).

[8] Z.J. Wang, Krzysztof Fidkowski, Rémi Abgrall, Francesco Bassi, Doru Caraeni, Andrew Cary, Herman Deconinck, Ralf Hartmann, Koen Hillewaert, H.T. Huynh, Norbert Kroll, Georg May, Per-Olof Persson, Bram van Leer, and Miguel Visbal. "High-order CFD methods: current status and perspective". In: *International Journal for Numerical Methods in Fluids* 72.8 (July 2013), pp. 811–845. ISSN: 02712091. DOI: 10.1002/fld.3767 (cit. on pp. 1–3).

[9] James C. Newman and William K. Anderson. "Investigation of Unstructured Higher-Order Methods for Unsteady flow and Moving Domains". In: *22nd AIAA Computational Fluid Dynamics Conference*. Reston, Virginia: American Institute of Aeronautics and Astronautics, June 2015. ISBN: 978-1-62410-366-7. DOI: 10.2514/6.2015-2917 (cit. on pp. 2, 41, 43).

[10] A. Nigro, A. Ghidoni, S. Rebay, and F. Bassi. "Modified extended BDF scheme for the discontinuous Galerkin solution of unsteady compressible flows". In: *International Journal for Numerical Methods in Fluids* 76.9 (Nov. 2014), pp. 549–574. ISSN: 10970363. DOI: 10.1002/fld.3944 (cit. on p. 2).

[11] Jeffrey Slotnick, Abdollah Khodadoust, Juan Alonso, David Darmofal, William Gropp, Elizabeth Lurie, and Dimitri Mavriplis. *CFD Vision 2030 Study: A Path to Revolutionary Computational Aerosciences*. Tech. rep. March 2014. NASA, 2014 (cit. on pp. 2, 3).

[12] Eric Ching, Yu Lv, and Matthias Ihme. "Development of Discontinuous Galerkin method for Hypersonic Heating Prediction". In: *55th AIAA Aerospace Sciences Meeting*. Reston, Virginia: American Institute of Aeronautics and Astronautics, Jan. 2017. ISBN: 978-1-62410-447-3. DOI: 10.2514/6.2017-0311 (cit. on pp. 3, 28, 29, 50).

[13] Hesam Abbassi, Farzad Mashayek, and Gustaaf B. Jacobs. "Shock capturing with entropy-based artificial viscosity for staggered grid discontinuous spectral element method". In: *Computers and Fluids* 98 (2014), pp. 152–163. ISSN: 00457930. DOI: 10.1016/j.compfluid.2014.01.022 (cit. on p. 3).

[14] Andrew W. Cook. "Effects of heat conduction on artificial viscosity methods for shock capturing". In: *Journal of Computational Physics* 255 (2013), pp. 48–52. ISSN: 00219991. DOI: 10.1016/j.jcp.2013.08.003 (cit. on pp. 3, 27).

[15] Britton J. Olson and Sanjiva K. Lele. "Directional artificial bulk viscosity for shock capturing on high aspect ratio grids". In: *Computational Science and Discovery* 5.1 (2012). ISSN: 17494680. DOI: 10.1088/1749-4699/5/1/014008 (cit. on pp. 3, 27, 29, 50).

[16] B. A. Finlayson and L. E. Scriven. "The Method of Weighted Residuals – A Review". In: *Appl. Mech. Rev* 19.9 (1966), pp. 735–748 (cit. on p. 6).

[17] Robert Nichols, Robert Tramel, and Pieter Buning. "Solver and Turbulence Model Upgrades to OVERFLOW 2 for Unsteady and High-Speed Applications". In: *24th AIAA Applied Aerodynamics Conference*. Reston, Virginia: American Institute of

Aeronautics and Astronautics, June 2006. ISBN: 978-1-62410-028-4. DOI: 10.2514/6.2006-2824 (cit. on p. 6).

[18] S V Patankar. *Numerical Heat Transfer and Fluid Flow*. Electro Skills Series. Hemisphere Publishing Corporation, 1980. ISBN: 9780070487406 (cit. on p. 7).

[19] Marcel Vinokur. "An analysis of finite-difference and finite-volume formulations of conservation laws". In: *Journal of Computational Physics* 81.1 (1989), pp. 1–52. ISSN: 10902716. DOI: 10.1016/0021-9991(89)90063-6 (cit. on p. 7).

[20] Y. I. Lim, J. M. Le Lann, and X. Joulia. "Accuracy, temporal performance and stability comparisons of discretization methods for the numerical solution of partial differential equations (PDEs) in the presence of steep moving fronts". In: *Computers and Chemical Engineering* 25.11-12 (2001), pp. 1483–1492. ISSN: 00981354. DOI: 10.1016/S0098-1354(01)00712-8 (cit. on p. 7).

[21] David Gottlieb and Chi-Wang Shu. "On the Gibbs Phenomenon and Its Resolution". In: *SIAM Review* 39.4 (1997), pp. 644–668. ISSN: 0036-1445. DOI: 10.1137/S0036144596301390 (cit. on p. 8).

[22] Edward Luke, Xiaoling Tong, Junxiao Wu, Pasquale Cinnella, and Rex Chamberlain. "CHEM 3.3: A Finite-Rate Viscous Chemistry Solver - The User Guide". In: *CHEM 3.3 User Guide* (2014), pp. 1–81 (cit. on p. 8).

[23] Robert T Biedron, Jan-Reneé Carlson, Joseph M Derlaga, Peter A Gnoffo, Dana P Hammond, William T Jones, Bil Kleb, Elizabeth M Lee-Rausch, Eric J Nielsen, Michael A Park, Christopher L Rumsey, James L Thomas, and William A Wood. *FUN3D Manual v13.2*. Tech. rep. Hampton, Virginia: NASA Langley Research Center, 2017 (cit. on p. 8).

[24] John Lamar and Khaled Abdol-Hamid. "USM3D Unstructured Grid Solutions for CAWAPI at NASA LaRC". In: *45th AIAA Aerospace Sciences Meeting and Exhibit*. Reston, Virginia: American Institute of Aeronautics and Astronautics, Jan. 2007. ISBN: 978-1-62410-012-3. DOI: 10.2514/6.2007-682 (cit. on p. 8).

[25] Graham V. Candler, Heath B. Johnson, Ioannis Nompelis, Vladimyr M. Gidzak, Pramod K. Subbareddy, and Michael Barnhardt. "Development of the US3D Code for Advanced Compressible and Reacting Flow Simulations". In: *53rd AIAA Aerospace Sciences Meeting*. Reston, Virginia: American Institute of Aeronautics and Astronautics, Jan. 2015. ISBN: 978-1-62410-343-8. DOI: 10.2514/6.2015-1893 (cit. on p. 8).

[26] H. G. Weller, G. Tabor, H. Jasak, and C. Fureby. "A tensorial approach to computational continuum mechanics using object-oriented techniques". In: *Computers in Physics* 12.6 (1998), p. 620. ISSN: 08941866. DOI: 10.1063/1.168744 (cit. on p. 8).

[27] Richard S. Varga. *Matrix Iterative Analysis*. Vol. 27. Springer Series in Computational Mathematics. Berlin, Heidelberg: Springer Berlin Heidelberg, 2000. ISBN: 978-3-642-05154-8. DOI: 10.1007/978-3-642-05156-2 (cit. on p. 8).

[28] Gerardine G. Botte, James A. Ritter, and Ralph E. White. "Comparison of finite difference and control volume methods for solving differential equations". In: *Computers and Chemical Engineering* 24.12 (2000), pp. 2633–2654. ISSN: 00981354. DOI: 10.1016/S0098-1354(00)00619-0 (cit. on p. 8).

[29] J D Anderson. *Computational Fluid Dynamics: The Basics with Applications*. McGraw-Hill international editions. McGraw-Hill, 1995. ISBN: 9780071132107 (cit. on p. 8).

[30] B. P. Leonard. "A stable and accurate convective modelling procedure based on quadratic upstream interpolation". In: *Computer Methods in Applied Mechanics and Engineering* 19.1 (1979), pp. 59–98. ISSN: 00457825. DOI: 10.1016/0045-7825(79)90034-3 (cit. on p. 8).

[31] M R Dorr, R H Cohen, P Colella, M A Dorf, J A Hittinger, and D F Martin. "Numerical Simulation of Phase Space Advection in Gyrokinetic Models of Fusion Plasma". In: *Proceedings of SciDAC 2010* (2010) (cit. on p. 8).

[32] Thomas J.R. Hughes. *The Finite Element Method: Linear Static and Dynamic Finite Element Analysis*. Dover, 2000 (cit. on p. 9).

[33] O. C. Zienkiewicz, R. L. Taylor, and P. Nithiarasu. *The Finite Element Method for Fluid Dynamics*. Seventh. The Finite Element Method. Oxford: Butterworth-Heinemann, 2014 (cit. on p. 9).

[34] J. Taylor Erwin, W. Kyle Anderson, Sagar Kapadia, and Li Wang. "Three-Dimensional Stabilized Finite Elements for Compressible Navier–Stokes". In: *AIAA Journal* 51.6 (2013), pp. 1404–1419. ISSN: 0001-1452. DOI: 10.2514/1.J051778 (cit. on p. 9).

[35] Florian Hindenlang, Jonathan Heudorfer, Gregor Gassner, and Claus-dieter Munz. "Unstructured three-dimensional High Order Grids for Discontinuous Galerkin Schemes". In: *20th AIAA Computational Fluid Dynamics Conference*. Reston, Virginia: American Institute of Aeronautics and Astronautics, June 2011. ISBN: 978-1-62410-148-9. DOI: 10.2514/6.2011-3853 (cit. on p. 9).

[36] A. Gargallo-Peiró, X. Roca, J. Peraire, and J. Sarrate. "Optimization of a regularized distortion measure to generate curved high-order unstructured tetrahedral meshes". In: *International Journal for Numerical Methods in Engineering* 103.5 (Aug. 2015), pp. 342–363. ISSN: 00295981. DOI: 10.1002/nme.4888 (cit. on p. 9).

[37] Steve L. Karman, J T. Erwin, Ryan S. Glasby, and Douglas Stefanski. "High-Order Mesh Curving Using WCN Mesh Optimization". In: *46th AIAA Fluid Dynamics Conference*. Reston, Virginia: American Institute of Aeronautics and Astronautics, June 2016. ISBN: 978-1-62410-436-7. DOI: 10.2514/6.2016-3178 (cit. on p. 9).

[38] William F. Mitchell. "How high a degree is high enough for high order finite elements?" In: *Procedia Computer Science* 51.1 (2015), pp. 246–255. ISSN: 18770509. DOI: 10.1016/j.procs.2015.05.235 (cit. on p. 10).

[39] Krzysztof J. Fidkowski, Todd A. Oliver, James Lu, and David L. Darmofal. "p-Multigrid solution of high-order discontinuous Galerkin discretizations of the compressible Navier-Stokes equations". In: *Journal of Computational Physics* 207.1 (2005), pp. 92–113. ISSN: 00219991. DOI: 10.1016/j.jcp.2005.01.005 (cit. on p. 10).

[40] Jean-François Remacle, Joseph E. Flaherty, and Mark S. Shephard. "An Adaptive Discontinuous Galerkin Technique with an Orthogonal Basis Applied to Compressible Flow Problems". In: *SIAM Review* 45.1 (2003), pp. 53–72. ISSN: 0036-1445. DOI: 10.1137/S00361445023830 (cit. on pp. 10, 13).

[41] N. Chevaugeon, J. Xin, P. Hu, X. Li, D. Cler, J. E. Flaherty, and M. S. Shephard. "Discontinuous galerkin methods applied to shock and blast problems". In: *Journal of Scientific Computing* 22-23.June (2005), pp. 227–243. ISSN: 08857474. DOI: 10.1007/s10915-004-4138-4 (cit. on pp. 10, 13).

[42] Jon Taylor Erwin. "Stabilized Finite Elements for Compressible Turbulent Navier-Stokes". PhD thesis. University of Tennessee at Chattanooga, 2013 (cit. on pp. 10, 11).

[43] W. Kyle Anderson, Li Wang, Sagar Kapadia, Craig Tanis, and Bruce Hilbert. "Petrov-Galerkin and discontinuous-Galerkin methods for time-domain and frequency-domain electromagnetic simulations". In: *Journal of Computational Physics* 230.23 (2011), pp. 8360–8385. ISSN: 00219991. DOI: 10.1016/j.jcp.2011.06.025 (cit. on pp. 11, 12).

[44] Ryan Glasby, Nicholas Burgess, Kyle Anderson, Li Wang, Steven Allmaras, and Dimitri Mavriplis. "Comparison of SU/PG and DG Finite-Element Techniques for the Compressible Navier-Stokes Equations on Anisotropic Unstructured Meshes". In: *51st AIAA Aerospace Sciences Meeting including the New Horizons Forum and Aerospace Exposition*. Reston, Virginia: American Institute of Aeronautics and Astronautics, Jan. 2013. ISBN: 978-1-62410-181-6. DOI: 10.2514/6.2013-691 (cit. on pp. 12, 13).

[45] Alexander N. Brooks and Thomas J.R. Hughes. "Streamline upwind/Petrov-Galerkin formulations for convection dominated flows with particular emphasis on the incompressible Navier-Stokes equations". In: *Computer Methods in Applied Mechanics and Engineering* 32.1-3 (1982), pp. 199–259. ISSN: 00457825. DOI: 10.1016/0045-7825(82)90071-8 (cit. on pp. 12, 13, 36).

[46] Dietmar Kröner, Mario Ohlberger, and Christian Rohde. *An introduction to recent developments in theory and numerics for conservation laws : proceedings*

of the International School on Theory and Numerics and Conservation Laws, Freiburg/Littenweiler, October 20-24, 1997. 5. 1999, vi, 285 p. ISBN: 3540650814 (alk. paper) (cit. on pp. 13, 36).

[47] D L Bonhaus. "A Higher Order Accurate Finite Element Method for Viscous Compressible Flows". PhD thesis. Virginia Polytechnic Institute and State University, 1998 (cit. on pp. 13, 36).

[48] Leopoldo P. Franca, Sergio L. Frey, and Thomas J.R. Hughes. "Stabilized finite element methods: I. Application to the advective-diffusive model". In: *Computer Methods in Applied Mechanics and Engineering* 95.2 (1992), pp. 253–276. ISSN: 00457825. DOI: 10.1016/0045-7825(92)90143-8 (cit. on pp. 13, 36).

[49] Thomas J.R. Hughes. "Recent progress in the development and understanding of SUPG methods with special reference to the compressible Euler and Navier– Stokes equations". In: *International Journal for Numerical Methods in Fluids* 7.11 (1987), pp. 1261–1275. ISSN: 10970363. DOI: 10.1002/fld.1650071108 (cit. on pp. 13, 36).

[50] Benjamin S. Kirk and Graham F. Carey. "Development and validation of a SUPG finite element scheme for the compressible Navier-Stokes equations using a modified inviscid flux discretization". In: *International Journal for Numerical Methods in Fluids* 57.3 (May 2008), pp. 265–293. ISSN: 02712091. DOI: 10.1002/fld.1635 (cit. on pp. 13, 36).

[51] Farzin Shakib, Thomas J.R. Hughes, and Zdeněk Johan. "A new finite element formulation for computational fluid dynamics: X. The compressible Euler and Navier-Stokes equations". In: *Computer Methods in Applied Mechanics and Engineering* 89.1-3 (1991), pp. 141–219. ISSN: 00457825. DOI: 10.1016/0045-7825(91)90041-4 (cit. on pp. 13, 36).

[52] Venkat Venkatakrishnan, Steven Allmaras, Dmitrii Kamenetskii, and Forrester Johnson. "Higher Order Schemes for the Compressible Navier-Stokes Equations". In: *16th AIAA Computational Fluid Dynamics Conference*. Reston, Virginia: American Institute of Aeronautics and Astronautics, June 2003. ISBN: 978-1-62410-086-4. DOI: 10.2514/6.2003-3987 (cit. on pp. 13, 36).

[53] Bernardo Cockburn, Suchung Hou, and Chi-Wang Shu. "The Runge-Kutta local projection discontinuous Galerkin finite element method for conservation laws. IV. The multidimensional case". In: *Mathematics of Computation* 54.190 (1990), pp. 545–545. ISSN: 0025-5718. DOI: 10.1090/S0025-5718-1990-1010597-0 (cit. on p. 13).

[54] F Bassi and S Rebay. "High-Order Accurate Discontinuous Finite Element Solution of the 2D Euler Equations". In: *Journal of Computational Physics* 138.2 (Dec. 1997), pp. 251–285. ISSN: 00219991. DOI: 10.1006/jcph.1997.5454 (cit. on p. 13).

[55] F Bassi and S. Rebay. "A High-Order Accurate Discontinuous Finite Element Method for the Numerical Solution of the Compressible Navier–Stokes Equations". In: *Journal of Computational Physics* 131.2 (Mar. 1997), pp. 267–279. ISSN: 00219991. DOI: 10.1006/jcph.1996.5572 (cit. on p. 13).

[56] Laslo T. Diosady and David L. Darmofal. "Preconditioning methods for discontinuous Galerkin solutions of the Navier–Stokes equations". In: *Journal of Computational Physics* 228.11 (June 2009), pp. 3917–3935. ISSN: 00219991. DOI: 10.1016/j.jcp.2009.02.035 (cit. on p. 13).

[57] Dimitri Mavriplis, Cristian Nastase, Li Wang, Khosro Shahbazi, and Nicholas Burgess. "Progess in High-Order Discontinuous Galerkin Methods for Aerospace Applications". In: *47th AIAA Aerospace Sciences Meeting including The New Horizons Forum and Aerospace Exposition*. Reston, Virginia: American Institute of Aeronautics and Astronautics, Jan. 2009. ISBN: 978-1-60086-973-0. DOI: 10.2514/6.2009-601 (cit. on p. 13).

[58] W. H. Reed and T. R. Hill. "Triangular Mesh Methods for the Neutron Transport Equation". In: *Los Alamos Report LA-UR-73-479* 836 (1973), p. 10 (cit. on p. 13).

[59] Francesco Bassi, Andrea Crivellini, Stefano Rebay, and Marco Savini. "Discontinuous Galerkin solution of the Reynolds-averaged Navier-Stokes and k-ω turbulence model equations". In: *Computers and Fluids* 34.4-5 SPEC.ISS. (2005), pp. 507–540. ISSN: 00457930. DOI: 10.1016/j.compfluid.2003.08.004 (cit. on p. 13).

[60] Endre Suli and David F. Mayers. *An Introduction to Numerical Analysis*. Cambridge: Cambridge University Press, 2003. ISBN: 9780511801181. DOI: 10.1017/CBO9780511801181 (cit. on pp. 14, 15, 18, 39).

[61] Ernst Hairer and Gerhard Wanner. *Solving Ordinary Differential Equations I*. Vol. 8. Springer Series in Computational Mathematics. Berlin, Heidelberg: Springer Berlin Heidelberg, 1993, p. 528. ISBN: 978-3-540-56670-0. DOI: 10.1007/978-3-540-78862-1 (cit. on pp. 15, 18, 22, 44).

[62] Germund G. Dahlquist. "A special stability problem for linear multistep methods". In: *Bit* 3.1 (1963), pp. 27–43. ISSN: 00063835. DOI: 10.1007/BF01963532 (cit. on pp. 15, 18).

[63] Ernst Hairer and Gerhard Wanner. *Solving Ordinary Differential Equations II*. Vol. 14. Springer Series in Computational Mathematics 4. Berlin, Heidelberg: Springer Berlin Heidelberg, 1996, p. 439. ISBN: 978-3-642-05220-0. DOI: 10.1007/978-3-642-05221-7 (cit. on pp. 15, 16, 20, 21, 39, 43).

[64] R. Courant, K. Friedrichs, and H. Lewy. "Über die partiellen Differenzengleichungen der mathematischen Physik". In: *Mathematische Annalen* 100.1 (Dec. 1928), pp. 32–74. ISSN: 00255831. DOI: 10.1007/BF01448839 (cit. on p. 17).

[65] J Blazek. *Computational Fluid Dynamics: Principles and Applications*. 3rd. Elsevier Science, 2015. ISBN: 9780128011720 (cit. on p. 17).

[66] G. Dahlquist. "Convergence and stability in the numerical integration of ordinary differential equations". In: *Mathematica Scandinavica* 4.1 (Dec. 1956), pp. 33–56. ISSN: 1903-1807. DOI: 10.7146/math.scand.a-10454 (cit. on p. 18).

[67] C. Runge. "Ueber die numerische Auflösung von Differentialgleichungen". In: *Mathematische Annalen* (1895), pp. 167–178 (cit. on p. 23).

[68] Martin Wilhelm Kutta. "Beitrag zur näherungweisen Integration totaler Differentialgleichungen". In: *Zeitschrift für Mathematik und Physik* 46 (1901), pp. 435–453 (cit. on p. 23).

[69] Will Pazner and Per Olof Persson. "Stage-parallel fully implicit Runge–Kutta solvers for discontinuous Galerkin fluid simulations". In: *Journal of Computational Physics* 335 (2017), pp. 700–717. ISSN: 10902716. DOI: 10.1016/j.jcp.2017.01.050 (cit. on p. 23).

[70] D. J L Chen. "The efficiency of Singly-implicit Runge-Kutta methods for stiff differential equations". In: *Numerical Algorithms* 65.3 (2014), pp. 533–554. ISSN: 10171398. DOI: 10.1007/s11075-013-9797-5 (cit. on p. 24).

[71] F Mesinger and A Arakawa. "Numerical methods used in atmospheric models". In: *GARP Publ. Ser. WMO* I.No 17 (1976) (cit. on p. 24).

[72] Paul Kultler, R.F. Warming, and Harvard Lomax. "Computation of Space Shuttle Flowfields Using Noncentered Finite-Difference Schemes". In: *AIAA Journal* 11.2 (Feb. 1973), pp. 196–204. ISSN: 0001-1452. DOI: 10.2514/3.50450 (cit. on p. 24).

[73] D Bouche, G. Bonnaud, and D Ramos. "Comparison of numerical schemes for solving the advection equation". In: *Applied Mathematics Letters* 16.2 (Feb. 2003), pp. 147–154. ISSN: 08939659. DOI: 10.1016/S0893-9659(03)80024-1 (cit. on p. 24).

[74] Louis J. Wicker and William C. Skamarock. "Time-Splitting Methods for Elastic Models Using Forward Time Schemes". In: *Monthly Weather Review* 130.8 (2002), pp. 2088–2097. ISSN: 0027-0644. DOI: 10.1175/1520-0493(2002)130<2088:TSMFEM>2.0.CO;2 (cit. on p. 24).

[75] Lawrence L. Takacs. "A Two-Step Scheme for the Advection Equation with Minimized Dissipation and Dispersion Errors". In: *Monthly Weather Review* 113.6 (June 1985), pp. 1050–1065. ISSN: 0027-0644. DOI: 10.1175/1520-0493(1985)113<1050:ATSSFT>2.0.CO;2 (cit. on pp. 24, 58).

[76] Brad Lee Holian, William G. Hoover, Bill Moran, and Galen K. Straub. "Shock-wave structure via nonequilibrium molecular dynamics and Navier-Stokes continuum mechanics". In: *Physical Review A* 22.6 (1980), pp. 2798–2808. ISSN: 10502947. DOI: 10.1103/PhysRevA.22.2798 (cit. on p. 25).

[77] J. O. Hirschfelder, C. F. Curtiss, and R. B. Bird. *Molecular theory of gases and liquids*. Structure of matter series. Wiley, 1954, p. 1219. ISBN: 9780471400653. DOI: 10.1002/pol.1955.120178311 (cit. on p. 25).

[78] Eswar Josyula, Kun Xu, and Dean C. Wadsworth. "Testing continuum and non-continuum descriptions in high speed flows". In: *AIP Conference Proceedings* 762 (2005), pp. 1217–1222. ISSN: 0094243X. DOI: 10.1063/1.1941699 (cit. on p. 25).

[79] Gino Moretti and Manuel D. Salas. "Numerical analysis of viscous one-dimensional flows". In: *Journal of Computational Physics* 5.3 (June 1970), pp. 487–506. ISSN: 10902716. DOI: 10.1016/0021-9991(70)90076-8 (cit. on p. 25).

[80] Maria Oliveira, Ping Lu, Xiaobing Liu, and Chaoqun Liu. "Universal High Order Subroutine with New Shock Detector for Shock Boundary Layer Interaction". In: *47th AIAA Aerospace Sciences Meeting including The New Horizons Forum and Aerospace Exposition*. Reston, Virginia: American Institute of Aeronautics and Astronautics, Jan. 2009. ISBN: 978-1-60086-973-0. DOI: 10.2514/6.2009-1139 (cit. on p. 25).

[81] J. Von Neumann and R. D. Richtmyer. "A method for the numerical calculation of hydrodynamic shocks". In: *Journal of Applied Physics* 21.3 (Mar. 1950), pp. 232–237. ISSN: 00218979. DOI: 10.1063/1.1699639 (cit. on pp. 26, 32, 47).

[82] S. K. Godunov. "A difference method for numerical calculation of discontinuous solutions of the equations of hydrodynamics". In: *Matematicheskii Sbornik* 89.3 (1959), pp. 271–306. ISSN: 01342452 (cit. on p. 26).

[83] P. L. Roe. "Approximate Riemann solvers, parameter vectors, and difference schemes". In: *Journal of Computational Physics* 43.2 (1981), pp. 357–372. ISSN: 10902716. DOI: 10.1016/0021-9991(81)90128-5 (cit. on pp. 26, 30).

[84] Stanley Osher and Fred Solomon. "Upwind difference schemes for hyperbolic systems of conservation laws". In: *Mathematics of Computation* 38.158 (May 1982), pp. 339–339. ISSN: 0025-5718. DOI: 10.1090/S0025-5718-1982-0645656-0 (cit. on pp. 26, 30).

[85] Renato Paciorri and Aldo Bonfiglioli. "Shock interaction computations on unstructured, two-dimensional grids using a shock-fitting technique". In: *Journal of Computational Physics* 230.8 (2011), pp. 3155–3177. ISSN: 00219991. DOI: 10.1016/j.jcp.2011.01.018 (cit. on pp. 26, 33).

[86] D Zaide and P Roe. "Shock Capturing Anomalies and the Jump Conditions in One Dimension". In: *20th AIAA Computational Fluid Dynamics Conference*. Reston, Virginia: American Institute of Aeronautics and Astronautics, June 2011. ISBN: 978-1-62410-148-9. DOI: 10.2514/6.2011-3686 (cit. on pp. 26, 48).

[87] George Gabriel Stokes. "On the Theories of the Internal Friction of Fluids in Motion, and of the Equilibrium and Motion of Elastic Solids". In: *Mathematical and Physical Papers vol.1*. Cambridge: Cambridge University Press, 1845, pp. 75–129. DOI: 10.1017/CBO9780511702242.005 (cit. on p. 26).

[88] Xin Dong Li, Zong Min Hu, and Zong Lin Jiang. "Continuum perspective of bulk viscosity in compressible fluids". In: *Journal of Fluid Mechanics* 812 (2017), pp. 966–990. ISSN: 14697645. DOI: 10.1017/jfm.2016.834 (cit. on p. 26).

[89] F M White. *Viscous Fluid Flow*. McGraw-Hill international edition. McGraw-Hill Higher Education, 2006. ISBN: 9780071244930 (cit. on p. 26).

[90] L. D. Landau and E. M. Lifshitz. *Fluid Mechanics*. v. 6. Elsevier Science, 2013. ISBN: 9781483140506 (cit. on p. 27).

[91] George Emanuel and Brian M. Argrow. "Linear dependence of the bulk viscosity on shock wave thickness". In: *Physics of Fluids* 6.9 (1994), pp. 3203–3205. ISSN: 10706631. DOI: 10.1063/1.868102 (cit. on p. 27).

[92] Andrew W. Cook and William H. Cabot. "Hyperviscosity for shock-turbulence interactions". In: *Journal of Computational Physics* 203.2 (Mar. 2005), pp. 379–385. ISSN: 00219991. DOI: 10.1016/j.jcp.2004.09.011 (cit. on p. 27).

[93] Soshi Kawai, Santhosh K. Shankar, and Sanjiva K. Lele. "Assessment of localized artificial diffusivity scheme for large-eddy simulation of compressible turbulent flows".

In: *Journal of Computational Physics* 229.5 (2010), pp. 1739–1762. ISSN: 00219991. DOI: 10.1016/j.jcp.2009.11.005 (cit. on p. 27).

[94] Andrew W. Cook. "Artificial fluid properties for large-eddy simulation of compressible turbulent mixing". In: *Physics of Fluids* 19.5 (2007). ISSN: 10706631. DOI: 10.1063/1.2728937 (cit. on p. 27).

[95] Andrew W. Cook. "Enthalpy diffusion in multicomponent flows". In: *Physics of Fluids* 21.5 (May 2009), p. 055109. ISSN: 1070-6631. DOI: 10.1063/1.3139305 (cit. on p. 27).

[96] S. Kawai and S. K. Lele. "Localized artificial diffusivity scheme for discontinuity capturing on curvilinear meshes". In: *Journal of Computational Physics* 227.22 (2008), pp. 9498–9526. ISSN: 00219991. DOI: 10.1016/j.jcp.2008.06.034 (cit. on p. 27).

[97] F. Ducros, V. Ferrand, F. Nicoud, C. Weber, D. Darracq, C. Gacherieu, and T. Poinsot. "Large-Eddy Simulation of the Shock/Turbulence Interaction". In: *Journal of Computational Physics* 152.2 (July 1999), pp. 517–549. ISSN: 00219991. DOI: 10.1006/jcph.1999.6238 (cit. on pp. 27, 28).

[98] Ali Mani, Johan Larsson, and Parviz Moin. "Suitability of artificial bulk viscosity for large-eddy simulation of turbulent flows with shocks". In: *Journal of Computational Physics* 228.19 (2009), pp. 7368–7374. ISSN: 00219991. DOI: 10.1016/j.jcp.2009.06.040 (cit. on p. 27).

[99] Britton J. Olson and Sanjiva K. Lele. "Directional artificial fluid properties for compressible large-eddy simulation". In: *Journal of Computational Physics* 246 (2013), pp. 207–220. ISSN: 00219991. DOI: 10.1016/j.jcp.2013.03.026 (cit. on pp. 27, 29, 49, 50, 112).

[100] A. Jameson, Wolfgang Schmidt, and Eli Turkel. "Numerical solution of the Euler equations by finite volume methods using Runge Kutta time stepping schemes". In: *14th Fluid and Plasma Dynamics Conference*. Reston, Virginia: American Institute of Aeronautics and Astronautics, June 1981. ISBN: 9781441976314. DOI: 10.2514/6.1981-1259 (cit. on p. 28).

[101] Garrett E. Barter and David L. Darmofal. "Shock capturing with PDE-based artificial viscosity for DGFEM: Part I. Formulation". In: *Journal of Computational Physics* 229.5 (2010), pp. 1810–1827. ISSN: 00219991. DOI: 10.1016/j.jcp.2009.11.010 (cit. on pp. 28, 29, 49, 52, 111).

[102] Kevin R. Holst, Ryan S. Glasby, Jon T. Erwin, Douglas L. Stefanski, Ryan B. Bond, and John D. Schmisseur. "High-Order Simulations of Shock Problems using HPCMP CREATE(TM)-AV Kestrel COFFE". In: *2018 AIAA Aerospace Sciences Meeting*. Reston, Virginia: American Institute of Aeronautics and Astronautics, Jan. 2018. ISBN: 978-1-62410-524-1. DOI: 10.2514/6.2018-1301 (cit. on pp. 28, 51, 154).

[103] Per-Olof Persson and Jaime Peraire. "Sub-Cell Shock Capturing for Discontinuous Galerkin Methods". In: *44th AIAA Aerospace Sciences Meeting and Exhibit*. Reston, Virginia: American Institute of Aeronautics and Astronautics, Jan. 2006. ISBN: 978-1-62410-039-0. DOI: 10.2514/6.2006-112 (cit. on pp. 28, 29).

[104] Masayuki Yano, James Modisette, and David Darmofal. "The Importance of Mesh Adaptation for Higher-Order Discretizations of Aerodynamic Flows". In: *20th AIAA Computational Fluid Dynamics Conference*. Reston, Virginia: American Institute of Aeronautics and Astronautics, June 2011. ISBN: 978-1-62410-148-9. DOI: 10.2514/6.2011-3852 (cit. on pp. 28, 29).

[105] Masayuki Yano. "An Optimization Framework for Adaptive Higher-Order Discretizations of Partial Differential Equations on Anisotropic Simplex Meshes". In: (2012) (cit. on p. 28).

[106] Antony Jameson. "Origins and Further Development of the Jameson–Schmidt–Turkel Scheme". In: *AIAA Journal* 55.5 (2017), pp. 1487–1510. ISSN: 0001-1452. DOI: 10.2514/1.j055493 (cit. on pp. 28, 29).

[107] Mark H. Carpenter and Jay H. Casper. "Accuracy of Shock Capturing in Two Spatial Dimensions". In: *AIAA Journal* 37.9 (1999), pp. 1072–1079. ISSN: 0001-1452. DOI: 10.2514/2.835 (cit. on pp. 29, 35).

[108] Christopher J Roy. "Grid Convergence Error Analysis for Mixed-Order Numerical Schemes". In: *AIAA Journal* 41.4 (2003), pp. 595–604. ISSN: 0001-1452. DOI: 10.2514/2.2013 (cit. on p. 29).

[109] J. W. Banks, T. Aslam, and W. J. Rider. "On sub-linear convergence for linearly degenerate waves in capturing schemes". In: *Journal of Computational Physics* 227.14 (2008), pp. 6985–7002. ISSN: 00219991. DOI: 10.1016/j.jcp.2008.04.002 (cit. on p. 30).

[110] Sergio Pirozzoli. "Numerical Methods for High-Speed Flows". In: *Annual Review of Fluid Mechanics* 43.1 (2011), pp. 163–194. ISSN: 0066-4189. DOI: 10.1146/annurev-fluid-122109-160718 (cit. on p. 30).

[111] Jay Casper and Mark H. Carpenter. "Computational Considerations for the Simulation of Shock-Induced Sound". In: *SIAM Journal on Scientific Computing* 19.3 (1998), pp. 813–828. ISSN: 1064-8275. DOI: 10.1137/S1064827595294101 (cit. on p. 30).

[112] Joseph M. Powers, Jeffrey D. Bruns, and Aleksandar Jemcov. "Physical Diffusion Cures the Carbuncle Phenomenon". In: *53rd AIAA Aerospace Sciences Meeting*. Reston, Virginia: American Institute of Aeronautics and Astronautics, Jan. 2015. ISBN: 978-1-62410-343-8. DOI: 10.2514/6.2015-0579 (cit. on pp. 30, 31).

[113] K. M. Peery and S. T. Imlay. "Blunt-body Flow Simulations". In: *24th Joint Propulsion Conference*. Reston, Virginia: American Institute of Aeronautics and Astronautics, July 1988. DOI: 10.2514/6.1988-2904 (cit. on p. 30).

[114] Farzad Ismail, Philip L. Roe, and Hiroaki Nishikawa. "A proposed cure to the carbuncle phenomenon". In: *Computational Fluid Dynamics 2006 - Proceedings of the Fourth International Conference on Computational Fluid Dynamics, ICCFD 2006*. July 2006. Berlin, Heidelberg: Springer Berlin Heidelberg, 2009, pp. 149–154. ISBN: 978-3-540-92778-5. DOI: 10.1007/978-3-540-92779-2-21 (cit. on p. 30).

[115] Joseph L. Steger and R. F. Warming. "Flux vector splitting of the inviscid gasdynamic equations with application to finite-difference methods". In: *Journal of Computational*

Physics 40.2 (Apr. 1981), pp. 263–293. ISSN: 00219991. DOI: 10.1016/0021-9991(81)90210-2 (cit. on p. 30).

[116] Bram van Leer. *Flux-vector splitting for the Euler equations*. Tech. rep. Leiden, The Netherlands: Leiden State University, 1982, pp. 507–512. DOI: 10.1007/3-540-11948-5_66 (cit. on p. 30).

[117] Hong Chia Lin. "Dissipation additions to flux-difference splitting". In: *Journal of Computational Physics* 117.1 (Mar. 1995), pp. 20–27. ISSN: 00219991. DOI: 10.1006/jcph.1995.1040 (cit. on p. 30).

[118] W. F. Noh. "Errors for calculations of strong shocks using an artificial viscosity and an artificial heat flux". In: *Journal of Computational Physics* 72.1 (1987), pp. 78–120. ISSN: 10902716. DOI: 10.1016/0021-9991(87)90074-X (cit. on pp. 30, 32, 83, 91, 95, 108, 111).

[119] M. Gehmeyr, B. Cheng, and D. Mihalas. "Noh's constant-velocity shock problem revisited". In: *Shock Waves* 7.5 (1997), pp. 255–274. ISSN: 0938-1287. DOI: 10.1007/s001930050081 (cit. on p. 31).

[120] J. Willard Gibbs. "Fourier's Series". In: *Nature* 59.1522 (Dec. 1898), pp. 200–200. ISSN: 0028-0836. DOI: 10.1038/059200b0 (cit. on p. 31).

[121] Howard W. Emmons. *The Numerical Solution of Compressible Fluid Flow Problems*. Tech. rep. NASA, 1944, NACA–TN 932 (cit. on p. 33).

[122] M. D. Salas. *A Shock-Fitting Primer*. Chapman & Hall/CRC Applied Mathematics & Nonlinear Science. CRC Press, 2009. ISBN: 9781439807590 (cit. on p. 33).

[123] A. Bonfiglioli, M. Grottadaurea, R. Paciorri, and F. Sabetta. "An unstructured, three-dimensional, shock-fitting solver for hypersonic flows". In: *Computers and Fluids* 73 (Mar. 2013), pp. 162–174. ISSN: 00457930. DOI: 10.1016/j.compfluid.2012.12.022 (cit. on p. 33).

[124] Mikhail S. Ivanov, Aldo Bonfiglioli, Renato Paciorri, and Filippo Sabetta. "Computation of weak steady shock reflections by means of an unstructured shock-fitting

solver". In: *Shock Waves* 20.4 (2010), pp. 271–284. ISSN: 09381287. DOI: 10.1007/s00193-010-0266-y (cit. on p. 33).

[125] Raffaele Pepe, Aldo Bonfiglioli, Antonio D'Angola, Gianpiero Colonna, and Renato Paciorri. "Shock-fitting versus shock-capturing modeling of strong shocks in nonequilibrium plasmas". In: *IEEE Transactions on Plasma Science* 42.10 (2014), pp. 2526–2527. ISSN: 00933813. DOI: 10.1109/TPS.2014.2324493 (cit. on p. 34).

[126] Dongyang Zou, Chunguang Xu, Haibo Dong, and Jun Liu. "A shock-fitting technique for cell-centered finite volume methods on unstructured dynamic meshes". In: *Journal of Computational Physics* 345 (Sept. 2017), pp. 866–882. ISSN: 10902716. DOI: 10.1016/j.jcp.2017.05.047 (cit. on p. 34).

[127] G Moretti. "Computation of Flows with Shocks". In: *Annual Review of Fluid Mechanics* 19.1 (Jan. 1987), pp. 313–337. ISSN: 0066-4189. DOI: 10.1146/annurev.fl.19.010187.001525 (cit. on p. 34).

[128] Aldo Bonfiglioli and Renato Paciorri. "Convergence Analysis of Shock-Capturing and Shock-Fitting Solutions on Unstructured Grids". In: *AIAA Journal* 52.7 (2014), pp. 1404–1416. ISSN: 0001-1452. DOI: 10.2514/1.J052567 (cit. on p. 34).

[129] Thomas-Peter Fries and Ted Belytschko. "The extended/generalized finite element method: An overview of the method and its applications". In: *International Journal for Numerical Methods in Engineering* 84.March (Aug. 2010), pp. 253–304. ISSN: 00295981. DOI: 10.1002/nme.2914 (cit. on p. 34).

[130] T. Belytschko and T. Black. "Elastic crack growth in finite elements with minimal remeshing". In: *International Journal for Numerical Methods in Engineering* 45.5 (June 1999), pp. 601–620. ISSN: 0029-5981. DOI: 10.1002/(SICI)1097-0207(19990620)45:5<601::AID-NME598>3.0.CO;2-S (cit. on p. 34).

[131] N. Moës, J. Dolbow, and T. Belytschko. "A finite element method for crack growth without remeshing". In: *International Journal for Numerical Methods in Engineering* 46.1 (1999), pp. 131–150. ISSN: 00295981. DOI: 10.1002/(SICI)1097-0207(19990910)46:1<131::AID-NME726>3.0.CO;2-J (cit. on p. 34).

[132] I. Babuška and J. M. Melenk. "The partition of unity method". In: *International Journal for Numerical Methods in Engineering* 40.4 (1997), pp. 727–758. ISSN: 00295981. DOI: 10.1002/(SICI)1097-0207(19970228)40:4<727::AID-NME86>3.0.CO;2-N (cit. on p. 34).

[133] J.M. Melenk and I. Babuška. "The partition of unity finite element method: Basic theory and applications". In: *Computer Methods in Applied Mechanics and Engineering* 139.1-4 (1996), pp. 289–314. ISSN: 00457825. DOI: 10.1016/S0045-7825(96)01087-0 (cit. on p. 34).

[134] Michael Griebel and Marc Alexander Schweitzer. "A Particle-Partition of Unity Method for the Solution of Elliptic, Parabolic, and Hyperbolic PDEs". In: *SIAM Journal on Scientific Computing* 22.3 (Jan. 2000), pp. 853–890. ISSN: 1064-8275. DOI: 10.1137/S1064827599355840 (cit. on p. 34).

[135] T. Strouboulis, I. Babuška, and K. Copps. "The design and analysis of the Generalized Finite Element Method". In: *Computer Methods in Applied Mechanics and Engineering* 181.1-3 (2000), pp. 43–69. ISSN: 00457825. DOI: 10.1016/S0045-7825(99)00072-9 (cit. on p. 34).

[136] T. Strouboulis, K. Copps, and I. Babuška. "The generalized finite element method: an example of its implementation and illustration of its performance". In: *International Journal for Numerical Methods in Engineering* 47.8 (Mar. 2000), pp. 1401–1417. ISSN: 0029-5981. DOI: 10.1002/(SICI)1097-0207(20000320)47:8<1401::AID-NME835>3.0.CO;2-8 (cit. on p. 34).

[137] Safdar Abbas, Alaskar Alizada, and Thomas-Peter Fries. "The XFEM for high-gradient solutions in convection-dominated problems". In: *International Journal for Numerical Methods in Engineering* 82.8 (Dec. 2009), pp. 1044–1072. ISSN: 00295981. DOI: 10.1002/nme.2815 (cit. on p. 35).

[138] Benjamin Krank and Wolfgang A Wall. "A new approach to wall modeling in LES of incompressible flow via function enrichment". In: *Journal of Computational Physics* 316 (2016), pp. 94–116. ISSN: 0021-9991. DOI: 10.1016/j.jcp.2016.04.001 (cit. on p. 35).

[139] Benjamin Krank, Martin Kronbichler, and Wolfgang A Wall. "Wall modeling via function enrichment within a high-order DG method for RANS simulations of incompressible flow". In: *International Journal for Numerical Methods in Fluids* 86.1 (Jan. 2018), pp. 107–129. ISSN: 02712091. DOI: 10.1002/fld.4409 (cit. on p. 35).

[140] Scott Morton, David McDaniel, David Sears, Brett Tillman, and Todd Tuckey. "Kestrel: A Fixed Wing Virtual Aircraft Product of the CREATE Program". In: *47th AIAA Aerospace Sciences Meeting including The New Horizons Forum and Aerospace Exposition*. Reston, Virginia: American Institute of Aeronautics and Astronautics, Jan. 2009. ISBN: 978-1-60086-973-0. DOI: 10.2514/6.2009-338 (cit. on p. 36).

[141] Scott A. Morton. "Kestrel Current Capabilities and Future Direction for Fixed Wing Aircraft Simulations". In: *53rd AIAA Aerospace Sciences Meeting*. Reston, Virginia: American Institute of Aeronautics and Astronautics, Jan. 2015. ISBN: 978-1-62410-343-8. DOI: 10.2514/6.2015-0039 (cit. on p. 36).

[142] Timothy A. Eymann, Robert H. Nichols, Todd Tuckey, and David R. McDaniel. "Cartesian Adaptive Mesh Refinement with the HPCMP CREATE™-AV Kestrel Solver". In: *53rd AIAA Aerospace Sciences Meeting*. Reston, Virginia: American Institute of Aeronautics and Astronautics, Jan. 2015. ISBN: 978-1-62410-343-8. DOI: 10.2514/6.2015-0040 (cit. on p. 36).

[143] Scott A. Morton and Robert E. Meakin. "HPCMP CREATE-AV Kestrel Architecture, Capabilities, and Long Term Plan for Fixed-Wing Aircraft Simulations". In: *54th AIAA Aerospace Sciences Meeting*. Reston, Virginia: American Institute of Aeronautics and Astronautics, Jan. 2016. ISBN: 978-1-62410-393-3. DOI: 10.2514/6.2016-0565 (cit. on p. 36).

[144] David R. McDaniel, Robert H. Nichols, Timothy A. Eymann, Robert E. Starr, and Scott A. Morton. "Accuracy and Performance Improvements to Kestrel's Near-Body Flow Solver". In: *54th AIAA Aerospace Sciences Meeting*. Reston, Virginia: American Institute of Aeronautics and Astronautics, Jan. 2016. ISBN: 978-1-62410-393-3. DOI: 10.2514/6.2016-1051 (cit. on p. 36).

[145] Ryan S. Glasby and Jon Taylor Erwin. "Introduction to COFFE: The Next-Generation HPCMP CREATE TM -AV CFD Solver". In: *54th AIAA Aerospace Sciences Meeting*. Reston, Virginia: American Institute of Aeronautics and Astronautics, Jan. 2016. ISBN: 978-1-62410-393-3. DOI: 10.2514/6.2016-0567 (cit. on pp. 36, 38, 176, 177).

[146] Benjamin P. Hallissy, Ryan S. Glasby, and Jon T. Erwin. "Comparison Between HPCMP CREATE TM -AV COFFE and Kestrel for Two and Three-Dimensional Turbulent Flow Cases". In: *54th AIAA Aerospace Sciences Meeting*. Reston, Virginia: American Institute of Aeronautics and Astronautics, Jan. 2016. ISBN: 978-1-62410-393-3. DOI: 10.2514/6.2016-1054 (cit. on p. 36).

[147] J. Taylor Erwin, Ryan S. Glasby, Douglas L. Stefanski, and Robert H. Nichols. "Application of HPCMP CREATE-AV COFFE for Three-Dimensional Turbulent Flow Cases". In: *54th AIAA Aerospace Sciences Meeting*. Reston, Virginia: American Institute of Aeronautics and Astronautics, Jan. 2016. ISBN: 978-1-62410-393-3. DOI: 10.2514/6.2016-1361 (cit. on p. 36).

[148] Youcef Saad and Martin H. Schultz. "GMRES: A Generalized Minimal Residual Algorithm for Solving Nonsymmetric Linear Systems". In: *SIAM Journal on Scientific and Statistical Computing* 7.3 (1986), pp. 856–869. ISSN: 0196-5204. DOI: 10.1137/0907058 (cit. on p. 38).

[149] C. F. Curtiss and J. O. Hirschfelder. "Integration of Stiff Equations". In: *Proceedings of the National Academy of Sciences* 38.3 (1952), pp. 235–243. ISSN: 0027-8424. DOI: 10.1073/pnas.38.3.235 (cit. on p. 39).

[150] C W Gear. *Numerical initial value problems in ordinary differential equations*. Prentice-Hall series in automatic computation. Prentice-Hall, 1971 (cit. on p. 39).

[151] Veer Vatsa, Mark Carpenter, and David Lockard. "Re-evaluation of an Optimized Second Order Backward Difference (BDF2OPT) Scheme for Unsteady Flow Applications". In: *48th AIAA Aerospace Sciences Meeting Including the New Horizons Forum and Aerospace Exposition*. Reston, Virginia: American Institute of Aeronautics and

Astronautics, Jan. 2010. ISBN: 978-1-60086-959-4. DOI: 10.2514/6.2010-122 (cit. on pp. 41, 42).

[152] Christopher A Kennedy and Mark H Carpenter. *Diagonally Implicit Runge-Kutta Methods for Ordinary Differential Equations. A Review*. Tech. rep. March. NASA TM-2016-219173, 2016, pp. 2016–219173 (cit. on p. 43).

[153] Roger Alexander. "Diagonally Implicit Runge-Kutta Methods for Stiff O.D.E.'s". In: *SIAM Journal on Numerical Analysis* 14.6 (Dec. 1977), pp. 1006–1021. ISSN: 0036-1429. DOI: 10.1137/0714068 (cit. on p. 43).

[154] Per-Olof Persson. "High-Order LES Simulations using Implicit-Explicit Runge-Kutta Schemes". In: *49th AIAA Aerospace Sciences Meeting including the New Horizons Forum and Aerospace Exposition*. Reston, Virginia: American Institute of Aeronautics and Astronautics, Jan. 2011. ISBN: 978-1-60086-950-1. DOI: 10.2514/6.2011-684 (cit. on p. 43).

[155] P. Moin. *Fundamentals of Engineering Numerical Analysis*. Cambridge University Press, 2010. ISBN: 9780521711234 (cit. on p. 44).

[156] Ralph Menikoff. "Errors when Shock Waves Interact due to Numerical Shock Width". In: *SIAM J. ScI. COMPUT* 15.5 (Sept. 1994), pp. 1227–1242. ISSN: 1064-8275. DOI: 10.1137/0915075 (cit. on p. 48).

[157] Weizhang Huang. "Metric tensors for anisotropic mesh generation". In: *Journal of Computational Physics* 204.2 (2005), pp. 633–665. ISSN: 00219991. DOI: 10.1016/j.jcp.2004.10.024 (cit. on p. 50).

[158] K.-F. Tchon, F. Guibault, J. Dompierre, and R. Camarero. "Adaptive hybrid meshing using metric tensor line networks". In: *17th AIAA Computational Fluid Dynamics Conference* June (2005). DOI: 10.2514/6.2005-5332 (cit. on p. 50).

[159] Masayuki Yano and David L. Darmofal. "An optimization-based framework for anisotropic simplex mesh adaptation". In: *Journal of Computational Physics* 231.22 (2012), pp. 7626–7649. ISSN: 00219991. DOI: 10.1016/j.jcp.2012.06.040 (cit. on p. 50).

[160] D. Marcum and F. Alauzet. "3D Metric-aligned and orthogonal solution adaptive mesh generation". In: *Procedia Engineering* 203 (2017), pp. 78–90. ISSN: 18777058. DOI: 10.1016/j.proeng.2017.09.790 (cit. on p. 50).

[161] Paul Woodward and Phillip Colella. "The numerical simulation of two-dimensional fluid flow with strong shocks". In: *Journal of Computational Physics* 54.1 (1984), pp. 115–173. ISSN: 10902716. DOI: 10.1016/0021-9991(84)90142-6 (cit. on pp. 51, 53, 54, 83, 100, 111).

[162] H C Yee, N D Sandham, and M J Djomehri. "Low-Dissipative High-Order Shock-Capturing Methods Using Characteristic-Based Filters 1". In: *Journal of Computational Physics* 150.May 1998 (1999), pp. 199–238 (cit. on pp. 55, 56).

[163] Li Wang and Dimitri J. Mavriplis. "Implicit solution of the unsteady Euler equations for high-order accurate discontinuous Galerkin discretizations". In: *Journal of Computational Physics* 225.2 (2007), pp. 1994–2015. ISSN: 00219991. DOI: 10.1016/j.jcp.2007.03.002 (cit. on pp. 55, 58).

[164] Seth C. Spiegel, HT Huynh, and James R. DeBonis. "A Survey of the Isentropic Euler Vortex Problem using High-Order Methods". In: *22nd AIAA Computational Fluid Dynamics Conference*. Reston, Virginia: American Institute of Aeronautics and Astronautics, June 2015. ISBN: 978-1-62410-366-7. DOI: 10.2514/6.2015-2444 (cit. on p. 55).

[165] M. M. Zdravkovich. *Flow Around Circular Cylinders*. Flow Around Circular Cylinders: A Comprehensive Guide Through Flow Phenomena, Experiments, Applications, Mathematical Models, and Computer Simulations. OUP Oxford, 1997. ISBN: 0198563965 (cit. on p. 64).

[166] R. Mittal and S. Balachandar. "Effect of three-dimensionality on the lift and drag of nominally two-dimensional cylinders". In: *Physics of Fluids* 7.8 (Aug. 1995), pp. 1841–1865. ISSN: 10706631. DOI: 10.1063/1.868500 (cit. on pp. 65, 70, 72).

[167] Ronald D. Henderson. "Nonlinear dynamics and pattern formation in turbulent wake transition". In: *Journal of Fluid Mechanics* 352 (1997), S0022112097007465. ISSN: 00221120. DOI: 10.1017/S0022112097007465 (cit. on pp. 65, 70, 82).

[168] C. H. K. Williamson and G. L. Brown. "A Series in 1/sqrt(Re) to Represent the Strouhal-Reynolds Number Relationship of the Cylinder Wake". In: *Journal of Fluids and Structures* 12.8 (Nov. 1998), pp. 1073–1085. ISSN: 08899746. DOI: 10.1006/jfls.1998.0184 (cit. on p. 65).

[169] B. N. Rajani, A. Kandasamy, and Sekhar Majumdar. "Numerical simulation of laminar flow past a circular cylinder". In: *Applied Mathematical Modelling* 33.3 (2009), pp. 1228–1247. ISSN: 0307904X. DOI: 10.1016/j.apm.2008.01.017 (cit. on pp. 70, 72, 82).

[170] C. H. K. Williamson. "The natural and forced formation of spot-like 'vortex dislocations' in the transition of a wake". In: *Journal of Fluid Mechanics* 243.-1 (Oct. 1992), p. 393. ISSN: 0022-1120. DOI: 10.1017/S0022112092002763 (cit. on pp. 70, 82).

[171] C. H. K. Williamson. "Vortex Dynamics in the Cylinder Wake". In: *Annual Review of Fluid Mechanics* 28.1 (Jan. 1996), pp. 477–539. ISSN: 0066-4189. DOI: 10.1146/annurev.fl.28.010196.002401 (cit. on pp. 70, 72).

[172] R. Mittalt and S. Balachandar. "on the Inclusion of Three-Dimensional Effects in Simulations of Two-Dimensional Bluff-Body Wake Flows". In: *The 1997 ASME Fluids Engineering Divison Summer Meeting FEDSM´97* (1997), pp. 1–9 (cit. on p. 70).

[173] C. Norberg. "Flow around a circular cylinder: Aspects of fluctuating lift". In: *Journal of Fluids and Structures* 15.3-4 (Apr. 2001), pp. 459–469. ISSN: 08899746. DOI: 10.1006/jfls.2000.0367 (cit. on p. 72).

[174] C. Wieselsberger. *New data on the laws of fluid resistance*. Tech. rep. NACA-TN-84, 1922 (cit. on p. 72).

[175] G. I. Taylor and A. E. Green. "Mechanism of the Production of Small Eddies from Large Ones". In: *Proceedings of the Royal Society A: Mathematical, Physical and Engineering Sciences* 158.895 (1937), pp. 499–521. ISSN: 1364-5021. DOI: 10.1098/rspa.1937.0036 (cit. on p. 72).

[176] Harold L. Atkins. "Simulations of Compressible Taylor-Green Flow by a Discontinuous Galerkin Method". In: *46th AIAA Fluid Dynamics Conference*. Reston, Virginia: American Institute of Aeronautics and Astronautics, June 2016. ISBN: 978-1-62410-436-7. DOI: 10.2514/6.2016-3330 (cit. on p. 73).

[177] J. C. R. Hunt, A. A. Wray, and P. Moin. "Eddies, streams, and convergence zones in turbulent flows". In: *Studying Turbulence Using Numerical Simulation Databases, 2. Proceedings of the 1988 Summer Program* 1.1970 (1988), pp. 193–208. DOI: CTR-S88 (cit. on p. 73).

[178] Wim M. van Rees, Anthony Leonard, D. I. Pullin, and Petros Koumoutsakos. "A comparison of vortex and pseudo-spectral methods for the simulation of periodic vortical flows at high Reynolds numbers". In: *Journal of Computational Physics* 230.8 (2011), pp. 2794–2805. ISSN: 00219991. DOI: 10.1016/j.jcp.2010.11.031 (cit. on pp. 74, 76–79, 82, 111).

[179] Georges-henri Cottet, Bertrand Michaux, and Sepand Ossia. "A Comparison of Spectral and Vortex Methods in Three-Dimensional Incompressible Flows". In: 712 (2002), pp. 702–712. DOI: 10.1006/jcph.2001.6963 (cit. on p. 74).

[180] Stephen B. Pope. *Turbulent Flows*. Vol. V. 1. Cambridge University Press, 2000, p. 771. ISBN: 0521598869. DOI: 10.1179/030801801679395 (cit. on p. 76).

[181] A. N. Kolmogorov. "The Local Structure of Turbulence in Incompressible Viscous Fluid for Very Large Reynolds Numbers". In: *Proceedings of the Royal Society A: Mathematical, Physical and Engineering Sciences* 434.1890 (2006), pp. 9–13. ISSN: 1364-5021. DOI: 10.1098/rspa.1991.0075 (cit. on p. 80).

[182] Robert H. Nichols and Pieter G. Buning. *User's Manual for OVERFLOW*. Tech. rep. 2010 (cit. on p. 84).

[183] Daniel W. Zaide and Philip L. Roe. "A Second-Order Finite Volume Method that Reduces Numerical Shockwave Anomalies in One Dimension". In: *21st AIAA Computational Fluid Dynamics Conference*. Reston, Virginia: American Institute of Aeronautics and Astronautics, June 2013. DOI: 10.2514/6.2013-2699 (cit. on p. 91).

[184] Ashley F. Emery. "An evaluation of several differencing methods for inviscid fluid flow problems". In: *Journal of Computational Physics* 2.3 (1968), pp. 306–331. ISSN: 10902716. DOI: 10.1016/0021-9991(68)90060-0 (cit. on p. 95).

[185] Phillip Colella and Paul R. Woodward. "The Piecewise Parabolic Method (PPM) for gas-dynamical simulations". In: *Journal of Computational Physics* 54.1 (1984), pp. 174–201. ISSN: 10902716. DOI: 10.1016/0021-9991(84)90143-8 (cit. on p. 95).

[186] Tyler R. Hendrickson, Anand Kartha, and Graham V. Candler. "An Improved Ducros Sensor for the Simulation of Compressible Flows with Shocks". In: *2018 Fluid Dynamics Conference* (2018). DOI: 10.2514/6.2018-3710 (cit. on pp. 95, 100).

[187] S. A. Isaev and D. A. Lysenko. "Testing of numerical methods, convective schemes, algorithms for approximation of flows, and grid structures by the example of a supersonic flow in a step-shaped channel with the use of the CFX and fluent packages". In: *Journal of Engineering Physics and Thermophysics* 82.2 (2009), pp. 321–326. ISSN: 10620125. DOI: 10.1007/s10891-009-0187-8 (cit. on p. 100).

[188] Jean Luc Guermond, Richard Pasquetti, and Bojan Popov. "Entropy viscosity method for nonlinear conservation laws". In: *Journal of Computational Physics* 230.11 (2011), pp. 4248–4267. ISSN: 00219991. DOI: 10.1016/j.jcp.2010.11.043 (cit. on p. 100).

[189] F. Daude, J. Berland, T. Emmert, P. Lafon, F. Crouzet, and C. Bailly. "A high-order finite-difference algorithm for direct computation of aerodynamic sound". In: *Computers and Fluids* 61 (2012), pp. 46–63. ISSN: 00457930. DOI: 10.1016/j.compfluid.2011.08.017 (cit. on p. 100).

[190] Matthias Sonntag and Claus Dieter Munz. "Efficient Parallelization of a Shock Capturing for Discontinuous Galerkin Methods using Finite Volume Sub-cells". In: *Journal of Scientific Computing* 70.3 (2017), pp. 1262–1289. ISSN: 08857474. DOI: 10.1007/s10915-016-0287-5 (cit. on p. 100).

[191] P. Dupont, C. Haddad, J. P. Ardissone, and J. F. Debiève. "Space and time organisation of a shock wave/turbulent boundary layer interaction". In: *Aerospace Science and Technology* 9.7 (Oct. 2005), pp. 561–572. ISSN: 12709638. DOI: 10.1016/j.ast.2004.12.009 (cit. on p. 146).

[192] S. Piponniau, J. P. Dussauge, J. F. Debiève, and Pierre Dupont. "A simple model for low-frequency unsteadiness in shock-induced separation". In: *Journal of Fluid Mechanics* 629 (June 2009), pp. 87–108. ISSN: 00221120. DOI: 10.1017/S0022112009006417 (cit. on p. 146).

[193] David S. Dolling and Mehmet E. Erengil. "Unsteady Wave Structure near Separation in a Mach 5 Compression Ramp Interation". In: *AIAA Journal* 29.5 (May 1991), pp. 728–735. ISSN: 0001-1452. DOI: 10.2514/3.10647 (cit. on p. 146).

[194] Minwei Wu and M. Pino Martin. "Direct Numerical Simulation of Supersonic Turbulent Boundary Layer over a Compression Ramp". In: *AIAA Journal* 45.4 (Apr. 2007), pp. 879–889. ISSN: 0001-1452. DOI: 10.2514/1.27021 (cit. on p. 146).

[195] Minwei Wu and M. Pino Martín. "Analysis of shock motion in shockwave and turbulent boundary layer interaction using direct numerical simulation data". In: *Journal of Fluid Mechanics* 594 (Dec. 2008), pp. 71–83. ISSN: 00221120. DOI: 10.1017/S0022112007009044 (cit. on p. 146).

[196] F. O. Thomas, C. M. Putnam, and H. C. Chu. "On the mechanism of unsteady shock oscillation in shock wave/turbulent boundary layer interactions". In: *Experiments in Fluids* 18.1-2 (Dec. 1994), pp. 69–81. ISSN: 07234864. DOI: 10.1007/BF00209362 (cit. on p. 146).

[197] Sergio Pirozzoli and Francesco Grasso. "Direct numerical simulation of impinging shock wave/turbulent boundary layer interaction at M=2.25". In: *Physics of Fluids* 18.6 (2006), p. 065113. ISSN: 10706631. DOI: 10.1063/1.2216989 (cit. on p. 146).

[198] Louis J. Souverein, Pierre Dupont, Jean-Francois Debiève, Bas W. Van Oudheusden, and Fulvio Scarano. "Effect of Interaction Strength on Unsteadiness in Shock-Wave-Induced Separations". In: *AIAA Journal* 48.7 (July 2010), pp. 1480–1493. ISSN: 0001-1452. DOI: 10.2514/1.J050093 (cit. on p. 146).

[199] Emile Touber and Neil D Sandham. "Oblique Shock Impinging on a Turbulent Boundary Layer : Low-Frequency Mechanisms". In: *38th Fluid Dynamics Conference and Exhibit*. Reston, Virginia: American Institute of Aeronautics and Astronautics, June 2008. ISBN: 9781563479427. DOI: 10.2514/6.2008-4170 (cit. on p. 146).

[200] Emile Touber and Neil D. Sandham. "Large-eddy simulation of low-frequency unsteadiness in a turbulent shock-induced separation bubble". In: *Theoretical and Computational Fluid Dynamics* 23.2 (May 2009), pp. 79–107. ISSN: 09354964. DOI: 10.1007/s00162-009-0103-z (cit. on p. 146).

[201] E. Garnier, N. Adams, and P. Sagaut. *Large Eddy Simulation for Compressible Flows*. 2009, p. 276. ISBN: 978-90-481-2818-1. DOI: 10.1007/978-90-481-2819-8 (cit. on pp. 146–148, 150).

[202] S. Ghosal and P. Moin. "The Basic Equations for the Large Eddy Simulation of Turbulent Flows in Complex Geometry". In: *Journal of Computational Physics* 118.1 (Apr. 1995), pp. 24–37. ISSN: 00219991. DOI: 10.1006/jcph.1995.1077 (cit. on p. 148).

[203] Pierre Sagaut. *Large Eddy Simulation for Incompressible Flows*. 2006, p. 575. ISBN: 3-540-26344-6. DOI: 10.1007/b137536 (cit. on p. 149).

[204] Massimo Germano, Ugo Piomelli, Parviz Moin, and William H. Cabot. "A dynamic subgrid-scale eddy viscosity model". In: *Physics of Fluids A* 3.7 (1991), pp. 1760–1765. ISSN: 08998213. DOI: 10.1063/1.857955 (cit. on p. 150).

[205] Alexandre Favre. "Turbulence: Space-time statistical properties and behavior in supersonic flows". In: *Physics of Fluids* 26.10 (1983), p. 2851. ISSN: 00319171. DOI: 10.1063/1.864049 (cit. on p. 150).

[206] M. Lesieur, Oliver Metais, and Pierre Comte. *Large-Eddy Simulations of Turbulence*. Cambridge University Press, 2005. ISBN: 9780521781244 (cit. on pp. 151, 152).

[207] Jay P. Boris. "On large eddy simulation using subgrid turbulence models Comment 1". In: *Whither Turbulence? Turbulence at the Crossroads*. Berlin, Heidelberg: Springer Berlin Heidelberg, 1990, pp. 344–353. ISBN: 978-3-540-52535-6. DOI: 10.1007/3-540-52535-1_53 (cit. on p. 153).

[208] Fernando F. Grinstein, Len G. Margolin, and William J. Rider. *Implicit Large Eddy Simulation*. Ed. by Fernando F. Grinstein, Len G. Margolin, and William J. Rider.

Cambridge: Cambridge University Press, 2007. ISBN: 9780511618604. DOI: 10.1017/CBO9780511618604 (cit. on p. 153).

[209] A. Uranga, P. O. Persson, M. Drela, and J. Peraire. "Implicit Large Eddy Simulation of transition to turbulence at low Reynolds numbers using a Discontinuous Galerkin method". In: *International Journal for Numerical Methods in Engineering* 87.1-5 (July 2011), pp. 232–261. ISSN: 00295981. DOI: 10.1002/nme.3036 (cit. on p. 153).

[210] Maigonis V. Krumins. *A Review of Sphere Drag Coefficients Applicable To Atmospheric Density Sensing*. Tech. rep. Naval Ordinance Laboratory, 1972 (cit. on p. 156).

[211] H. J. Kim and P. A. Durbin. "Observations of the frequencies in a sphere wake and of drag increase by acoustic excitation". In: *Physics of Fluids* 31.11 (1988), p. 3260. ISSN: 00319171. DOI: 10.1063/1.866937 (cit. on pp. 156, 159).

[212] H. Sakamoto and H. Haniu. "A Study on Vortex Shedding From Spheres in a Uniform Flow". In: *Journal of Fluids Engineering* 112.4 (1990), p. 386. ISSN: 00982202. DOI: 10.1115/1.2909415 (cit. on pp. 157, 168).

[213] Giwoong Yun, Dongjoo Kim, and Haecheon Choi. "Vortical structures behind a sphere at subcritical Reynolds numbers". In: *Physics of Fluids* 18.1 (2006). ISSN: 10706631. DOI: 10.1063/1.2166454 (cit. on pp. 158, 172).

[214] O. Reynolds. "On the Dynamical Theory of Incompressible Viscous Fluids and the Determination of the Criterion". In: *Philosophical Transactions of the Royal Society A: Mathematical, Physical and Engineering Sciences* 186.0 (Jan. 1895), pp. 123–164. ISSN: 1364-503X. DOI: 10.1098/rsta.1895.0004 (cit. on p. 173).

[215] H Tennekes and J L Lumley. *A First Course in Turbulence*. A First Course in Turbulence. Pe Men Book Company, 1972. ISBN: 9780262200196 (cit. on p. 173).

[216] Joseph Boussinesq. *Essai sur la théorie des eaux courantes*. Vol. 23. Mémoires présentés par divers savants à l'Académie des sciences de l'Institut national de France 1. Impr. nationale, 1877, p. 1 (cit. on p. 173).

[217] P. Spalart and S. Allmaras. "A one-equation turbulence model for aerodynamic flows". In: *30th Aerospace Sciences Meeting and Exhibit*. Reston, Virginia: American Institute of Aeronautics and Astronautics, Jan. 1992. ISBN: 0034-1223. DOI: 10.2514/6.1992-439 (cit. on pp. 174, 176, 177).

[218] Steven R. Allmaras, Forrester T. Johnson, and Philippe R. Spalart. "Modifications and clarifications for the implementation of the Spalart-Allmaras turbulence model". In: *Seventh International Conference on Computational Fluid Dynamics* ICCFD7-1902 (2012), pp. 1–11 (cit. on p. 174).

[219] Mortaza Mani, Deric Babcock, Chad Winkler, and Philippe Spalart. "Predictions of a Supersonic Turbulent Flow in a Square Duct". In: *51st AIAA Aerospace Sciences Meeting including the New Horizons Forum and Aerospace Exposition*. Reston, Virigina: American Institute of Aeronautics and Astronautics, Jan. 2013. ISBN: 978-1-62410-181-6. DOI: 10.2514/6.2013-860 (cit. on p. 175).

[220] Jon T. Erwin, Ryan S. Glasby, Douglas L. Stefanski, and Steve L. Karman. "Results from HPCMP CREATE TM -AV Kestrel Component COFFE for the 6th Drag Prediction Workshop Cases". In: *55th AIAA Aerospace Sciences Meeting* (2017). DOI: 10.2514/6.2017-0289 (cit. on p. 175).

[221] Mikhail L. Shur, Philippe R. Spalart, Mikhail Kh Strelets, and Andrey K. Travin. "A hybrid RANS-LES approach with delayed-DES and wall-modelled LES capabilities". In: *International Journal of Heat and Fluid Flow* 29.6 (2008), pp. 1638–1649. ISSN: 0142727X. DOI: 10.1016/j.ijheatfluidflow.2008.07.001 (cit. on pp. 176, 177).

[222] P. R. Spalart, S. Deck, M. L. Shur, K. D. Squires, M. Kh Strelets, and A. Travin. "A new version of detached-eddy simulation, resistant to ambiguous grid densities". In: *Theoretical and Computational Fluid Dynamics* 20.3 (2006), pp. 181–195. ISSN: 09354964. DOI: 10.1007/s00162-006-0015-0 (cit. on p. 177).

[223] M. Shur, P.R. Spalart, M. Strelets, and A. Travin. "Detached-eddy simulation of an airfoil at high angle of attack". In: *Engineering Turbulence Modelling and Experiments 4*. December. Elsevier, 1999, pp. 669–678. ISBN: 9780080433288. DOI: 10.1016/B978-008043328-8/50064-3 (cit. on p. 178).

[224] Elmar Achenbach. "Experiments on the flow past spheres at very high Reynolds numbers". In: *Journal of Fluid Mechanics* 54.3 (1972), pp. 565–575. ISSN: 14697645. DOI: 10.1017/S0022112072000874 (cit. on p. 178).

[225] Elmar Achenbach. "Vortex shedding from spheres". In: *Journal of Fluid Mechanics* 62.2 (Jan. 1974), pp. 209–221. ISSN: 14697645. DOI: 10.1017/S0022112074000644 (cit. on p. 178).

[226] David L. Bacon and Elliott G. Reid. *The resistance of spheres in wind tunnels and in air*. Tech. rep. NACA Report No. 185, 1924, p. 20. DOI: 10.1097/00152192-198911000-00004 (cit. on p. 178).

[227] Peter A. Gnoffo, William A. Wood, Bill Kleb, Stephen J. Alter, Jose Padilla, and Jeffery A. White. "Functional Equivalence Acceptance Testing of FUN3D for Entry, Descent, and Landing Applications". In: *21st AIAA Computational Fluid Dynamics Conference*. Reston, Virginia: American Institute of Aeronautics and Astronautics, June 2013. DOI: 10.2514/6.2013-2558 (cit. on pp. 184–187).

[228] Robert H. Nichols and Bonnie D. Heikkinen. "Validation of Implicit Algorithms for Unsteady Flows Including Moving and Deforming Grids". In: *Journal of Aircraft* 43.5 (2006), pp. 1341–1351. ISSN: 0021-8669. DOI: 10.2514/1.17111 (cit. on pp. 184, 187).

[229] Virginie Daru and Christian Tenaud. "Evaluation of TVD high resolution schemes for unsteady viscous shocked flows". In: *Computers & Fluids* 30.1 (Sept. 2000), pp. 89–113. ISSN: 00457930. DOI: 10.1016/S0045-7930(00)00006-2 (cit. on p. 184).

[230] Virginie Daru and Christian Tenaud. "Numerical simulation of the viscous shock tube problem by using a high resolution monotonicity-preserving scheme". In: *Computers and Fluids* 38.3 (2009), pp. 664–676. ISSN: 00457930. DOI: 10.1016/j.compfluid.2008.06.008 (cit. on p. 184).

[231] B. Sjögreen and H. C. Yee. "Grid convergence of high order methods for multiscale complex unsteady viscous compressible flows". In: *Journal of Computational Physics* 185.1 (2003), pp. 1–26. ISSN: 00219991. DOI: 10.1016/S0021-9991(02)00044-X (cit. on p. 184).

[232] Kyu Hong Kim and Chongam Kim. "Accurate, efficient and monotonic numerical methods for multi-dimensional compressible flows. Part II: Multi-dimensional limiting process". In: *Journal of Computational Physics* 208.2 (2005), pp. 570–615. ISSN: 00219991. DOI: 10.1016/j.jcp.2005.02.022 (cit. on p. 184).

Appendices

A Large Eddy Simulations

Large eddy simulations (LES) are CFD techniques by which perturbations in the calculated flow field at a scale smaller than Δx, which is associated with the grid spacing, are removed with a low-pass filter that is applied to the governing equations. The resulting filtered governing equations describe the flow field for eddies larger than the filter scale, and the contribution from the subgrid scales (SGS) is modeled. These techniques allow CFD practitioners to investigate time-resolved fluctuations of large eddies within a flow field. Large eddies in boundary layers and separation regions have been shown to be the driving force behind large-scale oscillations in SBLIs. [191–200]

The governing equations for LES flow modeling in COFFE are the compressible, filtered, Favre-averaged Navier-Stokes equations. The conservative form of the Navier-Stokes equations was presented in Eq. (3.1). Note that all equations in this section assume three spatial dimensions.

A.1 Low-pass Filtering Operation

In order to eliminate contributions from the subgrid scale, the Navier-Stokes equations are filtered using a low-pass filter. The filtering operation is the convolution of a field variable, ϕ, with a filtering kernel G. A spatial filtering operation[1] is shown in Eq. (A.1). Note that all variables with overbars represent filtered quantities.

$$\overline{\phi}(\boldsymbol{x}, t) = G * \phi(\boldsymbol{x}, t) = \int_{-\infty}^{\infty} \phi(\boldsymbol{r}, t) G(\boldsymbol{x} - \boldsymbol{r}) d\boldsymbol{r} \tag{A.1}$$

The field variable, ϕ, can be separated into filtered and SGS components, as shown in Eq. (A.2), where the prime denotes the SGS value.

$$\phi = \overline{\phi} + \phi' \tag{A.2}$$

[1] Currently no compressible LES formulations known by the authors employ temporal filtering. This is corroborated by Garnier, Adams, and Sagaut [201]

Table A.1: Filter kernels in physical space

Filter Type	Kernel, G
Top-hat	$G(x-r) = \begin{cases} \frac{1}{\Delta} & \lvert x-r \rvert \leq \frac{\Delta}{2} \\ 0 & \text{otherwise} \end{cases}$
Gaussian	$G(x-r) = \sqrt{\frac{\gamma}{\pi\Delta^2}} \cdot \exp\left(\frac{-\gamma(x-r)^2}{\Delta^2}\right)$, typically $\gamma = 6$
Sharp Cutoff	$G(x-r) = \frac{\sin(k_c(x-r))}{k_c(x-r)}$, where $k_c = \frac{\pi}{\Delta}$ is the cutoff frequency

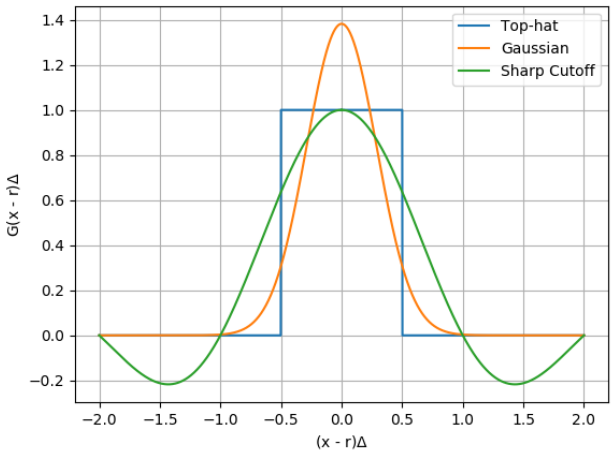

Figure A.1: Graphical depiction of filter kernels in physical space

Common Filter Types

Common filter types for LES formulations include the top-hat, Gaussian, and sharp cutoff filters. [201] The filter kernel for each in physical space is provided in Table A.1. Graphical depictions of the kernels in physical space are shown in Fig. A.1. The kernels in spectral space have been omitted because COFFE is not a spectral solver.

Filter Properties

Three filter and convolution properties are required in order to manipulate the filtered Navier-Stokes equations.

- The filter operation does not affect constant values because the integral from $-\infty$ to $+\infty$ of each of the filter kernels defined in the previous section is 1.

$$\int_{-\infty}^{\infty} G(\boldsymbol{r})d\boldsymbol{r} = 1 \quad \therefore \quad \overline{a} = a\int_{-\infty}^{\infty} G(\boldsymbol{r})d\boldsymbol{r} = a$$

- Convolution is distributive.

$$f * (g + h) = (f * g) + (f * h) \quad \therefore \quad \overline{\phi + \psi} = \overline{\phi} + \overline{\psi}$$

- Convolution commutes with differentiation.

$$f * g' = f' * g = (f * g)' \quad \therefore \quad \frac{\overline{\partial\phi}}{\partial x} = \frac{\partial\overline{\phi}}{\partial x}$$

This filter property *convolution commutes with differentiation* assumes that the filter width, Δ, is constant in all directions. When Δ increases in one direction, properties are "smeared" in that direction by an amount that increases with Δ due to a commutation error that is introduced. [202] The effect of this smearing is akin to the introduction of artificial diffusion. The computational grid serves as an implicit filter for a CFD solution, and stretching elements in the boundary layer is a common practice. This stretching changes the filter width in the surface-normal direction, which introduces a commutation error that has a similar effect or the simulation as the introduction of modeled eddy viscosity.

Following the lead of Garnier, Adams, and Sagaut [201], it is helpful at this point to define the commutator from Ring Theory. The commutator for two operators, f and g, acting on a field variable is shown in Eq. (A.3).

$$[f, g](\phi) = f(g(\phi)) - g(f(\phi)) \tag{A.3}$$

The commutator is useful in manipulating the filtered product of two field variables, $\overline{\phi\psi}$.[2] If we introduce the bilinear form, B, which is simply the multiplication operator when

[2] $\overline{\phi\psi}$ must be altered because $\bar{\phi}$ and $\bar{\psi}$ are variables of interest, not $\overline{\phi\psi}$.

applied to two scalar values, the commutator of the filtering and multiplication operators applied to the two field variables is,

$$[G*, B](\phi, \psi) = \overline{\phi\psi} - \bar{\phi}\bar{\psi}.$$

Rearranging this to solve for $\overline{\phi\psi}$ results in Eq. (A.4).

$$\overline{\phi\psi} = \bar{\phi}\bar{\psi} + [G*, B](\phi, \psi) \tag{A.4}$$

$[G*, B](\phi, \psi)$ is the error incurred from replacing $\overline{\phi\psi}$ with $\bar{\phi}\bar{\psi}$. This error accounts for SGS information and *must be modeled*.

Implicit and Explicit Filtering

Low-pass filters for the Navier-Stokes equations can be applied *implicitly* or *explicitly*. Implicit filtering occurs inherently when solving the Navier-Stokes equations on a finite grid. The finite spatial discretization links the filter width, Δ, of a top-hat filter to the grid spacing, h. This has the benefit of being easy to implement, since no additional filtering steps are necessary, and of maximizing the numerical grid resolution, since all of the grid points are used for spatial resolution of the flow field. The main drawback to implicit filtering is that, for most cases, the shape of the filter is not known because cell dimensions vary within grids for any useful application. [203]

Explicit filtering occurs when a filtering kernel (typically a top-hat or Gaussian) with $\Delta > h$ is applied directly to the numerical solution. The benefits to this approach are that it lowers numerical truncation error and the filter shape is well known. The drawbacks are that physical resolution of the solution is decreased in order to get these benefits because some of the degrees of freedom that would be increasing the physical resolution are now devoted to the application of the filter. Explicit filtering is typically quantified by the ratio of the filter width to the grid spacing, Δ/h. Numerical error in the simulation decreases as Δ/h increases; however, increasing this ratio by a factor of n increases the computational cost by n^4. [203]

In practice most filtering for non-academic applications is done implicitly due to its simplicity. Explicit filters are useful, however, when dynamically modeling the SGS terms, where the results from a test filter of size Δ are compared to the implicitly filtered results in order to determine the appropriate SGS model constants dynamically. [204]

A.2 Favre-averaging

Filtering the compressible continuity equation using simply the low-pass filter operation, given in Eqs. (A.1) and (A.2), results in an additional SGS term that would require modeling. To avoid this, Favre [205] introduced the density-weighted ensemble-averaging technique shown in Eq. (A.5). This results in a change in variables and eliminates the addition SGS term in the continuity equation. Note that all parameters with tildes represent Favre-averaged quantities.

$$\widetilde{\phi} = \frac{\overline{\rho\phi}}{\overline{\rho}} \implies \overline{\rho\phi} = \overline{\rho}\widetilde{\phi} \tag{A.5}$$

The filtered term that causes trouble in the continuity equation is shown in Eq. (A.6). Filtering ρu_j and then replacing $\overline{\rho u_j}$ with $\bar{\rho}\bar{u}_j$ introduces the additional SGS term $[G*, B](\rho, u_j)$, which has to be modeled. Using Favre-averaging $\overline{\rho u_j}$ can be directly replaced with $\overline{\rho}\widetilde{u}_j$.

$$\overline{\rho u_j} = \bar{\rho}\bar{u}_j + [G*, B](\rho, u_j) = \overline{\rho}\widetilde{u}_j \tag{A.6}$$

Garnier, Adams, and Sagaut [201] introduced the operator $H(a, b, c) = bc/a$. Using this operator and Favre-averaging, it is possible to decompose filtered parameters containing density and two other field variables, $\overline{\rho\phi\psi}$, as shown in Eq. (A.7). This is useful when manipulating the stress tensor in the momentum equation.

$$\overline{\rho\phi\psi} = \overline{\rho}\widetilde{\phi\psi} = \overline{\rho}\widetilde{\phi}\widetilde{\psi} + [G*, H](\rho, \rho\phi, \rho\psi) \tag{A.7}$$

A.3 Favre-averaged Filtered Navier-Stokes Equations

Continuity Equation

The continuity equation is given in Eq. (A.8). Favre-averaging allows the $\overline{\rho u_j}$ term that would normally arise from the filtering operation to be replaced with $\overline{\rho}\widetilde{u}_j$.

$$\frac{\partial \bar{\rho}}{\partial t} + \frac{\partial \bar{\rho}\widetilde{u}_j}{\partial x_j} = 0 \tag{A.8}$$

Energy Equation

Filtering and Favre-averaging the total energy definition, Eq. (3.7), results in Eq. (A.9).

$$\bar{\rho}\widetilde{e}_t = \frac{\overline{p}}{\gamma - 1} + \frac{1}{2}\bar{\rho}\widetilde{u_i u_i} \tag{A.9}$$

$\bar{\rho}\widetilde{u_i u_i}$ is not computable, and must be decomposed using Eq. (A.12). Lesieur, Metais, and Comte [206] introduces the following changes in variables for the filtered pressure and temperature, referred to as *macropressure* and *macrotemperature*.

$$\breve{p} = \overline{p} - \frac{1}{3}\mathcal{T}_{kk} \tag{A.10}$$

$$\breve{T} = \widetilde{T} - \frac{\mathcal{T}_{kk}}{2C_v\overline{\rho}} \tag{A.11}$$

$\mathcal{T}_{ij}$ is the SGS stress tensor after Favre-averaging and using the H operator from Eq. (A.7).

$$\mathcal{T}_{ij} = [G*, H](\rho, \rho u_i, \rho u_j) = \overline{\rho}\left(\widetilde{u_i u_j} - \widetilde{u}_i\widetilde{u}_j\right) \tag{A.12}$$

Lesieur, Metais, and Comte [206] splits the SGS stress tensor into isotropic and deviatoric parts, where the deviatoric part is referred to here as τ_{ij}^{SGS}.

$$\mathcal{T}_{ij} = \underbrace{\mathcal{T}_{ij} - \frac{1}{3}\mathcal{T}_{kk}\delta_{ij}}_{\tau_{ij}^{SGS}} + \frac{1}{3}\mathcal{T}_{kk}\delta_{ij} \tag{A.13}$$

The total energy definition, computed with $\breve{T}$, then becomes

$$\bar{\rho}\widetilde{e}_t = \bar{\rho}C_v\breve{T} + \frac{1}{2}\bar{\rho}\widetilde{u}_i\widetilde{u}_i, \tag{A.14}$$

and the equation of state becomes

$$\breve{p} = \bar{\rho}R\breve{T} + \frac{3\gamma - 5}{6}\mathcal{T}_{kk}. \tag{A.15}$$

The energy equation, with the change of variables from Lesieur, Metais, and Comte [206], is given in Eq. (A.16).

$$\frac{\partial\bar{\rho}\widetilde{e}_t}{\partial t} + \frac{\partial}{\partial x_j}\left[(\bar{\rho}\widetilde{e}_t + \breve{p})\widetilde{u}_j - \breve{q}_j^{SGS} - \widetilde{u}_i\widetilde{\tau}_{ij} - \breve{q}_j\right] = 0, \tag{A.16}$$

where $\breve{q}_j^{SGS}$ is the SGS heat flux. Eddy viscosity, ν_t, is used to model this term.

$$\breve{q}_j^{SGS} = (\bar{\rho}\widetilde{e}_t + \breve{p})\widetilde{u}_j - \overline{(\rho e_t + p)u_j} \simeq \bar{\rho}C_p\frac{\nu_t}{Pr_t}\frac{\partial\breve{T}}{\partial x_j} \tag{A.17}$$

Momentum Equation

Filtering and Favre-averaging the momentum equation, defined in Eqs. (3.1) to (3.4), results in Eq. (A.18).

$$\frac{\partial\bar{\rho}\widetilde{u}_j}{\partial t} + \frac{\partial}{\partial x_j}\left(\overline{\rho u_i u_j} + \bar{p}\delta_{ij} - \widetilde{\tau}_{ij}\right) = 0 \tag{A.18}$$

Introducing the SGS stress tensor from Eq. (A.13), $\mathcal{T}_{ij}$, yields Eq. (A.19).

$$\frac{\partial\bar{\rho}\widetilde{u}_j}{\partial t} + \frac{\partial}{\partial x_j}\left[\bar{\rho}\widetilde{u}_i\widetilde{u}_j + \underbrace{\left(\bar{p} - \frac{1}{3}\mathcal{T}_{kk}\right)}_{\breve{p}}\delta_{ij} - \widetilde{\tau}_{ij} - \underbrace{\left(\mathcal{T}_{ij} - \frac{1}{3}\mathcal{T}_{kk}\delta_{ij}\right)}_{\tau_{ij}^{SGS}}\right] = 0 \tag{A.19}$$

Eddy viscosity is used to model τ_{ij}^{SGS}.

$$\tau_{ij}^{SGS} \simeq \bar{\rho}\nu_t\widetilde{A}_{ij} \tag{A.20}$$

Combined Equations

The conservative form of the Favre-averaged, filtered Navier-Stokes equations are presented in Eq. (A.21).

$$\frac{\partial \overline{\boldsymbol{Q}}}{\partial t} + \frac{\partial}{\partial x_j}\left(\overline{\boldsymbol{F}}_c - \overline{\boldsymbol{F}}_v\right) = 0 \tag{A.21}$$

$\overline{\boldsymbol{Q}}$ contains the conservation variables, which are given in Eq. (A.22).

$$\overline{\boldsymbol{Q}} = \left\{ \begin{array}{c} \overline{\rho} \\ \overline{\rho}\widetilde{u}_j \\ \overline{\rho}\widetilde{e}_t \end{array} \right\} \tag{A.22}$$

$\overline{\boldsymbol{F}}_c$ and $\overline{\boldsymbol{F}}_v$ contain the convective and viscous fluxes.

$$\overline{\boldsymbol{F}}_c = \left\{ \begin{array}{c} \overline{\rho}\widetilde{u}_j \\ \overline{\rho}\widetilde{u}_i\widetilde{u}_j + \breve{p}\delta_{ij} \\ (\overline{\rho}\widetilde{e}_t + \breve{p})\widetilde{u}_j \end{array} \right\} \tag{A.23}$$

$$\overline{\boldsymbol{F}}_v = \left\{ \begin{array}{c} 0 \\ \widetilde{\tau}_{ij} + \tau_{ij}^{SGS} \\ \widetilde{u}_i\widetilde{\tau}_{ij} - (\breve{q}_j + \breve{q}_j^{SGS}) \end{array} \right\} \tag{A.24}$$

Implicit LES

Implicit LES (ILES) relies on the numerical dissipation inherent in a solution scheme and grid to act as a SGS model. This technique was introduced formally by Boris [207] as an alternative to explicit SGS schemes. There are no turbulence parameters to model, so this approach is clearly the easiest to implement. The rationale for employing ILES is described in great detail by Grinstein, Margolin, and Rider [208], and the method has been used by Uranga et al. [209] to predict laminar separation with a discontinuous Galerkin (DG) scheme.

A.4 Tandem Spheres

The tandem sphere test case was designed to appraise the accuracy and efficiency of a solver when applied to a complex, unsteady, multi-scale flow at low Mach and Reynolds numbers. The front sphere should feature a laminar separation and the back sphere a turbulent one, due to being in the wake of the first sphere.

The flow conditions and grids were supplied by the AIAA Fifth International Workshop on High-Order Methods in Computational Fluid Dynamics. Free stream conditions were a uniform inflow with $Re_D = 3,900$ and $M_\infty = 0.1$. Free stream values for temperature and density were $T_\infty = 300\ K$ and $\rho_\infty = 1.225\ kg/m^3$. The fluid is a perfect gas with $\gamma = 1.4$ and $Pr = 0.72$.

The geometry was simply two spheres with diameter D that were separated by $10D$. The sphere surfaces were set to an adiabatic, no-slip wall boundary condition. The grid was provided by Steve Karman of Pointwise®. It is available on the High-Order Workshop website[3], and the particular grid that was used was named "TandemSpheresTetMesh4P2.cgns". It consisted of 6.94 million $p = 2$ tetrahedral elements with 9.25 million nodes. The case was run using the SDIRK4 time-integration method [102] with a time step of 0.01. Pictures of the interaction region in the grid, the off-body grid, and the surface grid are shown in Fig. A.2.

The High-Order Workshop test case description provided computations to make with the simulation results. These included integral values of lift and drag coefficients, mean and RMS values of parameters, including Reynolds stresses, along specified lines, and frequency spectra at specified points for $t^* \in [100, 200]$, where $t^* = tU_\infty/L$. The lines and points of interest are shown in Fig. A.3. The locations of the lines and points are as follows, note the origin is in the center of the front sphere:

- Surface lines on $x-y$, $x-z$, and $y-z$ planes passing through the center of each sphere,
- Streamwise lines along centerline ($y = z = 0$) for $x \in [-5.5D, -0.5D]$, $[0.5D, 9.5D]$, and $[10.5D, 15.5D]$,

[3] https://how5.cenaero.be/content/cs1-tandem-spheres-re3900

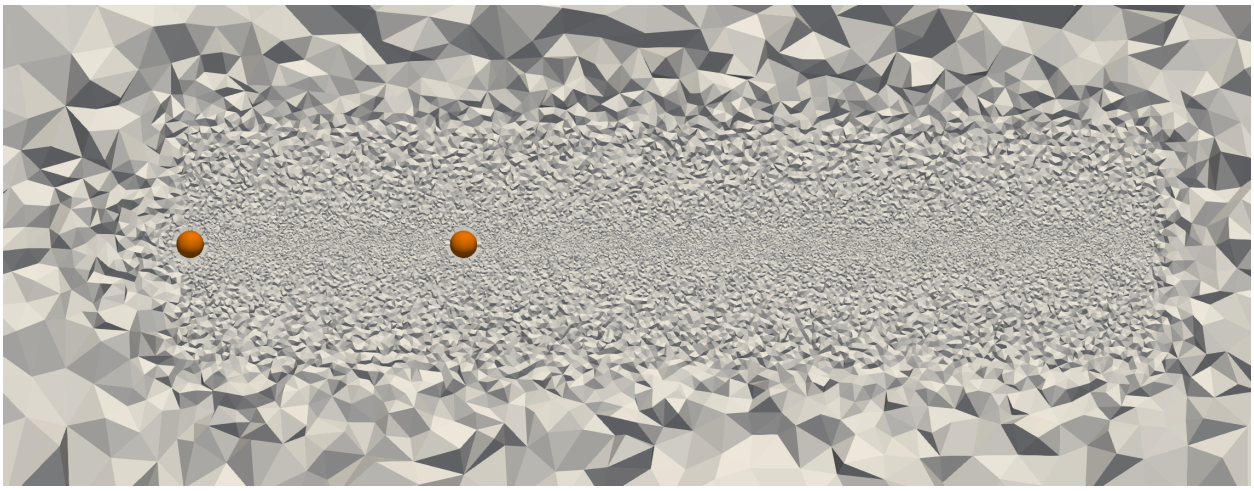

(a) Interaction region grid

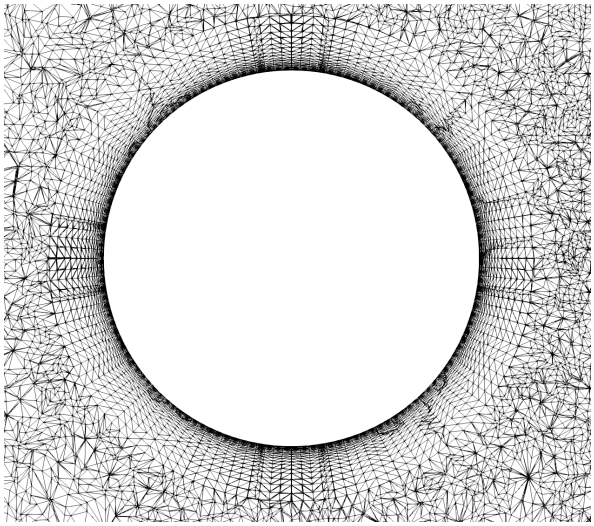

(b) Sphere off-body grid

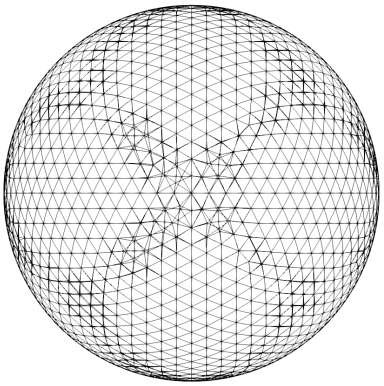

(c) Sphere surface grid

Figure A.2: Tandem sphere grid ("TandemSpheresTetMesh4P2.cgns") provided by Steve Karman of Pointwise

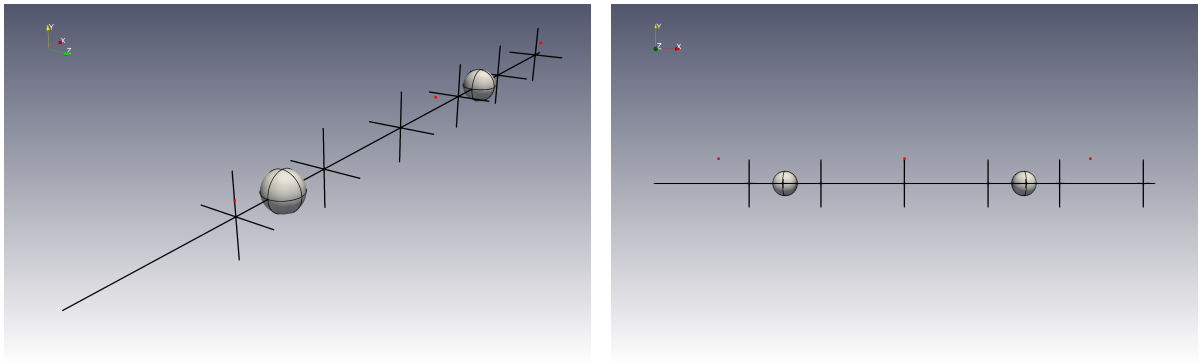

(a) Isometric view **(b)** Side view

Figure A.3: Data sampling locations (black lines and red points) for tandem sphere case.

Table A.2: Mean and RMS values of lift and drag coefficient on front and back spheres.

	Lift		Drag	
Sphere	Mean	RMS	Mean	RMS
Front	-0.00422	0.00732	0.387	0.387
Back	0.0110	0.0452	0.409	0.410

- y and z-transverse lines on $y, z \in [-D, D]$, respectively, at $x = -1.5D$, $1.5D$, $5D$, $8.5D$, $11.5D$, $15D$,
- Point 1, 2, and 3 at $x = -2.5D$, $5D$, and $12.5D$, respectively, with $y = z = D$.

Mean and RMS values of the lift and drag coefficients for the front and back spheres are given in Table A.2. The values of the lift and drag coefficients over time are shown in Fig. A.4, and the frequency spectra are presented in Fig. A.5. Based on the available experimental drag data, Krumins [210] recommended a C_D of 0.388 for $M_\infty = 0.1$ and $Re = 4,000$, which is excellent agreement with the current results.

Mean values of the surface pressure coefficient along on $x - y$, $x - z$, and $y - z$ planes passing through the center of each sphere are shown in Fig. A.6. The front sphere C_P results were in agreement with experimental results from Kim and Durbin [211] at $Re = 4,200$.

Mean values of u, v, and w velocity components along the centerline are shown in Fig. A.7, and RMS values are given in Fig. A.8. Mean values of the u velocity components along the transverse lines are displayed in Fig. A.9, and mean values of the v and w velocity components parallel and normal to the transverse lines are shown in Figs. A.10 and A.11, respectively.

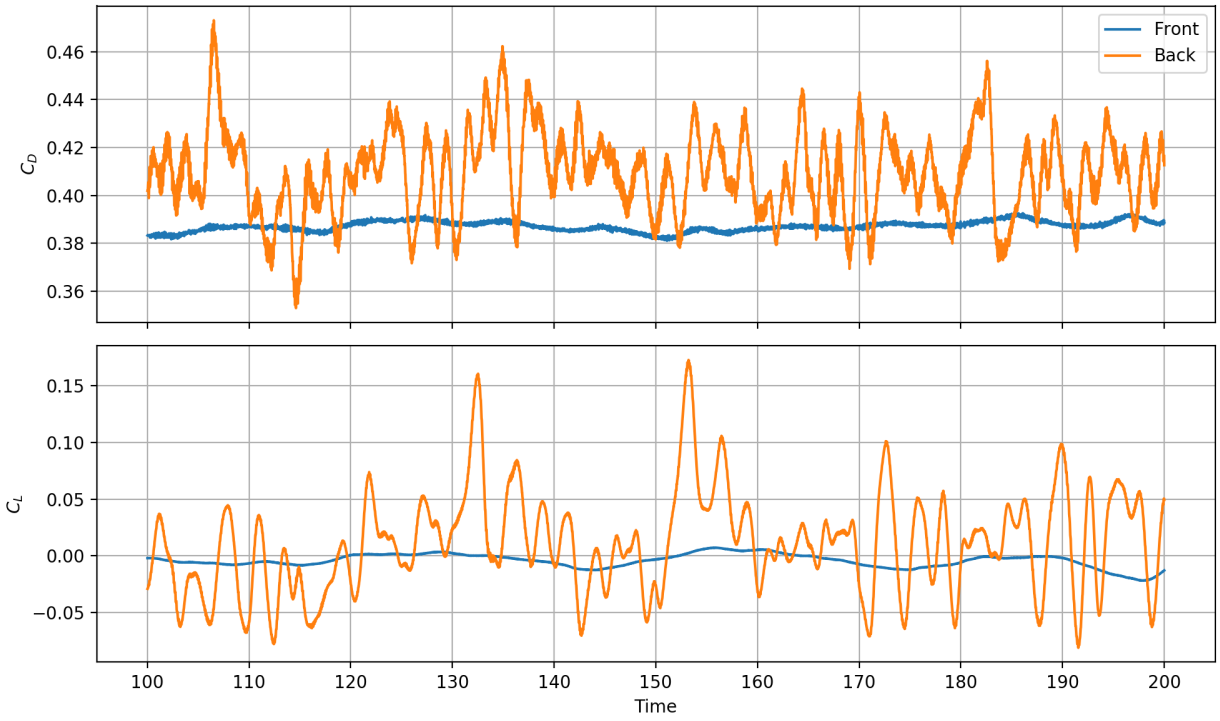

Figure A.4: Lift and drag coefficients on the front and back spheres at $Re = 3,900$ and $M_\infty = 0.1$ for $100 < t^* < 200$.

RMS values for the u, v, and w velocity components along the transverse lines are shown in Figs. A.12 to A.14.

Mean values of Reynolds stresses along the centerline are shown in Fig. A.15. Mean values of the normal Reynolds stress components along the transverse lines are displayed in Fig. A.16, and shear values are given in Fig. A.17.

Frequency spectra of the velocity magnitude, pressure coefficient, and turbulent kinetic energy at the point locations are shown in Figs. A.18 to A.20, respectively. Point 2 was close to the location where Sakamoto and Haniu [212] acquired hot wire measurements from spheres in uniform flow at various Reynolds numbers. A velocity magnitude peak for Point 2 occurred at $St = 0.24$. This point is plotted with data from Sakamoto and Haniu in Fig. A.21.

Instantaneous and mean contours of density, vorticity magnitude, and velocity magnitude on an $x - y$ slice are shown in Figs. A.22 to A.24. The instantaneous values are taken at $t^* = 150$. Instantaneous contours of Q-criterion colored by temperature are shown in Fig. A.25.

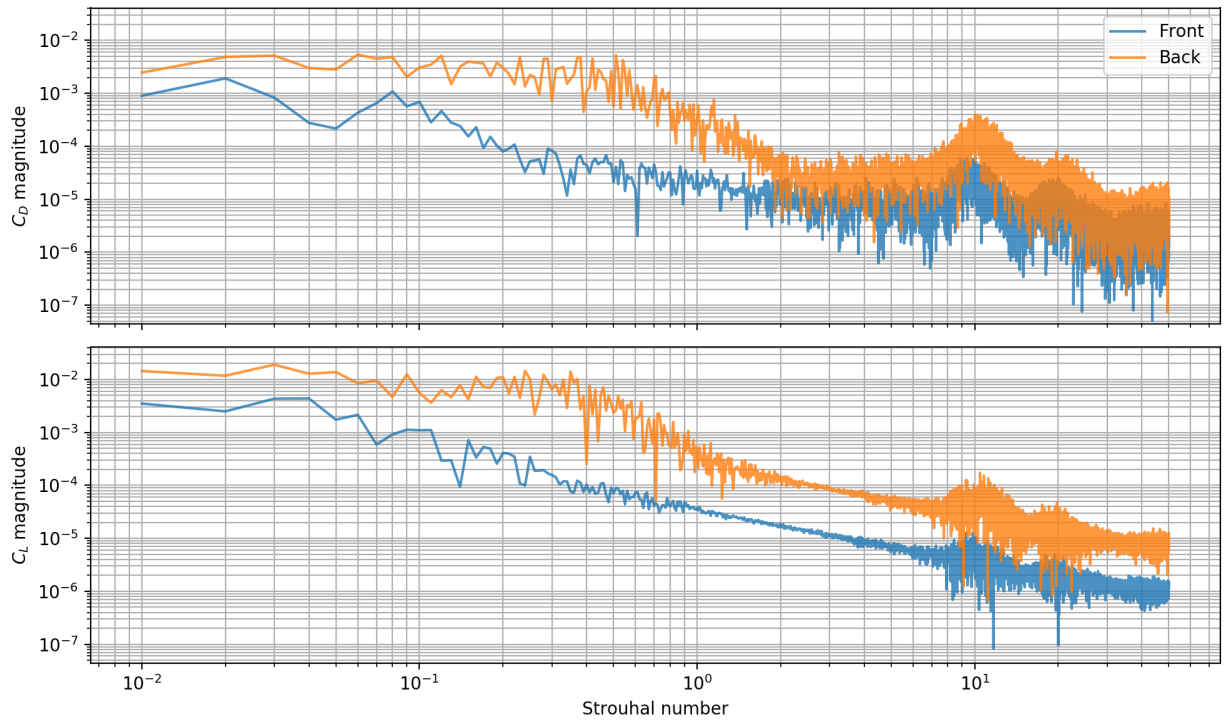

Figure A.5: Frequency spectra of lift and drag coefficients on the front and back spheres at $Re = 3,900$ and $M_\infty = 0.1$ for $100 < t^* < 200$.

A comparison of instantaneous contours of vorticity between the current results and results from Yun, Kim, and Choi [213] is shown in Fig. A.26. The extent of the separation region and the flow structures are qualitatively similar between the two cases.

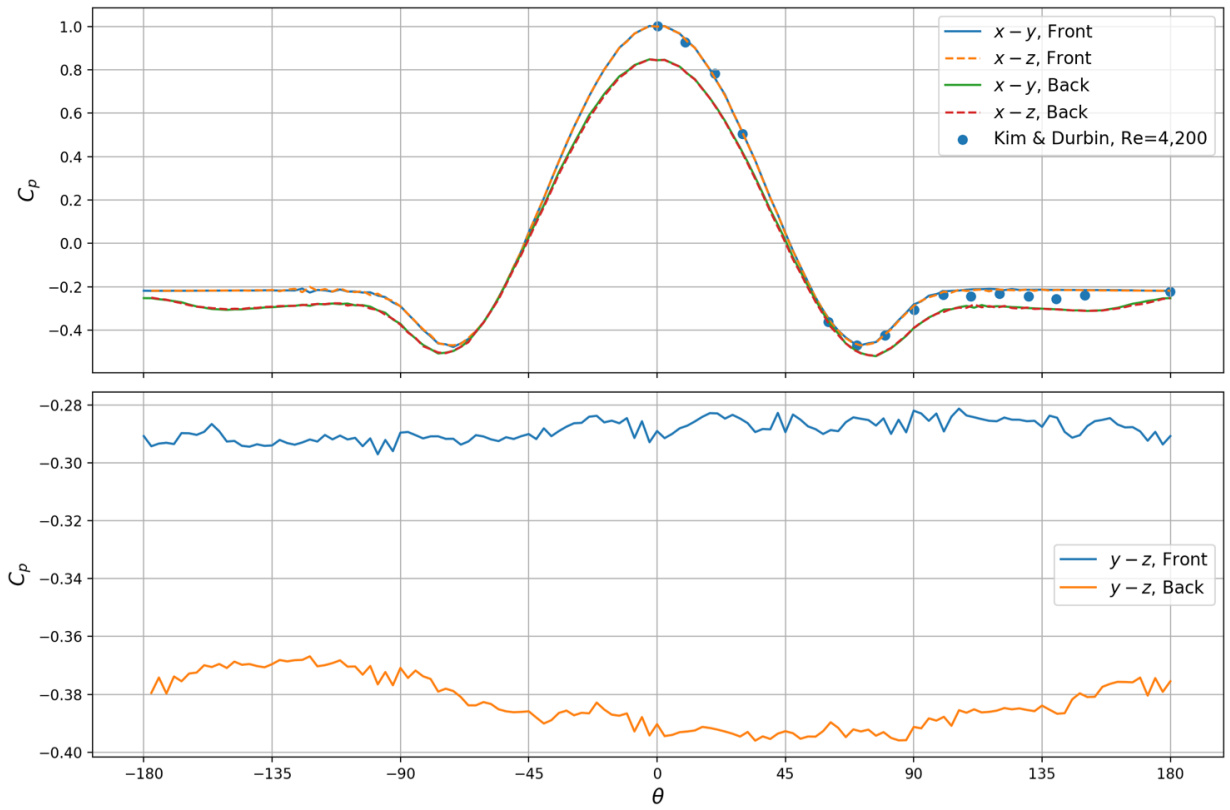

Figure A.6: Mean values of surface pressure coefficient on $x-y$, $x-z$, and $y-z$ planes passing through the center of each sphere of the tandem spheres case, with experimental results from Kim and Durbin [211] for $Re = 4,200$.

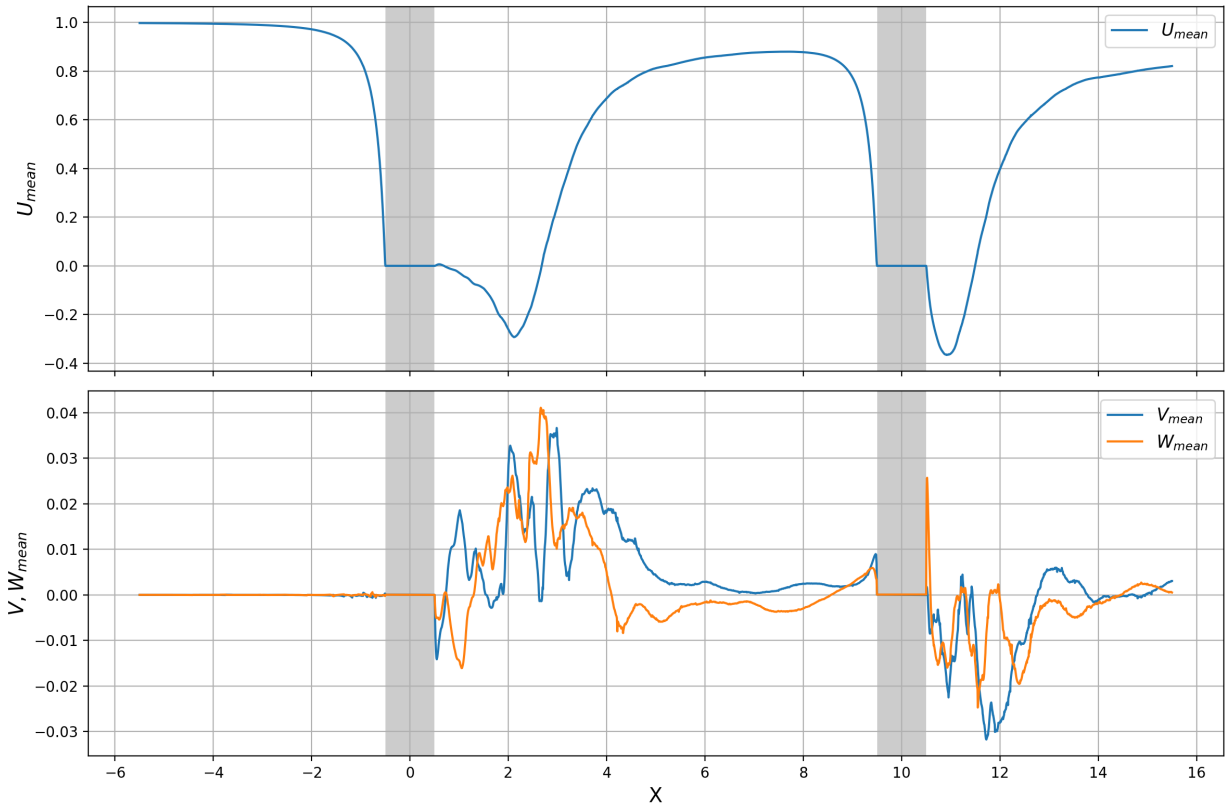

Figure A.7: Mean values of u, v, and w velocity components along centerline of the tandem spheres case.

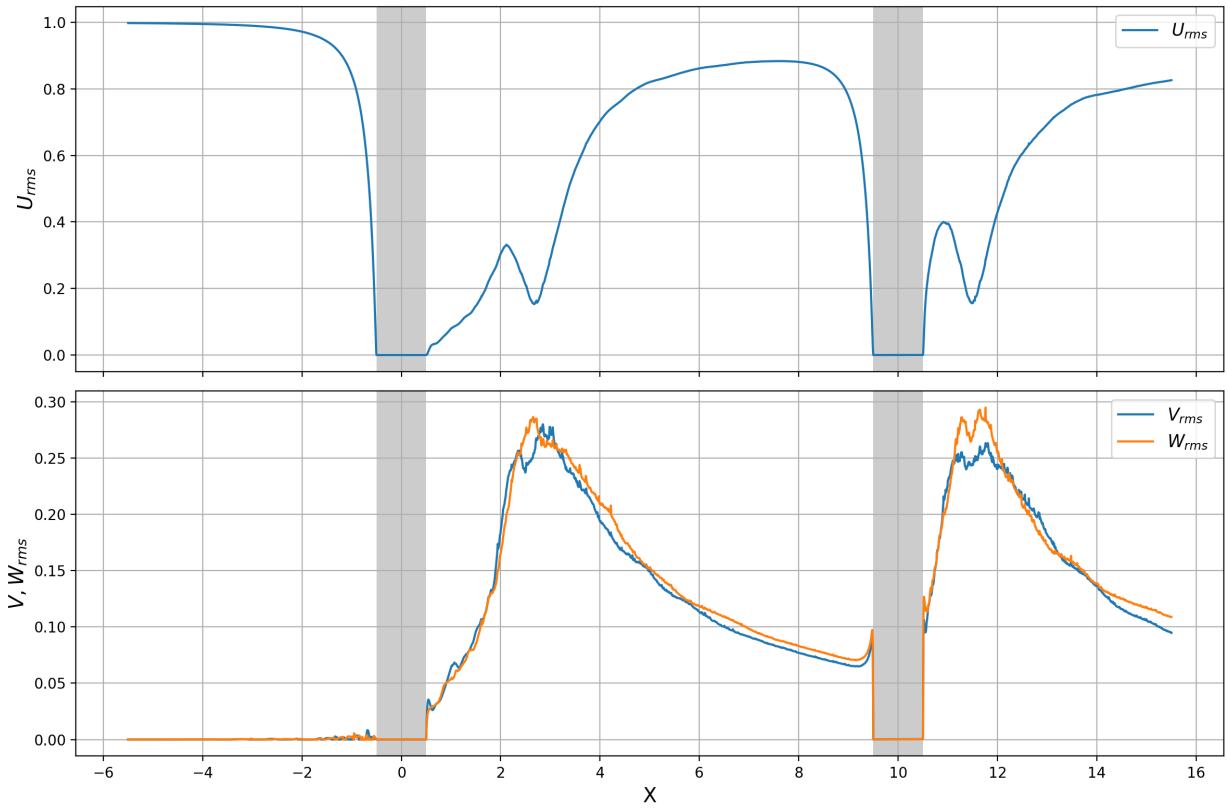

Figure A.8: RMS values of u, v, and w velocity components along centerline of the tandem spheres case.

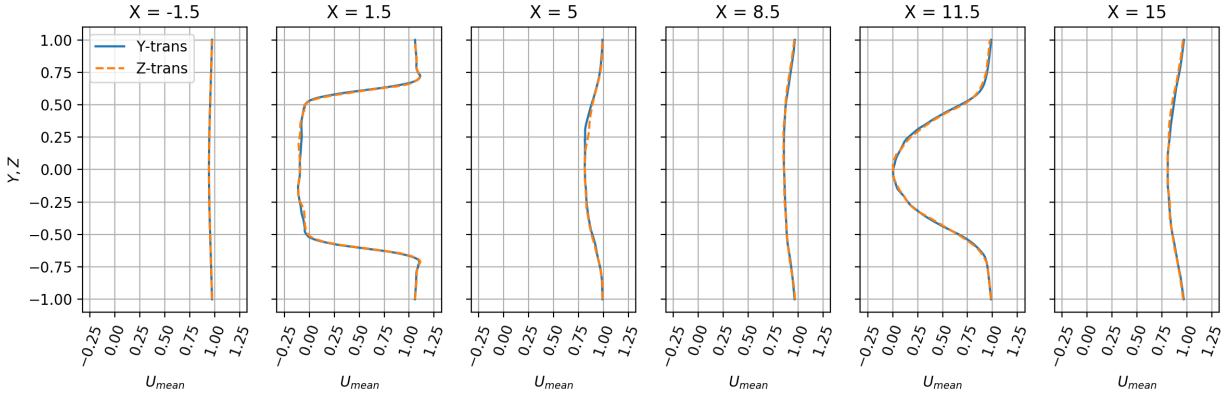

Figure A.9: Mean values of u velocity component along y and z transverse lines of the tandem spheres case.

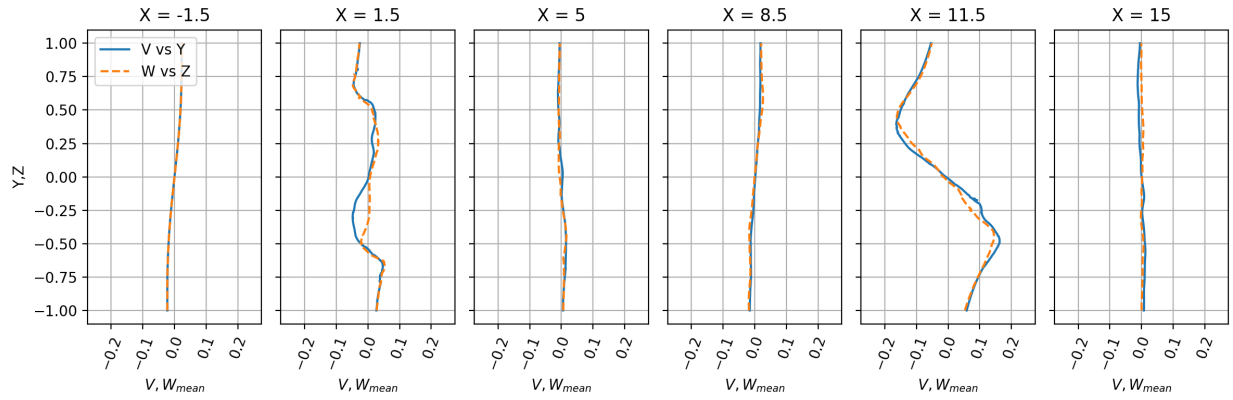

Figure A.10: Mean values of v and w velocity components parallel to y and z transverse lines of the tandem spheres case.

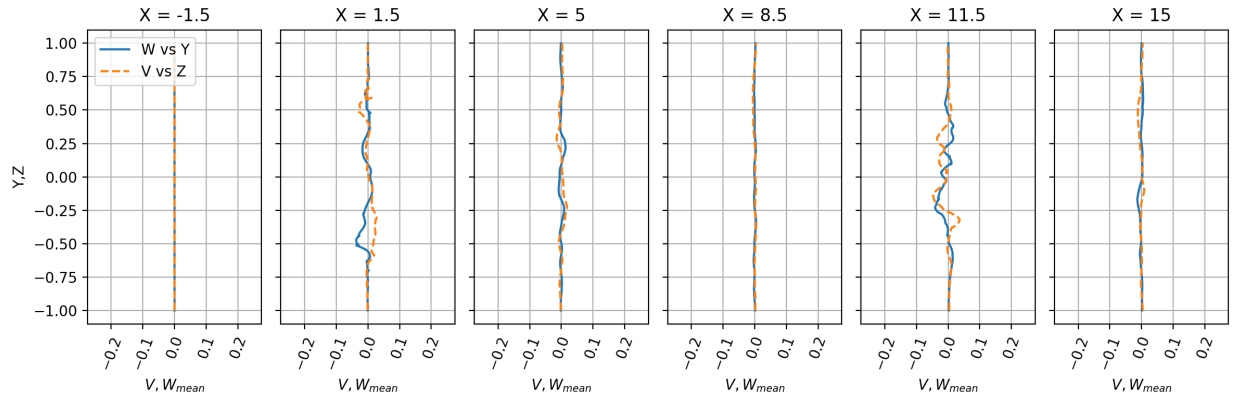

Figure A.11: Mean values of v and w velocity components normal to y and z transverse lines of the tandem spheres case.

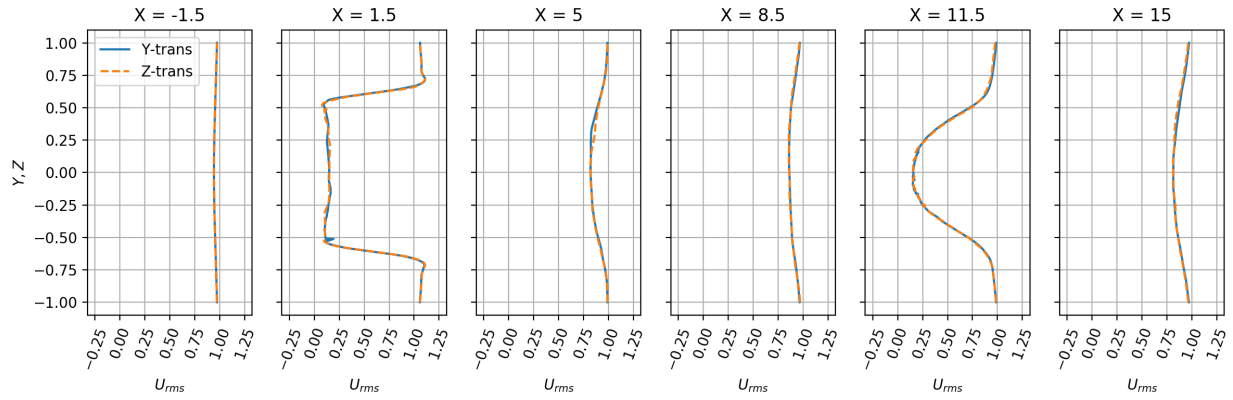

Figure A.12: RMS values of u velocity component along y and z transverse lines of the tandem spheres case.

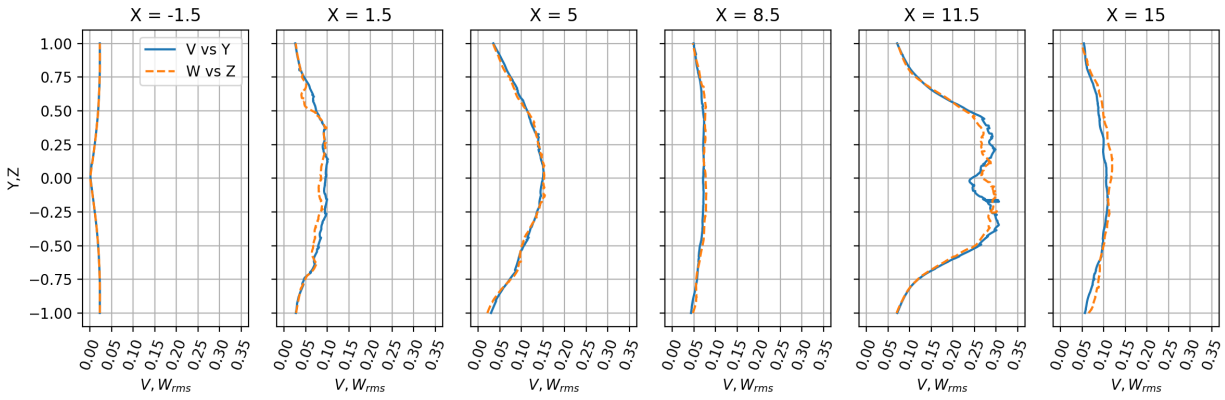

Figure A.13: RMS values of v and w velocity components along parallel to y and z transverse lines of the tandem spheres case.

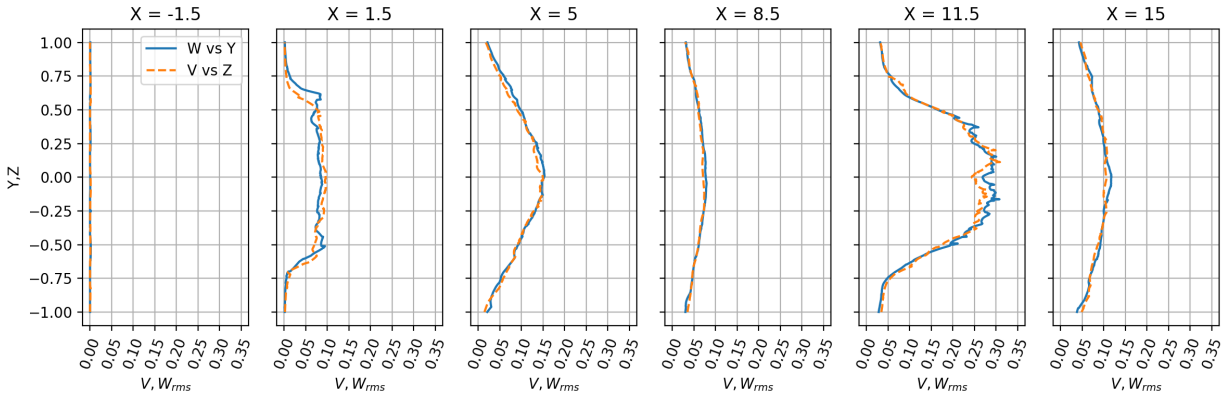

Figure A.14: RMS values of v and w velocity components along normal to y and z transverse lines of the tandem spheres case.

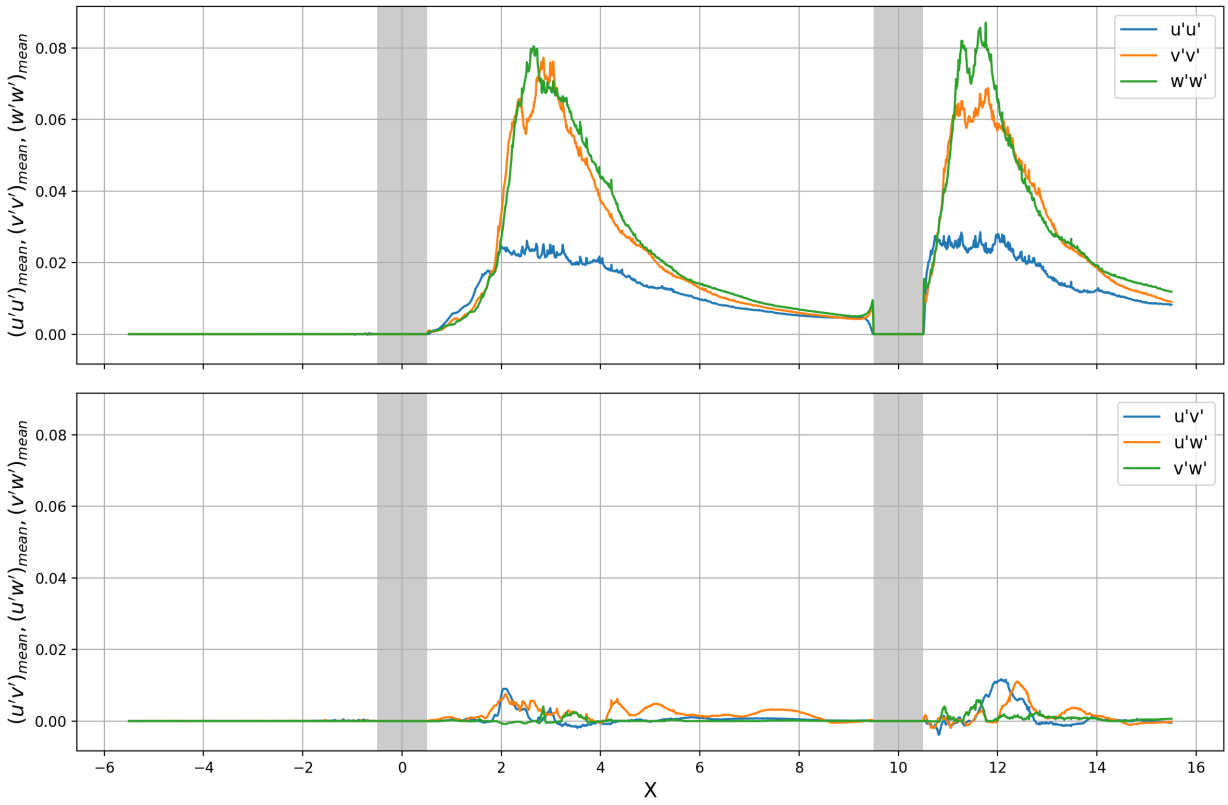

Figure A.15: Mean values of Reynolds stresses along centerline of the tandem spheres case.

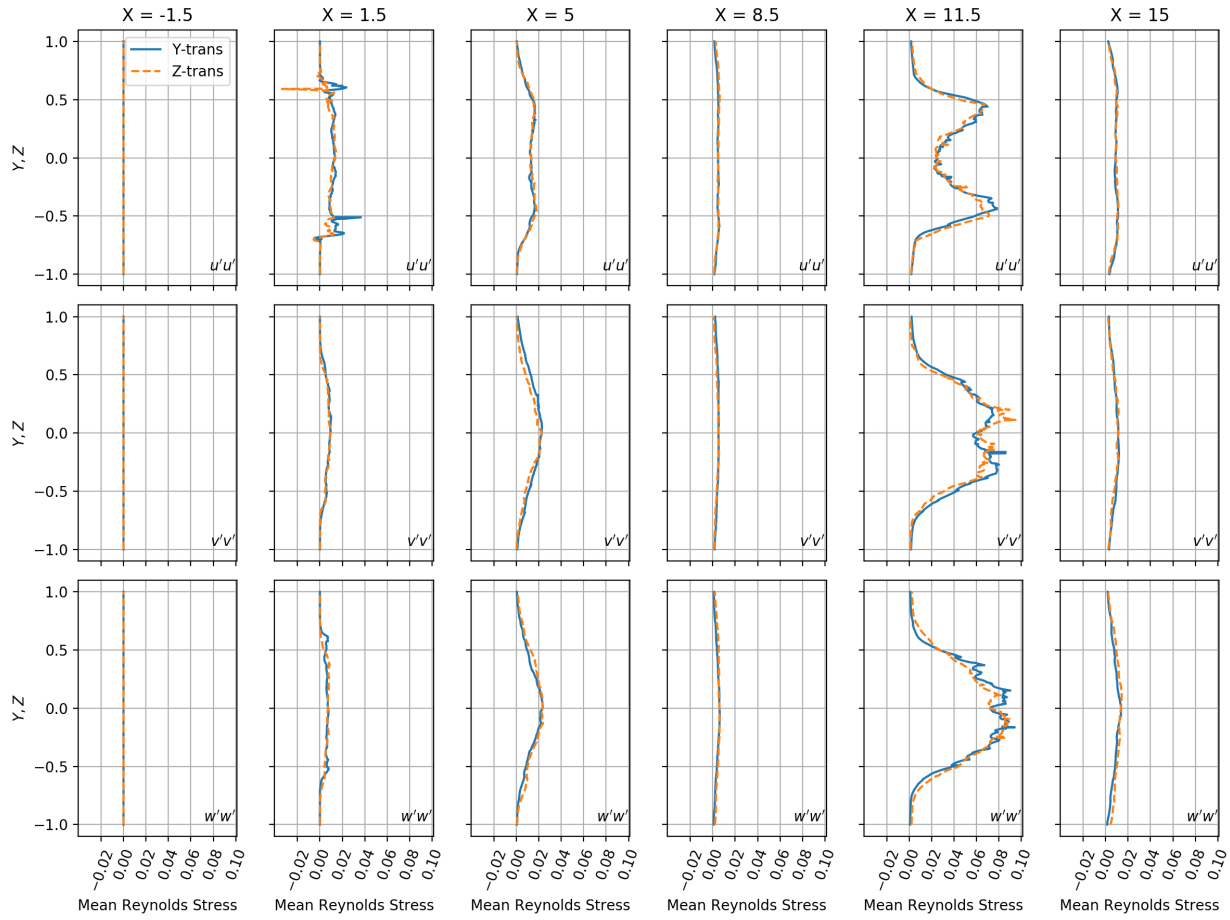

Figure A.16: Mean values of Reynolds normal stresses along y and z transverse lines of the tandem spheres case.

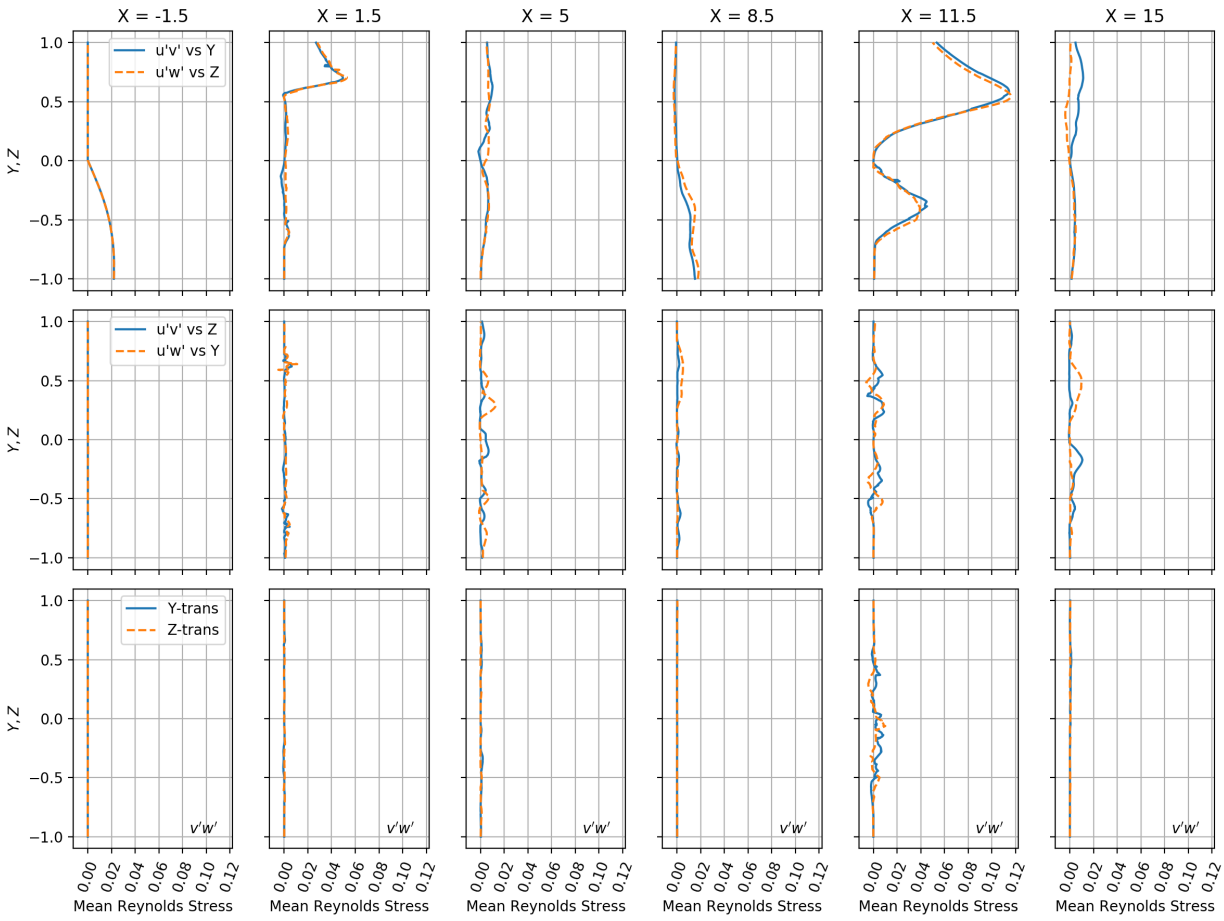

Figure A.17: Mean values of Reynolds shear stresses along y and z transverse lines of the tandem spheres case.

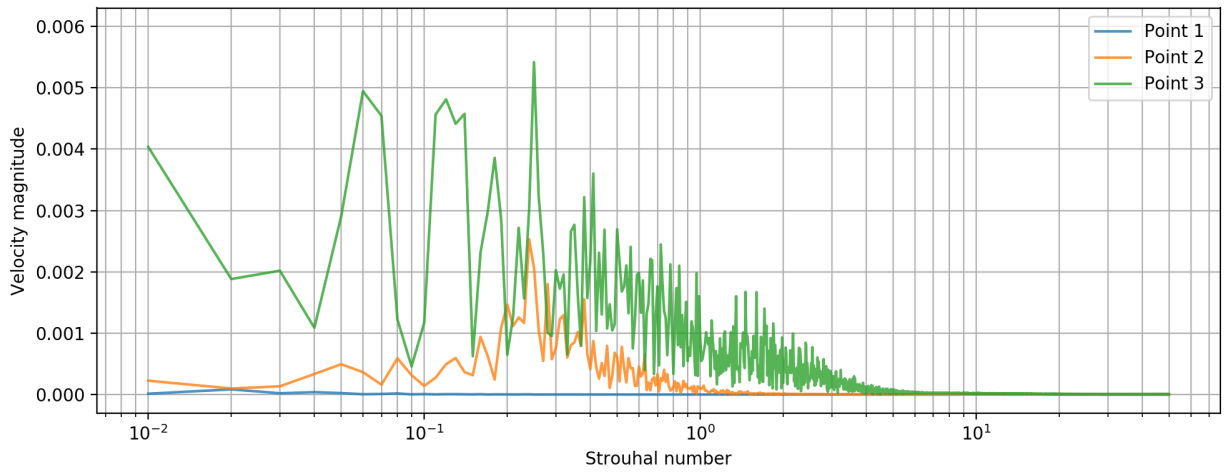

Figure A.18: Frequency spectra of velocity magnitude at specified points of the tandem spheres case.

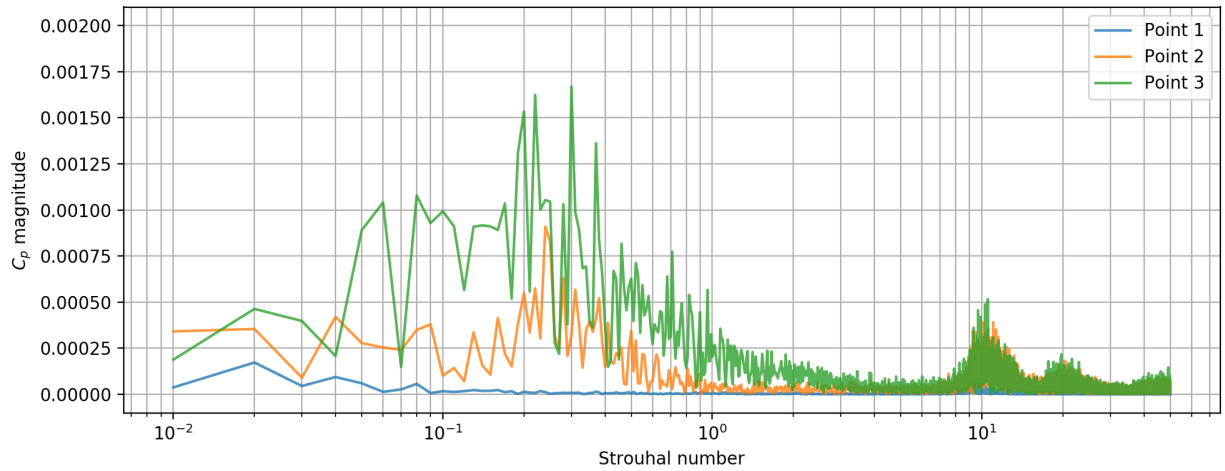

Figure A.19: Frequency spectra of pressure coefficient at specified points of the tandem spheres case.

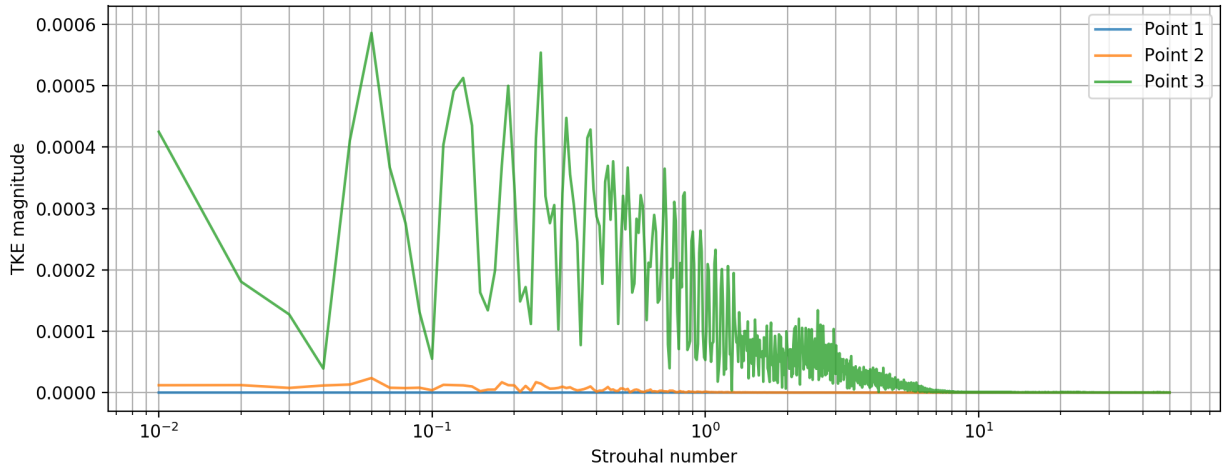

Figure A.20: Frequency spectra of turbulent kinetic energy at specified points of the tandem spheres case.

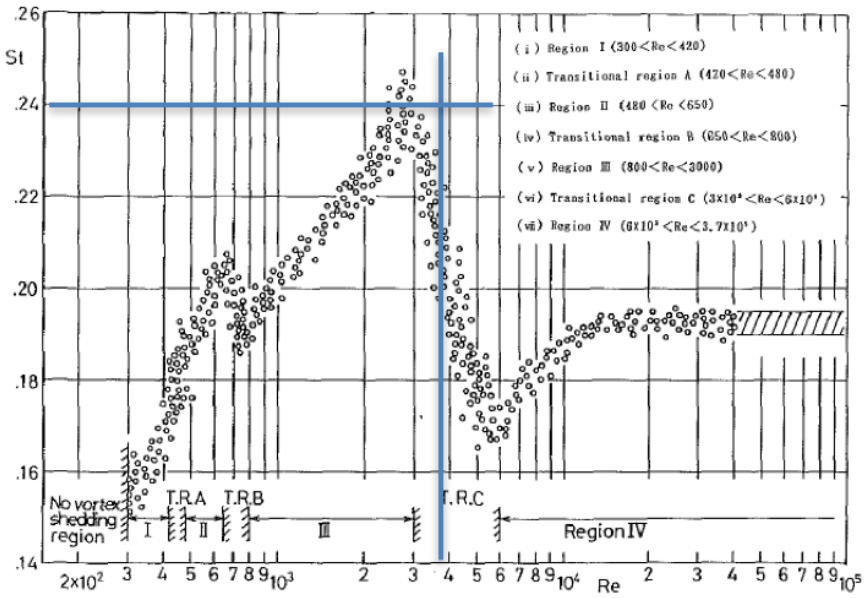

Figure A.21: Strouhal number for velocity magnitude peak at Point 2 compared to results from Sakamoto and Haniu [212].

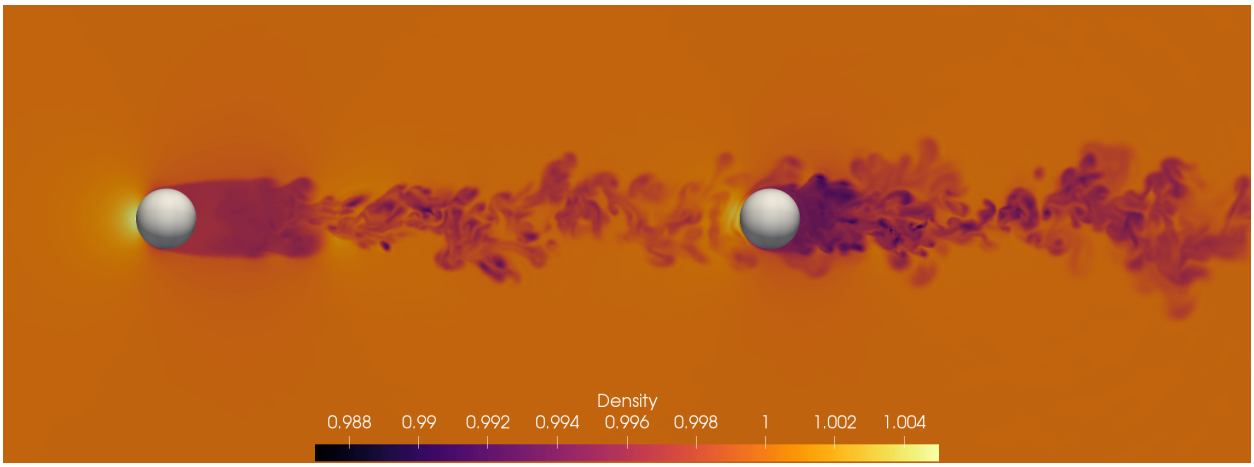

(a) Instantaneous density at $t^* = 150$

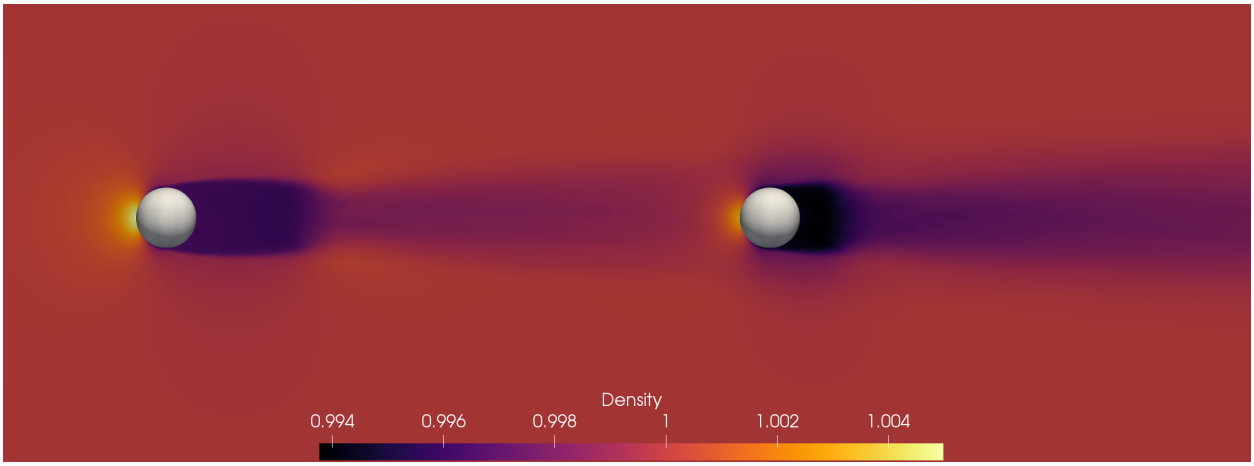

(b) Mean density

Figure A.22: Density contours on X-Y slice of tandem spheres.

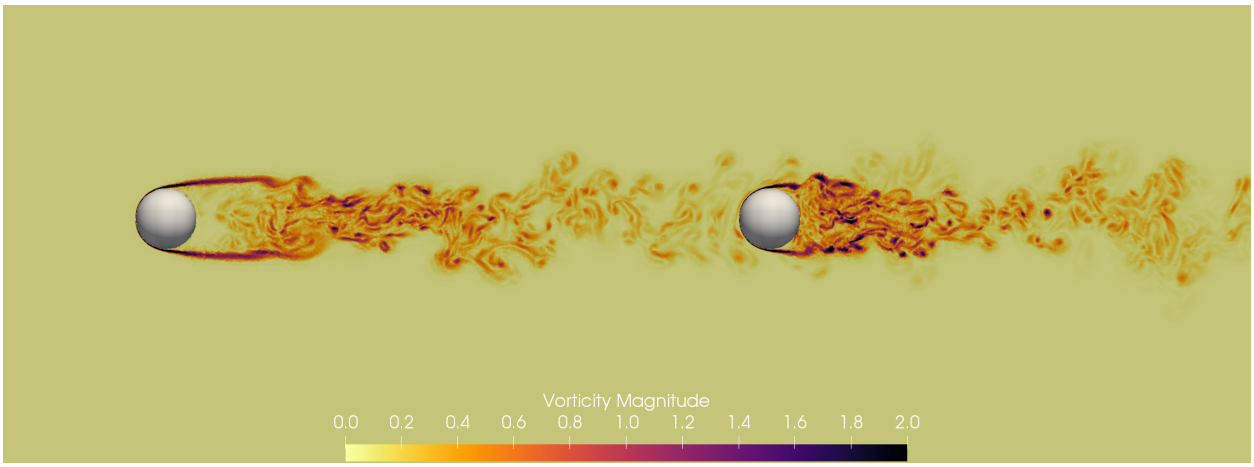

(a) Instantaneous vorticity magnitude at $t^* = 150$

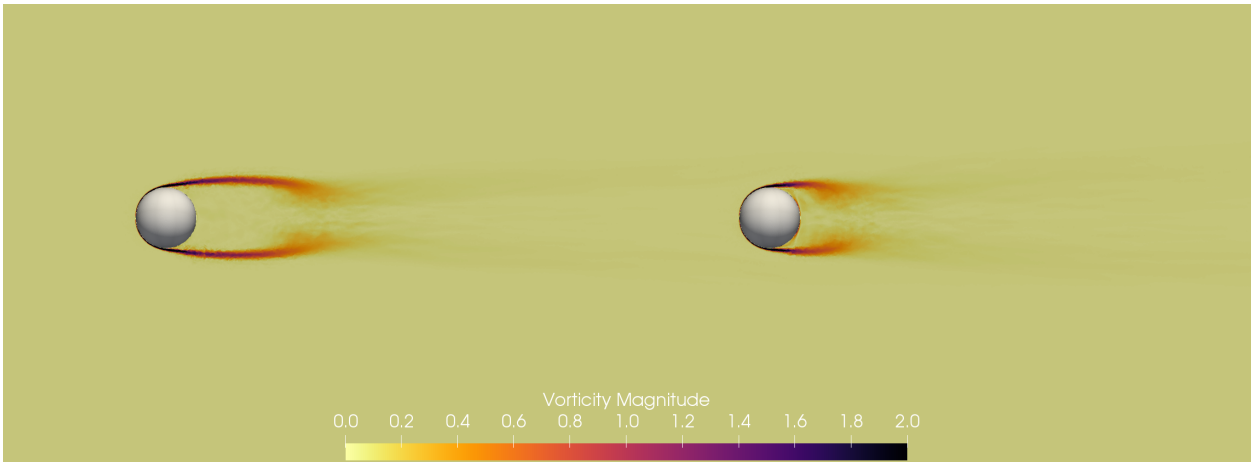

(b) Mean vorticity magnitude

Figure A.23: Vorticity magnitude contours on X-Y slice of tandem spheres.

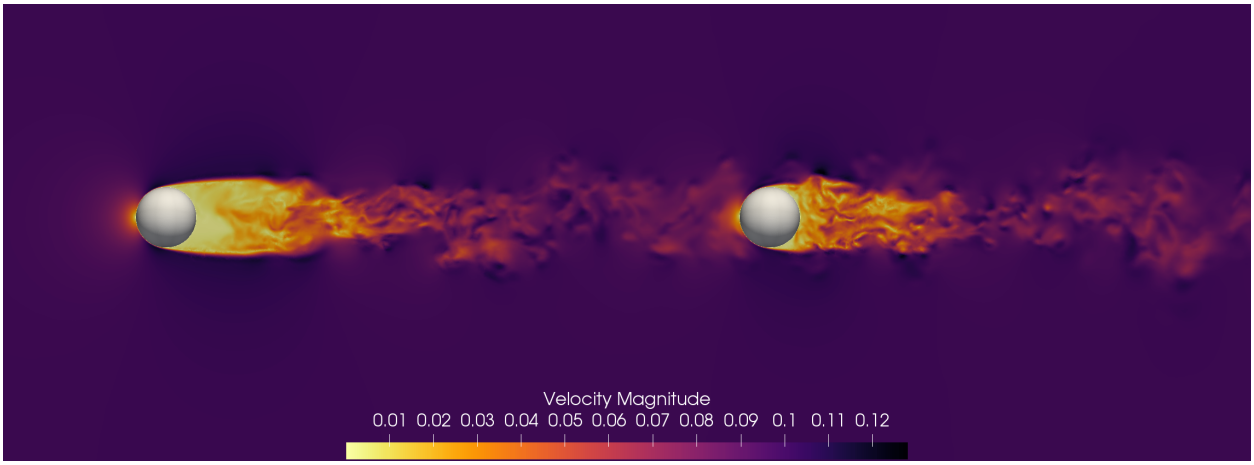

(a) Instantaneous velocity magnitude at $t^* = 150$

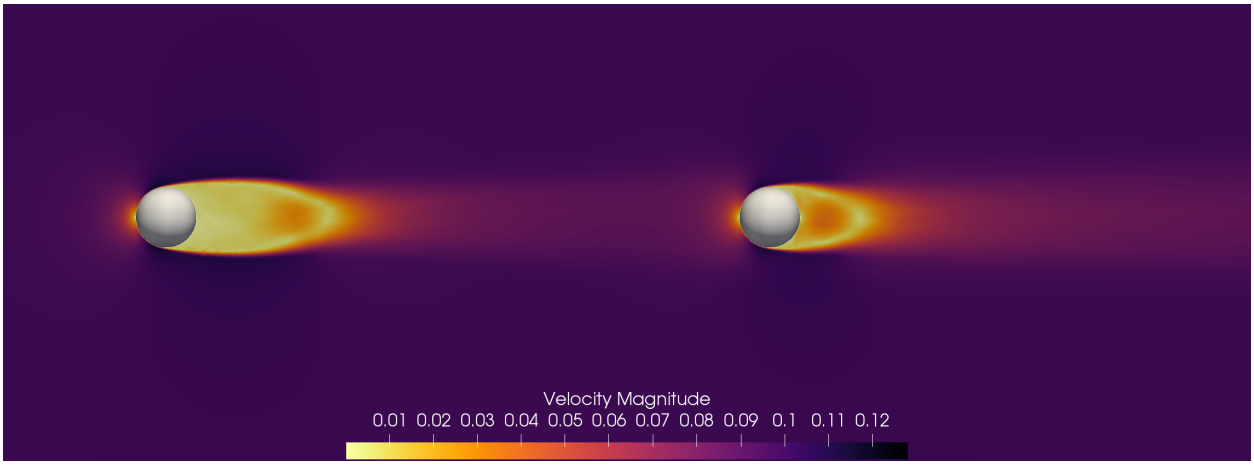

(b) Mean velocity magnitude

Figure A.24: Velocity magnitude contours on X-Y slice of tandem spheres.

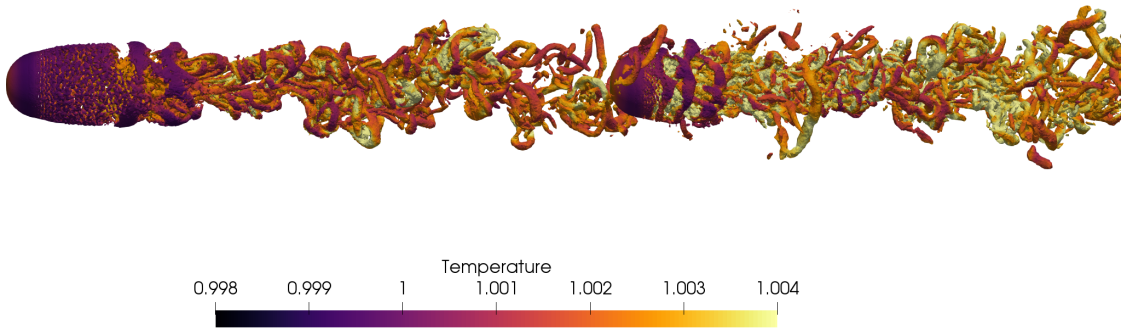

Figure A.25: Isosurfaces of Q-criterion of 0.01 colored by temperature for tandem spheres at $t^* = 150$.

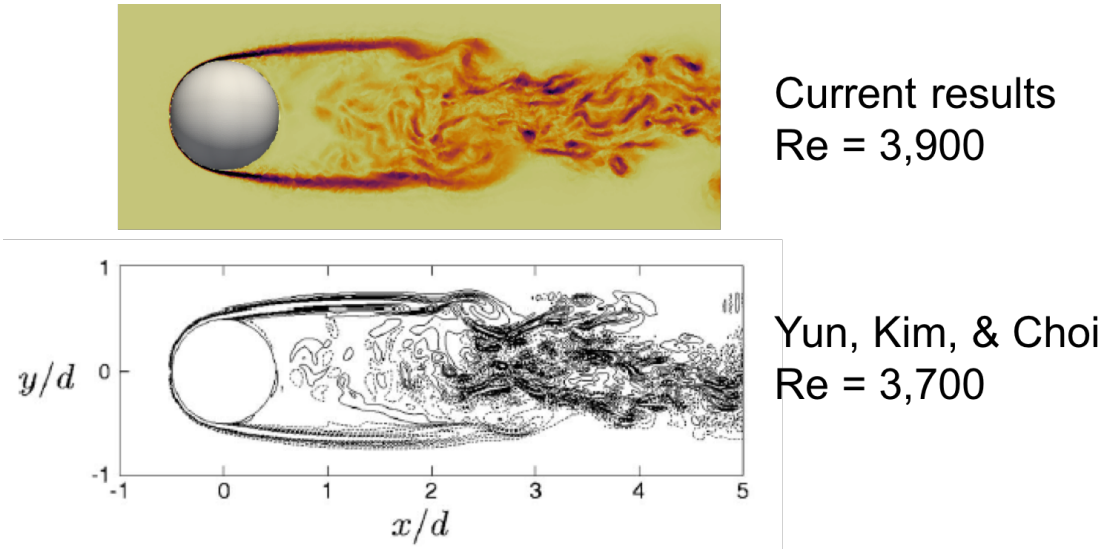

Figure A.26: Comparison of instantaneous vorticity contour at $t^* = 150$ to results from Yun, Kim, and Choi [213]

B Hybrid RANS/LES Modeling

B.1 Reynolds-Averaged Navier-Stokes Turbulence Modeling

Reynolds [214] developed the notion of describing instantaneous properties of turbulent flow (velocity, pressure, stress, strain, and other so called "passive contaminants" such as heat, chemical species, and particles) in terms of mean and fluctuating components. This is known as the *Reynolds decomposition*. Let the instantaneous value of a property be denoted by a lower-case letter, the mean component by an upper-case letter, and the fluctuating component by a lower-case letter with a prime. Taking the velocity as an example:

$$u_i = U_i + u_i' \tag{B.1}$$

U_i is the time averaged value of the instantaneous velocity, as given by:

$$U_i = \lim_{T\to\infty} \frac{1}{T} \int_{t_0}^{t_0+T} u_i dt \tag{B.2}$$

The time average of the fluctuating component is, by definition, zero.

When Reynolds decomposition is applied to the incompressible momentum equation, the *Reynolds momentum equation* results:

$$\rho \frac{\partial U_i}{\partial t} + \rho U_j \frac{\partial U_i}{\partial x_j} = -\frac{\partial p}{\partial x_i} + \frac{\partial}{\partial x_j}\left(2\mu S_{ij} - \rho\overline{u_i' u_j'}\right) \tag{B.3}$$

The $-\rho\overline{u_i' u_j'}$ term is known as the *Reynolds stress*. The off-diagonal components of this stress tensor are shear stresses that are the dominant mechanism for mean momentum transfer in turbulent flows. [215]

The Reynolds stress tensor, defined as $\tau_{ij}' = -\rho\overline{u_i' u_j'}$, represents six additional unknowns in the governing equations, which creates a closure problem. Rather than create six more independent equations to close the equation set, algebraic turbulence models commonly utilize the *Boussinesq approximation* (or more accurately, assumption) to reduce the number of unknowns from six to one. Boussinesq [216] suggested that the Reynolds stress could be modeled in the same manner analogous to the viscous stress, Eq. (3.5), where a new *eddy*

viscosity, μ_t, is used in place of the molecular viscosity, μ. The resulting value definition for the Reynolds stress tensor with the Boussinesq approximation is given in Eq. (B.4). The eddy viscosity is now the only unknown that must be modeled.

$$\tau'_{ij} = 2\mu_t A_{ij} \tag{B.4}$$

The governing equations are the same as those outlined in Section 3.1.1, but now the viscous stress tensor, Eq. (3.5), is replaced by Eq. (B.5), which includes turbulence contributions via the eddy viscosity. A turbulence model is used for closure.

$$\tau_{ij} = 2(\mu + \mu_t)A_{ij} \tag{B.5}$$

The one-equation, negative Spalart-Allmaras [217, 218] (SA) model without the trip term was coded into COFFE early in the solver's development. The overall transport equation is given in Eq. (B.6).

$$\begin{aligned}\frac{\partial \rho\tilde{\nu}}{\partial t} + \frac{\partial}{\partial x_j}\left(\rho\tilde{\nu}u_j - \frac{1}{\sigma}(\mu + f_n\rho\tilde{\nu})\frac{\partial\tilde{\nu}}{\partial x_j}\right) = \\ \frac{c_{b2}}{\sigma}\rho\left(\frac{\partial\tilde{\nu}}{\partial x_j}\frac{\partial\tilde{\nu}}{\partial x_j}\right) - \frac{1}{\sigma}(\nu - \tilde{\nu})\left(\frac{\partial\rho}{\partial x_j}\frac{\partial\tilde{\nu}}{\partial x_j}\right) + \rho P_n - \rho D_n\end{aligned} \tag{B.6}$$

Eddy viscosity, μ_t, is given by

$$\mu_t = \begin{cases}\rho\tilde{\nu}f_{v_1} & \tilde{\nu} \geq 0 \\ 0 & \tilde{\nu} < 0\end{cases} \qquad f_{v_1} = \frac{\chi^3}{\chi^3 + c_{v_1}^3} \qquad \chi \equiv \frac{\tilde{\nu}}{\nu}. \tag{B.7}$$

Within the SA transport equation, f_n is a modification to the diffusion coefficient,

$$f_n = \begin{cases}1 & \tilde{\nu} \geq 0 \\ \frac{c_{n1}+\chi^3}{c_{n1}-\chi^3} & \tilde{\nu} < 0\end{cases} \tag{B.8}$$

P_n and D_n are the production and wall destruction terms,

$$P_n = \begin{cases} c_{b1}(1 - f_{t_2})\tilde{S}\tilde{\nu} & \tilde{\nu} \geq 0 \\ c_{b1}(1 - c_{t_3})\tilde{S}\tilde{\nu} & \tilde{\nu} < 0 \end{cases} \tag{B.9}$$

$$D_n = \begin{cases} \left(c_{w1} f_w - \frac{c_{b1}}{\kappa^2}\right)\left(\frac{\tilde{\nu}}{d}\right)^2 & \tilde{\nu} \geq 0 \\ -c_{w1}\left(\frac{\tilde{\nu}}{d}\right)^2 & \tilde{\nu} < 0 \end{cases} \tag{B.10}$$

$\tilde{\omega}$ is the modified vorticity,

$$\tilde{\omega} = \begin{cases} \omega + \bar{\omega} & \bar{\omega} > -c_{v_2}\omega \\ \omega + \frac{\omega(c_{v_2}^2\omega + c_{v_3}\bar{\omega})}{(c_{v_3} - 2c_{v_2})\omega - \bar{\omega}} & \bar{\omega} \geq -c_{v_2}\omega \end{cases} \tag{B.11}$$

where ω is the magnitude of the vorticity and d is the distance to closest wall,

$$\omega = \left|\varepsilon_{ijk}\mathbf{e}_i \frac{\partial u_k}{\partial x_j}\right| \qquad \bar{\omega} = \frac{\tilde{\nu} f_{v_2}}{\kappa^2 d^2} \qquad f_{v_2} = 1 - \frac{\chi}{1 + \chi f_{v_1}} \tag{B.12}$$

f_{t_2} is the laminar suppression term,

$$f_{t_2} = c_{t_2} e^{-c_{t_4}\chi^2} \tag{B.13}$$

and the function f_w is given by

$$f_w = g\left(\frac{1 + c_{w3}^6}{g^6 + c_{w3}^6}\right)^{1/6} \qquad g = r + c_{w2}(r^6 - r) \qquad r = \min\left(\frac{\tilde{\nu}}{\tilde{\omega}\kappa^2 d^2}, r_{\lim}\right). \tag{B.14}$$

The constants are $\sigma = 2/3$, $\kappa = 0.41$, $c_{b1} = 0.1355$, $c_{b2} = 0.622$, $c_{n1} = 16$, $c_{t3} = 1.2$, $c_{t4} = 0.5$, $c_{v1} = 7.1$, $c_{v2} = 0.7$, $c_{v3} = 0.9$, $c_{w1} = c_{b1}/\kappa^2 + (1 + c_{b2})/\sigma$, $c_{w2} = 0.3$, $c_{w3} = 2$, and $r_{\lim} = 10$.

The 2013 version of Quadratic Constitutive Relation (QCR) for the SA model was also implemented earlier in development as an option for users to employ if necessary. SA-QCR2013 has shown a significant improvement over the standard SA model in corner flow applications. [219] Erwin et al. [220] made side-by-side comparisons of the SA and SA-QCR2013 models for test cases in the AIAA 6$^{\text{th}}$ Drag Prediction Workshop. They found that the QCR model was necessary to properly model the wing-body juncture.

QCR is essentially a modification to the standard Boussinesq approximation, wherein additional terms are added to model the directional dependance, or anisotropy, that creates secondary recirculation within complex flow fields. The modified Reynolds stress tensor is given in Eq. (B.15). τ'_{ij} is the turbulent stresses computed from the Boussinesq approximation, Eq. (B.4).

$$\tau'_{ij,QCR} = \tau'_{ij} - c_{cr1}(O_{ik}\tau'_{jk} + O_{jk}\tau'_{ik}) - c_{cr2}\mu_t\sqrt{2A_{mn}A_{mn}}\delta_{ij} \tag{B.15}$$

where

$$O_{ij} = \frac{2S_{ij}}{\sqrt{\frac{\partial u_m}{\partial x_n}\frac{\partial u_m}{\partial x_n}}}. \tag{B.16}$$

The constants are $c_{cr1} = 0.3$ and $c_{cr2} = 2.5$.

B.2 Single Sphere

Hybrid RANS/LES was employed for a test case studying vortex shedding around a sphere at a Mach number of 0.1 and a Reynolds number of 1×10^6, based on sphere diameter. A strictly laminar simulation with no turbulence modeling would not be appropriate at such a high Reynolds number for the given grid. The improved delayed detached eddy simulation (IDDES) model of Shur et al. [221], specifically the DDES branch with the Spalart-Allmaras (SA) one equation turbulence model of Spalart and Allmaras [217], was employed to address this issue. The SA model was already in place in COFFE to handle RANS simulations. [145]

The grid for this case was a sphere of diameter D centered in a larger sphere of diameter $50D$. It consisted of mixed $p = 1$ (2^{nd}-order accurate) elements, the counts of which are given below, with 2,281,468 nodes. The outer boundary was set to freestream, and the sphere boundary was set to no-slip wall. The BDF2 method was used with a non-dimensional time step of $\Delta t = 0.01$.

- tetrahedra: 10,407,113
- pyramids: 67,816
- hexahedra: 525,440
- prisms: 10,496

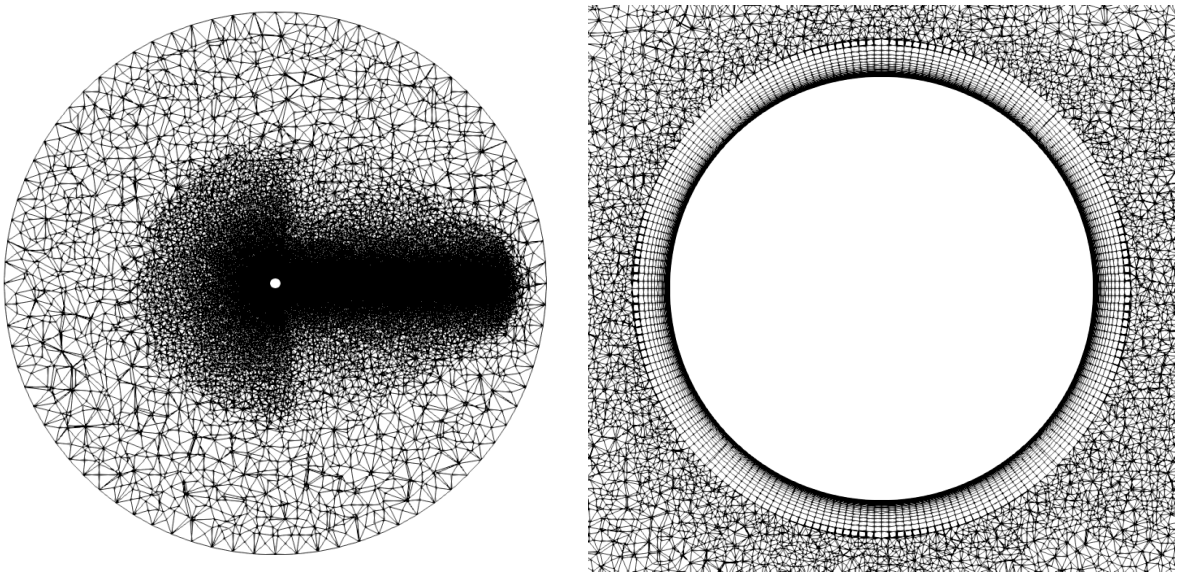

(a) Overall grid **(b)** Zoomed view of sphere

Figure B.1: Z-normal slice of grid for single sphere case

A strictly laminar simulation with no turbulence modeling would not be appropriate at such a high Reynolds number for the given grid. The improved delayed detached eddy simulation (IDDES) model of Shur et al. [221], specifically the DDES branch with the Spalart-Allmaras (SA) one equation turbulence model of Spalart and Allmaras [217], was employed to address this issue. The SA model was already in place in COFFE to handle RANS simulations. [145]

A short summary of the DDES branch of the IDDES model follows. In the original description of DDES, Spalart et al. [222] gave the DDES length scale, l_{DDES}, as

$$l_{DDES} = l_{RANS} - f_d \max\{0, (l_{RANS} - l_{LES})\} \tag{B.17}$$

where the delaying function, f_d, is defined as $f_d = 1 - \tanh[(8r_d)^3]$. This length scale replaces the RANS length scale, l_{RANS}, in subsequent calculations. r_d, defined in Eq. (B.18), is a marker that is 1 in the log layer and 0 in the freestream. It comes from the original SA model definition. [217]

$$r_d = \frac{\nu + \nu_t}{\kappa^2 d_w^2 \max\{[\sum_{i,j}(\partial u_i/\partial x_j)^2]^{1/2}, 10^{-10}\}} \tag{B.18}$$

The LES length scale, l_{LES}, is defined as

$$l_{LES} = C_{DES}\Psi\Delta \tag{B.19}$$

Within this equation, the subgrid length scale, Δ, is defined as

$$\Delta = \min\{\max[C_w d_w, C_w h_{max}, h_{wn}], h_{max}\},$$

where C_w is an empirical constant set to 0.15, d_w is the wall distance, and h_{wn} is the grid spacing in the wall-normal direction. Ψ is low Reynolds number correction. C_{DES} is the fundamental empirical constant of DES. [223]

Little experimental data were found at Reynolds numbers greater than 10^6. Achenbach [224, 225] conducted wind tunnel experiments on smooth spheres at high Reynolds numbers ($5 \times 10^4 \leq Re \leq 6 \times 10^6$) in the early 1970s, and Bacon and Reid [226] conducted wind tunnel and free flight experiments in the early 1920s.

The lift and drag coefficients as a function of time are shown in Fig. B.2. Also included in the plot is a radial force coefficient, that is defined as the force acting normal to the axis of flow. The simulation was started impulsively. Only data outside of the shaded startup region were used for subsequent calculations. Achenbach [225] reported that periodic vortex shedding could not be found beyond the upper critical Reynolds number, $Re > 3.7 \times 10^5$. No dominant frequency was found via spectral analysis of the lift and radial force coefficients for the current results, which corroborates the findings of Achenbach.

The mean drag coefficient for the current results is plotted with data from Achenbach [225] and Bacon and Reid [226] in Fig. B.3. The mean of the current results is indicated by the marker, and the shaded region around it is a violin plot that shows the probability distribution of the calculated drag coefficients. The current results are in good agreement with the experimental data, particularly with the free air data of Bacon and Reid.

Achenbach [224] also gave results for the friction contribution to the drag coefficient at high Reynolds numbers. The friction contribution for the current results is plotted, along with the data from Achenbach, in Fig. B.4. Again the shaded region around it is a violin

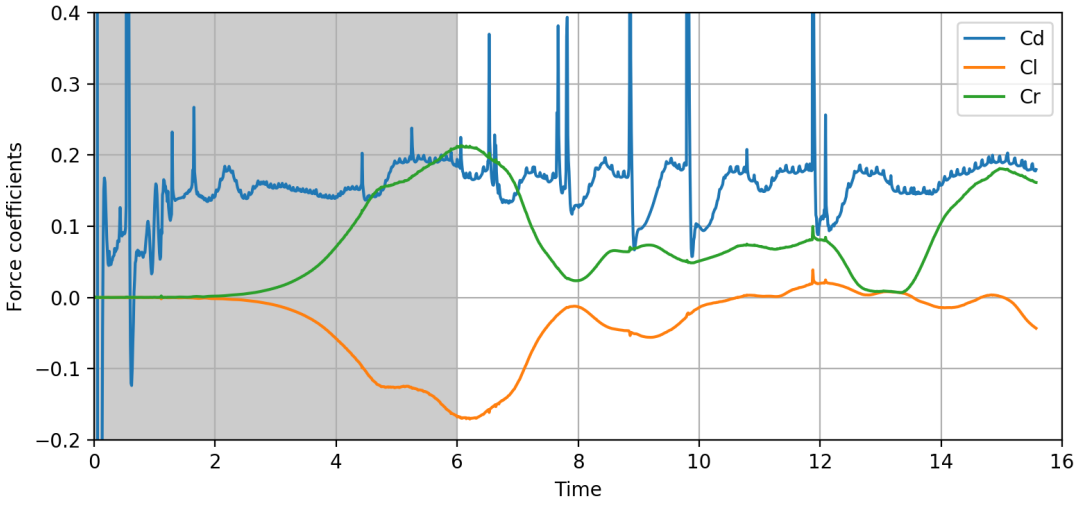

Figure B.2: Lift, drag, and radial force coefficients for a sphere at $Re = 10^6$

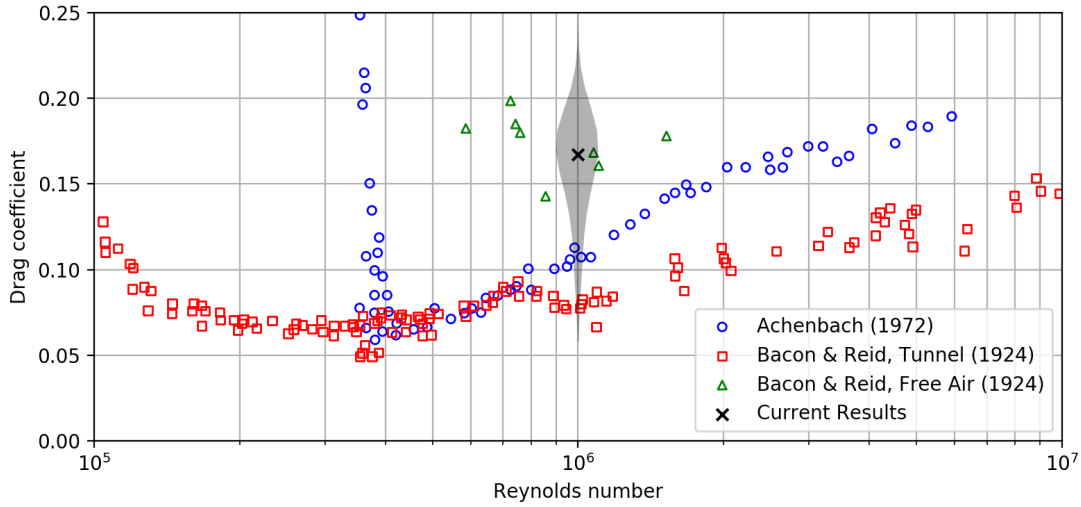

Figure B.3: Comparison of the mean drag coefficient for a sphere at $Re = 10^6$ to experiments at high Reynolds numbers. Shaded region represents the probability distribution of the calculated C_d from the current results.

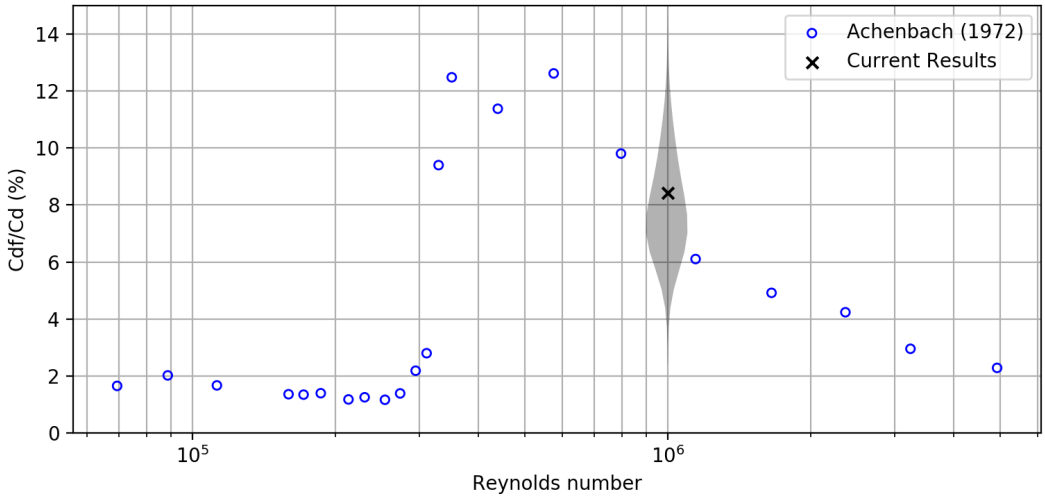

Figure B.4: Comparison of the friction contribution to the drag coefficient for a sphere at $Re = 10^6$ to experiments at high Reynolds numbers. Shaded region represents the probability distribution of the calculated C_{df}/C_d from the current results.

plot that shows the probability distribution of the calculated values. The current results are in very good agreement with Achenbach's data.

Qualitative images of the flow field at the last time step are given below. The vorticity magnitude on a longitudinal slice through the center of the sphere is shown in Fig. B.5. A Kármán vortex street, typical of flows around bluff bodies with periodically vortex shedding, is not apparent in this image. Isosurfaces of Q-criterion, which indicate coherent vortical structures, colored by density and vorticity magnitude are shown in Figs. B.6 and B.7, respectively.

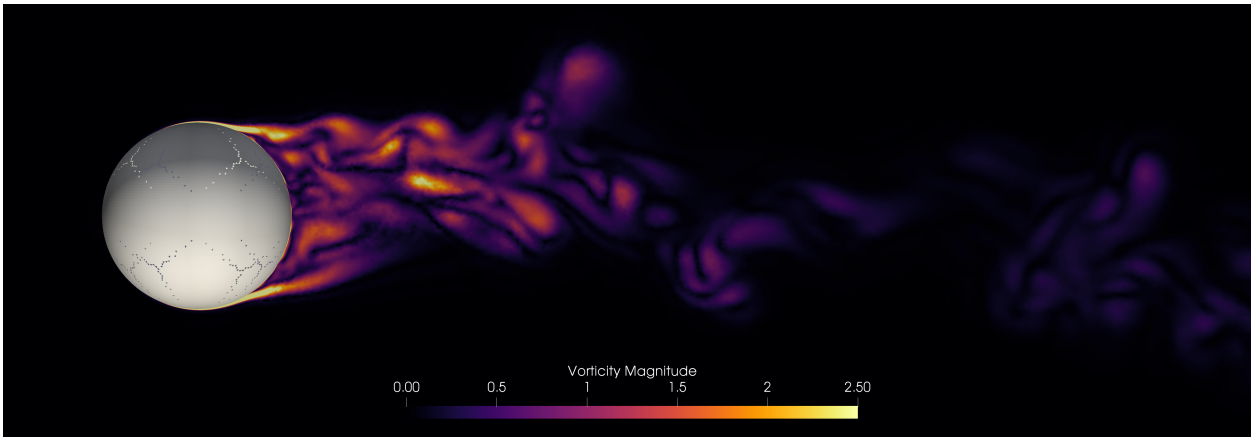

Figure B.5: Contour of vorticity magnitude on longitudinal slice of sphere solution at $Re = 10^6$

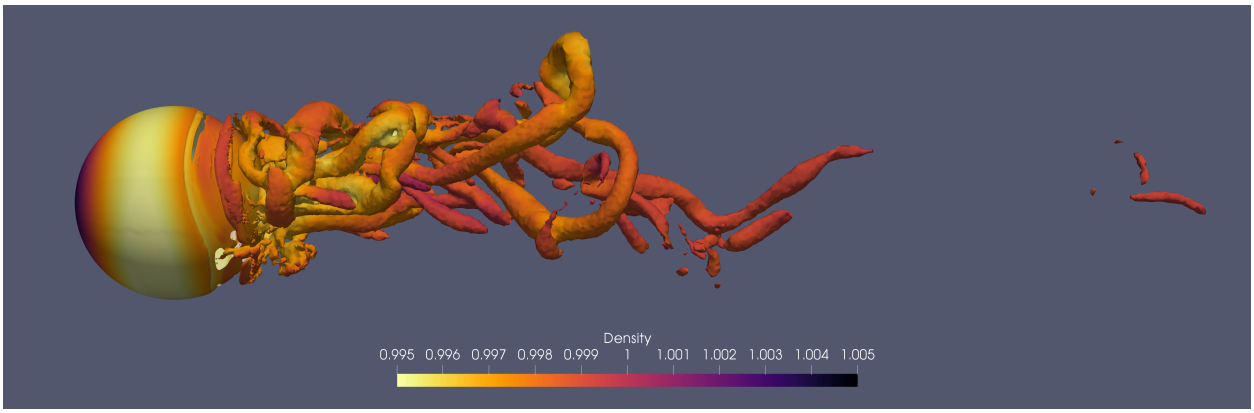

Figure B.6: Isosurface of 0.1 Q-criterion colored by density for sphere solution at $Re = 10^6$, side view

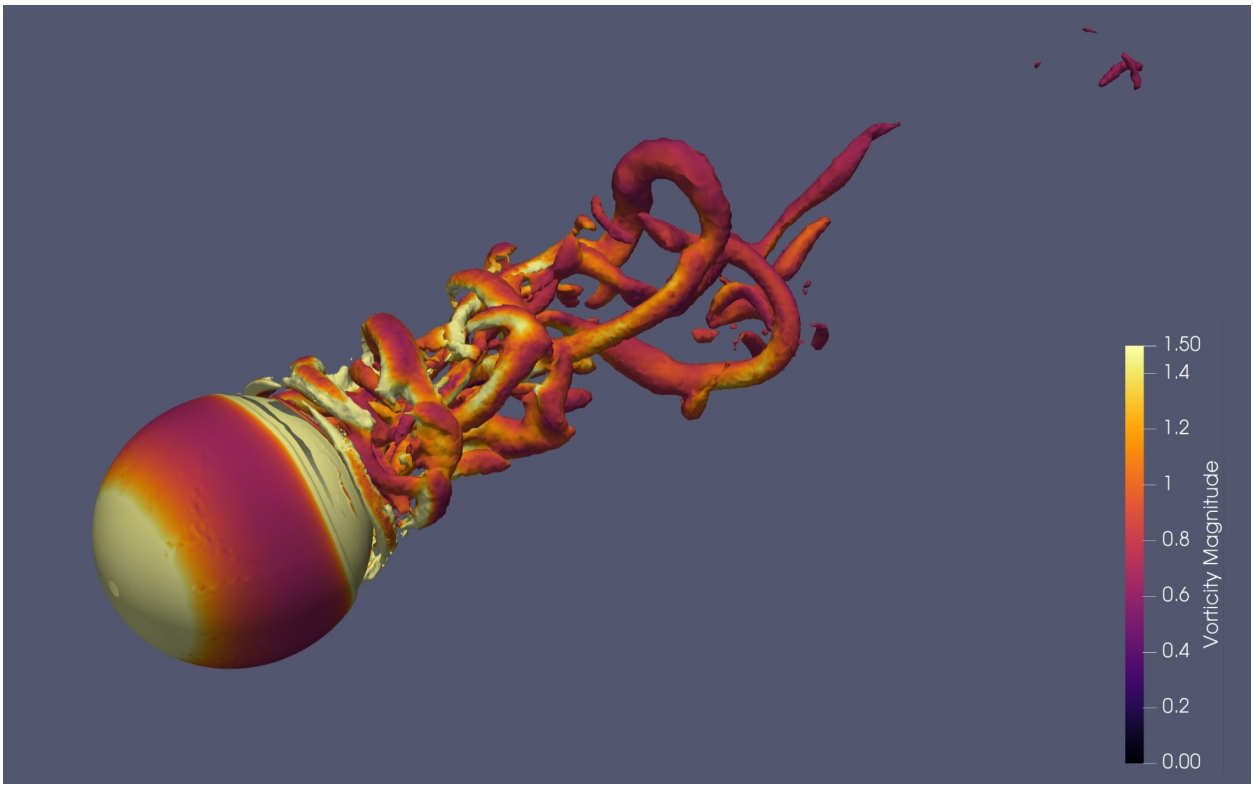

Figure B.7: Isosurface of 0.1 Q-criterion colored by vorticity magnitude for sphere solution at $Re = 10^6$, isometric view

C Current Sensor Shock Simulations

COFFE's current shock capturing technique, described in Section 3.4, was applied to two viscous cases: the hypersonic circular cylinder and the viscous shock tube. The hypersonic cylinder is a steady case used to evaluate the current shock capturing technique on a grid with high spatial order, independent of time, and the viscous shock tube case is an unsteady case used to evaluate the combined effect of high spatial and high temporal order. The current shock capturing approach was run for viscous cases to demonstrate that it is capable of capturing shocks when viscosity is present in the flow. The current approach failed when running on inviscid cases because of its inability to dissipate numerical errors.

C.1 Hypersonic Circular Cylinder

The hypersonic circular cylinder case is commonly used to test a solver for the carbuncle phenomenon, which is described in Section 2.3.1. The freestream conditions for this case were taken from the FUN3D website[4], and they are shown below.

U_∞	$5,000\ m/s$
ρ_∞	$0.001\ kg/m^3$
T_∞	$200\ K$
T_{wall}	$500\ K$
M_∞	17.605
Re_R	376,930

The grid, shown in Fig. C.1, consisted of 160-by-160 P2 quadrilateral elements. The initial wall spacing was 1×10^{-5}, and the grid was stretched radially by a factor of 1.075. The circular cylinder was set to an isothermal, no-slip wall, the outer boundary condition away from the wall was inflow, and the boundaries above and below the cylinder were outflow.

Temperature and pressure contours are shown in Fig. C.2. These plots show that the carbuncle phenomenon is not present. This is also confirmed in the temperature, pressure, and density traces along the stagnation streamline, shown in Fig. C.3. The stagnation

[4] https://fun3d.larc.nasa.gov

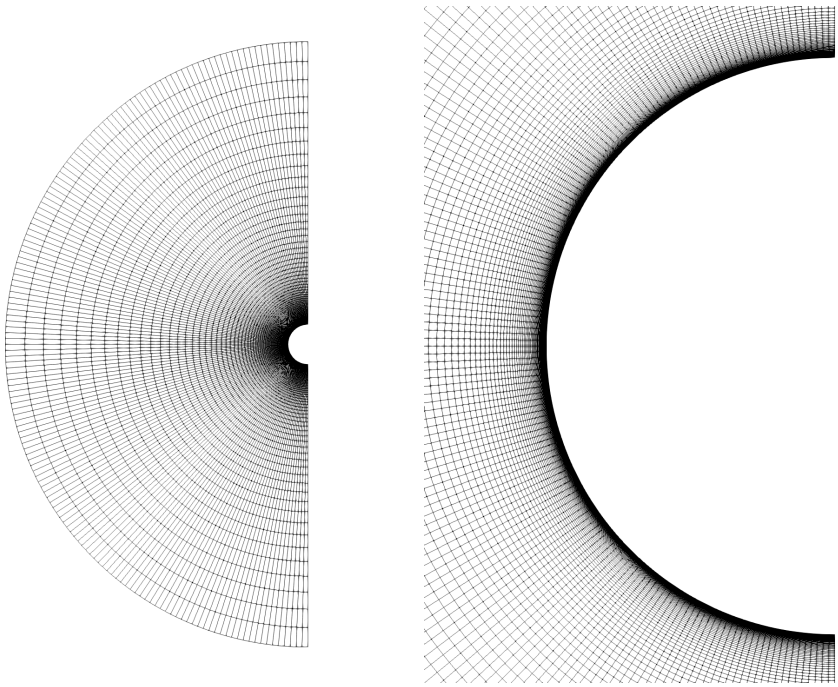

(a) Overall view **(b)** Zoomed view of cylinder

Figure C.1: Grid for hypersonic circular cylinder test case

streamline traces compare well with values from NASA's LAURA code. [227] The current results have steeper property gradients at the shock than the LAURA code, which may account for the slight overshoots. The thermodynamic property oscillations in Fig. C.2 and Fig. C.3 are manifestations of Gibb's phenomenon, discussed in Section 2.3.1, which is present in the vicinity of the shock.

The pressure coefficient and wall heat transfer are displayed in Fig. C.4, along with results from the LAURA code. [227] The pressure coefficients were nearly identical between the two codes. The heat transfer, however, showed similar trends, but COFFE predicted an increase in heat transfer just off of the stagnation point that the LAURA code did not. This increase may be the result of Gibb's phenomenon.

C.2 Viscous Shock Tube

Shock-tube configurations have often been used as test cases for transient numerical methods. [228–232] This case, based on the one run by Nichols and Heikkinen [228], is attractive because the position and strength of the normal shock, expansion, and contact surface can

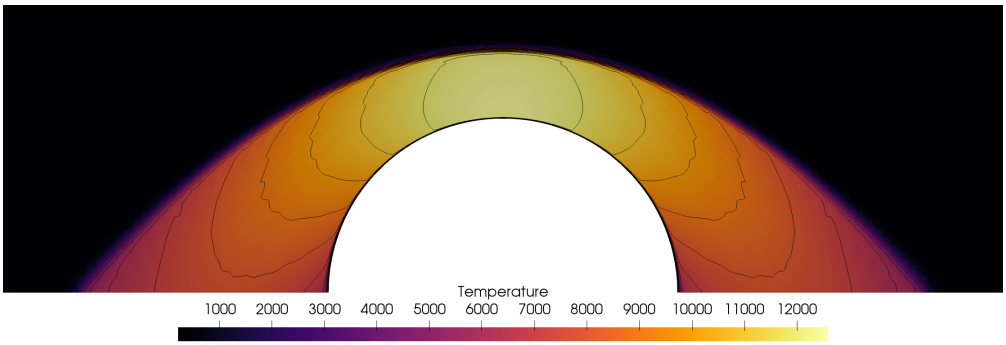

(a) Temperature (K)

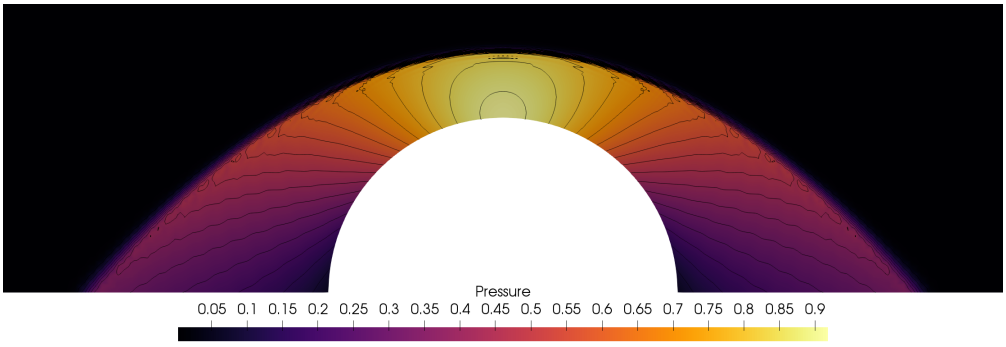

(b) Pressure ($p/\rho_\infty u_\infty^2$)

Figure C.2: Temperature and pressure contours for circular cylinder at $Re_R = 376,930$, $M_\infty = 17.605$

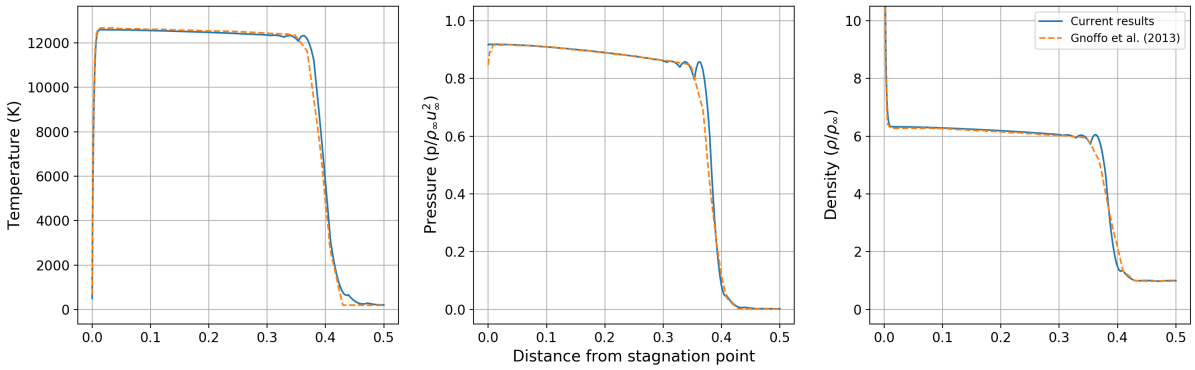

Figure C.3: Temperature, pressure, and density along stagnation streamline for circular cylinder at $Re_R = 376,930$, $M_\infty = 17.605$. Results compared to values from the NASA LAURA code. [227]

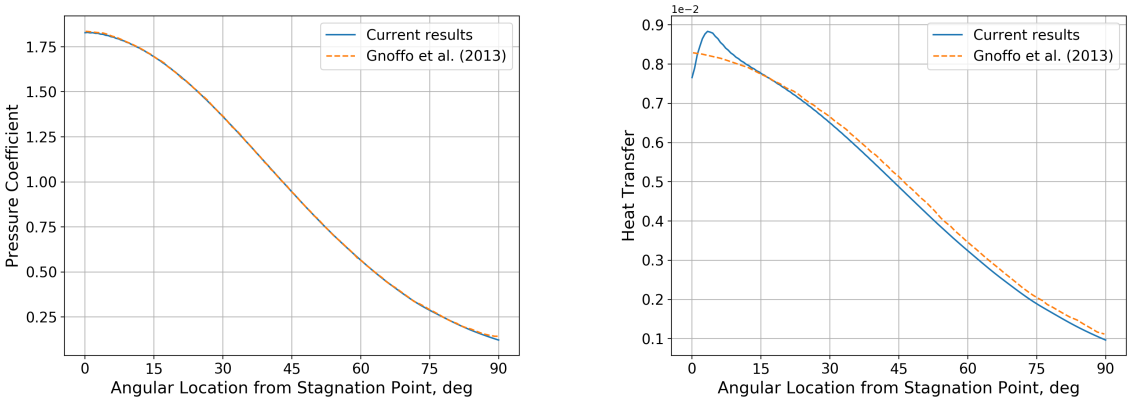

(a) Pressure Coefficient **(b)** Wall Heat Transfer

Figure C.4: Surface pressure coefficient and heat transfer for circular cylinder at $Re_R = 376,930$, $M_\infty = 17.605$. Results compared to values from the NASA LAURA code. [227]

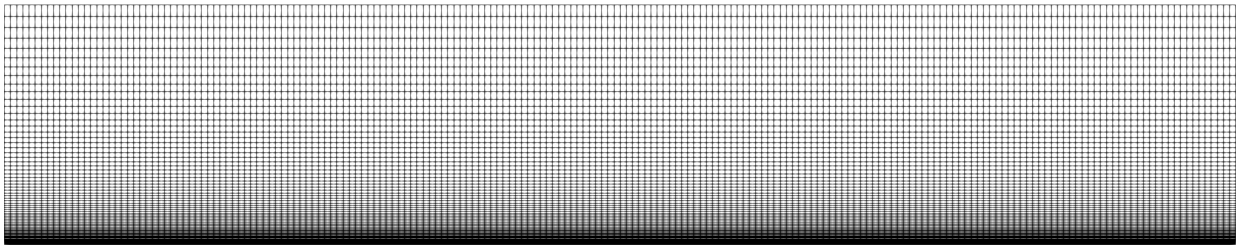

Figure C.5: Shock tube grid

be compared to inviscid flow theory, and heat transfer results from the viscous, isothermal wall can be compared to the previous numerical results.

This case was run on a rectangular grid, shown in Fig. C.5, consisting of 200-by-80 P2 quadrilateral elements. The grid spanned $0 < x < 1$, and the initial spacing in the y-direction was 0.0002, which provided a $y+$ value of approximately 0.1 at the bottom wall. Cells were grown off of the bottom wall with a growth factor of 1.05. The bottom boundary was a viscous, isothermal wall set to $T_{wall}/T_{ref} = 1$, and the remaining 3 walls were set to inviscid walls.

The solution was initialized with left and right states separated at $x = 0.5$. The left state was set to $(\rho_L, u_L, v_L, T_L) = (1, 0, 0, 1)$, and the right state was set to $(\rho_R, u_R, v_R, T_R) = (0.1, 0, 0, 1)$. The Reynolds number per unit length for this simulation, based on a_∞, was

10,000[5]. Simulations were completed for a non-dimensional time step[6] of 0.000625 using each of the time integration methods discussed above. The results were evaluated at $t = 0.2$.

The density and mass, momentum, and energy fluxes along the top boundary, along with the inviscid values, are given in Fig. C.6. Detailed views of the density at the normal shock, contact surface, and expansion are shown in Fig. C.7. Generally speaking, the BDF1 method smoothed out the changes in density across the shock, the contact surface, and between the expansion and the quiescent high-pressure driver region more than the other time integration methods. The BDF2 methods and the SDIRK45 method provided a much steeper density gradient across the shock, and the SDIRK45 method did so without producing the overshoot that is present in the BDF2 results.

Heat transfer along the bottom wall is shown in Fig. C.8. These results are qualitatively similar to those given by Nichols and Heikkinen [228], but the magnitude is reduced by a factor of 10 because the Reynolds number was also reduced by that amount. The heat transfer peak occurs just after the shock wave, and the peak value, shown in Fig. C.8b, shows that the BDF1 method smooths out the value, just as it did with density, resulting in a peak value that is approximately 33% lower than the BDF2 and SDIRK45 values.

C.3 Summary

The hypersonic circular cylinder case was used to ensure that COFFE does not produce a carbuncle phenomenon for supersonic bluff body simulations. The current results showed that the inviscid flux calculation in COFFE does not induce the carbuncle phenomenon for this case. Values of density, pressure, and temperature along the stagnation streamline compared favorably to results from the LAURA code, [227] as did surface pressure coefficient and heat transfer. Slight overshoots in the thermodynamic properties downstream of the shock were identified, which may be related to the steep property gradients at the shock. COFFE also predicted a higher heat transfer just off of the stagnation point.

[5]The Reynolds number run by Nichols and Heikkinen [228] was 100,000, so the results with respect to heat transfer are expected to be diminished proportionally.

[6]Time step non-dimensionalized by L/a_∞.

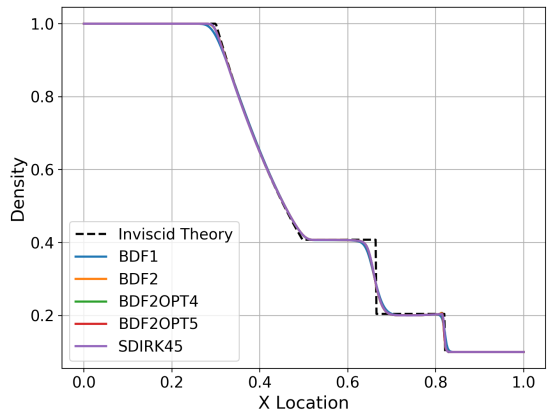

(a) Density

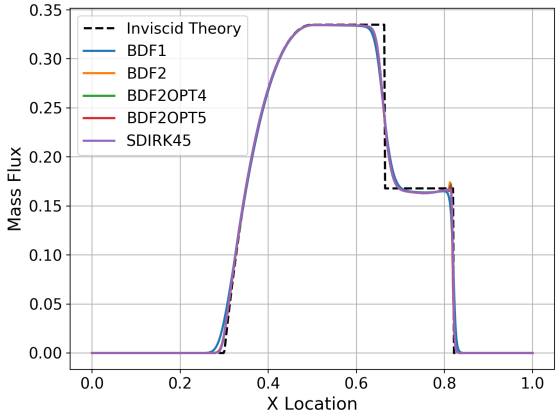

(b) Mass flux

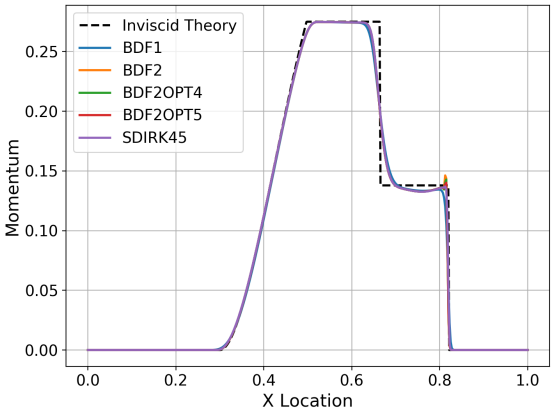

(c) Momentum flux

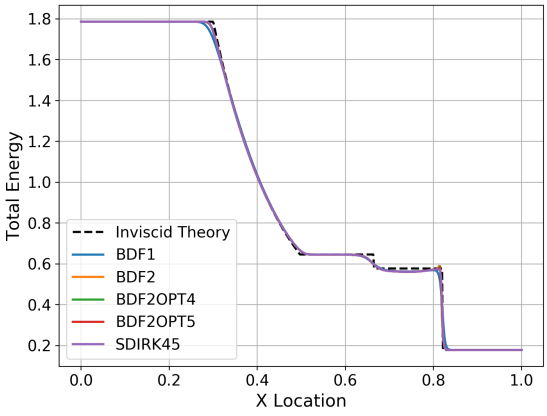

(d) Total energy flux

Figure C.6: Shock tube centerline conditions at $t = 0.2$

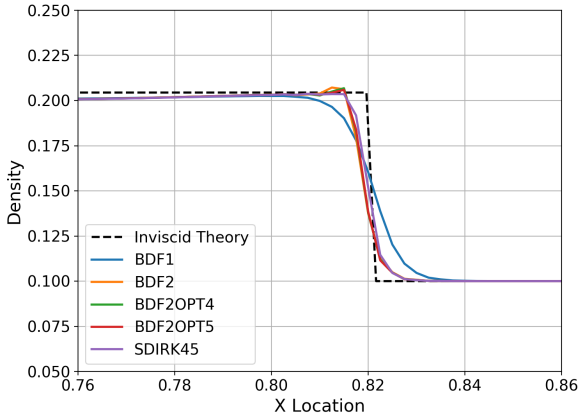

(a) Normal shock

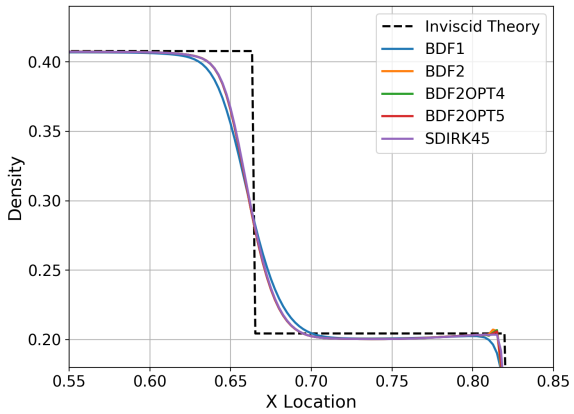

(b) Contact surface

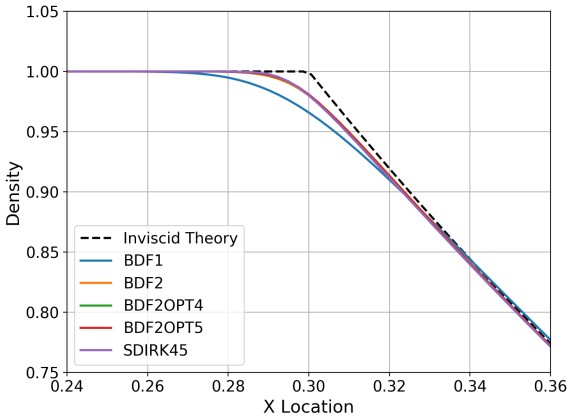

(c) Expansion

Figure C.7: Detailed shock tube centerline density at $t = 0.2$

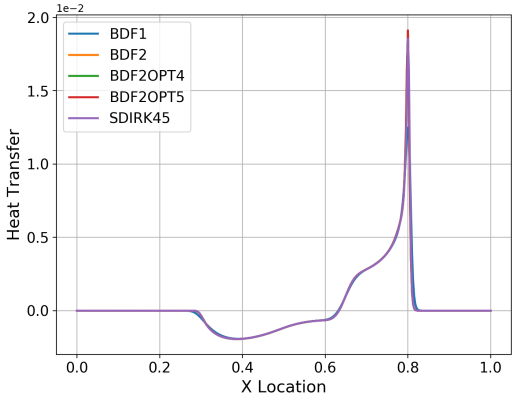

(a) Heat Transfer

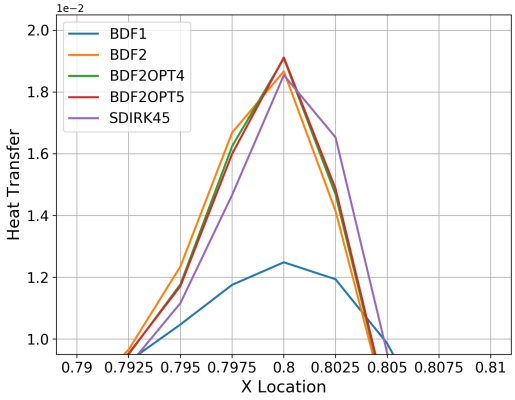

(b) Peak after Shock

Figure C.8: Shock tube wall heat transfer at $t = 0.2$

The viscous shock tube problem assessed COFFE's ability to handle a moving shock wave using various temporal methods. The BDF1 method, with the highest temporal error, tended to smooth out the discontinuous jumps in flow and surface properties, such as density and heat transfer, due to the shock. The SDIRK45 method provided a steeper density gradient across the shock without overshooting, like the BDF2 method did. The flow properties at the centerline matched the inviscid values, and the heat transfer along the isothermal, no-slip wall matched expected results.

Vita

Kevin Raymond Holst was born on October 31, 1983, in Fort Belvoir, Virginia, to Herbert and Susan Holst. He graduated from Bartlett High School in May of 2002 and pursued interests in aviation at Middle Tennessee State University, earning his private pilot certificate in December of 2002. In May of 2007 Kevin received his B.S. in Aerospace Engineering from the University of Tennessee, Knoxville. He then start working as an analysis engineer at Arnold Engineering Development Complex (AEDC) and began work on his M.S. in Aerospace Engineering at the University of Tennessee Space Institute. He was awarded his M.S. degree in May of 2012 and immediately began work on his Ph.D. Kevin currently works for the United States Air Force as a CFD code developer at AEDC.